SCULPTING LIGHT
USING DNA ORIGAMI-TEMPLATED
NANOPARTICLE ASSEMBLIES

MIHIR DASS

Munich 2023

SCULPTING LIGHT
USING DNA ORIGAMI-TEMPLATED
NANOPARTICLE ASSEMBLIES

MIHIR DASS

Dissertation

durchgeführt an der Fakultät für Physik
der Ludwig-Maximilians-Universität
München

vorgelegt von
Mihir Dass
aus Delhi, India

München, 20.11.2023

Erstgutachter: Prof. Dr. Tim Liedl

Zweitgutachter: Prof. Alexander Govorov

Tag der Einreichung: 20.11.2023

Tag der mündlichen Prüfung: 18.12.2023

Science and everyday life cannot and should not be separated. Science, for me, gives a partial explanation of life. In so far as it goes, it is based on fact, experience and experiment.

- Rosalind Franklin, in a letter to her father, 1940.

It feels so nice to enjoy life.

- Overheard in the Salinenhof, LMU.

ZUSAMMENFASSUNG

Das optische Verhalten von Materialien auf der Makroebene wird durch ihre Nanostruktur beeinflusst. Die Fähigkeit, neue Nanoarchitekturen zu schaffen und zu gestalten, ermöglicht es uns, Materialien mit neuartigen Eigenschaften zu entwickeln. Die DNA-Nanotechnologie, insbesondere die DNA-Origami-Technik, ermöglicht es mittels Selbstorganisation, um nanoskopische Objekte in benutzerdefinierten Geometrien anzuordnen. In dieser Doktorarbeit nutzen wir dies Eigenschaft, um die optische Reaktion von plasmonischen Nanopartikel-Assemblagen in zwei Bereichen zu steuern: chirale Plasmonik und physisch unkopierbare Funktionen (PUFs). Zunächst diskutieren wir Fortschritte bei der Verwendung mithilfe von DNA-Origami entworfenen plasmonischen Materialien zur empfindlichen Biomoleküldetektion. Dann behandeln wir die Synthese und Eigenschaften von chiralen Nanostab-Dimeren, wobei wir uns auf Silber-Gold Kern-Schale-Nanostäbe konzentrieren. Durch die Verwendung einer neuartigen Ein-Topf-Methode erreichen wir monodisperse Nanostäbe mit präziser Kontrolle über Größe, Seitenverhältnis und Silberschalendicke. Diese Nanopartikel bieten abstimmbare optische Eigenschaften und sind mit DNA funktionalisiert, was ihre Organisation in spezifischen chiralen Geometrien durch DNA-Origami ermöglicht. Unsere Erkenntnisse erweitern die spektrale Kontrolle über das zirkulardichroische Signal und bieten potenzielle Anwendungen in der empfindlichen Biomoleküldetektion.

Wir verwenden die Kern-Schale-Partikel und DNA-Origami in Kombination mit Nanosphären-Lithographie, um ein neuartiges, unkopierbares Etikett zur Bekämpfung von Fälschungen zu schaffen. Traditionelle kryptografische Methoden, die auf Einwegfunktionen basieren, werden diskutiert, zusammen mit ihren technologischen und theoretischen Einschränkungen. Wir führen PUFs als Alternative ein, mit einem Schwerpunkt auf optischen PUFs, die gegen verschiedene Arten von Angriffen und Klonversuchen robust sind. Unsere PUFs weisen ein breites Spektrum an Farbtönen aufgrund starker plasmonischer Kopplung auf, was ihre Sicherheitsmerkmale verbessert. Darüber hinaus werden diese PUFs nahtlos mit einem kostengünstigen, 3D-gedruckten Auslesewerkzeug integriert, wodurch die Lücke zwischen experimenteller Technologie und praktischer Anwendung geschlossen wird.

Die Arbeit trägt somit wesentlich zur Weiterentwicklung der Verwendung von DNA-templierten optischen Materialien sowohl für die wissenschaftliche Forschung als auch für gesellschaftlich relevante Anwendungen bei. Sie zeigt die Vielseitigkeit und das Potenzial der DNA-Origami-Techniken für die präzise Nano-Assemblierung und ebnet den Weg für praktische Anwendungen wie sichere Authentifizierungssysteme und empfindliche biochemische Sensoren.

ABSTRACT

The optical behavior of materials at the macroscale is influenced by their nanoscale structure. Developing techniques to influence and create new nanoscale architectures can enable us to assemble materials with novel properties. DNA nanotechnology, and especially the DNA origami technique allows the use of self-assembly to arrange nanoscopic objects in user-defined geometries. In this doctoral thesis, we use this feature to engineer the optical response of plasmonic nanoparticle assemblies in two areas: chiral plasmonics and physical unclonable functions (PUFs). Initially, we discuss advances in the use of DNA origami-templated plasmonic materials to achieve sensitive biomolecule detection. We then explore the synthesis and properties of chiral nanorod dimers, focusing on silver-gold core-shell nanorods. Utilising a novel one-pot method, we achieve monodisperse nanorods with precise control over size, aspect ratio, and silver shell thickness. These nanoparticles offer tunable optical characteristics and are functionalized with DNA, enabling their organization into specific chiral geometries via DNA origami. Our findings extend the spectral control over the circular dichroic signal, offering potential applications in catalysis and biosensing.

We use the core-shell particles and DNA origami in combination with nanosphere lithography to create a novel unclonable tag to combat counterfeiting. Traditional cryptographic methods based on one-way functions are discussed, along with their limitations, both technological and theoretical. We describe PUFs as an alternative, with an emphasis on optical PUFs, which are robust against various types of attacks and cloning attempts. Our PUFs exhibit a broad range of hues due to plasmonic coupling, enhancing their security features. Moreover, these PUFs are seamlessly integrated with a cost-effective 3D-printed read-out tool, bridging the gap between experimental technology and practical application.

The thesis thus contributes significant advancements in using DNA-templated optical materials for both scientific inquiry and societal applications. It showcases the versatility and potential of the DNA origami technique for precise nanoscale assembly and paves the way for practical applications such as secure authentication systems and biochemical sensing.

PUBLICATIONS

PEER-REVIEWED AND SUBMITTED PUBLICATIONS THAT ARE A PART OF THIS THESIS

1. **Mihir Dass**, Fatih N. Gür, Karol Kołątaj, Maximilian J. Urban and Tim Liedl
   "DNA Origami-Enabled Plasmonic Sensing"
   The Journal of Physical Chemistry C **2021** 125 (11), 5969-5981
   10.1021/acs.jpcc.0c11238

2. Linh Nguyen, **Mihir Dass**, Martina F. Ober, Lucas V. Besteiro, Zhiming M. Wang, Bert Nickel, Alexander O. Govorov, Tim Liedl and Amelie Heuer-Jungemann
   "Chiral Assembly of Gold–Silver Core–Shell Plasmonic Nanorods on DNA Origami with Strong Optical Activity"
   ACS Nano **2020** 14 (6), 7454-7461
   10.1021/acsnano.0c03127

3. **Mihir Dass**, Lilli Kuen, Gregor Posnjak, Sven Burger and Tim Liedl
   "Visible wavelength spectral tuning of absorption and circular dichroism of DNA-assembled Au/Ag core–shell nanorod assemblies"
   Material Advances **2022**, 3, 3438
   10.1039/D1MA01211H

4. **Mihir Dass**, Lena Raab, Christoph Pauer, Christoph Sikeler, Larissa Heinze, Joseph Tavacoli, Irina Martynenko, Ulrich Rührmair, Gregor Posnjak, Tim Liedl
   "Self-assembled physical unclonable function labels based on plasmonic coupling"
   Arxiv **2023**
   10.48550/arXiv.2310.19587

OTHER PEER-REVIEWED AND SUBMITTED PUBLICATIONS

1. Gregor Posnjak, Xin Yin, Paul Butler, Oliver Bienek, **Mihir Dass**, Ian D. Sharp, Tim Liedl
   "Diamond photonic crystals assembled from DNA origami"
   Arxiv **2023**
   10.48550/arXiv.2310.10884

2. Irina V. Martynenko, Elisabeth Erber, Veronika Ruider, **Mihir Dass**, Gregor Posnjak, Xin Yin, Philipp Altpeter & Tim Liedl
   "Site-directed placement of three-dimensional DNA origami"
   Nature Nanotechnology **2023**
   10.1038/s41565-023-01487-z

3. Pauline J. Kolbeck, **Mihir Dass**, Irina V. Martynenko, Relinde J. A. van Dijk-Moes, Kelly J. H. Brouwer, Alfons van Blaaderen, Willem Vanderlinden, Tim Liedl, and Jan Lipfert
   "DNA Origami Fiducial for Accurate 3D Atomic Force Microscopy Imaging"
   Nano Letters **2023** 23 (4), 1236-1243
   10.1021/acs.nanolett.2c04299

4. Ece Büber, Tim Schröder, Michael Scheckenbach, **Mihir Dass**, Henri G. Franquelim, and Philip Tinnefeld
"DNA Origami Curvature Sensors for Nanoparticle and Vesicle Size Determination with Single-Molecule FRET Readout"
ACS Nano **2023** 17 (3), 3088-3097
10.1021/acsnano.2c11981

5. Christoph Pauer, Aron Venczel, **Mihir Dass**, Tim Liedl, Joe Tavacoli
"Propulsion of Magnetic Beads Asymmetrically Covered with DNA Origami Appendages"
Advanced Materials Technologies **2022**, 7, 2200450
10.1002/admt.202200450

6. Bingru Zhang, Kevin Martens, Luisa Kneer, Timon Funck, Linh Nguyen, Ricarda Berger, **Mihir Dass**, Susanne Kempter, Jurgen Schmidtke, Tim Liedl and Heinz-S. Kitzerow
"DNA Origami Nano-Sheets and Nano-Rods Alter the Orientational Order in a Lyotropic Chromonic Liquid Crystal"
Nanomaterials **2020**, 10, 1695
10.3390/nano10091695

PATENT APPLICATION

Tim Liedl, Ulrich Rührmair, **Mihir Dass**, Gregor Posnjak, Lena Raab
"Physically unclonable function (PUF) label, system and methods"
European Patent Office **2023** (submitted)
European patent application no. EP23166190.1

ACKNOWLEDGEMENTS

"If I have seen further it is by standing on the shoulders of giants."

- Sir Isaac Newton, in a letter to Robert Hooke, 1675.

CONTENTS

11

LIST OF FIGURES

ACRONYMS

2D	two-dimensional
3D	three-dimensional
DNA	deoxyribonucleic acid
dsDNA	double-stranded DNA
ssDNA	single-stranded DNA
RNA	ribonucleic acid
AFM	atomic force microscope
SEM	scanning electron microscope
TEM	transmission electron microscope
DFM	dark field microscope
bp	base pair
NP	nanoparticle
NS	nanosphere
NR	nanorod
Au	gold
Ag	silver
PUF	physical unclonable function
LSPR	localised surface plasmon resonance

1. INTRODUCTION

1.1 Nanotechnology in brief

The advent of civilization brought with it new needs to be addressed; tools suitable for harvesting crops, weapons for territorial defense, and fibres for clothing and sailing. The importance of advances in material science is highlighted in the use of *metal ages*: Copper Age, Bronze Age and Iron Age to classify human prehistory (Fig. 1). The use of copper marked the capability to smelt; bronze indicated the understanding and skill to create alloys. High temperatures, up to 1250°C, needed to smelt iron placed it outside of reach of common use until around 1200 BC. Access to a broader range of materials allowed early humans to build objects of greater complexity, usable for newer applications. Most materials used by humans were, and still are, macroscopic in nature. However, examples of nanomaterials appear as early as the 4th century AD. A notable example is the Roman Lycurgus cup; it contains colloidal gold and silver nanoparticles, making it appear green when lit from outside and red when illuminated through the inside. Ultimately, a material's properties arise from its atomic/molecular structure. Understanding and manipulating matter at the nanoscale is the domain of the interdisciplinary field of *nanotechnology*.

Figure 1. Metal Age artefacts. a) Reconstruction of the copper axe of Ötzi the Iceman, dating to between 3350 and 3105 BC. b) The Alaca Höyük disc bronze standard, dating to around 2000 BC. c) The Wandsworth Shield, dated to the 2nd century BC. Permissions: All images are licensed under Creative Commons, a) CC BY 3.0, b) and c) CC BY-SA 3.0.

Two paradigms for constructing nanoscale materials are widely accepted. The top-down paradigm starts with a bulk material and then miniaturises it to achieve finer features (Fig. 2a (left)). Lithographic techniques like photo- and e-beam lithography, used for nanofabrication of integrated circuits, exemplify this approach. These techniques are highly scalable and have reached a high level of sophistication, particularly in the semiconductor industry. However, limitations arise as feature size decreases; top-down techniques are serial in nature (Fig. 2b) and parallelization comes at significant costs.

The bottom-up paradigm relies on self-assembly. It engineers interactions between building blocks to establish a preferential minimal energy state for the assembled structure (Fig. 2c). While still under research and refinement for large-scale use, they offer two main advantages. They can position features with near-atomic precision and enable highly parallel fabrication, often fabricating trillions of structures simultaneously.
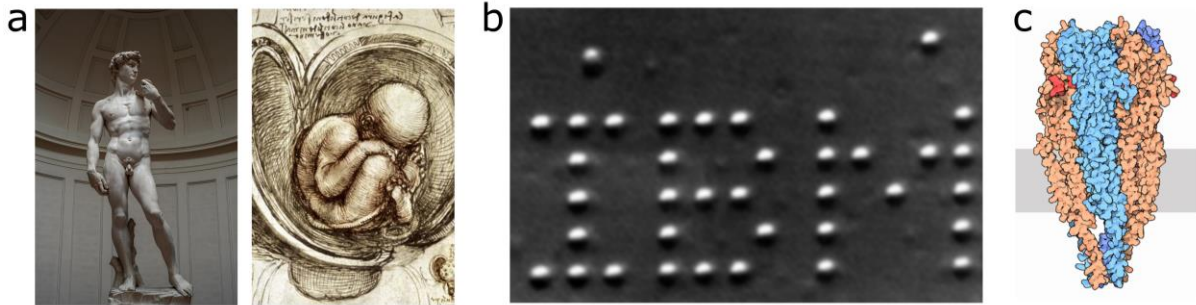
Figure 2. Top-down vs. bottom-up fabrication. a) (left) Michaelangelo's *David*, sculpted from a single block of marble, is an example of top-down fabrication. (right) A portion of *Studies of the Fetus in the Womb* by Leonardo da Vinci. A foetus is the result of cellular processes where biological materials are self-assembled with near-atomic precision, exemplifying bottom-up fabrication. b) IBM logo made from 35 Xenon atoms moved into position one-by-one using a scanneling tunnelling microscope. Each letter is 50 Å in height.[1] c) Goodsell structure of an acetylcholine receptor. Its structure is made of five protein chains which self-assemble into a long tube that crosses the cell membrane (shown in grey). It changes its structure upon binding molecules like Coniine, found in Hemlock. Permissions: a) (left) CC BY-SA 4.0, (right) Public domain, b) Reprinted by permission from Springer Nature Limited, copyright (1990), c) CC BY 4.0. Image credit: David S. Goodsell and RCSB PDB.

1.2 Structural DNA nanotechnology

Structural DNA nanotechnology is an interdisciplinary science that harnesses the molecular recognition and self-assembling properties of DNA to design and fabricate nanoscale synthetic structures, devices, and systems. Pioneered by crystallographer Ned Seeman in the 1980s, the field leverages the predictability of Watson-Crick base pairing. This feature, along with DNA sequence design, allows precise control over DNA interactions, allows precise assembly of DNA structures and patterns through spontaneous organization.

In 1982, Ned Seeman introduced the rational design of an immobile *Holliday junction* (Fig. 3a)[2], synthesising it a year later.[3] He wrote:

> It appears to be possible to generate covalently joined three-dimensional networks
> of nucleic acids which are periodic in connectivity and perhaps in space.

This approach transformed DNA into a nanoscale polymer extending in two dimensions instead of linear double helices. Seeman used these principles to assemble a DNA cube, the first polyhedral structure made of DNA (Fig. 3b).[4]

Seeman was interested in protein crystallography, which while arduous, was the conventional method to decipher protein structures at the time. Protein crystals, if sufficiently ordered, could be studied using X-ray diffraction. Drawing inspiration from M.C. Escher's woodcut *Depth*, Seeman chose DNA as a building block for creating structures and eventually protein-ordering crystals. Early DNA nanostructures used *tile assembly*, with the Holliday junction as the crossover motif. This has expanded to include double-crossovers[5], triple-crossovers[6], 4 × 4[7] and three-point star structures[8] using junctions of multiple short single-stranded DNAs (ssDNAs). These tiles can assemble into nanotubes[9], 2D lattices[10] (Fig. 3c,d), and 3D structures like polyhedra, hydrogels,[11] and crystals (Fig. 3e,f)[12].
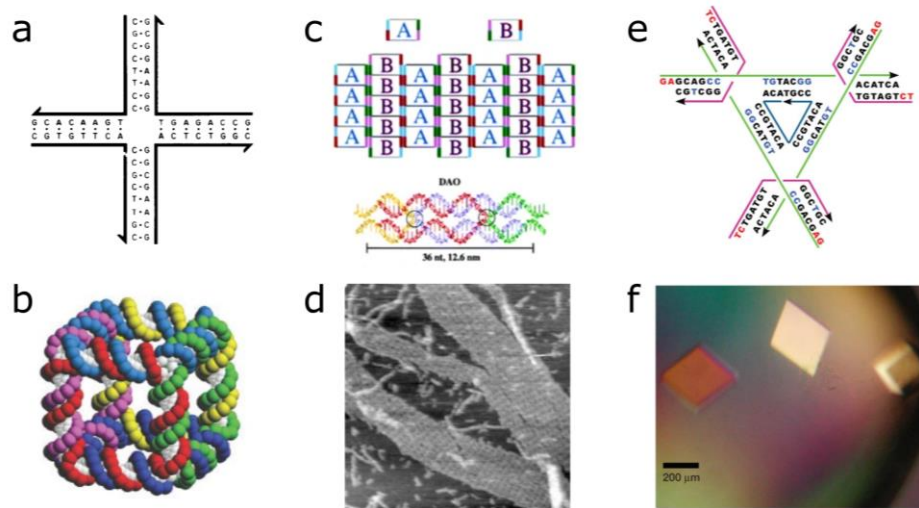
Figure 3. Ned Seeman's contributions to DNA nanotechnology. a) An immobile Holliday junction, the building block of DNA nanotechnology.[2] b) A DNA nanocube[4]. c) and e) schematics for d) 2D lattices[10] and e) 3D crystals[12] respectively. Permissions: a) Reproduced with permission from Springer Nature Limited, copyright (1982), b) a) Reproduced with permission from Springer Nature Limited, copyright (2003), b) Reproduced with permission from Springer Nature Limited, copyright (1991),gra c) & d) Reproduced with permission from Springer Nature Limited, copyright (1998) Macmillan Magazines Ltd., e) & f) Reproduced with permission from Springer Nature Limited, copyright (2009), Macmillan Publishers Ltd.

In 2006, Paul W.K. Rothemund invented the DNA origami technique,[13] using it to craft various 2D objects with arbitrary geometry, including the world's smallest smiley face. The DNA origami technique employs a *scaffolded* assembly approach. A long (~ 7000 nt) single-stranded scaffold is *folded* into shape by hundreds of shorter (~ 40 nt) oligonucleotides. This contrasts with tile assembly, where oligonucleotides assemble without a scaffold (more details on DNA origami are in section 2.2). Shawn Douglas *et al.* extended the DNA origami technique into 3D, assembling both single structures and their hierarchical assembly into larger formations.[14] This technique serves as the foundation of all associated publications in this thesis. Shawn Douglas also influenced the DNA nanotech field with the creation of the *cadnano* design software.[15] Subsequent to this, various DNA design software have also been developed.[16–22]

DNA NANOTECHNOLOGY

INTERESTING MILESTONES

Conceptual Framework[2] by Ned Seeman, describing immobile DNA junctions.
1 — 1982

1991 — **2** **DNA Cube**[4] the first closed polyhedral object made of DNA.

DNA Octahedron[23] by folding a 1.7kb ssDNA 'scaffold' using five staples.
3 — 2004

2006 — **4** **DNA Origami**[13] scaffolded assembly of 2D DNA Origami structures.

3D Origami[14] design space extended to 3D structures.
5 — 2009

2010 — **6** **DNA PAINT**[24] super-resolution imaging using DNA Origami.

DNA-assembled plasmonic chirality,[25] **Logic-Gated Nanorobots**[26]
7 — 2012

2014 — **8** **DNA Origami Placement**[27,28] optimized for placement on silicon wafers.

Absolute and arbitrary[29] orientation of DNA origami structures on a substrate.
9 — 2016

2018 — **10** **DNA Origami Roboarm**[30] Switching a DNA Origami structure using electric fields.

BenchTop DNA Origami Nanoarrays[31] scalable single-molecule placement.
11 — 2021

2023 — **12** **Site-directed placement of 3D DNA origami**[32] precise placement of 3D DNA origami structures.

Figure 4. Interesting DNA nanotechnology milestones relevant to this thesis.

1.3 State-of-the-art of DNA origami

The DNA origami technique has synergized with multiple scientific fields due to its unique capabilities, the most notable being high-precision positioning of moieties. DNA origami structures have been used to assemble metallic nanoparticles[23–26], carbon nanotubes[27], quantum dots and fluorescent particles. DNA origami structures have also been integrated with biological structures like antibodies[28,29] and proteins[30]. DNA origami has been employed to study localize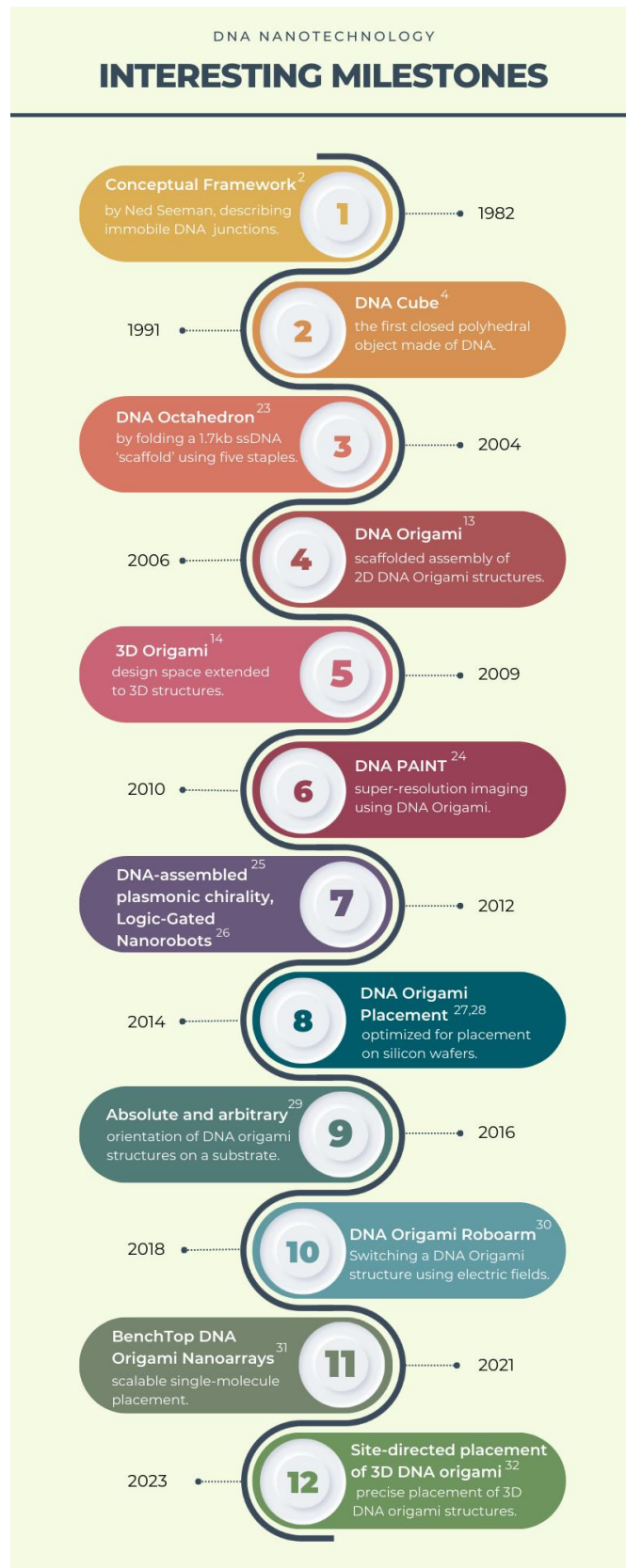d DNA- and enzymatic-reaction cascades[31–33] and for biophysical studies of collective behaviour of motor proteins[34,35] and biomolecular interactions[36,37]. Crystals with various lattice types have been constructed using DNA origami.[38–40] Post-assembly silicification results in rigid structures[41,42] compatible with traditional solid-state techniques.[43] Self-assembled systems like an electrically actuated arm[44] and a ratchet motor[45] have been fabricated using DNA origami. Additionally, DNA origami is increasingly being combined with lithography to explore new nanofabrication possibilities.[46–50]

1.4 Content of this work

The structure of this thesis is as follows: Chapter 2 provides an overview of the DNA molecule's structure (Section 2.1) and delves into the DNA origami technique (Section 2.2). Section 2.3 briefly outlines the plasmon hybridization model, fundamental to interactions within plasmonic nanoparticles. Plasmonic chirality (Section 2.4) and light scattering (Section 2.5) are discussed to support Associated Publications 2 and 3, respectively.

Chapter 3 and Associated Publication 1 explore the use of DNA origami for plasmonic biosensing. Created during the Covid-19 pandemic, this work reflects the zeitgeist and focuses on output signals from sensors based on plasmonic coupling between nanoparticles or between a nanoparticle and a dye molecule.

Associated publication 2 is covered in chapter 4, which describes the creation of silver shells on gold nanoparticles to improve their plasmonic properties, silver being a superior plasmonic material compared to gold. We combine silver-gold core-shell nanoparticles with DNA origami to form chiral assemblies, allowing us to tune both their spectral properties in the visible wavelength range and their chiral response.

Chapter 5 proposes a technique for creating anti-counterfeit labels. It combines DNA origami placement with core-shell nanoparticles and employs nanosphere lithography to pattern plasmonic nanoparticle assemblies on a substrate. Plasmonic coupling between the nanoparticles gives rise to new colors absent at the discrete particle level, which we detect using Dark Field microscopy. Due to the stochastic assembly and extreme sensitivity of the scattering color to particle size and spacing, the optical signal is inherently secure against spoofing.

2. THEORETICAL BASICS

2.1 Deoxyribonucleic acid (DNA)

DNA, or deoxyribonucleic acid, is a molecule crucial for life as we know it. It carries genetic instructions for the growth, development, and functioning of organisms. Swiss physician Friedrich Miescher first isolated DNA, which he called "*nuclein*", in 1869.[51] However, its importance as a genetic molecule was not immediately realised. Frederick Griffith, in his eponymous 'Griffith's Experiment' in 1928, suggested that a "transforming principle" could transfer traits between bacteria[52], hinting at a molecule carried genetic information. In the 1940s, Oswald Avery, Colin MacLeod, and Maclyn McCarty proved that DNA, not protein, was this transforming substance.[53]

The 1950s marked a critical discovery: the double helix structure of DNA. Rosalind Franklin and Raymond Gosling's X-ray crystallography work in 1952 produced the famous *photo 51* (Fig. 5)[54]*,* revealing the DNA structure.[55] James Watson and Francis Crick, building on these x-ray crystallography images and other data, proposed the double helix model in 1953, published in the same issue of *Nature* as Franklin's image.[56]

After the double helix model was established, the focus shifted to understanding how DNA functions. The genetic code was decoded in the 1960s, revealing how sequences of bases encode amino acids and hence proteins. This led to the discovery of messenger RNA[57,58] and the processes of transcription and translation. In 2001, the Human Genome Project completed a rough draft of the human genome, significantly advancing our understanding of DNA's role in human biology and paving the way further for genetic research.
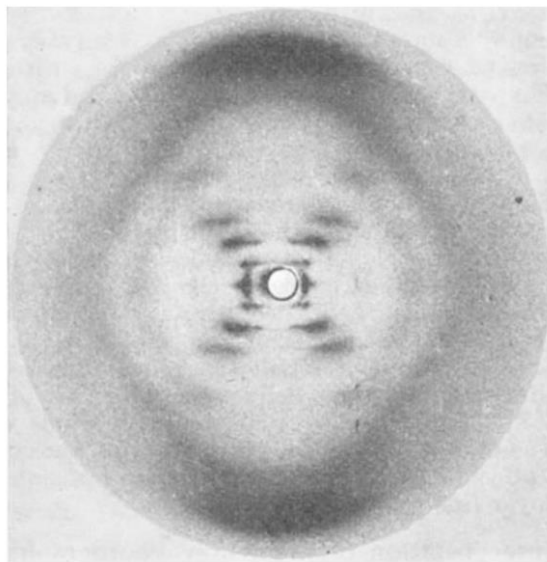
Figure 5. Photo 51. Features like the separation between the layer lines (dark horizontal dashes) helped uncover the structure and dimensions of the DNA double helix.[59] Permissions: Reproduced with permission from Springer Nature, copyright (1953)[55].

2.1.1   The DNA molecule – structure and properties

DNA is a biopolymer. In its double helix configuration, two antiparallel strands of DNA coil around each other. Each strand is a polymer chain made of nucleotides, which serve as the fundamental units. A nucleotide consists of three main components: a phosphate group, a sugar molecule (deoxyribose), and a nitrogenous base (Fig. 6a). Nucleotides play a central role in the metabolism of each organism: serving as energy storage entities (e.g., adenosine triphosphate), participating in signalling pathways (e.g., cyclic adenosine monophosphate), and acting as enzymatic cofactors (e.g. Flavin mononucleotide).

The four nucleobases in DNA are adenine (A), thymine (T), cytosine (C), and guanine (G). Long polymers of an arbitrary composition of monophosphate nucleotides are formed by linking phosphate of one nucleotide to the 3' carbon of another nucleotide's deoxyribose ring. These polymers are then termed polynucleotides or single-stranded DNA (*ssDNA)*. The phosphate and sugar form the backbone of each strand, while the bases protrude toward the centre of the helix. The asymmetric phosphodiester bond between adjacent deoxyribose rings provides directionality to the ssDNA molecule.
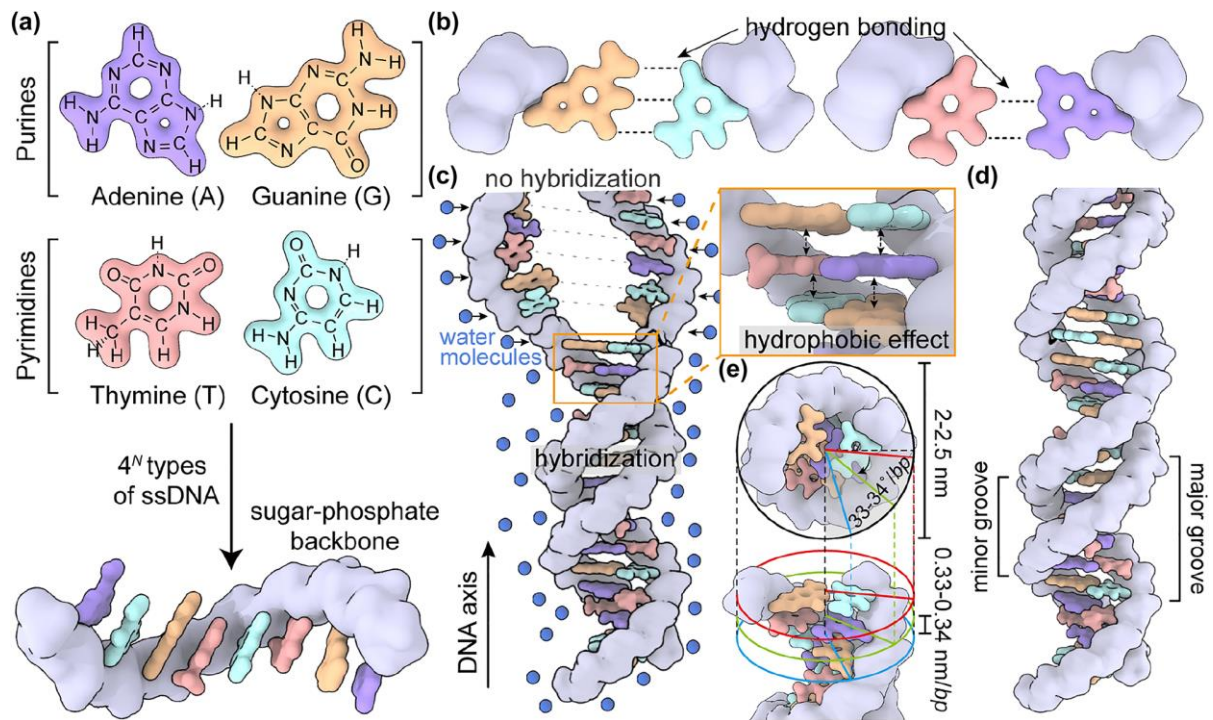
Figure 6. Schematic representation of the fundamentals of the DNA structure.[60] Permissions: Original work is licensed under the Creative Commons Attribution 4.0 International License.

The two strands are bound by hydrogen bonds between complementary bases (Fig. 6b). Adenine pairs with thymine using two hydrogen bonds; cytosine pairs with guanine using three. G and C form the slightly more stable base pair (bp). This specificity, known as complementary base pairing, is critical for biological processes and serves as the foundational property for structural DNA nanotechnology. The double helix is further stabilized by

hydrophobic π-π interactions among the delocalised electron clouds of adjacent bases (Fig. 6c). This 'base-stacking' expels water from the space between nucleobases and is partially responsible for the DNA adopting a helical structure.

DNA has a negative charge due to its phosphate groups, which is partially neutralized using cations like magnesium for higher-order assembly of DNA. Under physiological conditions, the DNA double helix usually adopts the right-handed B-form with a major and a minor groove (Fig. 6d). One full turn (10.5 base pairs) stretches over 3.5 nm with a diameter of ~ 2 nm and a vertical distance between two adjacent bp of 3.32 Å (Fig. 6e). Under special buffer conditions, other conformations of the double helix such as the A-form (right-handed, 11 bp per turn, 2.3 nm diameter) or the Z-form (left-handed, 12 bp per turn, 1.8 nm diameter) can occur.

2.2 DNA origami

The DNA origami technique involves folding a long ssDNA strand called the *scaffold* with a known sequence (typically ~ 7000 nt long m13mp18 bacteriophage DNA) using ~ 200 short (~ 40 nt long) designed oligonucleotides called *staples* (Fig. 7). The staples have multiple binding domains complementary to different regions of the scaffold, effectively 'knitting' the DNA origami structure via a combination of base pairing and Holliday junctions. The design of the staples determines the structure's shape and size, which can be done *in silico*.

Assembly of the structures requires mixing of the scaffold with the staple strands in a molar excess (typically each staple is present at 5-10x excess relative to the scaffold) and heated to 65°C, ensuring denaturation of the DNA strands. Two methods can be used for annealing: a slow cool to room temperature or a rapid cool to a set temperature, followed by a hold period before being cooled to room temperature. The folding time depends on the complexity of the structure. Buffer is used to maintain pH, and cations ensure screening of the negatively-charged DNA backbone, enabling the packing of the DNA into a dense, stable structure. Since the self-assembly is deterministic, the designer possesses atomic-level knowledge of the final structure. Functionality using base modifications can thus be introduced with near-atomistic precision.
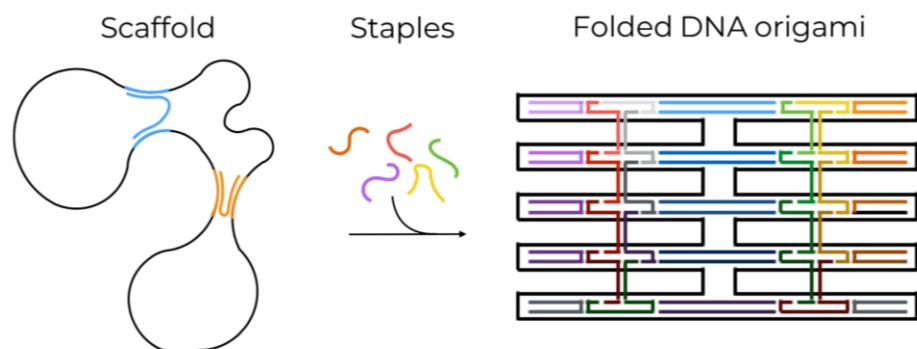

Figure 7. Schematic illustration of DNA origami folding. A long ssDNA scaffold strand (black) is folded by short ssDNA staple strands (coloured) which have binding domains complementary

to different regions on the scaffold. The result is a DNA origami structure which folds into a predesigned shape, in this case a 2D rectangle. Adjacent antiparallel helices are held in place by double crossovers in the form of Holliday junctions.

Paul Rothemund invented the technique in his 2006 work, where he designed (Fig. 8a) and assembled planar 2D structures such as smileys, triangles and stars showing that virtually any 2D shape could be made (Fig. 8b) and labelled arbitrarily (Fig. 8c).[13] He used extended staples for controlled structure combinations and free ssDNA on the edges of structures to prevent unwanted aggregation. (Fig. 8d).
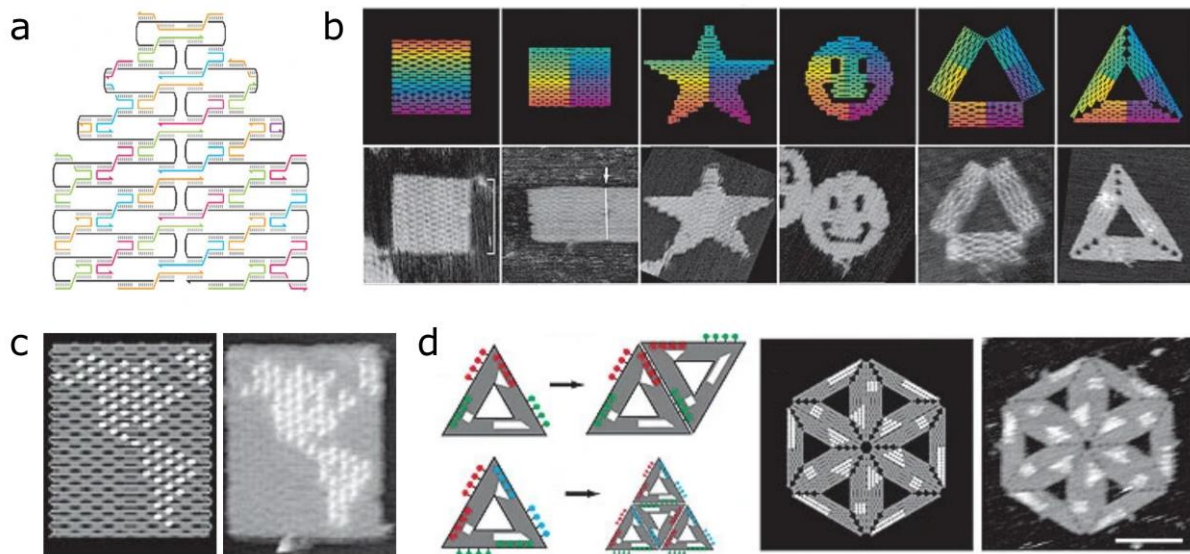
Figure 8. DNA origami by Paul Rothemund. a) Stand design of a DNA origami structure. b) Planar 2D shapes assembled using DNA. c) Map of the western hemisphere, scale 1:2 × 10^14. The features are created using 'dumbbell hairpins' inserted at predefined locations. d) Structures can be combined using complementary design elements. Permissions: Reproduced with permission from Springer Nature Limited, copyright (2006).

The technique was developed further to create 3D structures by the groups of Kurt Gothelf and William Shih using two different approaches. In the former, Andersen *et al.* used 2D sheets joined at the edges to assemble a 3D box with a controllable lid.[61] In the latter, Douglas *et al.* used pleated layers of helices arranged in a honeycomb lattice to build 3D shapes (Fig. 9a)[14], which was extended to the square[62] and hexagonal lattices (and a hybrid lattice)[63]. Curved DNA nanostructures of virtually any geometry can be assembled (Fig. 9b).[64,65] Hierarchical assembly of 3D DNA formations can be achieved using shape-complementary base-stacking (Fig. 9c, d).[66–68] Sticky end-based assembly of DNA origami tiles into 2D lattices has been shown with both repeating[69] and unique sub-units (Fig. 9e)[70], along with lipid bilayer-assisted assembly[71,72]. 3D supra-assemblies, especially crystals, can also be constructed with the sticky end-based approach (Fig. 9f).[38,39,73] The same approach can be used to host structures like nanoparticles functionalised with DNA in exquisite geometries (Fig. 9g). Combined with e-beam lithography, DNA origami offers the possibility to locate single structures and thus

molecules at any arbitrary point in space (Fig. 9h-j).[48] A cargo-sorting algorithm has been implemented on DNA origami structures (Fig. 9k).[74] Recently, studies on dynamic DNA rotors based on external actuation (Fig. 9l)[44] or osmotic flows through a nanopore (Fig. 9m)[75] have been shown.

Two key features make DNA origami a potent nanofabrication technique. First, being a self-assembly technique, it is massively parallel; a typical 100 uL folding process at a scaffold concentration of 10 nM yields ~ 10^{11} individual structures simultaneously in a one-pot reaction. Second, theoretically every base in the DNA origami structure can be uniquely addressed. Modern nucleic acid synthesis techniques offer a wealth of possible base modifications such as biotin, thiols, carboxyl and amine groups along with optically active moieties like fluorophores. This makes DNA origami a molecular pegboard, giving designers the capability of arranging molecules suitable for various applications with precision.
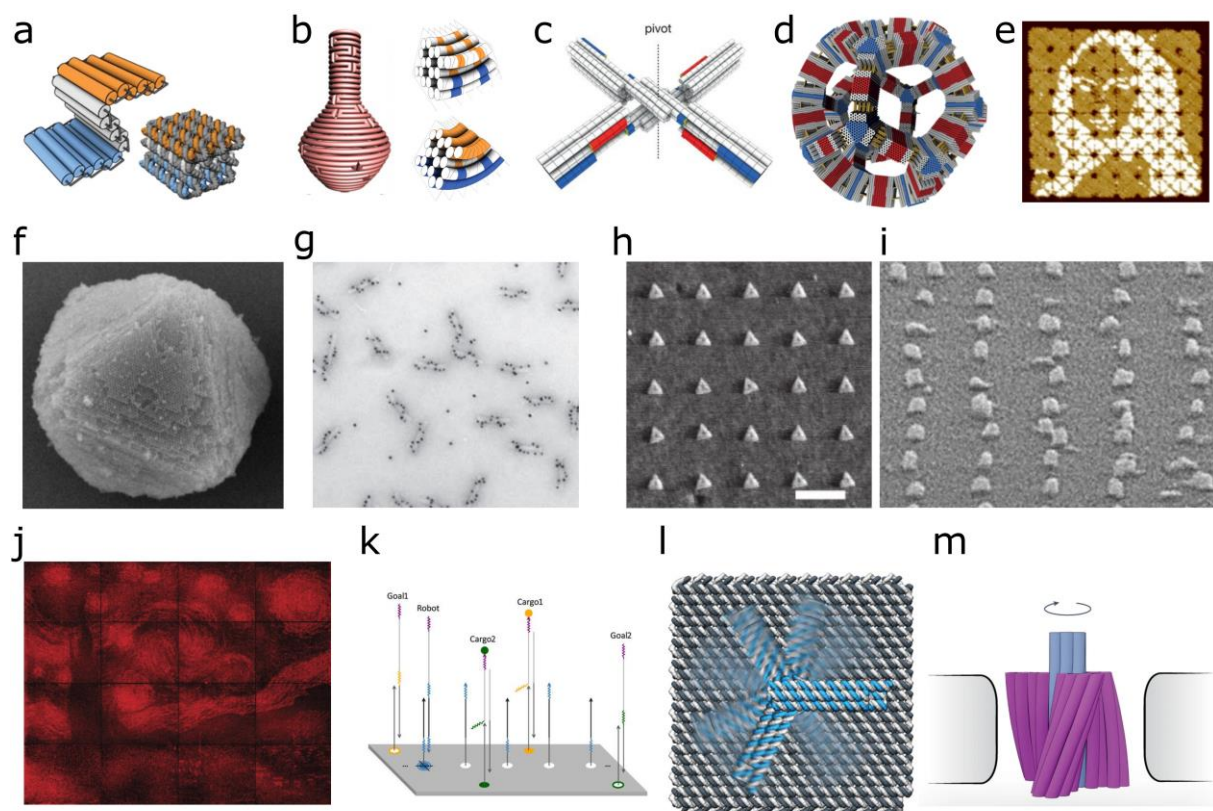
Figure 9. DNA origami over the years. a) Folding 3D DNA origami structures.[14] b) Introducing curvature in DNA origami.[64,65] c) Dynamic switch based on shape-complementary base-stacking, with one rotational degree of freedom.[66] d) A self-assembled 1.2 gigadalton dodecahedron.[67] e) AFM image of an 8 x 8 DNA origami array with a *Mona Lisa* pattern.[70] f) DNA origami cubic diamond crystals, covered with a layer of SiO_2. g) TEM image of assembled left-handed gold nanohelices.[23] h) DNA origami placement of 2D[47] and i) 3D structures[76]. j) Van Gogh's The Starry Night approximated with 65,536 photonic crystal cavities each having from zero to seven binding sites for dye-carrying DNA origami structures.[77] k) Schematic showing

implementation of a cargo-sorter on a DNA origami.[74] l) A self-assembled nanoscale robotic arm.[44] m) Schematic of a right-handed DNA turbine docked into a nanopore.[75] Permissions: a) Reproduced with permission from Springer Nature, copyright (2009), Macmillan Publishers Limited. B) Reproduced with permission from the American Association for the Advancement of Science, copyright (2009). d) & e) Reproduced with permission from Springer Nature, copyright 2017, Macmillan Publishers Limited. f) Reproduced with permission from Springer Nature, copyright (2012). j) Reproduced with permission from Springer Nature, copyright (2016). m) Licensed under Creative Commons CC-BY, copyright (2023), The Author(s).

2.3 Plasmon hybridisation model

The plasmon hybridisation model, introduced by Prodan *et al.*[78], applies principles from molecular orbital theory to describe interactions between plasmons in metals. Treating them like molecular orbitals, it draws parallels between plasmonic interactions and the orbital hybridisation model suggested by Linus Pauling in 1931.[79] Plasmons are quanta of electron oscillations in metals, which can be excited by incident light. For nanoscale objects smaller than the excitation wavelength, a uniform electromagnetic field can be considered across the extent of the nanoparticle. In the case of nanoparticles, these electron oscillations can propagate along the surface at optical frequencies and are thus called surface plasmons. Classical Mie scattering theory aligns well with electromagnetic theory for explaining properties like plasmon resonance frequency in minimal plasmonic systems, strengthening the model's foundation.[80]
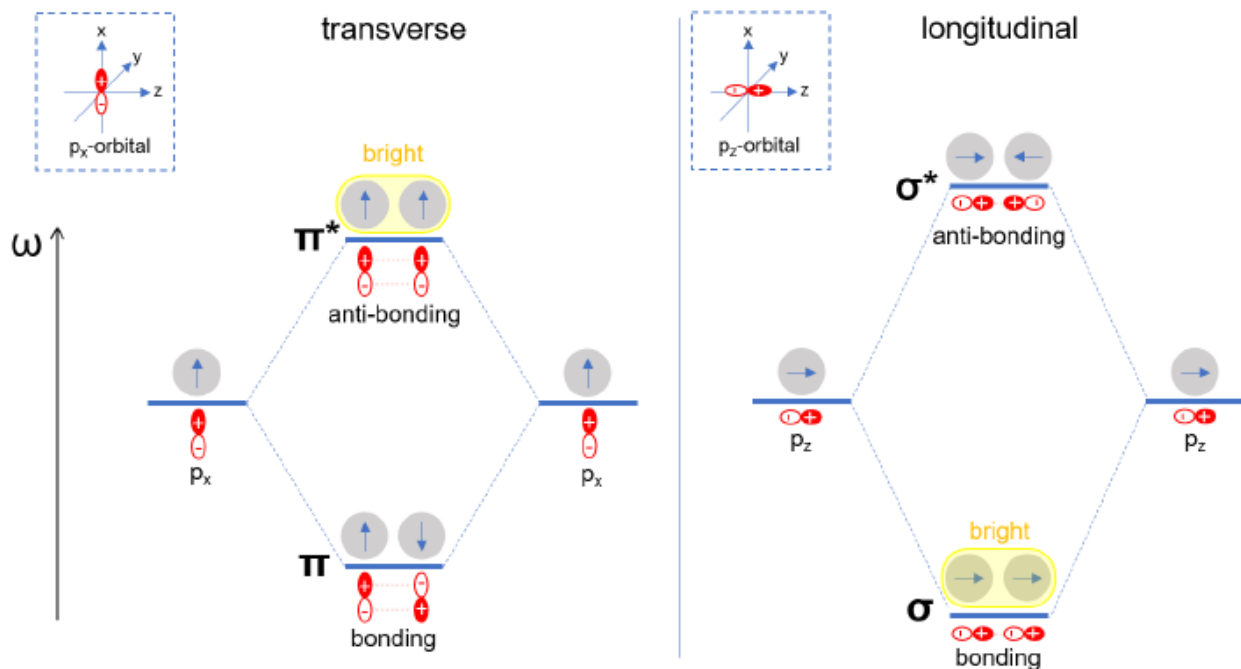
Figure 10. Plasmon hybridisation in a nanosphere-dimer system.

The plasmon hybridisation model extends to complex systems such as dimers of nanospheres and nanorods (Fig. 10, 11). Upon excitation by polarised light, the plasmon hybridisation leads to energetic splitting of the plasmon modes. In longitudinal polarisation (along the axis of the dimer), the dipoles of the bonding mode (σ) are oscillating parallel to, and therefore in-phase, with each other. This results in a non-zero dipole moment and an effective reduction in the restoring force that arises due to electrostatic repulsion. In the case of the antibonding mode (σ^*), the dipoles oscillate out-of-phase, leading to extinction of the net dipole moment. Since the dipoles are aligned antiparallel to each other, the restoring force is stronger. This difference in the restoring forces between the two modes results in their splitting. The lower-energy bonding mode shifts to lower frequencies, and the higher-energy antibonding mode to higher frequencies compared to a single particle. In the case of transverse polarisation, normal to the axis of the dimer, the dynamics change. With parallel orientation, the dipoles experience an increased restoring force and have a net-positive dipole moment in the antibonding (π^*) mode. In contrast, antiparallel orientation decreases the restoring force and results in zero dipole moment in the bonding (π) mode. Since the far-field optical properties of the dimer are dependent on a net-positive dipole moment, the σ and π^* modes are bright modes while the σ^* and π modes are dark.

For geometrically asymmetric nanoparticles like nanorods, the plasmon oscillations are also asymmetric for different polarisation directions. Similar to the case with nanospheres, nanorods in close proximity couple and undergo plasmon hybridisation. The strength of this coupling depends directly on several factors like:-

- the distance between the interacting nanorods,
- the aspect ratio of the interacting nanorods,[81]
- the number of interacting nanorods.
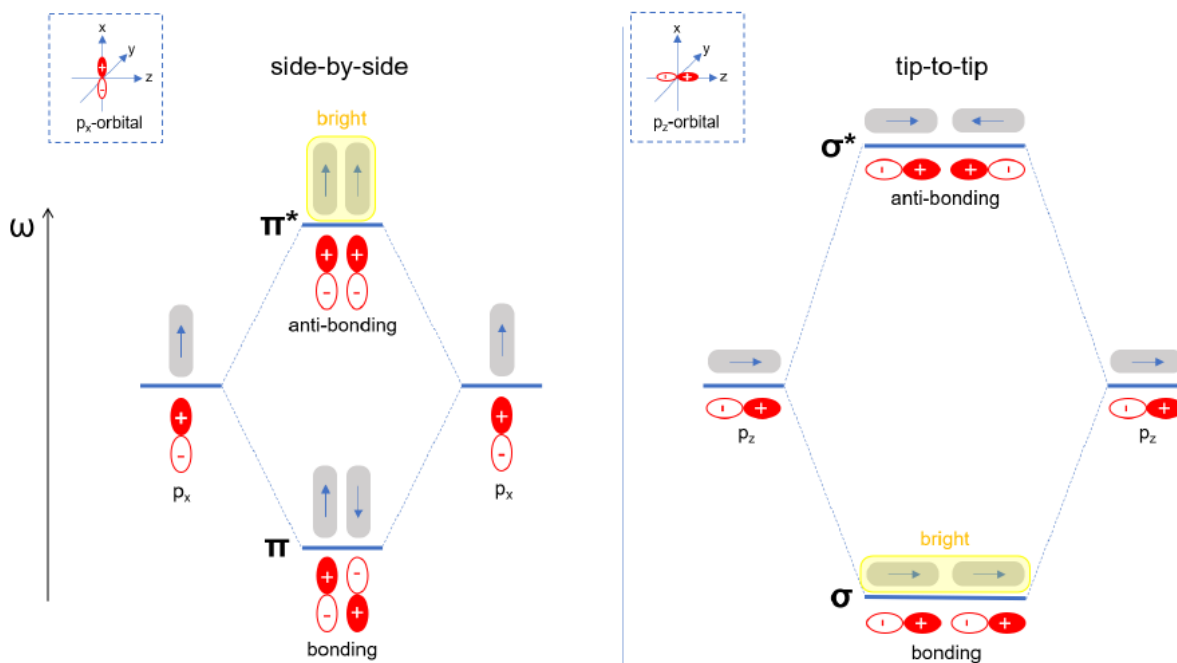
Figure 11. Plasmon hybridisation in a nanorod-dimer system.

The plasmon hybridisation picture for two nanorods is geometry dependent and can take two conformations (Fig. 11). In the tip-tip geometry, the energetic splitting between the bonding (σ) and antibonding mode (σ*) is much larger relative to the side-side geometry (π-π*). This results from stronger interactions between the longitudinal plasmons due to their much higher polarizability.[82] Since the hybridisation is distance dependent, increasing distance results in a convergence of the two modes as the EM field interactions between the particles get weaker; conversely, decreasing distances lead to stronger coupling. Interparticle distances of around 0.5 nm bring tunnelling effects into play. Upon contact, a new charge-transfer plasmon mode which involves a continuous polarisation of the charge distribution over both particles, thus behaving as a single longer plasmonic structure.[83]

2.4 Chirality and plasmonic circular dichroism

Chirality is a geometrical property: if an object cannot be superposed on its mirror-image, it is termed chiral. Our hands are an example of a pair of chiral objects, giving rise to the use of *'handedness'* to describe the chirality of an object. The importance of this property can be judged by its ubiquity. An understanding of chirality is important in

- predicting the behaviour of molecules and biomolecules. *In biological organisms, amino acids appear almost exclusively in the left-handed form (L-amino acids) and sugars in the right-handed form (R-sugars)*
- explaining aspects of the body plan of vertebrates. *For example, the left-side of the forebrain represents the right side of the body*

- the development of pharmaceutical drugs. Chiral partner molecules (enantiomers) could have extremely different impact reaction schemes (e.g. see "Contergan Thalidomide affair").

These reasons and more make it a worthwhile endeavour to understand chirality and chiral materials. An object can be chiral in two dimensions e.g. a flat spiral or a *gammadion* as long as it is placed on a surface which prevents 3D rotation. The DNA helix shows three-dimensional chirality. 2D geometries, like an 'L', are achiral in 3D (Fig. 12a). 3D chirality can be introduced in such geometries by creating asymmetry in the third dimension, for example by either placing them on a surface, or by moving one section of the 'L' in the z-direction to introduce intrinsic structural asymmetry (Fig. 12b).
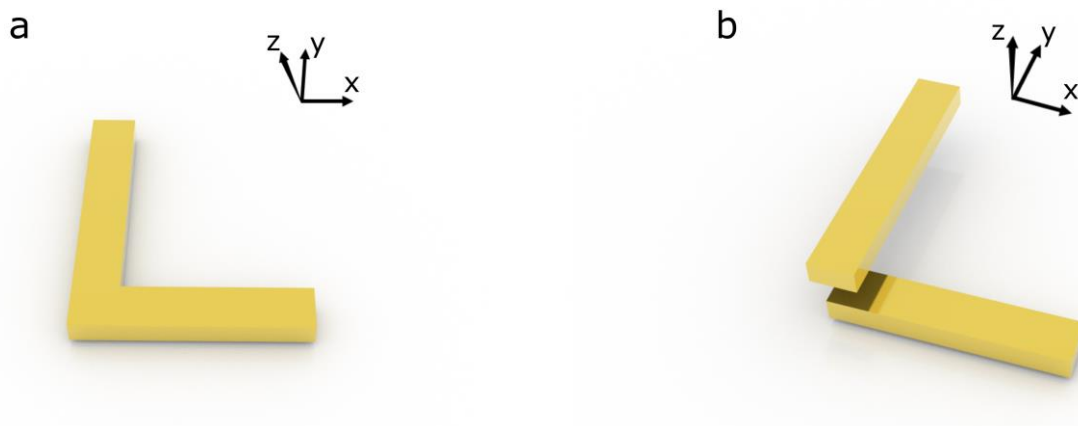
Figure 12. Illustrating 2D and 3D chirality. a) A flat L-shaped structure. b) Introducing asymmetry in 3D.

Harald Giessen *et al.* took inspiration from the Born-Kuhn model for coupled oscillators to expand the plasmon hybridisation model to chiral plasmonic systems. They represent the plasmonic Born-Kuhn model as two corned-stacked, vertically displaced nanorods that have a 90° angle between them (Fig. 13a). Right- and left circularly polarised (RCP and LCP respectively) light impinging on a *D*-enantiomer in the –z direction (Fig. 13b) excites the symmetric mode (analogous to the antibonding mode) and the antisymmetric mode respectively (Fig. 13c). The excitation for the *L*-enantiomer is analogous and leads to swapped bonding and antibonding modes.
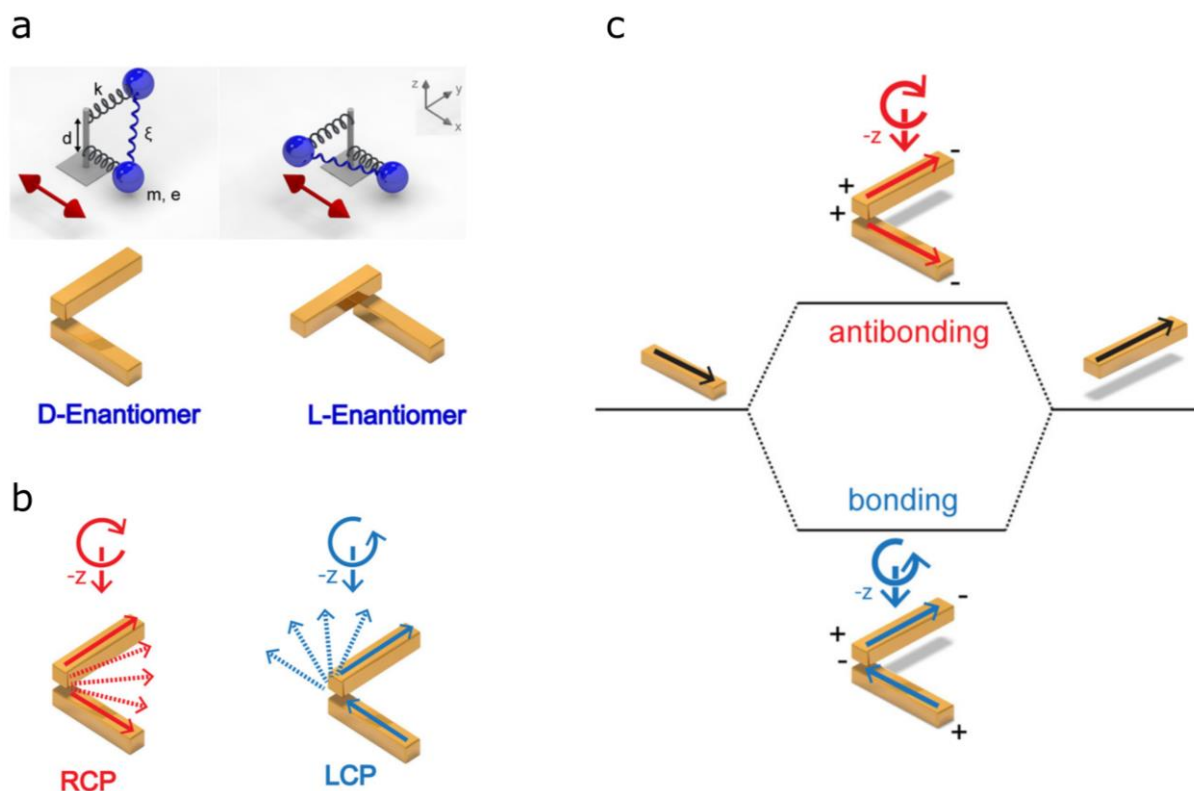
Figure 13. Plasmon hybridisation in chiral systems. a) Right (D)- and left (L)-handed classical coupled-oscillator models of optical activity (top) and their plasmonic analogues (below). b) Modes excited by right- and left-handed circularly polarized light for the d-enantiomer. c) Hybridization model for chiral plasmonic Born–Kuhn modes. Permissions: Reproduced with permission from American Chemical Society, Nano Letters[84], copyright (2013).

Chiral materials give rise to an optical phenomenon called *circular dichroism (CD)*. A chiral molecule or object preferentially interacts with (a combination of scattering and absorption) circularly polarized light of the same chirality at specific wavelengths. The enantiomer of the same object would interact strongly with light of inverted chirality. The CD signal strength is determined by the difference in interaction between light of opposite chiralities passing through the sample.

$$\text{Difference in absorption, } \Delta A = A_{LCP} - A_{RCP}$$

A variety of materials including biomolecules can be analysed through CD, typically using a CD spectrometer. A standard CD spectrometer uses Xenon or Tungsten lamps as light sources. The light from the lamp enters the *monochromator*, which selects horizontal linearly polarised light of a defined wavelength and bandwidth. Our spectrometer uses a series of prisms to achieve this. The first prism splits the incoming light into the component wavelengths and separate vertical and horizontal linearly polarised components of light. The second prism separates the contaminating vertical linearly polarised light from the horizontal linearly polarised light. This is then converted to circularly polarised light by a photoelastic modulator

(PEM). The polarized light beam passes through the sample cuvette to the detector, which detects the transmitted light. Most biomolecules show CD in the UV-range. If plasmonic particles are arranged in a chiral geometry, a CD signal centered at the corresponding resonance frequency can be obtained (Fig. 14). The bisignate shape of structures like the X-shaped isomer can be explained by the different energies and signs of the bonding and antibonding modes as explained by the plasmonic Born-Kuhn model (Fig. 13).
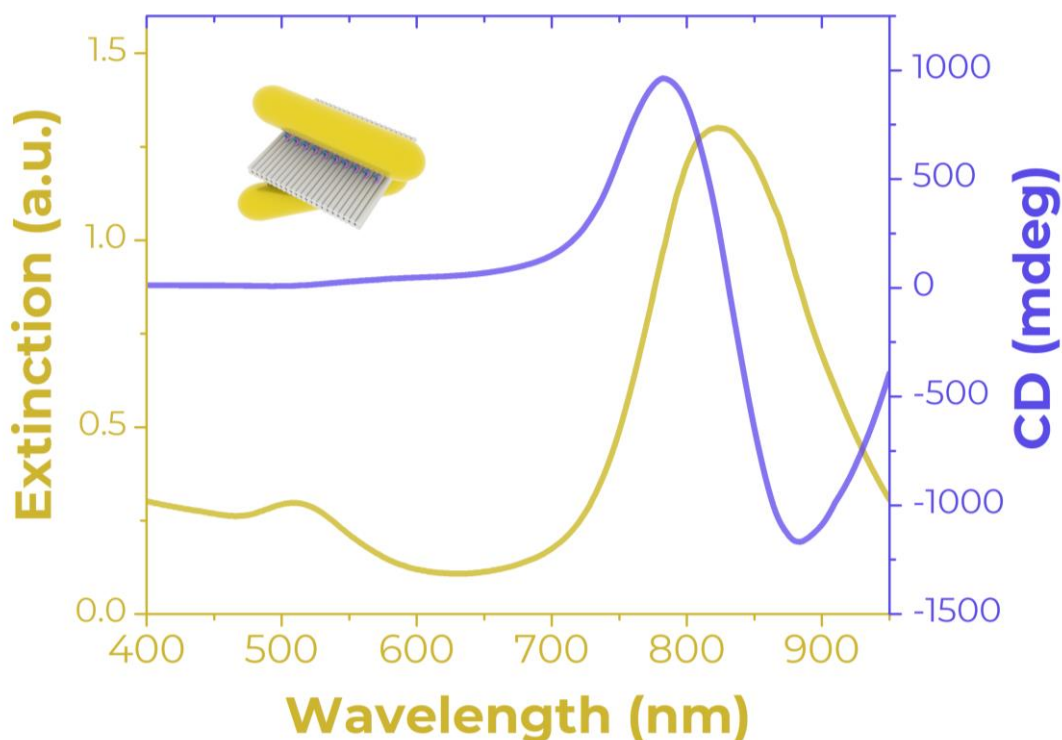
Figure 14. Extinction and CD spectra of a gold nanorod dimer arranged in a left-handed 'X' geometry using DNA Origami.

A plasmonic CD signal can arise from[85]:-

1. CD effects of metal nanoclusters with chiral atomic structures, chiral molecules on the surface of nanoparticles, or chiral environments around a cluster.

2. Coulomb interactions between chiral molecules and metal nanoparticles.

3. Plasmon-plasmon interactions between non-chiral particles, which are arranged in a chiral geometry.

The experimental systems in this work rely on the last type of interaction. In associated publication P1, we provide perspectives on the variety of plasmonic structures developed using DNA nanotechnology that have found use in the sensing of various biomolecules. In associated publication P2, we use nanorods to assemble 3D chiral objects and tune their plasmonic response over the visible spectrum to showcase simultaneous control over multiple optical aspects of the system.

2.5 Light scattering and Dark Field microscopy

Light scattering is a fundamental phenomenon where electromagnetic waves, including visible light, interact with matter, leading to a redirection of the incident light in various directions. It is a commonly encountered phenomenon in everyday life and is one of the two major physical processes that contribute to the visible appearance of most objects, the other being absorption. The phenomenon can be described by Maxwell's equations, which elucidate how electric and magnetic fields propagate in space.[86] Different types of scattering include Rayleigh, Mie, and geometric scattering, each described by distinct mathematical models and dependent on factors such as particle size and wavelength of light.[87]

In colloidal systems, Rayleigh scattering is often observed where the size of the scattering particles is much smaller than the wavelength of the incident light. Mie scattering comes into play when the particle sizes are on the order of the light wavelength. Geometric scattering is observed for particles much larger than the wavelength.[88]
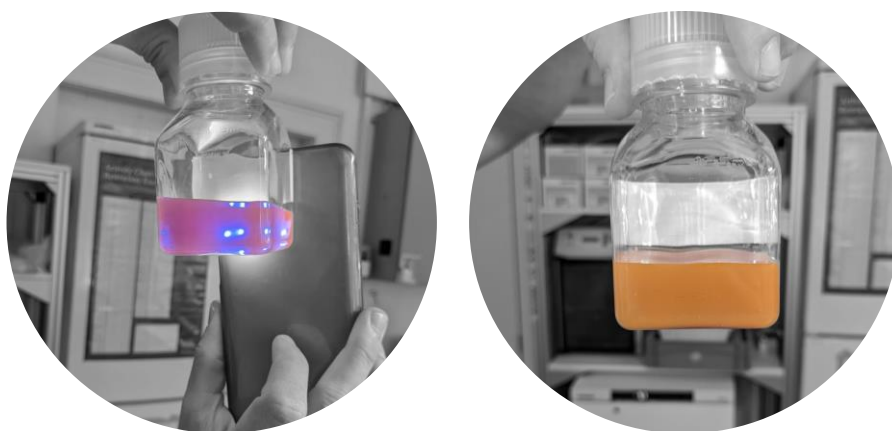
Figure 15. Light scattering by nanoparticles. A suspension of AuNS (100 nm diameter) appears to have a different colour when illuminated from behind or the front relative to the observer.

Transitioning to plasmonic nanoparticles (Fig. 15), light scattering takes on unique properties. These nanoparticles support localized surface plasmon resonances (LSPRs), collective oscillations of conduction electrons activated by the interaction with electromagnetic radiation (discussed in section 2.3). LSPRs can significantly enhance the scattering cross-section of the nanoparticle, exceeding what classical models predict for particles of similar size and composition.[89] The scattering profiles of plasmonic nanoparticles can be tuned by altering particle size, shape, and composition.[90] Additionally, arrays of plasmonic nanoparticles can induce collective effects, such as Fano resonances and coupling phenomena.[91] Therefore, light scattering by plasmonic nanoparticles is not only a topic of fundamental interest but also of technological relevance for applications in sensing, imaging, and therapeutics.

Only scattered light transmitted

Objective

Scattered light

Sample

Condenser

Dark field stop

Light source
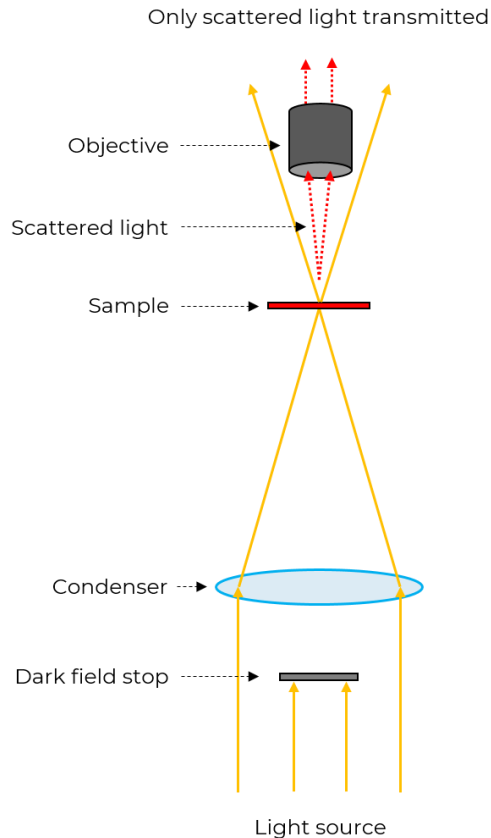
Figure 16. Schematic of a dark field microscope.

Dark field microscopy (DFM) is a specialized optical microscopy technique that enhances the contrast in unstained samples by illuminating the specimen with light that will not be collected by the objective lens. The basic principle of DMF was described in 1837 by Joseph Reade.[92] In a standard optical microscope, light passes through a specimen and then through an objective lens to form an image. However, in DFM, an opaque disc, known as a dark-field stop, is placed in the condenser to block most of the light from entering the objective lens (Fig. 16).[93] When light encounters an object smaller than its wavelength, scattering occurs. In DFM, only this scattered light enters the objective and forms the image. The background appears dark because transmitted light is obstructed by the dark-field stop.[94]

Dark-field microscopy is particularly useful for viewing transparent, colorless, or thinly-sectioned specimens, such as microorganisms or cellular structures, which are otherwise difficult to observe through standard bright-field microscopy.[95]

The technique has also been adapted for use with plasmonic nanoparticles. DFM is especially adept at detecting the scattering from these particles, leveraging their high scattering cross-sections (Fig. 17).[89] Upon excitation, the LSPR in a nanoparticle results in a strongly enhanced electric near-field localized at the particle surface, which can interact with that on an adjacent particle in close proximity, coupling the plasmon oscillations together. The coupled-particle LSPR occurs at a frequency that is shifted from the single-particle LSPR frequency. The

magnitude of this plasmon shift correlates with the strength of the interparticle coupling, which strongly depends on the proximity of the individual nanoparticles. Jain *et al.* studied the distance-based decay of plasmon coupling in nanoparticle dimers constructed using lithography, and derived the "plasmon ruler equation":

$$\frac{\Delta\lambda}{\lambda_o} \approx 0.18 \exp(\frac{-(s/D)}{0.23})$$

where $\frac{\Delta\lambda}{\lambda_o}$ is the fractional plasmon shift, s is the interparticle edge-to-edge separation, and D is the particle diameter.[96] Sönnichsen *et al.* were able to use the LSPR shift to create a 'molecular ruler' using DNA-functionalised plasmonic particles.[97] The authors utilised Debye screening effects and DNA hybridisation interactions to manipulate the interparticle distance between a AuNS-AgNS pair. Changing the NaCl concentration of the solution led to a measurable change in the wavelength of scattered light, corresponding to the separation distance between the two particles. This ability to detect scattered light from nanoparticles allows for applications in single-molecule detection and bioimaging, among other fields.[98]
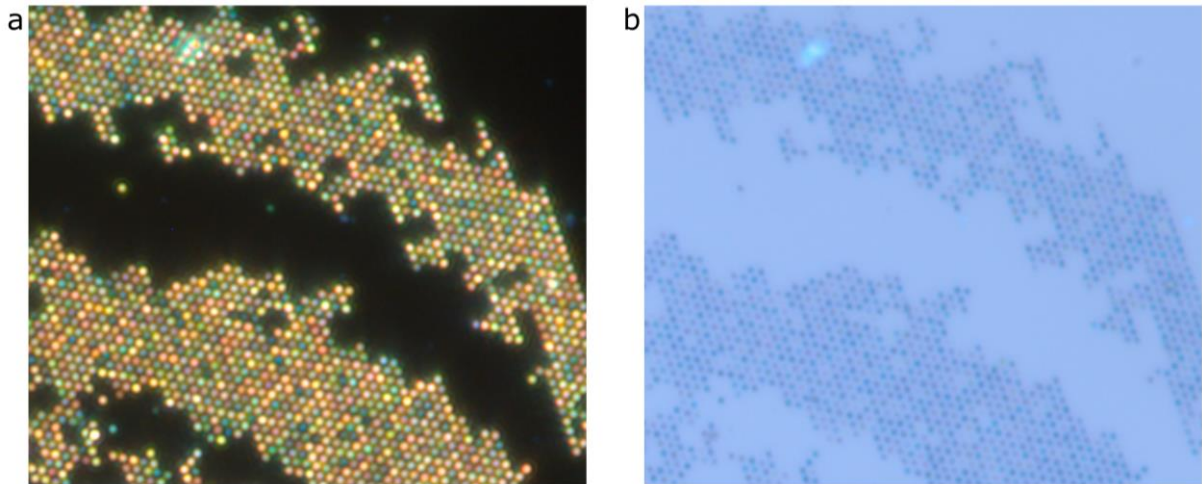
Figure 17. Dark field vs bright field imaging of nanoparticles on a silicon wafer. a) Only scattered light from sample contributes to the dark field image. b) The bright field image is dominated by the light reflected from the sample. The particles appear darker because they absorb and scatter away some of the incident light.

3. DNA ORIGAMI-ENABLED PLASMONIC SENSING

The ability to sense and respond to stimuli is a defining trait of living systems. In motile bacteria, for example, the binding of attractants (or repellents) to transmembrane receptors activates proteins that modify the bacteria's tumbling frequency.[99] In medicine, effective biomolecular sensing is highly desirable for the early detection of disease biomarkers at low concentrations. The recent Covid-19 pandemic has underscored the importance of clinical diagnostics, particularly through the widespread use of PCR and lateral flow assays.

An ideal biomolecular sensor transduces a binding event (stimulus) into a strong output signal. Plasmonic particles excel in this role due to their strong interaction with light, making them prevalent in most lateral flow assays. Since plasmonic particles can undergo coupling, their relative arrangement can be used to enable or enhance signal transduction. Two strategies to capitalise on this feature include (i) biomolecular assays that utilise plasmonic "hot-spots" and (ii) sensing mechanisms that operate through dynamic structural reconfiguration.

The DNA origami technique distinguishes itself by employing molecular self-assembly to arrange molecules and nanoparticles (NPs) into precise, user-defined 3D conformations. Compared to top-down nanofabrication techniques such as electron-beam lithography, the DNA origami technique possesses two advantages. First, it allows control of the position and spacing between neighbouring nanoparticles with sub-10-nm spatial resolution.[100] Second, the technique is high throughput, enabling the fabrication of trillions of high quality structures in parallel.

Figure 18. Artistic representation of biomolecular sensors constructed using DNA origami and plasmonic nanoparticles. Reproduced with permission from American Chemical Society, ACS Nano[101], copyright (2020).

In associated publication **P1**[102], we discuss fluorescence, Surface-enhanced Raman spectroscopy (SERS), and plasmonic chirality-based sensing strategies made possible through DNA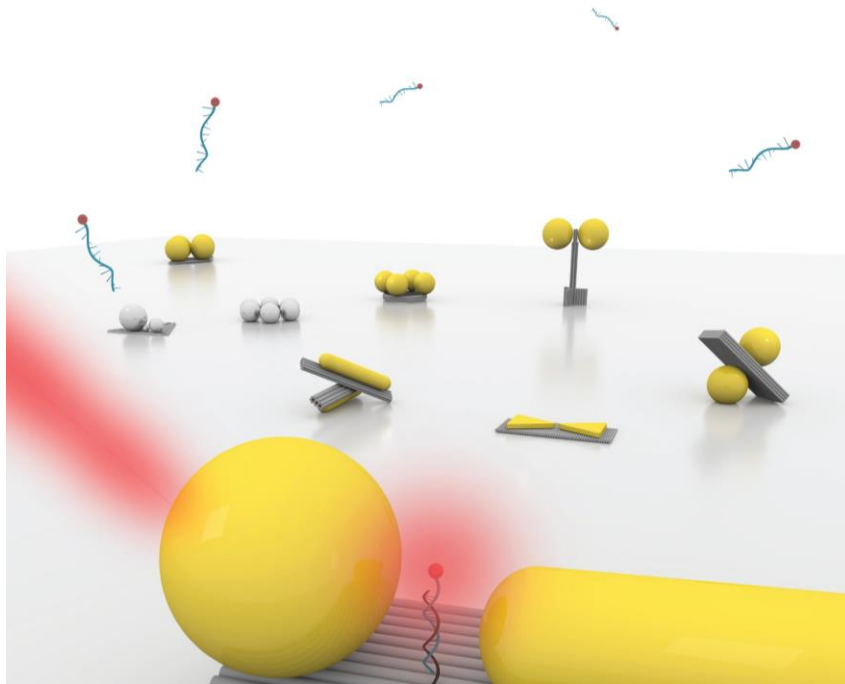 origami-templating of plasmonic particles (Fig. 18). Plasmonic NPs generate highly localized electric fields that can enhance the fluorescence of nearby molecules. This phenomenon, known as *fluorescence enhancement*, is strongly influenced by the distance between the metallic NP and the fluorescent molecule.[103,104] Close proximity between the NP and the dye can also lead to quenching of the dye, thus decreasing the output signal.[105,106] Therefore, achieving consistent enhancement demands precise control over the relative positions of the NP and dye molecules.

Acuna *et al.* were the first to report the bottom-up fabrication of DNA origami nanoantennas. Their nanoantennas are composed of a DNA nanopillar that arranges two AuNPs with a defined gap in between. The NPs couple to form a plasmonic hotspot, resulting in the enhancement of an ATTO 647N molecule situated between the NPs. This illustrates the advantage of using DNA origami to construct nanoantennas over top-down fabrication, in which dye molecules have to diffuse into the hotspot for enhancement to occur. Moreover, staple modifications can be employed to place a wide variety of molecules and assays directly inside the hotspot region.[107–109]

SERS also occurs due to enhancement of the electric field in close vicinity of plasmonic NPs, which leads to an amplification of the molecular Raman signal. Various NP shapes and arrangements on DNA origami structures have been used to give rise to SERS effects, including dimers made from nanospheres[110,111] and triangular nanoprisms[112].

Chiral plasmonic sensing leverages the chiroptical properties of plasmonic nanostructures or the plasmon-enhanced detection of chiral molecules using circular dichroism spectroscopy (discussed in section 2.4). Unlike biomolecules which display CD signals in the ultraviolet region[113], chiral plasmonic systems exhibit CD responses in the visible regime.[23,114] This minimizes the background signal in the visible range, making chiral plasmonic devices an attractive choice for the detection of biomolecules in solution.

Dynamic DNA origami structures hosting AuNRs, capable of switching between chiral geometries, have emerged as a viable method to detect biomolecules. They have been used to sense analytes such as viral RNA[115], adenosine triphosphate, and cocaine[116]. In these structures, binding of the analyte molecule to strategically placed receptors alters the relative angle between the AuNRs, consequently altering the structure's CD signal. This method of chiral plasmonic sensing has also been adapted for sensing physical stimuli such as temperature[116] and light[117–119], demonstrating the approach's adaptability.

3.1 Associated publication P1

DNA Origami-Enabled Plasmonic Sensing

By

Mihir Dass, Fatih N. Gür, Karol Kołątaj, Maximilian J. Urban, and Tim Liedl

published in

The Journal of Physical Chemistry C, **2021**

as

Dass, M., Gür, F. N., Kołątaj, K., Urban, M. J. & Liedl, T. DNA Origami-Enabled Plasmonic Sensing. *J. Phys. Chem. C* **125**, 5969–5981 (2021)

Perspective

DNA Origami-Enabled Plasmonic Sensing

Mihir Dass, Fatih N. Gür, Karol Kołątaj, Maximilian J. Urban, and Tim Liedl*

Read Online

ACCESS | Metrics & More | Article Recommendations

ABSTRACT: The reliable programmability of DNA origami makes it an extremely attractive tool for bottom-up self-assembly of complex nanostructures. Utilizing this property for the tuned arrangement of plasmonic nanoparticles holds great promise particularly in the field of biosensing. Plasmonic particles are beneficial for sensing in multiple ways, from enhancing fluorescence to enabling a visualization of the nanoscale dynamic actuation via chiral rearrangements. In this Perspective, we discuss the recent developments and possible future directions of DNA origami-enabled plasmonic sensing systems. We start by discussing recent advancements in the area of fluorescence-based plasmonic sensing using DNA origami. We then move on to surface-enhanced Raman spectroscopy sensors followed by chiral sensing, both utilizing DNA origami nanostructures. We conclude by providing our own views on the future prospects for plasmonic biosensors enabled using DNA origami.
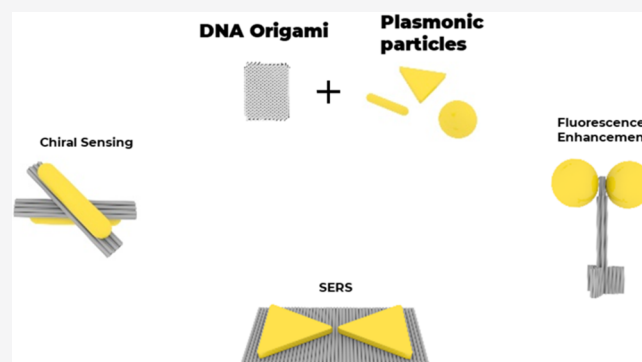
INTRODUCTION

The ability to sense external or internal stimuli is a key feature of life. Indeed, sensing allows natural systems to adapt to environmental changes thus improving their chances of propagation. In such systems, molecules detect changes in the environment, for example, concentration of nutrients or intensity of light irradiation, and turn them into biochemical stimuli. In medicine, the sensing of biomolecules is of great interest in clinical diagnostics to enable an early and low-concentration detection of disease biomarkers without the need for expensive equipment. Therefore, highly sensitive devices with simple readout capabilities are the need of the hour.

An ideal biomolecular sensor transduces a binding event into a strong output signal. In this work, we cover recent advances in plasmonic sensing using bottom-up fabricated DNA-based nanostructures. We will focus on assemblies of metallic nanoparticles that take advantage of optical near-field effects, in particular, electric field enhancement and plasmonic chirality. For the well-established sensors based on shifting surface plasmon resonances, we point the reader to the existing literature.[1−3] Other, very recent, reviews cover related focus areas ranging from the interaction of DNA with pathogens to the use of DNA in nanophotonics.[4−6]

Another established sensing scheme utilizing noble metal nanoparticles is the lateral flow assay. Here, the strong absorption and scattering capabilities of nanoparticles (AuNPs) play a key role along with reliable particle synthesis and conjugation methods to enable the easily visible bands on test strips, an example being the severe acute respiratory syndrome coronavirus 2 (SARS-CoV-2) rapid antigen tests. However, these strips are limited in sensitivity and selectivity as well as the type of output signals (scattering and fluorescence color). Advances in nanofabrication, optical detection, and conjugation chemistry lead to the development of higher performance devices with more functional capabilities. Two such strategies are (i) biomolecular assays making use of plasmonic "hot-spots" and (ii) sensing enabled through a dynamic structural reconfiguration. Both of these sensing principles require an excellent control over molecular placement at the nanoscale. While a precise positioning of objects at the macroscopic scale is a trivial task, it is extremely challenging to achieve at the nanoscale. This is due to a combination of the effects of Brownian motion that prevails at such dimensions, a lack of tools to precisely manipulate nanoscale objects, as well as a lack of strategies capable of positioning multitudes of objects deterministically at the same time for a parallel assembly.

Among current nanofabrication strategies, DNA nanotechnology has emerged as one of the most successful. The description of the dynamic "Holliday junction" by Holliday[7]

led Seeman to design an immobile Holliday junction,[8] kickstarting the use of DNA as a material and thus the field of DNA nanotechnology.[9,10] Today, there are two main approaches to build bottom-up assembled DNA nanostructures. For the longest time, DNA structures were exclusively assembled from oligonucleotides, that is, synthetic DNA strands up to several tens of nucleotides long. Examples of this approach are "tile assembly" and "DNA bricks".[11–13] The second approach involves the use of a long scaffolding molecule and is widely known as (scaffolded) "DNA origami".[14–16] DNA origami structures are thus created from a "scaffold" strand that usually is of biological origin and multiple short, synthetic "staple" oligonucleotides. Consequently, each synthetic nucleotide can be easily customized to achieve an intended purpose. Analogous to a breadboard in electronics, various components can be placed at predefined positions to achieve structures that can perform programmed functions. Since its advent,[15] the DNA origami technique has been used for the bottom-up assembly of functional structures aimed at a variety of uses, from a DNA "box" potentially capable of triggered drug-release[17] to a controllable robotic arm at the nanoscale.[18] This variety in application is driven by a molecular addressability that enables the placement of moieties with a resolution that is theoretically equal to the distance from base pair to base pair in a double helix, that is, 0.34 nm. Remarkably, also in experiments, position accuracy below 1 nm has been achieved with DNA self-assembly.[19,20] Clearly, the strong functional capability of plasmonic DNA origami, the subject of this Perspective, relies on such a precise placement of plasmonic particles in user-defined configurations.

The attachment of plasmonic particles, most commonly gold, is achieved through a complementary base-pairing between DNA-covered nanoparticles and the DNA origami structure. Simply put, the surface of the plasmonic particle is functionalized with thiolated DNA oligonucleotides of a defined sequence. Specific staple strands of the origami structure are then extended with a sequence—we often refer to it as the "handle" sequence—that is complementary to the DNA on the plasmonic particles, the "anchor" sequences. The geometrical configuration of the handles on the origami defines the placement of the particles on the origami. Since each nucleotide's position and sequence in the origami structure are deterministically known, the placement of particles can be controlled with the step size between two base pairs thus allowing sub-nanometer precision.

Mirkin et al. and Alivisatos et al. reported the first instances of using a thiol-capped DNA sequence to functionalize and arrange gold nanoparticles.[21,22] Since then, thiolated DNA has become ubiquitous for functionalizing gold and other plasmonic nanoparticles. The gold–thiol bond is well-studied for its pseudocovalent nature leading to strong binding strengths. It is, however, challenging to achieve a high-density loading of DNA on colloidal particles due to its negatively charged phosphate backbone. A slow addition of salt (salt-aging) mitigates this by screening the charges on adjacent DNA oligonucleotides, allowing the DNA to pack closely on the surface of metal nanoparticles.[23–26]

An alternative to this approach is the freeze–thaw method reported by Liu and Liu.[27,28] The authors showed that freezing a solution containing AuNPs, DNA, and salt could help to speed up the conjugation process dramatically. The freezing results in ice crystals composed of pure water,

pushing the nonwater components into gaps between the crystals, where they reach saturated concentrations, allowing the DNA to efficiently bind to gold via its thiolated end. The robustness, simplicity, and rapidity of this technique can be instrumental both to be adopted by a wider scientific community as well as being easily transferable to industrial applications. We point readers to a review that discusses this and other attachment protocols in more detail.[29]

Plasmonics coupled with DNA origami has opened up the opportunity to apply fundamentally new approaches to sensing. In this Perspective, we discuss recent advances in molecular sensing using plasmonic DNA origami structures, beginning with plasmon-enhanced fluorescence-based detection, followed by surface-enhanced Raman spectroscopy (SERS) sensing, and last, chiral plasmonic sensing. Finally, we will try to outline the major hurdles that must be overcome in the near future to expedite these advances, from accurate biomolecule detection using off-the-shelf products to the detection of analytes at the single-molecule level.

■ FLUORESCENCE-BASED PLASMONIC SENSING WITH DNA ORIGAMI

The structural arrangement of metal nanoparticles in the proximity of fluorophores can lead to a variety of physical effects, ranging from fluorescence enhancement (FE) over distance-dependent quenching to permanent photobleaching. Of these, FE holds special promise in the realm of biosensing and diagnostics. Plasmonic nanostructures can create highly localized electric fields, which can enhance the fluorescence of molecules in their vicinity.[30] The degree of enhancement is influenced by the size of the plasmonic particle (in a first approximation the larger the size, the higher the enhancement) and its shape (high-aspect-ratio nanorods or bipyramids can have strongly enhanced fields at their tips) as well as its chemical composition (e.g., silver leading to stronger plasmon coupling than gold).

The placement of metallic nanoparticles near fluorescent entities can affect the fluorescence emission in many ways: influencing the distance-dependent radiative and nonradiative decay rate and enhancing the local electric field as well as generally increasing the apparent cross section of small organic dyes with the help of comparatively large plasmonic antennas. As the nanoparticle diameter increases, the relative contribution of the scattering in the total extinction increases.[31] This increase of the scattering cross section for larger particles has been suggested to account for a part of the FE, with a further contribution coming from the radiative rate enhancement.[32,33] Control over the distance between the metallic nanoparticle and the fluorescent molecule is extremely crucial for influencing the radiative and nonradiative decay rates as shown by Acuna et al.[34,35] and others.[36–41] We will see below that FE effects can be enhanced over 5000-fold by placing two or more particles in close proximity, which leads to the creation of a plasmonic "hot-spot" between them due to the coupling of their respective electromagnetic fields.

An important aspect of achieving control over a particle placement on DNA origami is the DNA connector configuration. Generally, two connection strategies are available for binding AuNPs to a DNA origami structure: the shear and the zipper configuration. In the former, the same terminal ends (either both 5′ or both 3′ ends) of the handles and the anchors are protruding from their respective surface (gold or origami), and thus, after antiparallel
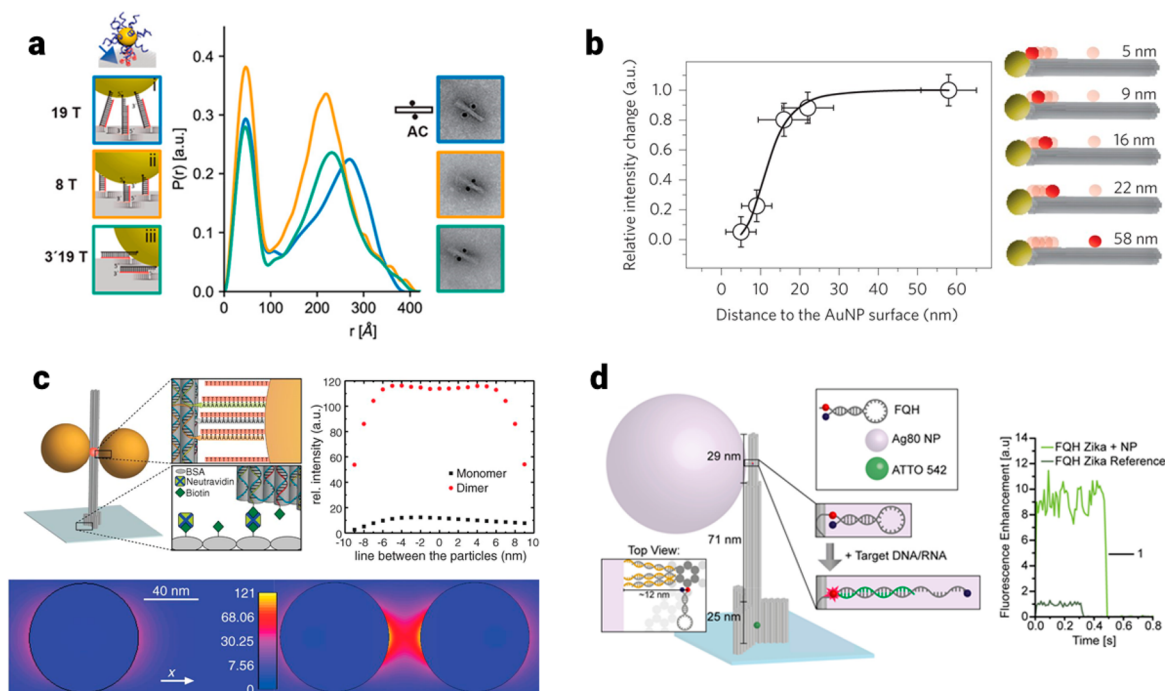
Figure 1. Nanoparticle placement on DNA origami for fluorescence enhancement. (a) (left) Scheme of different connector types: (i) A_{15} to T_{19} (blue), (ii) A_9 to T_8 (orange), and (iii) A_{15} to $3'$ T_{19} (green, zipper configuration). (right) PDDF for each of the three different connector types for dimers shown together with corresponding TEM images.[20] (b) Normalized and threshold-corrected fluorescence intensity measurements (circles) of Cy5 dyes at varying distances from a AuNP and the corresponding fit (curve).[42] (c) (top, left) Sketch of the DAN with two AuNPs forming a dimer, with a dye (red sphere) between the NPs. (top, right) Numerical simulations of the FE for a dye oriented in the radial direction in a plasmonic hot spot. a.u., arbitrary units. (bottom) Numerical simulation of electric field intensity for a monomer (left) and dimer (right).[35] (d) (left) DAN with a fluorescence quenching hairpin. (right) FE in a DAN with a AgNP compared to a reference without AgNP.[39] (a) Reproduced with permission from ref 20. Copyright 2018 American Chemical Society. (b) Reproduced with permission from ref 42. Copyright 2013 Springer Nature. (c) Reproduced with permission from ref 35. Copyright 2012 The American Association for the Advancement of Science. (d) Reproduced with permission from ref 39. Copyright 2017 American Chemical Society.

hybridization of the two strands, the duplex is oriented perpendicular to the bound surfaces (Figure 1a). For the zipper configuration, the two different terminal ends protrude, which, upon binding, results in a duplex that is oriented tangentially to the bound surfaces. In a study by Hartl et al.[20] small-angle X-ray scattering (SAXS) was used to accurately determine the distances between spherical nanoparticles bound to predefined positions on a rectangular DNA origami block in the zipper and the shear configuration with varying lengths of sequences (Figure 1a). Interparticle distances for structures utilizing shear geometry connectors followed an expected trend, with the longer T19 connector spacing the particles 5 nm further apart than the T8 connector, a difference coinciding with the difference in the connector lengths. Notably, the zipper configuration did not yield the smallest interparticle distances. This was explained by the presence of the single-stranded DNA shell around the particles, which sterically hinders the placement of particles close to a surface. The formation and application of complex hybrid structures where both fluorescent dyes and metal nanoparticles are arranged on the same DNA origami structure was shown, for example, by Schreiber et al. (Figure 1b).[42] By arranging Cy5 dye molecules at varying discrete distances from a central core gold nanoparticle, the authors were able to verify a $1/d^4$ distance dependence model of quenching.

Detection of single molecules with a fluorescence microscope requires sensitive cameras, and the discrimination of

real events from noise can be tedious. A plasmonic enhancement can lower the bar for the complexity of the instrumentation required for the detection of fluorescence events.[43] Although ensemble-averaged biosensors for the detection of RNA, DNA, and proteins have depended on plasmon-enhanced fluorescence for years, the advent of DNA origami-based single-molecule sensors relying on plasmon enhancement is a relatively new development. Acuna et al. reported the bottom-up fabrication of DNA-assembled nanoantennas (DANs), which are composed of a DNA nanopillar arranging two AuNPs with a 23 nm gap between them (Figure 1c).[35] An ATTO 647N dye molecule was placed in this plasmonic hot spot between the two particles, and the fluorescence properties of the hybrid structure were then probed. The authors reported FE of up to 117-fold for DANs carrying 100 nm particles. This significance of the DANs lies in the deterministically assembled nanoparticle dimers for the signal detection and amplification of individual dye molecules. This work opened up space for numerous studies building on this concept.

One challenge, for example, in molecular diagnostics is the low signal-to-noise ratio in biological samples, since analytes often contain not only the target molecules but also many other species that can contribute to binding interactions and cause spurious detection events. Single-molecule detection, therefore, requires the isolation of the fluorescence signal of the molecule of interest from background contributions by other equivalent molecules or impurities. Additionally, using

diffraction-limited optics to observe single-molecule events restricts detection volumes to the femtoliter range (the space of 1 μm^3, which is a lot of space for nanometer-sized molecules) and concentrations to pico- or nanomolar ranges, whereas most biological reactions occur at the micromolar range and on the nanometer scale. Tinnefeld and co-workers overcame these obstacles in a series of works. Puchkova et al. used the DANs described above to achieve a single-molecule detection of ATTO 647N dye molecules at dye concentrations of up to 25 μM in the presence of NiCl$_2$ acting as a quencher.[36] They also achieved an FE of 5468×, the highest enhancement factor for a dimer nanoantenna at the time. The FE capacity of an optical nanoantenna is the result of two contributions: the electric-field intensity enhancement at the dye's excitation wavelength and the relative change in the dye's quantum yield induced by the nanoantenna at the dye's emission wavelength range. To optimize these two parameters, the authors controlled distinct characteristics in their nanoantenna system: they used the zipper geometry to reduce the interparticle distance, the dimer orientation and the incident polarization were aligned, and they quenched the intrinsic quantum yield of the fluorophore to measure its effect on the fluorescence enhancement in DANs.

When using gold nanoparticles as the active material species, the FE is restricted to the red−near-infrared (NIR) spectral range. To expand the spectral range and increase the signal strength, various strategies have been pursued. Zhang et al. fabricated gold nanorod dimers on a DNA origami structure to construct DANs, which they then used to study the FE of ATTO 655 dye molecules.[44] The authors probed the effect of varying gap distances between the nanorod tips on the FE, where the lowest gap distance of 6.1 nm resulted in the highest experimental FE factor of 473, whereas finite-difference time-domain (FDTD) simulations provided a theoretical maximum FE factor of ∼1200. Vietz et al. replaced the AuNPs with spherical silver nanoparticles (AgNPs), which show both a lower absorption and higher scattering cross-section over a broader spectral band in the visible range compared to AuNPs.[37] The authors measured the FE of three different types of dyes—Alexa 488, ATTO 542, and ATTO 647N—and found that the AgNP DANs resulted in mean FE values of ∼139, 149, and 162 for the three dyes, respectively. This established the superior plasmonic performance and broadband FE capabilities of AgNPs compared to the AuNP DANs, which gave FE values of 1.53, 3.07, and 176, respectively. It is worth mentioning that circularly polarized light was employed in the experiments to minimize the dispersion of FE distributions due to the random orientation of the DANs on glass slides. However, this created a challenge when comparing experimental and simulated results, because the dyes were free to rotate on time scales orders of magnitude faster than the acquisition integration time. With the goal to employ their nanoantenna devices as a sensing platform, Vietz et al. then introduced a fluorescence quenching hairpin (FQH) that exhibits a 217 (±31)-fold FE for the unquenched dye configuration (corresponding to an open hairpin).[38] The authors further designed the hairpin to promote a direct contact between the dye ATTO 647N and the quencher BBQ650, leading to the formation of ground-state complexes that exhibit a negligible radiative rate. Notably, this nanoantenna utilized only a single AgNP, as the presence of the hairpin sterically hindered the attachment of a second particle.

In the next step, the same group used the AgNP DAN in combination with FQH for a single-molecule detection of a synthetic Zika virus-specific sequence in a buffer as well as human blood serum (Figure 1d).[39] Kaminska et al. then used DANs for the FE of a single peridinin−chlorophyll a−protein complex, a light-harvesting complex, placed in the plasmonic hot spot of both Ag and AuNP dimer antennas.[40] Although there had been previous reports on the plasmonic enhancement of light-harvesting complexes,[45,46] further development was hindered by the lack of a technique for their precise placement inside hot spots. The AuNP and AgNP nanoantennas resulted in FEs of up to 526-fold and 250-fold, respectively. Interestingly, the DANs show a considerable dispersion in both fluorescence intensity and fluorescence lifetime. Possible reasons for this include the occasional formation of monomer antennas along with dimer antennas, as well as inhomogeneities in the NP shape and size as well as variable interparticle gap sizes. Recently, Trofymchuk et al. developed a new DNA origami design that features a "window" in the hot spot of the DANs.[41] The rationale of this design change is to expand the space and reduce the influence of steric effects on the binding of incoming target molecules to ligands positioned in the hot spot. The new design yielded equivalent and higher values of FE (up to 417×) of ATTO 647N dye molecules. The authors then placed a sandwich binding assay for the detection of a DNA fragment specific to Oxa-48, an enzyme providing resistance to a certain antibiotic. This type of test is used for the diagnosis of Klebsiella pneumonia infections. By positioning three capture strands in the hot spots, FE values of up to 461× could be achieved. Again, the FE distribution exhibits a broad distribution, attributed to the effects mentioned above. Along with this, comparatively low binding efficiencies of 66% (with AgNPs) compared to 84% (for reference structures without AgNPs) might also limit the degree of the FE. Nevertheless, an impressive achievement of the work is the successful use of a smartphone camera for a single-molecule detection using the DANs. Integrating these components into a simple microscope setup, the observation of single-molecule blinking and bleaching events was possible with off-the-shelf consumer products.

■ SERS SENSORS BASED ON DNA ORIGAMI

Surface-enhanced Raman spectroscopy (SERS) is a surface-specific spectroscopic technique that employs metal surfaces to enhance Raman signals of molecules. Next to rugged metal surfaces, metal nanoparticles are routinely used in a SERS application. During the interaction of light with the plasmonic nanoparticles, oscillations of the electron plasma are excited on the metallic surfaces leading to an enhancement of the electric field in close vicinity to the particles and, hence, to an amplification of the molecular Raman signal.[47] Importantly, the intensity of the electric field is not evenly distributed around the nanoparticles, but hot spots emerge where nanoparticles come close together or nanoparticles exhibit spikes or tips.[48] In such regions, the Raman scattering intensity is extremely enhanced, as the Raman signal grows with the fourth power of the electric field. Hence, signal boosts up to 15 orders of magnitude in comparison with nonenhanced Raman scattering can be achieved.[48] Because of the huge signal enhancement provided by plasmonic hot spots, SERS can become a highly sensitive spectroscopic method and provide the means for single-molecule studies.[49]
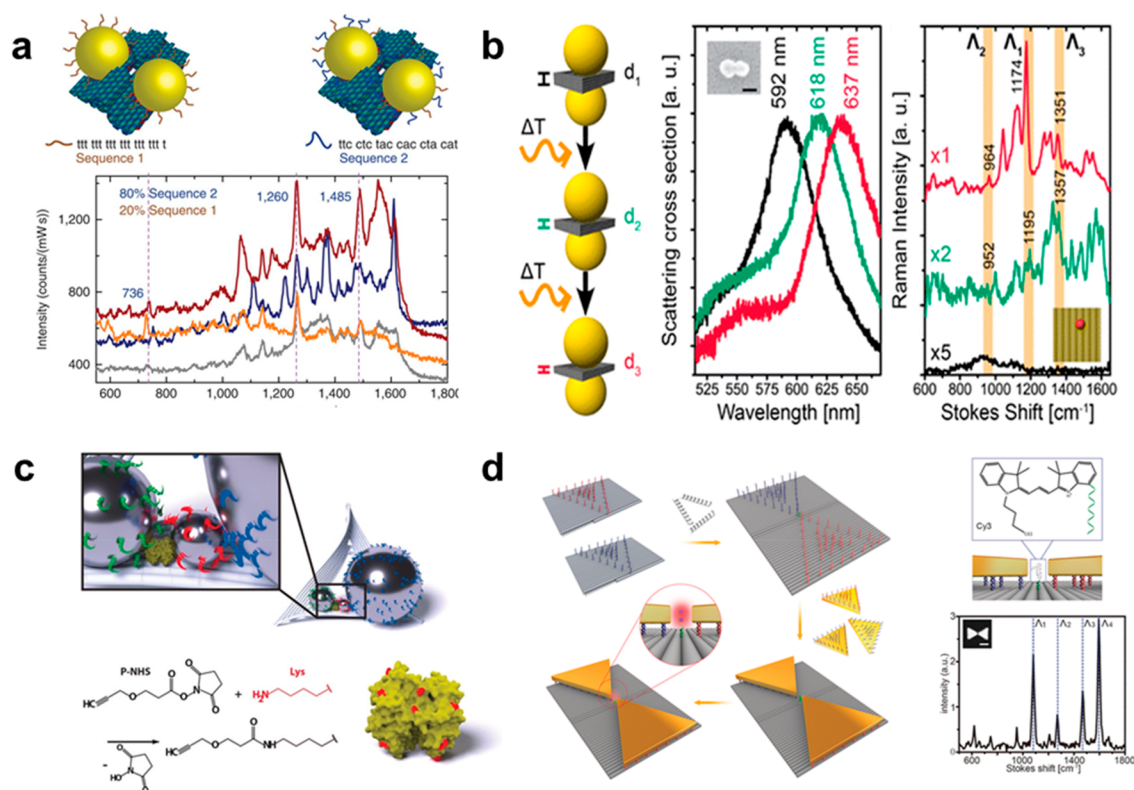
Figure 2. DNA origami-based SERS nanoantennas. (a) Plasmonic dimers of gold spheres covered with two different DNA sequences. (below) Their SERS spectra.[52] (b) Thermally induced hot-spot shrinkage and corresponding scattering (middle) and Raman (right) spectra with different gap size.[55] (c) Single streptavidin molecule immobilized in the hot spot of silver nanolenses.[56] (d) Schematic representation of the synthesis of a gold bowtie nanoantenna (left) and Raman spectrum of single Cy3 molecule (right).[57] (a) Reproduced with permission from ref 52. Copyright 2014 Springer Nature. (b) Reproduced with permission from ref 55 .Copyright 2016 American Chemical Society. (c) Reproduced with permission from ref 56. Copyright 2018 Wiley-VCH. (d) Reproduced with permission from ref 57. Copyright 2018 Wiley-VCH.

It is thus crucial to find precise and reliable ways for the fabrication of versatile hot-spot-based SERS sensors. The first requirement for such a sensor is the accurate arrangement of plasmonic nanoparticles with small interparticle gaps of ~5 nm or below. Second, the molecule of interest must be precisely placed in the hot spot to provide a strong and targeted Raman signal. These conditions are hard to fulfill using conventional top-down fabrication methods such as electron-beam lithography. Thanks to its addressability, specificity, and nanometer precision, DNA molecules, along with DNA origami structures, become natural candidates for the fabrication of versatile Raman-active antenna structures. The standout example of such structures is the synthesis of nanogap core−shell gold particles presented by Lim et al. In their approach the synthesis of the homogeneous Raman-active gap of 1 nm between the core and the shell was facilitated by DNA molecules on the core's surface, which enabled the detection of single molecules placed in the gap.[50] A pioneering study using DNA origami in SERS was performed by Prinz et al. in 2013.[51] They used two spherical gold nanoparticles attached to a triangular DNA origami to obtain Raman spectra of molecules embedded in the DNA structure. Shortly after, Thacker et al. used a more sophisticated DNA origami design for binding spherical gold nanoparticles with a predetermined sub-5 nm gap. The synthesized structures were used for Raman measurements of Rhodamine 6G and DNA enveloping nanoparticles (Figure 2a).[52] At the same time, Kühler et al. observed Raman spectra of SYBR-Gold molecules that accumulated in the designed

gap of a DNA origami−gold nanoparticle hybrid structure.[53] For single-molecule measurements, further shrinkage of the interparticle gap had to be realized, which was achieved by two different approaches.[54,55] The first approach was based on the overgrowth of a silver shell on gold nanoparticles attached to DNA origami,[54] while the second approach utilized a thermally induced shrinkage of the DNA origami structure to which the gold particles were anchored (Figure 2b).[55]

Significant effort has been put into developing DNA sensors with novel plasmonic properties and enhanced sensitivity, obtained often via the synthesis of plasmonic arrays.[56,58−62] One possible fabrication methodology of nanoantenna arrangements is a "polymerization" of monomeric DNA origami units into long chains or two-dimensional (2D) lattices using complementary strand hybridization.[58,59] The most straightforward realization of this concept was reported by Zhao et al., where long plasmonic chains were obtained by linking rectangular DNA origamis, each containing two 30 nm gold nanoparticles.[58] An enhanced Raman signal of mercaptobenzoic acid (MBA) molecules was explained by the formation of multiple hot spots, a result of the chain formation. Furthermore, because of its programmability, DNA nanotechnology enables the synthesis of more sophisticated plasmonic systems. For example, Ag@Au core−shell nanoparticles were arranged into a series of hexagonal clusters using DNA origami and then used for the detection of MBA molecules.[60] Another interesting refinement of DNA origami-based sensors was presented by Moeinian et al.[61] In their approach, a silicon nanowire was functionalized with nano-

particle-decorated 6-helix bundles to realize a sub-wavelength spatial precision of SERS measurements. Despite the significant advantages of plasmonic sensors, many of them rely on the random deposition of molecules on the surface of plasmonic particles for SERS measurements and hence do not utilize virtues of DNA origami, namely, programmability and nanometer precision. A "quantized" molecular sensor using DNA origami multimers with precisely localized dye molecules was reported by Fang et al.[62] Because of finely organized large gold nanoparticles, a plasmonic coupling between nanoparticles was achieved. The calculated enhancement factor was on the order of 10^8, which enabled the detection of a single carboxy-X-rhodamine molecule anchored in the hot-spot region. Recently, DNA origami has also been applied to precisely accommodate a single protein in the hot spot of silver nanolenses.[56] Subsequently, the plasmonic nanoparticles' arrangement enabled measurements of a single molecule of alkyne-functionalized Streptavidin, indicating future applications of DNA origami-based nanoantennas in biosensing (Figure 2c).

Thus, DNA origami-based nanoantennas have already helped to strongly increase the sensing utility of Raman spectroscopy. This was mainly realized by shrinking the gap sizes, by multiplication of hot-spots, or by the growth of silver layers on the antenna particles. However, the plasmonic properties of such antenna systems can be tuned further. For example, anisotropic nanoparticles with sharp edges can be integrated into DNA origami SERS sensors. Anisotropic nanostructures display exquisite plasmonic properties due to the tremendous field enhancement at their tips.[63] Moreover, the use of anisotropic nanoparticles allows a convenient tuning of plasmonic properties, which are strongly correlated with particle shape and size.[48,63] Despite these advances, to our knowledge, only two DNA origami sensors utilizing anisotropic nanoparticles have been reported.[57,64] Tanwar et al. reported the synthesis of gold nanostar dimers and their use in the single-molecule measurement of Texas Red, a fluorescent dye.[64] Coupling between the sharp tips of the nanoparticles contributed to very strong signal enhancement, up to 8×10^9, in the hot spot between nanostars. A similar signal enhancement was recently obtained by the tip-to-tip arrangement of two gold nanolenses on DNA origami, enabling the detection of single Cy3 and Cy5 molecules (Figure 2d).[57]

■ DNA ORIGAMI-BASED CHIRAL PLASMONIC SENSING

Another promising route toward the development of biosensing platforms is the use of chiroptical properties of plasmonic nanostructures or the plasmon-enhanced detection of chiral molecules.[65,66] For this, circular dichroism (CD) spectroscopy is employed to analyze the chirality of the structures by measuring the difference in the absorption of left-handed (LH) and right-handed (RH) circularly polarized light. Most of the biomolecules such as DNA and proteins typically exhibit CD signals in the ultraviolet range.[67] In contrast to biomolecules, chiral plasmonic systems display strong and characteristic CD responses in the visible regime due to the surface plasmon resonances.[68−70] This makes chiral plasmonic devices ideal for the detection of biomolecules in solution, since many biological samples show a very low "background" CD signal in the visible range. Surface plasmons of colloidal metal nanoparticle assemblies can significantly

enhance the CD signals[71] and thus enable the detection of biomolecules in the visible wavelengths with increased sensitivity.[72]

By leveraging the programmability and scalability of DNA self-assembly, colloidal nanoparticles have been self-assembled into LH or RH plasmonic helical structures,[69,73] pyramids,[74] tetramers,[75] toroidal superstructures,[76] or helical super-structures.[77,78] Such static chiral assemblies show strong plasmon-mediated CD responses. However, for sensing applications dynamic chiral plasmonic structures proved to be more viable thus far.[6] Among various dynamic chiral plasmonic assemblies,[70,79,80] the reconfigurable three-dimensional (3D) plasmonic metamolecules introduced by Kuzyk et al.[81] have been particularly successful as sensing devices. This chiral metamolecule is composed of two linked DNA origami bundles each hosting a gold nanorod at the top and bottom, forming a 3D plasmonic cross structure (Figure 3a). The relative angle between the rods and therefore the chiral state of the device can be modulated by DNA-, RNA-, or aptamer-based locks, which are extended from the edges of the DNA origami bundles. With an addition of specifically designed DNA fuel strands or with a target molecule binding, the sensing devices switch their conformation from an "open" or "relaxed" achiral state to one of the "locked" chiral states (LH or RH). These structural configurations can be correlated with the corresponding optical responses using CD spectroscopy in real time.

By using the original plasmonic metamolecule or similar chiral plasmonic structures, this versatile approach was extended to stimuli including light,[82−84] pH,[84−86] temperature,[87] small molecules,[87,88] proteins,[89] DNA,[81,90] and viral RNA.[91] Figure 3a,b shows examples of DNA origami-based switchable chiral plasmonic biosensors for the detection of various analytes. Our research group demonstrated a selective detection of viral RNA from the hepatitis C virus genome at target concentrations of below 100 pM in buffer[91] (Figure 3a). For the biorecognition, two complementary locking DNA strands are extended from the DNA origami bundles, and the hybridization of these two strands to each other is prevented by a third strand that is complementary and therefore bound to one of the two locking strands. This blocking strand is removed by the target RNA sequence by a toehold-mediated strand displacement. After this removal step, the two locking DNA strands are now free to hybridize to each other leading to the formation of the RH state of the device with a distinct optical response measured by CD spectroscopy (Figure 3a). We further proved that our sensors are still stable and functional after 30 min of incubation in 10% human blood serum and can detect the target RNA at concentrations below 1 nM in 10% serum. This sensing device can readily be applied to detect RNA from the SARS-Cov-2 (to be published).

In 2018, Zhou et al. reported a dual responsive plasmonic sensing device that can respond to temperature and aptamer-target interactions.[87] The versatility and addressability of DNA origami enabled the detection of adenosine triphosphate (ATP) and cocaine (COC) molecules in a single device by jointly introducing split ATP and COC aptamers to the DNA origami structure. Chiroptical responses of this reversible sensing device in the presence of target ATP (1 mM) and COC (1 mM) molecules could be monitored by CD spectroscopy. As shown by the black curve in the CD spectra in Figure 3b, without target binding the device displays slight
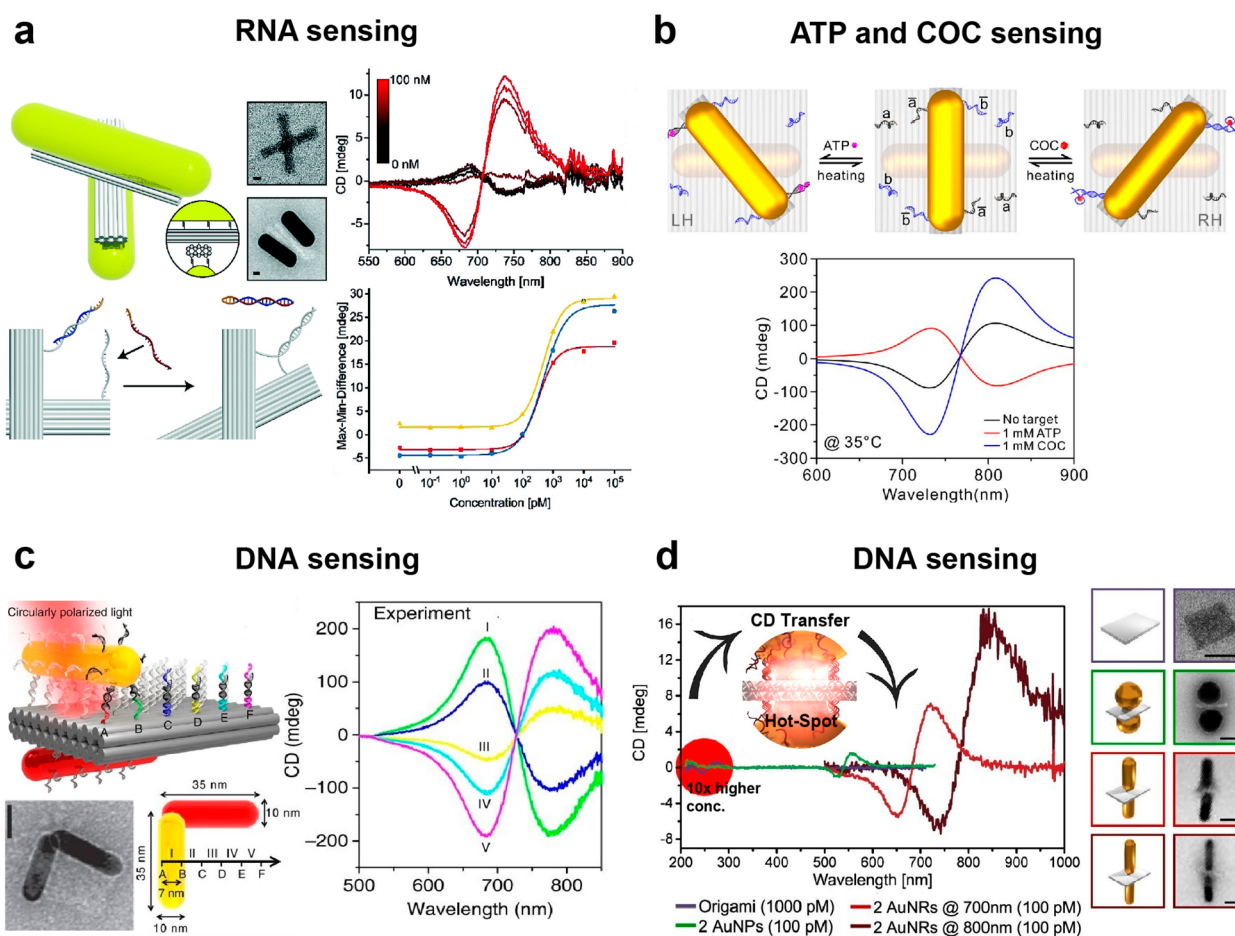
Figure 3. DNA origami-enabled chiral plasmonic sensing systems. DNA origami-based switchable chiral plasmonic biosensors for detection of viral RNA (a), ATP, and COC (b), and their corresponding CD responses at different target concentrations. Chiral plasmonic walker assembled on DNA origami and measured CD spectra at different stations, potentially acting as nucleic acid sensor (c). DNA origami-supported nanoantennas for the detection of chiral B-form DNA molecules and CD measurements of nanoantennas in solution (d). Schematics and TEM micrographs (in a, c, d) of assembled sensing devices, scale bars are 20 nm (in a, c) and 40 nm (in d). (a) Reproduced with permission from ref 91. Copyright 2018 Wiley-VCH. (b) Reproduced with permission from ref 87. Copyright 2018 American Chemical Society. (c) Reproduced with permission from ref 90. Copyright 2015 The Authors. (d) Reproduced with permission from ref 72. Copyright 2018 American Chemical Society.

signatures of the RH state. After addition of the ATP molecules, the CD spectra flipped (red curve), indicating that the device switched into the LH state. Contrarily, when COC molecules were added, the device was driven further into the RH state reflected in stronger CD responses (blue curve). The authors also showed in this study that the chiral state of the device can be tuned by temperature. Using a similar geometry, Dong et al. recently reported DNA origami-based adaptive plasmonic logic gates that read multiple DNA molecules as input and return plasmonic chiroptical signals as output.[92] Such self-assembled systems perform logical computations and could also work as plasmonic sensors. Similarly, Huang et al. demonstrated a reconfigurable chiral plasmonic sensor where "double-stranded" and "split aptamer" locks are employed as biorecognition elements for adenosine sensing.[88] They tested different lock systems at different adenosine concentrations and achieved the detection limit of 20 μM with a response time of 1 min. They found that shortening the hybridization length of the locks is crucial to improve the detection limit and response time. Subsequently, Funck et al. reported a dual-aptamer-functionalized sensing device that could reliably detect the human α-thrombin protein in solution with a detection limit of 100 pM.[89] This device could potentially be

further improved by introducing multiple copies of the thrombin aptamers to the DNA origami structures.

Next, Zhou et al.[90] demonstrated a chiral plasmonic walker system that, in principle, can be used as a sensor to detect a target nucleic acid sequence. As shown in Figure 3c, the chiral plasmonic walking system formed by assembling a walker AuNR (yellow) and a stator AuNR (red) in a chiral geometry on two opposite faces of a DNA origami structure. After the sequential addition of respective blocking and removal strands, the walker performs a progressive and directional movement with a "rolling" fashion. The overall walking process was in situ optically monitored with an immediate spectral response by CD spectroscopy (Figure 3c, CD spectra). This approach was further advanced by introducing a walker couple that performs independent or simultaneous stepwise walking along the same track,[93] a rotary plasmonic nanoclock that can perform a directional and reversible 360° rotation,[94] and a sliding system that can slide two DNA origami filaments using gold nanoparticles.[95] Remarkably, these dynamic plasmonic systems could resolve the stepwise movement with nanoscale step size, which is far below the optical diffraction limit.

Thus far, we have reviewed DNA origami-templated reconfigurable chiral plasmonic sensing devices. Alternatively,

there is another approach to use DNA origami-based static plasmonic nanostructures for the detection of chiral biomolecules. This approach is based on an enhanced CD spectroscopy and an ultrasensitive detection of (chiral) molecules by surface plasmon-generated near-fields.[96−100] Figure 3d shows an example of DNA origami-supported nanoantennas for the detection of a B-form DNA chirality.[72] In this report, our research group demonstrated that the UV-CD response of DNA molecules can be transferred into the resonance frequency range of plasmonic nanoantennas. The high electromagnetic field enhancement in the antenna hot spot allowed detection of the transferred CD signal at much lower analyte concentrations than the amount needed to obtain discernible CD signals from the pristine DNA molecules in the UV. Figure 3d shows the experimental design and the transfer of the UV-CD signal of a two-layered DNA origami sheet to the visible regime and its amplification by a factor of 30 with the help of two spherical AuNPs (green curve). By using AuNRs antenna structures, the CD transfer into the near-infrared regime is realized with an up to 300-fold stronger CD signal (red and dark red curves). We also showed that the use of other materials (gold−silver, core−shell particles) for the antenna element enables the shifting of the CD signal into yet another wavelength range.

■ CONCLUSION AND GENERAL PERSPECTIVES

In the past decade, the DNA origami-based fabrication of plasmonic sensors has advanced rapidly.[101−104] In summary, DNA origami is a successful nanofabrication technology to arrange plasmonic nanoparticles with nanometer precision.[69,105−109]

Specificity and sensitivity are key variables when describing the performance of a sensor. To study these parameters and to increase performances of sensors, DNA origami provides the molecular breadboard for well-defined interactions of target molecules with the recognition elements.

The addressability of DNA origami allows, for example, the accurate positioning of fluorescent markers in the plasmonic hot spot of nanoparticle antennas, and this has been used to achieve a single-molecule sensing of a variety of targets. Currently, when studying FE-based sensing, spherical nanoparticles have received the greatest attention, while nanorods have been explored to a lesser extent. This highlights an area of interest with a high potential that has remained relatively unexplored, as anisotropic morphologies like nanorods as well as more exotic structures such as bipyramids are known to have higher field-intensity increases at their tips.[110] This property could lead to a further enhancement in the sensitivity of such sensors. An interesting development is the use of an off-the-shelf consumer smartphone to readout the fluorescence signals from DNA-assembled antennas. This line of research could be extended to increase both the limit of detection from such instruments as well as the range of analytes that can be detected potentially enabling pathogen detection in remote areas.

The ability to arrange plasmonic nanoparticles on DNA origami also renders it an exquisite platform for the fabrication of plasmonic SERS sensors, especially for single-molecule measurements. Moreover, DNA nanostructures are fully biocompatible and can be readily functionalized with a variety of targeting entities including aptamers and antibodies.[111−114] Nevertheless, up to now, DNA origami-based SERS sensors were primarily used for the detection of small dyes, with only one functional biomolecule measurement reported.[56] Hence, future efforts in the field should be focused on the enhancement of sensitivity and versatility of such SERS sensors and their use in studies of various biomolecules both in vitro and in situ.

The combination of chiral plasmonics and DNA origami has enabled chirality-based biosensors for the selective and sensitive detection of various analytes. For a wide range of detection windows (UV−vis−NIR), the optical responses can be tuned and amplified by size, shape, and material composition of plasmonic building blocks. For example, recently we demonstrated that chiral assemblies of gold−silver core−shell plasmonic nanorods show strongly increased CD responses compared to their gold counterparts.[115] Furthermore, by controlling the size, aspect ratio, and silver shell thickness, the spectral responses could be tuned as desired. This could dramatically improve the performance of the aforementioned devices. In addition, programmable and fully addressable DNA origami enables incorporating multiple biorecognition elements. This opens numerous sensing systems that respond to various molecular binding events, facilitating the detection of a wide variety of molecular targets with a high specificity and selectivity. Recently, "single-structure" CD measurements were shown without DNA origami in plasmonic nanorod dimers assembled with the help of bovine serum albumin (BSA).[116] On the one hand, it will be of outstanding interest to study a single-structure CD in a well-controlled DNA origami nanofabrication scheme. On the other end, a naked-eye detection of chiral structures is possible with a simple configuration of two crossed polarizers.[69] This could, at some point, enable a sensitive pathogen detection without the need for expensive equipment. Thus, the overall concept of chirality-based detection holds great potential for the further development of plasmonic biosensing.

DNA origami-based plasmonic sensors are fabricated in an aqueous solution and are therefore, in principle, suited for sensing applications inside cells and tissues. Such plasmonic probes could be applied to study, for example, single-molecule processes on cell surfaces. Nevertheless, because of the reduced stability of DNA origami-assembled plasmonic nanostructures in in vivo conditions, real-life sensing applications are challenging and will require more in-depth research. Besides natural cells, these probes can be integrated into more defined synthetic biology systems, for example, synthetic cells. One example could be chiral plasmonic walkers that sense their biochemical surroundings, transport cargo in synthetic cells, and report their status optically in real-time.

To achieve a more widespread adoption of DNA origami-based plasmonic sensors, it is crucial to apply these sensors without specialized and expensive equipment such as CD spectrometers or single-molecule fluorescence setups. Improvements in DNA origami nanofabrication will enable stronger signals. In consequence, this enables optical readouts with as little instrumentation as a smartphone or a standard optical microscope with built-in polarizers.[117] This will bring the benefits of DNA origami-assembled plasmonic nanodevices to researchers of various fields, from cell biology to medical diagnostics and optics. Interestingly, custom-made DNA origami nanostructures assembled with fluorophores and nanoparticles are already commercially available (tilibit GmbH, gattaquant GmbH).

One factor that has limited the application of DNA origami structures is their reduced stability in the presence of DNA

nucleases, at low salt concentrations, at elevated temperatures, and at varying pH values. In recent years, a variety of stabilization strategies have been developed. Examples include coating layers with polymers,[118−120] silica,[121] peptoids,[122] as well as cross-linking,[123,124] among others. In the next years, it will be important to study the performance of stabilized DNA origami-assembled plasmonic sensors in application-oriented settings, for example, in blood.

With increasing knowledge about the fabrication of DNA origami-based plasmonic nanostructures, larger 3D structures can be built.[125−128] Mastering the complex assembly processes of, for example, lattices would enable the self-assembly of photonic crystals with tailored photonic band gaps that could be integrated into optical circuitry or deposited on surfaces. At the same time, many commercial applications are not profitable due to the high price of DNA. Because of advances in the production of DNA, costs are falling rapidly. With this, DNA origami-based sensors become economically viable. A biological mass production of DNA in bioreactors enables prices of 200 € per gram. This equals to ∼10^{17} DNA origami-assembled plasmonic sensors.[129]

In conclusion, the DNA origami-based fabrication of plasmonic sensors is a new technological platform to engineer sensors with great control over dimensions and the very building blocks on the molecular scale. DNA origami-assembled plasmonic sensors thus probably have reached a level of technological maturity that enables their application in real-world settings.

■ AUTHOR INFORMATION

Corresponding Author

Tim Liedl − *Faculty of Physics and Center for NanoScience, Ludwig-Maximilians-University, 80539 Munich, Germany;* orcid.org/0000-0002-0040-0173; Email: tim.liedl@physik.lmu.de

Authors

Mihir Dass − *Faculty of Physics and Center for NanoScience, Ludwig-Maximilians-University, 80539 Munich, Germany*

Fatih N. Gür − *Faculty of Physics and Center for NanoScience, Ludwig-Maximilians-University, 80539 Munich, Germany*

Karol Kołątaj − *Faculty of Physics and Center for NanoScience, Ludwig-Maximilians-University, 80539 Munich, Germany*

Maximilian J. Urban − *Faculty of Physics and Center for NanoScience, Ludwig-Maximilians-University, 80539 Munich, Germany*

Complete contact information is available at:
https://pubs.acs.org/10.1021/acs.jpcc.0c11238

Author Contributions

The manuscript was written through the contributions of all authors. All authors have given approval to the final version of the manuscript.

Notes

The authors declare no competing financial interest.

Biographies

Mihir Dass is currently a Marie Skłodowska-Curie doctoral fellow in the group of Prof. Tim Liedl at LMU, Munich. He received his Bachelor's and Master's degree in Nanotechnology (2017) from Amity University, India. His research interests include dynamic DNA nanotechnology, plasmonics, and nanofabrication.

Fatih N. Gür is currently a postdoctoral fellow in the group of Prof. Tim Liedl, LMU Munich. He received his B.Sc. degree (2010) in Physics from Izmir Institute of Technology, Turkey, M.Sc. degree (2012) in Nanoscience and Nanotechnology from KU Leuven, Belgium, and Ph.D. degree (2018) in Physical Chemistry from the Center for Advancing Electronics Dresden, TU Dresden, Germany. His research interests lie in the field of DNA nanotechnology including DNA-assembled plasmonic nanostructures, dynamic DNA nanodevices, and their applications.

Karol Kolataj is currently a Marie Skłodowska-Curie fellow and a postdoc in the group of Prof. Tim Liedl, LMU Munich. He received his B.Sc. degree (2012) in Biotechnology from Warsaw University of

Life Sciences and his M.Sc. degree (2014) in Chemistry and Ph.D. degree in Physical Chemistry from the University of Warsaw. His areas of expertise include the fabrication of plasmonic nanoparticles, DNA nanotechnology, and surface-enhanced Raman spectroscopy.

Maximilian J. Urban is currently a postdoctoral fellow in the group of Prof. Tim Liedl, LMU Munich. He received his B.Sc. and M.Sc. (2014) degrees in Life Science from the Universität Konstanz, Germany, and his Ph.D. degree in Physical Chemistry from the Universität Heidelberg and the Max Planck Institute for intelligent Systems, Stuttgart, Germany. His research interest is the application of DNA nanotechnology and plasmonics for sensing.

Tim Liedl is professor for experimental physics at LMU. He received his diploma in physics in 2004 in the group of Wolfgang J. Parak, where he worked on the development of hydrophilic coatings for fluorescent semiconductor nanoparticles. In 2007 he obtained his Ph.D. in the group of Friedrich C. Simmel studying DNA-based nanodevices and switches, which are driven by chemical oscillations. From 2007 to 2009 he visited William M. Shih's laboratory at the Dana-Farber Cancer Institute/Harvard Medical School, where he used the DNA-origami method to construct self-assembling two- and three-dimensional structures. The research of Tim Liedl currently focuses on the application of DNA-based nanostructures in biophysics and for self-assembled plasmonic materials.

REFERENCES

(1) Stewart, M. E.; Anderton, C. R.; Thompson, L. B.; Maria, J.; Gray, S. K.; Rogers, J. A.; Nuzzo, R. G. Nanostructured Plasmonic Sensors. *Chem. Rev.* **2008**, *108* (2), 494−521.

(2) Homola, J. Surface Plasmon Resonance Sensors for Detection of Chemical and Biological Species. *Chem. Rev.* **2008**, *108* (2), 462−493.

(3) Li, M.; Cushing, S. K.; Wu, N. Plasmon-Enhanced Optical Sensors: A Review. *Analyst* **2015**, *140* (2), 386−406.

(4) Smith, D. M.; Keller, A. DNA Nanostructures in the Fight Against Infectious Diseases. *Adv. NanoBiomed Res.* **2021**, 2000049.

(5) Shen, B.; Kostiainen, M. A.; Linko, V. DNA Origami Nanophotonics and Plasmonics at Interfaces. *Langmuir* **2018**, *34* (49), 14911−14920.

(6) Loretan, M.; Domljanovic, I.; Lakatos, M.; Rüegg, C.; Acuna, G. P. DNA Origami as Emerging Technology for the Engineering of Fluorescent and Plasmonic-Based Biosensors. *Materials* **2020**, *13* (9), 2185.

(7) Holliday, R. A Mechanism for Gene Conversion in Fungi. *Genet. Res.* **1964**, *5* (2), 282−304.

(8) Kallenbach, N. R.; Ma, R.-I.; Seeman, N. C. An Immobile Nucleic Acid Junction Constructed from Oligonucleotides. *Nature* **1983**, *305* (5937), 829−831.

(9) Seeman, N. C. Nucleic Acid Junctions and Lattices. *J. Theor. Biol.* **1982**, *99* (2), 237−247.

(10) Seeman, N. C. DNA in a Material World. *Nature* **2003**, *421* (6921), 427−431.

(11) Winfree, E.; Liu, F.; Wenzler, L. A.; Seeman, N. C. Design and Self-Assembly of Two-Dimensional DNA Crystals. *Nature* **1998**, *394* (6693), 539−544.

(12) Ke, Y.; Ong, L. L.; Shih, W. M.; Yin, P. Three-Dimensional Structures Self-Assembled from DNA Bricks. *Science* **2012**, *338* (6111), 1177−1183.

(13) Hong, F.; Jiang, S.; Lan, X.; Narayanan, R. P.; Šulc, P.; Zhang, F.; Liu, Y.; Yan, H. Layered-Crossover Tiles with Precisely Tunable Angles for 2D and 3D DNA Crystal Engineering. *J. Am. Chem. Soc.* **2018**, *140* (44), 14670−14676.

(14) Shih, W. M.; Quispe, J. D.; Joyce, G. F. A 1.7-Kilobase Single-Stranded DNA That Folds into a Nanoscale Octahedron. *Nature* **2004**, *427* (6975), 618−621.

(15) Rothemund, P. W. K. Folding DNA to Create Nanoscale Shapes and Patterns. *Nature* **2006**, *440* (7082), 297−302.

(16) Douglas, S. M.; Dietz, H.; Liedl, T.; Högberg, B.; Graf, F.; Shih, W. M. Self-Assembly of DNA into Nanoscale Three-Dimensional Shapes. *Nature* **2009**, *459* (7245), 414−418.

(17) Andersen, E. S.; Dong, M.; Nielsen, M. M.; Jahn, K.; Subramani, R.; Mamdouh, W.; Golas, M. M.; Sander, B.; Stark, H.; Oliveira, C. L. P.; et al. Self-Assembly of a Nanoscale DNA Box with a Controllable Lid. *Nature* **2009**, *459* (7243), 73−76.

(18) Kopperger, E.; List, J.; Madhira, S.; Rothfischer, F.; Lamb, D. C.; Simmel, F. C. A Self-Assembled Nanoscale Robotic Arm Controlled by Electric Fields. *Science* **2018**, *359* (6373), 296−301.

(19) Funke, J. J.; Dietz, H. Placing Molecules with Bohr Radius Resolution Using DNA Origami. *Nat. Nanotechnol.* **2016**, *11* (1), 47−52.

(20) Hartl, C.; Frank, K.; Amenitsch, H.; Fischer, S.; Liedl, T.; Nickel, B. Position Accuracy of Gold Nanoparticles on DNA Origami Structures Studied with Small-Angle X-Ray Scattering. *Nano Lett.* **2018**, *18* (4), 2609−2615.

(21) Mirkin, C. A.; Letsinger, R. L.; Mucic, R. C.; Storhoff, J. J. A DNA-Based Method for Rationally Assembling Nanoparticles into Macroscopic Materials. *Nature* **1996**, *382* (6592), 607−609.

(22) Alivisatos, A. P.; Johnsson, K. P.; Peng, X.; Wilson, T. E.; Loweth, C. J.; Bruchez, M. P.; Schultz, P. G. Organization of "nanocrystal Molecules" Using DNA. *Nature* **1996**, *382* (6592), 609−611.

(23) Liu, J.; Lu, Y. Preparation of Aptamer-Linked Gold Nanoparticle Purple Aggregates for Colorimetric Sensing of Analytes. *Nat. Protoc.* **2006**, *1* (1), 246−252.

(24) Cutler, J. I.; Auyeung, E.; Mirkin, C. A. Spherical Nucleic Acids. *J. Am. Chem. Soc.* **2012**, *134* (3), 1376−1391.

(25) Liu, B.; Liu, J. Methods for Preparing DNA-Functionalized Gold Nanoparticles, a Key Reagent of Bioanalytical Chemistry. *Anal. Methods* **2017**, *9* (18), 2633−2643.

(26) Gür, F. N.; Schwarz, F. W.; Ye, J.; Diez, S.; Schmidt, T. L. Toward Self-Assembled Plasmonic Devices: High-Yield Arrangement of Gold Nanoparticles on DNA Origami Templates. *ACS Nano* **2016**, *10* (5), 5374−5382.

(27) Liu, B.; Liu, J. Freezing-Driven DNA Adsorption on Gold Nanoparticles: Tolerating Extremely Low Salt Concentration but Requiring High DNA Concentration. *Langmuir* **2019**, *35* (19), 6476−6482.

(28) Liu, B.; Wu, T.; Huang, Z.; Liu, Y.; Liu, J. Freezing-Directed Stretching and Alignment of DNA Oligonucleotides. *Angew. Chem.* **2019**, *131* (7), 2131−2135.

(29) Liu, B.; Liu, J. Interface-Driven Hybrid Materials Based on DNA-Functionalized Gold Nanoparticles. *Matter* **2019**, *1* (4), 825−847.

(30) Dulkeith, E.; Morteani, A. C.; Niedereichholz, T.; Klar, T. A.; Feldmann, J.; Levi, S. A.; van Veggel, F. C. J. M.; Reinhoudt, D. N.; Möller, M.; Gittins, D. I. Fluorescence Quenching of Dye Molecules near Gold Nanoparticles: Radiative and Nonradiative Effects. *Phys. Rev. Lett.* **2002**, *89* (20), 203002.

(31) Coronado, E. A.; Encina, E. R.; Stefani, F. D. Optical Properties of Metallic Nanoparticles: Manipulating Light, Heat and Forces at the Nanoscale. *Nanoscale* **2011**, *3* (10), 4042−4059.

(32) Anger, P.; Bharadwaj, P.; Novotny, L. Enhancement and Quenching of Single-Molecule Fluorescence. *Phys. Rev. Lett.* **2006**, *96* (11), 113002.

(33) Giannini, V.; Fernández-Domínguez, A. I.; Heck, S. C.; Maier, S. A. Plasmonic Nanoantennas: Fundamentals and Their Use in Controlling the Radiative Properties of Nanoemitters. *Chem. Rev.* **2011**, *111* (6), 3888−3912.

(34) Acuna, G. P.; Bucher, M.; Stein, I. H.; Steinhauer, C.; Kuzyk, A.; Holzmeister, P.; Schreiber, R.; Moroz, A.; Stefani, F. D.; Liedl, T.; et al. Distance Dependence of Single-Fluorophore Quenching by Gold Nanoparticles Studied on DNA Origami. *ACS Nano* **2012**, *6* (4), 3189−3195.

(35) Acuna, G. P.; Möller, F. M.; Holzmeister, P.; Beater, S.; Lalkens, B.; Tinnefeld, P. Fluorescence Enhancement at Docking Sites of DNA-Directed Self-Assembled Nanoantennas. *Science* **2012**, *338* (6106), 506−510.

(36) Puchkova, A.; Vietz, C.; Pibiri, E.; Wünsch, B.; Sanz Paz, M.; Acuna, G. P.; Tinnefeld, P. DNA Origami Nanoantennas with over 5000-Fold Fluorescence Enhancement and Single-Molecule Detection at 25 MM. *Nano Lett.* **2015**, *15* (12), 8354−8359.

(37) Vietz, C.; Kaminska, I.; Sanz Paz, M.; Tinnefeld, P.; Acuna, G. P. Broadband Fluorescence Enhancement with Self-Assembled Silver Nanoparticle Optical Antennas. *ACS Nano* **2017**, *11* (5), 4969−4975.

(38) Vietz, C.; Lalkens, B.; Acuna, G. P.; Tinnefeld, P. Synergistic Combination of Unquenching and Plasmonic Fluorescence Enhancement in Fluorogenic Nucleic Acid Hybridization Probes. *Nano Lett.* **2017**, *17* (10), 6496−6500.

(39) Ochmann, S. E.; Vietz, C.; Trofymchuk, K.; Acuna, G. P.; Lalkens, B.; Tinnefeld, P. Optical Nanoantenna for Single Molecule-Based Detection of Zika Virus Nucleic Acids without Molecular Multiplication. *Anal. Chem.* **2017**, *89* (23), 13000−13007.

(40) Kaminska, I.; Bohlen, J.; Mackowski, S.; Tinnefeld, P.; Acuna, G. P. Strong Plasmonic Enhancement of a Single Peridinin-Chlorophyll a-Protein Complex on DNA Origami-Based Optical Antennas. *ACS Nano* **2018**, *12* (2), 1650−1655.

(41) Trofymchuk, K.; Glembockyte, V.; Grabenhorst, L.; Steiner, F.; Vietz, C.; Close, C.; Pfeiffer, M.; Richter, L.; Schütte, M. L.; Selbach, F.; et al. Addressable Nanoantennas with Cleared Hotspots for Single-Molecule Detection on a Portable Smartphone Microscope. *Nat. Commun.* **2021**, *12*, 950.

(42) Schreiber, R.; Do, J.; Roller, E.-M.; Zhang, T.; Schüller, V. J.; Nickels, P. C.; Feldmann, J.; Liedl, T. Hierarchical Assembly of Metal Nanoparticles, Quantum Dots and Organic Dyes Using DNA Origami Scaffolds. *Nat. Nanotechnol.* **2014**, *9* (1), 74−78.

(43) Wei, Q.; Acuna, G.; Kim, S.; Vietz, C.; Tseng, D.; Chae, J.; Shir, D.; Luo, W.; Tinnefeld, P.; Ozcan, A. Plasmonics Enhanced Smartphone Fluorescence Microscopy. *Sci. Rep.* **2017**, *7* (1), 2124.

(44) Zhang, T.; Gao, N.; Li, S.; Lang, M. J.; Xu, Q.-H. Single-Particle Spectroscopic Study on Fluorescence Enhancement by Plasmon Coupled Gold Nanorod Dimers Assembled on DNA Origami. *J. Phys. Chem. Lett.* **2015**, *6* (11), 2043−2049.

(45) Albinsson, B.; Hannestad, J. K.; Börjesson, K. Functionalized DNA Nanostructures for Light Harvesting and Charge Separation. *Coord. Chem. Rev.* **2012**, *256* (21), 2399−2413.

(46) Hemmig, E. A.; Creatore, C.; Wünsch, B.; Hecker, L.; Mair, P.; Parker, M. A.; Emmott, S.; Tinnefeld, P.; Keyser, U. F.; Chin, A. W. Programming Light-Harvesting Efficiency Using DNA Origami. *Nano Lett.* **2016**, *16* (4), 2369−2374.

(47) Kerker, M.; Wang, D.-S.; Chew, H. Surface Enhanced Raman Scattering (SERS) by Molecules Adsorbed at Spherical Particles. *Appl. Opt.* **1980**, *19* (19), 3373−3388.

(48) Krajczewski, J.; Kołątaj, K.; Kudelski, A. Plasmonic Nano-particles in Chemical Analysis. *RSC Adv.* **2017**, *7* (28), 17559−17576.

(49) Almehmadi, L. M.; Curley, S. M.; Tokranova, N. A.; Tenenbaum, S. A.; Lednev, I. K. Surface Enhanced Raman Spectroscopy for Single Molecule Protein Detection. *Sci. Rep.* **2019**, *9*, 12356.

(50) Lim, D.-K.; Jeon, K.-S.; Hwang, J.-H.; Kim, H.; Kwon, S.; Suh, Y. D.; Nam, J.-M. Highly Uniform and Reproducible Surface-Enhanced Raman Scattering from DNA-Tailorable Nanoparticles with 1-Nm Interior Gap. *Nat. Nanotechnol.* **2011**, *6* (7), 452−460.

(51) Prinz, J.; Schreiber, B.; Olejko, L.; Oertel, J.; Rackwitz, J.; Keller, A.; Bald, I. DNA Origami Substrates for Highly Sensitive Surface-Enhanced Raman Scattering. *J. Phys. Chem. Lett.* **2013**, *4* (23), 4140−4145.

(52) Thacker, V. V.; Herrmann, L. O.; Sigle, D. O.; Zhang, T.; Liedl, T.; Baumberg, J. J.; Keyser, U. F. DNA Origami Based Assembly of Gold Nanoparticle Dimers for Surface-Enhanced Raman Scattering. *Nat. Commun.* **2014**, *5* (1), 3448.

(53) Kühler, P.; Roller, E.-M.; Schreiber, R.; Liedl, T.; Lohmüller, T.; Feldmann, J. Plasmonic DNA-Origami Nanoantennas for Surface-Enhanced Raman Spectroscopy. *Nano Lett.* **2014**, *14* (5), 2914−2919.

(54) Prinz, J.; Heck, C.; Ellerik, L.; Merk, V.; Bald, I. DNA Origami Based Au-Ag-Core-Shell Nanoparticle Dimers with Single-Molecule SERS Sensitivity. *Nanoscale* **2016**, *8* (10), 5612−5620.

(55) Simoncelli, S.; Roller, E.-M.; Urban, P.; Schreiber, R.; Turberfield, A. J.; Liedl, T.; Lohmüller, T. Quantitative Single-Molecule Surface-Enhanced Raman Scattering by Optothermal Tuning of DNA Origami-Assembled Plasmonic Nanoantennas. *ACS Nano* **2016**, *10* (11), 9809−9815.

(56) Heck, C.; Kanehira, Y.; Kneipp, J.; Bald, I. Placement of Single Proteins within the SERS Hot Spots of Self-Assembled Silver Nanolenses. *Angew. Chem., Int. Ed.* **2018**, *57* (25), 7444−7447.

(57) Zhan, P.; Wen, T.; Wang, Z.; He, Y.; Shi, J.; Wang, T.; Liu, X.; Lu, G.; Ding, B. DNA Origami Directed Assembly of Gold Bowtie Nanoantennas for Single-Molecule Surface-Enhanced Raman Scattering. *Angew. Chem., Int. Ed.* **2018**, *57* (11), 2846−2850.

(58) Zhao, M.-Z.; Wang, X.; Xing, Y.-K.; Ren, S.-K.; Teng, N.; Wang, J.; Chao, J.; Wang, L.-H. DNA Origami-Templated Assembly of Plasmonic Nanostructures with Enhanced Raman Scattering. *Nucl. Sci. Tech.* **2018**, *29* (1), 6.

(59) Ren, S.; Wang, J.; Song, C.; Li, Q.; Yang, Y.; Teng, N.; Su, S.; Zhu, D.; Huang, W.; Chao, J.; et al. Single-Step Organization of Plasmonic Gold Metamaterials with Self-Assembled DNA Nano-structures. *Research* **2019**, *2019*. DOI: 10.34133/2019/7403580.

(60) Zhou, C.; Yang, Y.; Li, H.; Gao, F.; Song, C.; Yang, D.; Xu, F.; Liu, N.; Ke, Y.; Su, S.; et al. Programming Surface-Enhanced Raman

Scattering of DNA Origami-Templated Metamolecules. *Nano Lett.* **2020**, *20* (5), 3155−3159.

(61) Moeinian, A.; Gür, F. N.; Gonzalez-Torres, J.; Zhou, L.; Murugesan, V. D.; Dashtestani, A. D.; Guo, H.; Schmidt, T. L.; Strehle, S. Highly Localized SERS Measurements Using Single Silicon Nanowires Decorated with DNA Origami-Based SERS Probe. *Nano Lett.* **2019**, *19* (2), 1061−1066.

(62) Fang, W.; Jia, S.; Chao, J.; Wang, L.; Duan, X.; Liu, H.; Li, Q.; Zuo, X.; Wang, L.; Wang, L. et al. Quantizing Single-Molecule Surface-Enhanced Raman Scattering with DNA Origami Metamolecules. *Sci. Adv.* **2019**, *5* (9). DOI: 10.1126/sciadv.aau4506.

(63) Reguera, J.; Langer, J.; Jimenez de Aberasturi, D.; Liz-Marzan, L. M. Anisotropic Metal Nanoparticles for Surface Enhanced Raman Scattering. *Chem. Soc. Rev.* **2017**, *46* (13), 3866−3885.

(64) Tanwar, S.; Haldar, K. K.; Sen, T. DNA Origami Directed Au Nanostar Dimers for Single-Molecule Surface-Enhanced Raman Scattering. *J. Am. Chem. Soc.* **2017**, *139* (48), 17639−17648.

(65) Ma, W.; Xu, L.; Wang, L.; Xu, C.; Kuang, H. Chirality-Based Biosensors. *Adv. Funct. Mater.* **2019**, *29* (1), 1805512.

(66) Neubrech, F.; Hentschel, M.; Liu, N. Reconfigurable Plasmonic Chirality: Fundamentals and Applications. *Adv. Mater.* **2020**, *32*, 1905640.

(67) *Circular Dichroism and the Conformational Analysis of Biomolecules*; Fasman, G. D., Ed.; Springer: United States, 1996; DOI: 10.1007/978-1-4757-2508-7.

(68) Fan, Z.; Govorov, A. O. Plasmonic Circular Dichroism of Chiral Metal Nanoparticle Assemblies. *Nano Lett.* **2010**, *10* (7), 2580−2587.

(69) Kuzyk, A.; Schreiber, R.; Fan, Z.; Pardatscher, G.; Roller, E.-M.; Högele, A.; Simmel, F. C.; Govorov, A. O.; Liedl, T. DNA-Based Self-Assembly of Chiral Plasmonic Nanostructures with Tailored Optical Response. *Nature* **2012**, *483* (7389), 311−314.

(70) Schreiber, R.; Luong, N.; Fan, Z.; Kuzyk, A.; Nickels, P. C.; Zhang, T.; Smith, D. M.; Yurke, B.; Kuang, W.; Govorov, A. O.; et al. Chiral Plasmonic DNA Nanostructures with Switchable Circular Dichroism. *Nat. Commun.* **2013**, *4* (1), 2948.

(71) Lieberman, I.; Shemer, G.; Fried, T.; Kosower, E. M.; Markovich, G. Plasmon-Resonance-Enhanced Absorption and Circular Dichroism. *Angew. Chem., Int. Ed.* **2008**, *47* (26), 4855−4857.

(72) Kneer, L. M.; Roller, E.-M.; Besteiro, L. V.; Schreiber, R.; Govorov, A. O.; Liedl, T. Circular Dichroism of Chiral Molecules in DNA-Assembled Plasmonic Hotspots. *ACS Nano* **2018**, *12* (9), 9110−9115.

(73) Shen, X.; Song, C.; Wang, J.; Shi, D.; Wang, Z.; Liu, N.; Ding, B. Rolling Up Gold Nanoparticle-Dressed DNA Origami into Three-Dimensional Plasmonic Chiral Nanostructures. *J. Am. Chem. Soc.* **2012**, *134* (1), 146−149.

(74) Yan, W.; Xu, L.; Xu, C.; Ma, W.; Kuang, H.; Wang, L.; Kotov, N. A. Self-Assembly of Chiral Nanoparticle Pyramids with Strong R/S Optical Activity. *J. Am. Chem. Soc.* **2012**, *134* (36), 15114−15121.

(75) Shen, X.; Asenjo-Garcia, A.; Liu, Q.; Jiang, Q.; García de Abajo, F. J.; Liu, N.; Ding, B. Three-Dimensional Plasmonic Chiral Tetramers Assembled by DNA Origami. *Nano Lett.* **2013**, *13* (5), 2128−2133.

(76) Urban, M. J.; Dutta, P. K.; Wang, P.; Duan, X.; Shen, X.; Ding, B.; Ke, Y.; Liu, N. Plasmonic Toroidal Metamolecules Assembled by DNA Origami. *J. Am. Chem. Soc.* **2016**, *138* (17), 5495−5498.

(77) Lan, X.; Lu, X.; Shen, C.; Ke, Y.; Ni, W.; Wang, Q. Au Nanorod Helical Superstructures with Designed Chirality. *J. Am. Chem. Soc.* **2015**, *137* (1), 457−462.

(78) Shen, C.; Lan, X.; Zhu, C.; Zhang, W.; Wang, L.; Wang, Q. Spiral Patterning of Au Nanoparticles on Au Nanorod Surface to Form Chiral AuNR@AuNP Helical Superstructures Templated by DNA Origami. *Adv. Mater.* **2017**, *29* (16). DOI: 10.1002/adma.201606533.

(79) Lan, X.; Liu, T.; Wang, Z.; Govorov, A. O.; Yan, H.; Liu, Y. DNA-Guided Plasmonic Helix with Switchable Chirality. *J. Am. Chem. Soc.* **2018**, *140* (37), 11763−11770.

(80) Wang, M.; Dong, J.; Zhou, C.; Xie, H.; Ni, W.; Wang, S.; Jin, H.; Wang, Q. Reconfigurable Plasmonic Diastereomers Assembled by DNA Origami. *ACS Nano* **2019**, *13* (12), 13702−13708.

(81) Kuzyk, A.; Schreiber, R.; Zhang, H.; Govorov, A. O.; Liedl, T.; Liu, N. Reconfigurable 3D Plasmonic Metamolecules. *Nat. Mater.* **2014**, *13* (9), 862.

(82) Kuzyk, A.; Yang, Y.; Duan, X.; Stoll, S.; Govorov, A. O.; Sugiyama, H.; Endo, M.; Liu, N. A Light-Driven Three-Dimensional Plasmonic Nanosystem That Translates Molecular Motion into Reversible Chiroptical Function. *Nat. Commun.* **2016**, *7* (1), 10591.

(83) Liu, Q.; Kuzyk, A.; Endo, M.; Smalyukh, I. I. Colloidal Plasmonic DNA-Origami with Photo-Switchable Chirality in Liquid Crystals. *Opt. Lett.* **2019**, *44* (11), 2831−2834.

(84) Jiang, Q.; Liu, Q.; Shi, Y.; Wang, Z.-G.; Zhan, P.; Liu, J.; Liu, C.; Wang, H.; Shi, X.; Zhang, L.; et al. Stimulus-Responsive Plasmonic Chiral Signals of Gold Nanorods Organized on DNA Origami. *Nano Lett.* **2017**, *17* (11), 7125−7130.

(85) Kuzyk, A.; Urban, M. J.; Idili, A.; Ricci, F.; Liu, N. Selective Control of Reconfigurable Chiral Plasmonic Metamolecules. *Sci. Adv.* **2017**, *3* (4), No. e1602803.

(86) Man, T.; Ji, W.; Liu, X.; Zhang, C.; Li, L.; Pei, H.; Fan, C. Chiral Metamolecules with Active Plasmonic Transition. *ACS Nano* **2019**, *13* (4), 4826−4833.

(87) Zhou, C.; Xin, L.; Duan, X.; Urban, M. J.; Liu, N. Dynamic Plasmonic System That Responds to Thermal and Aptamer-Target Regulations. *Nano Lett.* **2018**, *18* (11), 7395−7399.

(88) Huang, Y.; Nguyen, M.-K.; Natarajan, A. K.; Nguyen, V. H.; Kuzyk, A. A DNA Origami-Based Chiral Plasmonic Sensing Device. *ACS Appl. Mater. Interfaces* **2018**, *10* (51), 44221−44225.

(89) Funck, T.; Liedl, T.; Bae, W. Dual Aptamer-Functionalized 3D Plasmonic Metamolecule for Thrombin Sensing. *Appl. Sci.* **2019**, *9* (15), 3006.

(90) Zhou, C.; Duan, X.; Liu, N. A Plasmonic Nanorod That Walks on DNA Origami. *Nat. Commun.* **2015**, *6* (1), 8102.

(91) Funck, T.; Nicoli, F.; Kuzyk, A.; Liedl, T. Sensing Picomolar Concentrations of RNA Using Switchable Plasmonic Chirality. *Angew. Chem.* **2018**, *130* (41), 13683−13686.

(92) Dong, J.; Wang, M.; Zhou, Y.; Zhou, C.; Wang, Q. DNA-Based Adaptive Plasmonic Logic Gates. *Angew. Chem., Int. Ed.* **2020**, *59* (35), 15038−15042.

(93) Urban, M. J.; Zhou, C.; Duan, X.; Liu, N. Optically Resolving the Dynamic Walking of a Plasmonic Walker Couple. *Nano Lett.* **2015**, *15* (12), 8392−8396.

(94) Xin, L.; Zhou, C.; Duan, X.; Liu, N. A Rotary Plasmonic Nanoclock. *Nat. Commun.* **2019**, *10* (1), 5394.

(95) Urban, M. J.; Both, S.; Zhou, C.; Kuzyk, A.; Lindfors, K.; Weiss, T.; Liu, N. Gold Nanocrystal-Mediated Sliding of Doublet DNA Origami Filaments. *Nat. Commun.* **2018**, *9* (1), 1454.

(96) Govorov, A. O.; Fan, Z.; Hernandez, P.; Slocik, J. M.; Naik, R. R. Theory of Circular Dichroism of Nanomaterials Comprising Chiral Molecules and Nanocrystals: Plasmon Enhancement, Dipole Interactions, and Dielectric Effects. *Nano Lett.* **2010**, *10* (4), 1374−1382.

(97) Hendry, E.; Carpy, T.; Johnston, J.; Popland, M.; Mikhaylovskiy, R. V.; Lapthorn, A. J.; Kelly, S. M.; Barron, L. D.; Gadegaard, N.; Kadodwala, M. Ultrasensitive Detection and Characterization of Biomolecules Using Superchiral Fields. *Nat. Nanotechnol.* **2010**, *5* (11), 783−787.

(98) Slocik, J. M.; Govorov, A. O.; Naik, R. R. Plasmonic Circular Dichroism of Peptide-Functionalized Gold Nanoparticles. *Nano Lett.* **2011**, *11* (2), 701−705.

(99) Maoz, B. M.; Chaikin, Y.; Tesler, A. B.; Bar Elli, O.; Fan, Z.; Govorov, A. O.; Markovich, G. Amplification of Chiroptical Activity of Chiral Biomolecules by Surface Plasmons. *Nano Lett.* **2013**, *13* (3), 1203−1209.

(100) Nesterov, M. L.; Yin, X.; Schäferling, M.; Giessen, H.; Weiss, T. The Role of Plasmon-Generated Near Fields for Enhanced Circular Dichroism Spectroscopy. *ACS Photonics* **2016**, *3* (4), 578−583.

(101) Schlichthaerle, T.; Strauss, M. T.; Schueder, F.; Woehrstein, J. B.; Jungmann, R. DNA Nanotechnology and Fluorescence Applications. *Curr. Opin. Biotechnol.* **2016**, *39*, 41−47.

(102) Samanta, A.; Banerjee, S.; Liu, Y. DNA Nanotechnology for Nanophotonic Applications. *Nanoscale* **2015**, *7* (6), 2210−2220.

(103) Pilo-Pais, M.; Acuna, G. P.; Tinnefeld, P.; Liedl, T. Sculpting Light by Arranging Optical Components with DNA Nanostructures. *MRS Bull.* **2017**, *42* (12), 936−942.

(104) Liu, N.; Liedl, T. DNA-Assembled Advanced Plasmonic Architectures. *Chem. Rev.* **2018**, *118* (6), 3032−3053.

(105) Ding, B.; Deng, Z.; Yan, H.; Cabrini, S.; Zuckermann, R. N.; Bokor, J. Gold Nanoparticle Self-Similar Chain Structure Organized by DNA Origami. *J. Am. Chem. Soc.* **2010**, *132* (10), 3248−3249.

(106) Tian, Y.; Wang, T.; Liu, W.; Xin, H. L.; Li, H.; Ke, Y.; Shih, W. M.; Gang, O. Prescribed Nanoparticle Cluster Architectures and Low-Dimensional Arrays Built Using Octahedral DNA Origami Frames. *Nat. Nanotechnol.* **2015**, *10* (7), 637−644.

(107) Liu, W.; Li, L.; Yang, S.; Gao, J.; Wang, R. Self-Assembly of Heterogeneously Shaped Nanoparticles into Plasmonic Metamolecules on DNA Origami. *Chem. - Eur. J.* **2017**, *23* (57), 14177−14181.

(108) Liu, W.; Halverson, J.; Tian, Y.; Tkachenko, A. V.; Gang, O. Self-Organized Architectures from Assorted DNA-Framed Nanoparticles. *Nat. Chem.* **2016**, *8* (9), 867−873.

(109) Gür, F. N.; McPolin, C. P. T.; Raza, S.; Mayer, M.; Roth, D. J.; Steiner, A. M.; Löffler, M.; Fery, A.; Brongersma, M. L.; Zayats, A. V.; et al. DNA-Assembled Plasmonic Waveguides for Nanoscale Light Propagation to a Fluorescent Nanodiamond. *Nano Lett.* **2018**, *18* (11), 7323−7329.

(110) Liu, M.; Guyot-Sionnest, P.; Lee, T.-W.; Gray, S. K. Optical Properties of Rodlike and Bipyramidal Gold Nanoparticles from Three-Dimensional Computations. *Phys. Rev. B: Condens. Matter Mater. Phys.* **2007**, *76* (23), 235428.

(111) Godonoga, M.; Lin, T.-Y.; Oshima, A.; Sumitomo, K.; Tang, M. S. L.; Cheung, Y.-W.; Kinghorn, A. B.; Dirkzwager, R. M.; Zhou, C.; Kuzuya, A.; et al. DNA Aptamer Recognising a Malaria Protein Biomarker Can Function as Part of a DNA Origami Assembly. *Sci. Rep.* **2016**, *6* (1), 21266.

(112) Bell, N. A. W.; Keyser, U. F. Digitally Encoded DNA Nanostructures for Multiplexed, Single-Molecule Protein Sensing with Nanopores. *Nat. Nanotechnol.* **2016**, *11* (7), 645−651.

(113) Shaw, A.; Hoffecker, I. T.; Smyrlaki, I; Rosa, J.; Grevys, A.; Bratlie, D.; Sandlie, I.; Michaelsen, T. E.; Andersen, J. T.; Högberg, B. Binding to Nanopatterned Antigens Is Dominated by the Spatial Tolerance of Antibodies. *Nat. Nanotechnol.* **2019**, *14* (2), 184−190.

(114) Zhang, P.; Liu, X.; Liu, P.; Wang, F.; Ariyama, H.; Ando, T.; Lin, J.; Wang, L.; Hu, J.; Li, B.; et al. Capturing Transient Antibody Conformations with DNA Origami Epitopes. *Nat. Commun.* **2020**, *11* (1), 3114.

(115) Nguyen, L.; Dass, M.; Ober, M. F.; Besteiro, L. V.; Wang, Z. M.; Nickel, B.; Govorov, A. O.; Liedl, T.; Heuer-Jungemann, A. Chiral Assembly of Gold-Silver Core-Shell Plasmonic Nanorods on DNA Origami with Strong Optical Activity. *ACS Nano* **2020**, *14* (6), 7454−7461.

(116) Zhang, Q.; Hernandez, T.; Smith, K. W.; Hosseini Jebeli, S. A.; Dai, A. X.; Warning, L.; Baiyasi, R.; McCarthy, L. A.; Guo, H.; Chen, D.-H.; et al. Unraveling the Origin of Chirality from Plasmonic Nanoparticle-Protein Complexes. *Science* **2019**, *365* (6460), 1475−1478.

(117) Vietz, C.; Schütte, M. L.; Wei, Q.; Richter, L.; Lalkens, B.; Ozcan, A.; Tinnefeld, P.; Acuna, G. P. Benchmarking Smartphone Fluorescence-Based Microscopy with DNA Origami Nanobeads: Reducing the Gap toward Single-Molecule Sensitivity. *ACS Omega* **2019**, *4* (1), 637−642.

(118) Agarwal, N. P.; Matthies, M.; Gür, F. N.; Osada, K.; Schmidt, T. L. Block Copolymer Micellization as a Protection Strategy for DNA Origami. *Angew. Chem., Int. Ed.* **2017**, *56* (20), 5460−5464.

(119) Hahn, J.; Wickham, S. F. J.; Shih, W. M.; Perrault, S. D. Addressing the Instability of DNA Nanostructures in Tissue Culture. *ACS Nano* **2014**, *8* (9), 8765−8775.

(120) Kielar, C.; Xin, Y.; Shen, B.; Kostiainen, M. A.; Grundmeier, G.; Linko, V.; Keller, A. On the Stability of DNA Origami Nanostructures in Low-Magnesium Buffers. *Angew. Chem., Int. Ed.* **2018**, *57* (30), 9470−9474.

(121) Nguyen, L.; Döblinger, M.; Liedl, T.; Heuer-Jungemann, A. DNA-Origami-Templated Silica Growth by Sol-Gel Chemistry. *Angew. Chem., Int. Ed.* **2019**, *58* (3), 912−916.

(122) Wang, S.-T.; Gray, M. A.; Xuan, S.; Lin, Y.; Byrnes, J.; Nguyen, A. I.; Todorova, N.; Stevens, M. M.; Bertozzi, C. R.; Zuckermann, R. N.; et al. DNA Origami Protection and Molecular Interfacing through Engineered Sequence-Defined Peptoids. *Proc. Natl. Acad. Sci. U. S. A.* **2020**, *117* (12), 6339−6348.

(123) Gerling, T.; Kube, M.; Kick, B.; Dietz, H. Sequence-Programmable Covalent Bonding of Designed DNA Assemblies. *Sci. Adv.* **2018**, *4* (8), No. eaau1157.

(124) Cassinelli, V.; Oberleitner, B.; Sobotta, J.; Nickels, P.; Grossi, G.; Kempter, S.; Frischmuth, T.; Liedl, T.; Manetto, A. One-Step Formation of "Chain-Armor"-Stabilized DNA Nanostructures. *Angew. Chem., Int. Ed.* **2015**, *54* (27), 7795−7798.

(125) Ke, Y.; Ong, L. L.; Sun, W.; Song, J.; Dong, M.; Shih, W. M.; Yin, P. DNA Brick Crystals with Prescribed Depths. *Nat. Chem.* **2014**, *6* (11), 994−1002.

(126) Tian, Y.; Zhang, Y.; Wang, T.; Xin, H. L.; Li, H.; Gang, O. Lattice Engineering through Nanoparticle-DNA Frameworks. *Nat. Mater.* **2016**, *15* (6), 654−661.

(127) Liu, W.; Tagawa, M.; Xin, H. L.; Wang, T.; Emamy, H.; Li, H.; Yager, K. G.; Starr, F. W.; Tkachenko, A. V.; Gang, O. Diamond Family of Nanoparticle Superlattices. *Science* **2016**, *351* (6273), 582−586.

(128) Zhang, T.; Hartl, C.; Frank, K.; Heuer-Jungemann, A.; Fischer, S.; Nickels, P. C.; Nickel, B.; Liedl, T. 3D DNA Origami Crystals. *Adv. Mater.* **2018**, *30* (28), 1800273.

(129) Praetorius, F.; Kick, B.; Behler, K. L.; Honemann, M. N.; Weuster-Botz, D.; Dietz, H. Biotechnological Mass Production of DNA Origami. *Nature* **2017**, *552* (7683), 84−87.

4. VISIBLE WAVELENGTH SPECTRAL CONTROL OF CHIRAL NANORODS ASSEMBLIES

Artificially engineered systems can give rise to natural optical activity. The shape and material of a system are crucial for its properties. For instance, nanorods exhibit localized field enhancement and optical nonlinearities due to their anisotropic shape.[120] Sections 2.3 and 2.4 detailed the plasmon hybridisation model for nanorod dimers arranged in both achiral and chiral configurations. Conventionally, gold is favoured for the synthesis of plasmonic nanoparticles due to its chemical stability. However, gold nanoparticles are limited in spectral tunability. Spherical gold nanoparticles absorb in the 520–600 nm region[121], while gold nanorods usually absorb in the NIR-IR region.[122,123]

Silver shares similarities with gold in its general plasmonic activity but has advantages like a greater extinction cross-section than gold[124] along with the lowest losses of all metals in the visible and near-infrared spectrum.[125] These properties result in a stronger near-field enhancement, even when the silver forms the shell in a core-shell system.[126] However, the chemical instability of silver has hindered its study. Effects like oxidation cause the disintegration of silver nanoparticles, which can induce aggregation and hinders functionalisation. The application of silver particles in chiral plasmonics has been limited as well, in part due to oxidation susceptibility, particularly in aqueous solutions and saline buffers used in DNA assembly.
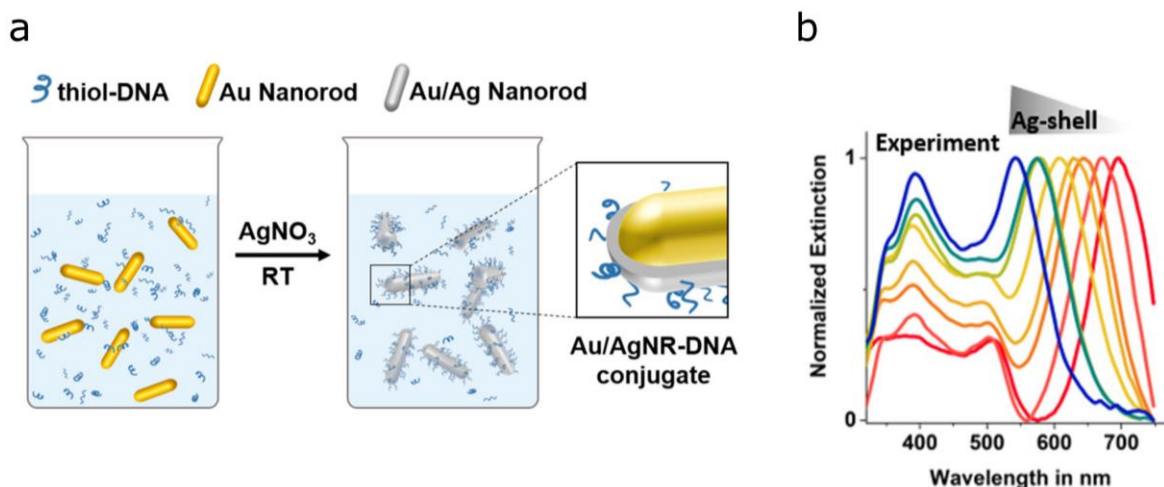

Figure 19. Gold–Silver Core–Shell Plasmonic Nanorods (Au/AgNRs). a) Schematic showing one-pot synthesis of DNA-functionalised Au/AgNRs. b) Experimental extinction spectra of Au/AgNRs with varying silver-shell thicknesses, from thinnest ~1.1 (red line) to ~5.4 nm (blue line). Reproduced with permission from American Chemical Society, ACS Nano[101], copyright (2020).

In our work[101], we presented a straightforward, rapid one-pot method to synthesise monodisperse Au/AgNRs and achieve simultaneous functionalisation with DNA (Fig. 19). This method provided precise control over the size, aspect ratio and crucially, the shell thickness of the Au/AgNRs, allowing us to tune their spectral properties. DNA functionalisation imparts stability to the Au/AgNRs and allowed the use of DNA origami technique to arrange the rods in specific geometries. This was followed by associated publication **P2**[127], where we assembled Au/AgNRs onto DNA origami structures in chiral geometries, thereby extending spectral control over the circular dichroic signal in the visible spectrum (Fig. 20). We created right- and left-handed structures in two chiral geometries – X- and L- shape. The experimental CD spectra of these chiral metamolecules were in accord with simulations, with additional signatures in the 300–400 nm also being reflected in the simulations. Our structures could be used for sensitive detection of biomolecules.[115] The freedom to fine-tune the optical response could facilitate enhanced LSPR-dependant coupling to optically active molecules like dyes[128] and photo-active compounds[129].
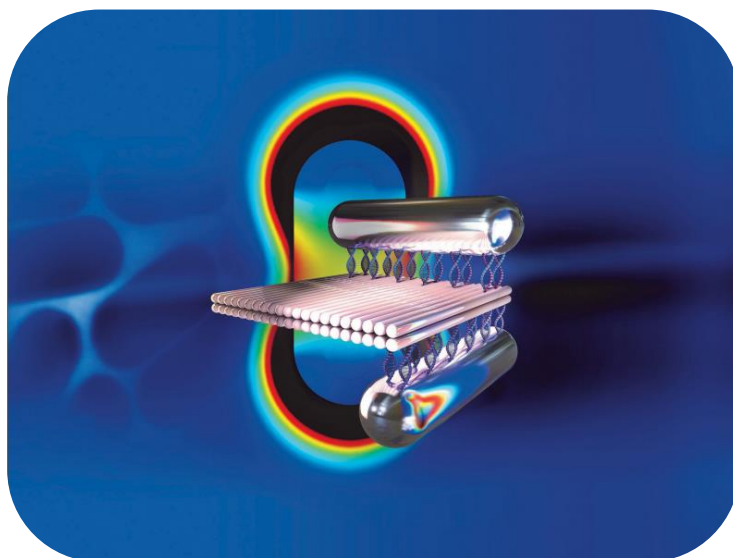

Figure 20. Artistic representation of a chiral dimer constructed with Au/AgNRs, with the field map of a single Au/AgNR in the background. Reproduced from Ref.[130] with permission from the Royal Society of Chemistry. Image credits: Lisa Kulot.

4.1 Associated publication P2

Visible wavelength spectral tuning of absorption and circular dichroism of DNA-assembled Au/Ag core–shell nanorod assemblies

by

Mihir Dass, Lilli Kuen, Gregor Posnjak, Sven Burger, and Tim Liedl

published in
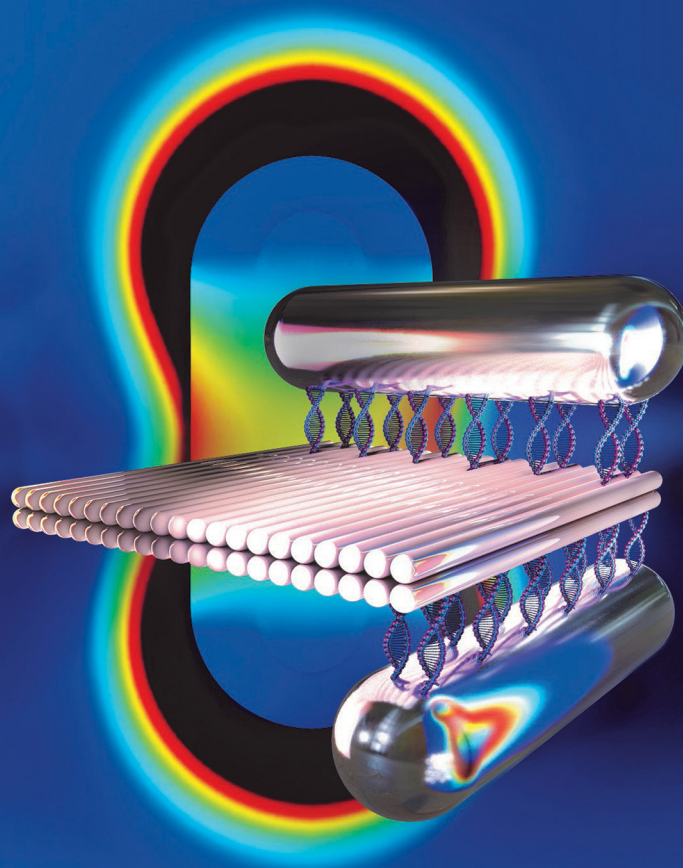
Material Advances, 2022

as

Dass, M., Kuen, L., Posnjak, G., Burger, S. & Liedl, T. Visible wavelength spectral tuning of absorption and circular dichroism of DNA-assembled Au/Ag core–shell nanorod assemblies. *Mater. Adv.* **3**, 3438–3445 (2022).

Materials Advances

ROYAL SOCIETY
OF CHEMISTRY

PAPER
Tim Liedl *et al.*
Visible wavelength spectral tuning of absorption and circular
dichroism of DNA-assembled Au/Ag core–shell nanorod
assemblies

PAPER

Check for updates

Visible wavelength spectral tuning of absorption and circular dichroism of DNA-assembled Au/Ag core–shell nanorod assemblies†

Mihir Dass, [ID] [a] Lilli Kuen, [ID] [b] Gregor Posnjak, [ID] [a] Sven Burger [ID] [b] and Tim Liedl [ID] *[a]

Plasmonic nanoparticles have unique properties which can be harnessed to manipulate light at the nanoscale. With recent advances in synthesis protocols that increase their stability, gold–silver core–shell nanoparticles have become suitable building blocks for plasmonic nanostructures to expand the range of attainable optical properties. Here we tune the plasmonic response of gold–silver core–shell nanorods over the visible spectrum by varying the thickness of the silver shell. Through the chiral arrangement of the nanorods with the help of various DNA origami designs, the spectral tunability of the plasmon resonance frequencies is transferred into circular dichroism signals covering the spectrum from 400 nm to 700 nm. Our approach could aid in the construction of better sensors as well as metamaterials with a tunable optical response in the visible region.

Introduction

Circular dichroism (CD) is the differential extinction of light of different handedness by chiral materials, and as such, serves as a fingerprinting method for the characterisation of biomolecules like proteins[1,2] and DNA.[3,4] However, the magnitude of CD displayed by these biomolecules is low and is generally exhibited in the UV region.[5,6] Metals such as gold interact much more strongly with light and can be useful in studying chirality.[7–9] A wide variety of artificial chiral nanostructures have been presented using quantum dots,[10–12] silica[13] and metallic nanoparticles.[8,14,15] DNA nanotechnology, due to its programmability, has emerged as an elegant tool to enable precise placement of nanoscale objects such as plasmonic nanoparticles,[16–20] biological materials such as antibodies,[21,22] enzymes[23] and proteins,[24,25] as well as polymers.[26,27] DNA origami enables the construction of chiral structures using nanoparticles that exhibit strong CD in the visible region.[28–30] These and other studies[31,32] increase comprehension of the underlying near field processes responsible for the emergence of plasmonic circular dichroism. With improving design and manufacturing, chiral arrangements of gold nanoparticles have been employed for novel molecular sensing approaches[33] and the construction of metasurfaces.[34] However, gold nanoparticles are

limited in spectral tunability. For example, spherical gold nanoparticles absorb in the 520–600 nm region[35] whereas gold nanorods, which allow the construction of strongly chiral objects due to their anisotropic nature,[33,36–39] usually absorb in the NIR-IR region.[40,41] On the other hand, silver is an excellent plasmonic material exhibiting lower optical losses[42] and a greater extinction cross-section compared to gold.[43] Chiral assemblies constructed with silver nanorods are also predicted to have stronger chiral plasmonic interactions compared to gold.[44] Despite these advantages, the application of silver particles in chiral plasmonics has been limited, partly due to the susceptibility to oxidation of the silver surfaces in aqueous solutions or even salty buffers required in DNA assembly.

We recently reported the synthesis of gold/silver core/shell nanorods (Au/AgNRs) functionalised with DNA in a one-pot reaction.[45] Au/AgNRs with different silver shell thicknesses could be constructed, thus allowing spectral tuning of the nanorods. The DNA coating serves a dual purpose: it imparts additional stability to the nanorods and makes the nanorods functional to allow their assembly on a DNA origami template. Chiral assemblies constructed from the Au/AgNRs exhibit stronger g-factors compared to assemblies constructed solely from gold nanorods (AuNRs). Here we expand on that work by illustrating another plasmonic chiral enantiomer in an 'L-shaped' geometry and showcasing the spectral tuning of the circular dichroic signal in the visible region of the spectrum. Because of their increased stability, Au/AgNRs can serve as a viable alternative to AuNRs and expand the parameter space in future studies focused on exploring the nature of plasmonic chirality.

[a] Faculty of Physics and Center for NanoScience (CeNS), Ludwig-Maximilians-University, Geschwister-Scholl-Platz 1, 80539 Munich, Germany.
E-mail: tim.liedl@physik.lmu.d
[b] Computational Nano Optics, Zuse Institute Berlin, 14195 Berlin, Germany
† Electronic supplementary information (ESI) available. See DOI: 10.1039/d1ma01211h

Experimental methods

DNA origami folding and purification

Staple strands (Integrated DNA Technologies, 200 µM each in water) and the scaffold strand (8064 nt long M13mp18 ssDNA) were mixed to a target concentration of 200 nM for each staple and 25 nM for the scaffold in 16 mM $MgCl_2$, 10 mM Tris and 1 mM EDTA. The mixture was divided into 100 µL aliquots in PCR tubes and annealed from 65 °C to 20 °C over ~16 hours (see ESI†). The origami structures were purified using 100 kDa MWCO Amicon filters (Millipore).

Gold and silver/gold nanorod synthesis

The gold nanorods were synthesised as in ref. 41 The procedure was optimised for the desired size (see supplementary Note S1, ESI†). The rods were then washed in 0.1 M CTAB (Roth) and 0.01 M CTAB and stored in 0.01 M CTAB at 15 OD (optical density) before use. For the silver coating, the AuNRs were added to 0.1 M CTAB under stirring (500 rpm) and allowed to mix for 10 s. Then, thiolated ssDNA strands (Biomers, 100 µM, aq.) were added to the rod mixture. $AgNO_3$ solution was added next, after which the stirring speed was increased (1500 rpm). L-Ascorbic acid (0.2 M) and NaOH (0.2 M) were added rapidly in quick succession. A colour change after 5–10 s indicates the successful synthesis of a silver coating. The reaction was allowed to proceed for 10 min. Both the AuNRs and Au/AgNRs were washed to remove excess reactants from their respective growth solutions (see supplementary note S1, ESI†) and then redispersed in 0.1% sodium dodecyl sulfate (SDS) before further use.

DNA-nanorod hybridisation

A second DNA-functionalisation step increases the stability and binding of the nanorods. Au/AgNRs were mixed with an adequate volume of thiolated ssDNA (Biomers, 100 µM, aq.) followed by freezing @ −80 °C for 30 minutes. They were then thawed and purified from excess ssDNA using agarose gel electrophoresis. The DNA origami and functionalised nanorods were mixed to a final concentration of 1–2 nM and 20–40 nM, respectively, *i.e.* the rods were added in ~20× excess. The mixture was then annealed from 45 °C to 20° at 10 min °C^{-1}, and this ramp was repeated four times.[36] The assemblies were then separated from excess unbound rods and aggregates using agarose gel electrophoresis.

Characterisation

Agarose gel electrophoresis. The nanorods and origami–rod hybrids were analysed and purified using a 1% agarose gel. The gels were run in a buffer containing 40 mM Tris, 20 mM acetic acid, 1 mM EDTA and 11 mM $MgCl_2$ at 100 V for 2 hours. 1× SybrSafe (Thermo Fisher) was included in gels for DNA origami analysis.

UV-Vis spectroscopy

The nanorods and DNA samples were analysed using a Nanodrop-1000 spectrometer. A 1.5 µL droplet of the sample and a path length of 1 mm was used to determine the optical density (OD) values.

TEM imaging

5 µL of a sample was incubated for 30 s–5 min, depending on concentration, on glow discharged TEM grids (formvar/carbon, 300 mesh Cu; Ted Pella) at room temperature. After incubation on the grids, the sample was wicked off by bringing the grid into contact with a filter paper strip. Nanorod samples were imaged as-is. Samples containing DNA origami went through an additional staining step with a 2% uranyl formate aqueous solution containing 25 mM sodium hydroxide. After incubating and wicking the sample off, a 5 µL drop of uranyl formate staining solution was applied to the grid, immediately wicked off, followed by applying another 5 µL drop of uranyl formate staining solution. This drop was allowed to incubate on the grid for 10 seconds and then wicked off. The grid was allowed to dry for 5 minutes before imaging. Imaging was performed with a JEM1011 transmission electron microscope (JEOL) operated at 80 kV.

CD spectroscopy

All CD measurements were performed in a Chirascan plus CD spectrometer (Applied Photophysics) with 10 mm path length quartz cuvettes (Hellma). The cuvettes were cleaned with fresh aqua regia, washed thoroughly with MilliQ water and dried with compressed N_2 before each measurement. The baseline measurements were performed with 40 mM Tris, 20 mM acetic acid, 1 mM EDTA buffer with 11 mM $MgCl_2$. The scanning step size was set to 1.0 nm with an acquisition time of 1.0 s for each step.

Simulation

The total extinction and CD spectra were computed numerically, solving the linear, time-harmonic Maxwell's equations. A single arrangement was included in the computational domain for each setup (single nanorod arrangement, NR–NR arrangement in 'X-shape', and NR–NR arrangement in 'L-shape'). Tabulated data was used for modelling the permittivities of gold and silver.[46,47] For the background solution, a constant permittivity of $\varepsilon_r = 1.8$ was assumed. In the numerical experiment, the arrangement was illuminated by pairs of left- and right-handed circularly polarised plane waves incident along the coordinate directions. The total extinction and CD spectra were derived from the near-field solution (see supplementary note S2, ESI†).

Results and discussion

Gold nanorods (AuNRs, ~65 × 15 nm) were synthesised using a modified protocol (see supplementary note S1, ESI†) from González-Rubio *et al.*[41] These AuNRs serve as seeds for the growth of silver shells around them using the protocol outlined by Nguyen *et al.*[45] Specifically, $AgNO_3$ (aq.) and thiolated-DNA are added to the dispersion of AuNRs. Then, in the presence of L-ascorbic acid, $AgNO_3$ is reduced to metallic silver

preferentially on the AuNRs, resulting in the formation of silver-coated AuNRs (Au/AgNRs). The presence of thiolated-DNA in the growth solution leads to simultaneous functionalisation of the rods. Importantly, wide and small angle X-ray scattering data indicate that the DNA conjugation occurs only on the surface, not within the shell.[45] The shell growth proceeds in an anisotropic fashion, with the shell usually being thicker on the sides compared to the tips, which could arise from different crystal facets being exposed at the sides and tips of a nanorod.[48] The shell growth results in a visible change of the colour of the rod suspensions, with the color varying as a function of the shell thickness (Fig. 1a). The nanorods were characterised using transmission electron microscopy and UV-Vis spectroscopy.

Structural characterisation

TEM micrographs confirm good monodispersity of the rods before and after shell growth, with the size deviation increasing with increasing shell thickness (ESI,† Fig. S9). The AuNR 'core' is visible in the centre of the Au/AgNRs due to gold and silver's different electronic densities (Fig. 1b). A noteworthy aspect of the growth is that in some Au/AgNRs the shell growth is asymmetric, with the shell being thicker on one side of the rod. This is in line with previous studies which show that this asymmetry arises from preferential deposition of Ag on certain crystal facets on the Au surface, which is believed to arise from selective adsorption of CTAB along certain crystal planes of

Ag.[49] As the shells grown by this method are thicker on the sides compared to the tips, increasing the shell thickness leads to a decrease in the aspect ratio of the rods. Shells between ~5 nm to ~14 nm thickness (measured perpendicular to the long axis) were grown, with their aspect ratio changing from 4, in the case of bare AuNRs, to ~2 for Au/AgNRs in the case of 14 nm shells grown with 10 mM AgNO$_3$ (Fig. 1b). Growing thicker shells resulted in rods with an aspect ratio ~1, thus making the identification of the long axis unreliable (ESI,† Fig. S14a and b).

Optical characterisation

The absorption spectra of gold nanorods exhibit two peaks, for the transverse and longitudinal modes of localised surface plasmon resonances (LSPR) perpendicular to and along the long axis of the rods, respectively (Fig. 1c).[50] The transverse mode usually occurs around ~500 nm, which also corresponds to the LSPR of spherical particles.[50] The longitudinal mode peak, at a constant thickness, shifts depending on the rods' length (and thus the aspect ratio), with longer lengths red-shifting the peak. Growth of Ag shells leads to a blueshift in the longitudinal LSPR of the rods, with thicker shells resulting in a stronger blueshift. Since the shell thickness depends on the concentration of Ag$^+$ ions present during shell growth, the longitudinal LSPR can be tuned over a wide range of wavelengths.[45] Here, we show stepwise manipulation of the longitudinal LSPR from 820 nm, *i.e.* the NIR spectral region
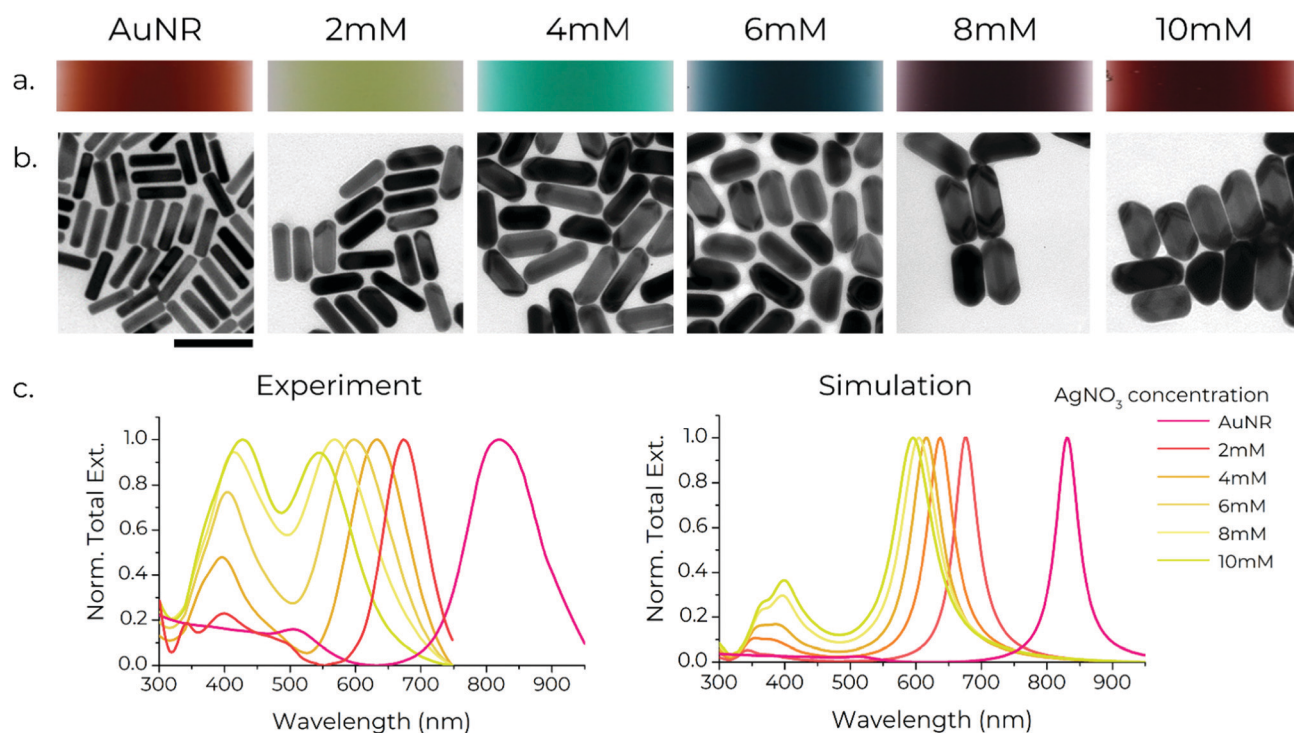

Fig. 1 Synthesis of Au/AgNRs with varying shell thickness. (a) Variation of colour of Au/AgNR suspensions grown with different concentrations of Ag$^+$ ions. (b) Transmission electron micrographs of Au/AgNRs with Ag shells of different thicknesses. The concentration of Ag$^+$ in the growth solution is shown at the top. All images are to scale. Scale bar: 100 nm. (c) Experimental and theoretical extinction spectra of the AuNRs and Au/AgNRs with varying shell thickness.

(for bare AuNRs) down to 540 nm, *i.e.* the green spectral region (for Au/AgNRs synthesised using 10 mM AgNO$_3$, Fig. 1c). We are able to create particles with thicker shells that push the longitudinal LSPR to 480 nm *i.e.* the blue spectral region. However, the shape of particles is no longer consistently anisotropic (ESI,† Fig. S14c). Numerical simulations satisfactorily replicate the experimental spectra, with increasing shell thickness blue-shifting the LSPR. The LSPR peaks in the numerically calculated data are much narrower than experimental spectra because they exclude the size polydispersity of bulk nanorod samples. The agreement between the simulations and experimental spectra is remarkable for the AuNRs and Au/AgNRs with thin Ag shells. The deviation increases for Au/AgNRs with thicker shells, consistent with an observed increase in their shape inhomogeneity (see also supplementary note S3, ESI†). The large spectral gap between the LSPR of the AuNRs and the Au/AgNRs with the thinnest Ag shell (grown using 2 mM AgNO$_3$) is worth noting, which is also reproduced by our simulations. Generally, we believe this effect arises as a combination of the silver shell as well as a decrease in the aspect ratio of the rods, which results in a blue-shift of the LSPR[40] (ESI,† Fig. S10). Unfortunately, we were not able to obtain stable samples with thinner shells.

The Ag shell also results in a more complex transversal mode appearing at shorter wavelengths, with a strong peak at $\sim$400 nm and a secondary feature at shorter wavelengths $\sim$350 nm. Both of these redshift with increasing shell thickness. Simulations revealed that the latter mode arises due to the transversal excitation of the Au/AgNRs, leading to the formation of charged dipoles between the Au–Ag interface and the outer surface of the Au/AgNRs.[45,51] This secondary peak increases in intensity with increasing Ag shell thickness and becomes more intense than the longitudinal mode in Au/AgNRs with very thick shells. The appearance of this secondary mode agrees very well with the simulations (Fig. 1c), with the simulations reproducing the spectra – including the increase in intensity and redshift of the new transverse peak with increasing shell thickness.

Chiral metamolecule fabrication

AuNRs and Au/AgNRs were functionalised with DNA for attachment to DNA origami templates using DNA anchors (Fig. 2a). We utilised the freeze-and-thaw method, which is an effective and facile method for functionalising various plasmonic particles.[52–54] While the DNA strands attached to the Au/AgNRs during the shell growth already provide long-term stability, an additional freeze-and-thaw functionalisation step is performed to ensure a dense coverage of the nanorod surface with DNA strands. Different volumes of thiolated DNA were added to AuNRs (at OD 15) suspended in 0.1% SDS for the functionalisation optimisation. The mixture was vortexed together and frozen at −80 °C for 30 min. We aim to cover the nanorods with a dense blanket of DNA oligos to maximise their long-term stability in the salt conditions conventionally used for DNA origami buffers (typically $\sim$12 mM MgCl$_2$), and maximise their hybridisation probability with DNA origami.[55] The successful
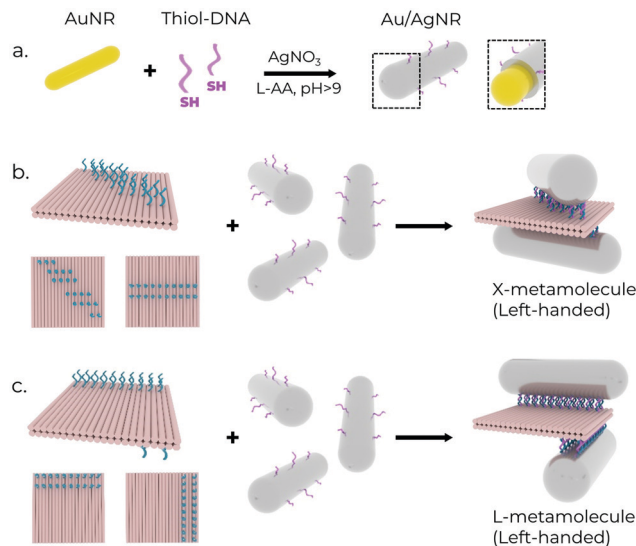

Fig. 2 Schematic showing the fabrication of the chiral metamolecules. (a) One-pot growth and functionalisation of the Ag shells on AuNRs. (b) and (c) Assembly of 'X' and 'L'-shaped chiral structures, respectively, constructed by varying the anchor configuration (blue strands) on the 2-layer sheet DNA Origami (left). The 'upper' (left) and 'lower' (right) faces of the sheet are shown below the respective sheet structures.

functionalisation of the rods is verified by agarose gel electrophoresis, which also serves as a purification method for separating the functionalised rods from excess oligonucleotides. Successfully functionalised rods travel as a single band in the gel and can be separated from aggregates and unfunctionalised rods (ESI,† Fig. S1a).

While these bimetallic Au/AgNRs possess novel optical properties, utilising the high degree of addressability of DNA origami to create predefined assemblies offers the opportunity to study more complex physical phenomena, *e.g.* plasmonic chirality. A square 2-layer DNA origami sheet (side length $\sim$55 nm, thickness $\sim$5 nm) was used as a template to construct the chiral metamolecules. 16–20 anchors with 8 nt long poly-A sequences at the 3′ end were extended from opposite faces to act as linkers for the nanorods. The layout of the anchors determines the final chirality of the resultant assembly. Two chiral geometries were utilised in this manuscript (Fig. 2b and c). In the first, the anchor positions on the 'upper' face were rotated by $\sim$50° relative to the 'lower' face to obtain a left-handed 'X'-shaped rod assembly, resulting in strongly asymmetric optical performance.[45] In the second, the anchor positions on the two faces were rotated 90° around one corner to obtain a left-handed 'L'-shaped assembly. It is worth mentioning that while the 'X'-configuration is chiral only if the angle between the two nanorods $\neq$90°, the 'L'-configuration has broken inversion symmetry, so it is chiral even when the nanorods are perpendicular to each other. For the hybridisation reaction, amicon-purified DNA origami was slowly pipetted into a tube containing purified functionalised rods under vortexing.[56] The aim here is to introduce the DNA origami to a 'reactant' (nanorods) present in excess to maximise the

chances of dimer formation and minimise the formation of spurious aggregates by saturating the binding sites on the DNA origami. The resulting mixture was then annealed using a modified protocol (see Supplementary Note S1, ESI†) to maximise binding yield and prevent partially bound rods.[36] The metamolecule dimers were separated from unbound excess nanorods and aggregates using agarose gel electrophoresis due to their different migration speeds in the gel matrix (ESI,† Fig. S1b). The relevant gel bands were excised and squeezed between a glass slide and parafilm to extract the liquid sample, on which further measurements were performed. TEM imaging of the gel-purified sample showed the successful assembly of the desired metamolecule configurations with a high degree of fidelity (Fig. 3).

CD spectroscopy

We performed CD spectroscopy of chiral metamolecules purified with agarose gel electrophoresis. The absorption during CD measurements was set to ∼0.6–0.7. The spectra of the chiral metamolecules, shown in Fig. 4, indicate a strong chiral signal, noteworthy being the signature peak-to-dip bisignate profile of the spectra.[36–39,57] This profile arises from plasmon-mediated near-field interactions of the individual NRs in each assembly when excited by circularly polarised light. A plasmonic dipolar moment is induced in the rods when excited by light. This results in the rise of two distinct modes with opposite chirality – namely a high-energy and a low-energy mode – centred around the longitudinal mode of the nanorods.[58] The high-energy mode is blue-shifted compared to the resonance of the individual nanorods, while the low-energy mode is red-shifted (ESI,† Fig. S15). The CD spectra of chiral metamolecules assembled with Au/AgNRs blueshifts with increasing silver shell thickness, in line with the longitudinal resonances of the corresponding Au/AgNRs. This trend of the CD response is in accord with the simulations (Fig. 4).

In chiral metamolecules constructed with Au/AgNRs, additional signatures appear between 300–400 nm, also seen in the simulations. A possible explanation for this is the coupling of the transverse modes seen in Au/AgNRs, as this CD signature appears in the same spectral region and increases with increasing Ag shell thickness similar to the individual Au/AgNRs. Another reason could be the coupling of multipolar plasmonic modes observed in anisotropic silver nanostructures, although they occur at longer wavelengths compared to our structures.[59–61] The lineshape of the experimental spectra is also qualitatively in accord with simulations, noteworthy being the various dips around 400 nm that differ between the X- and L-shaped dimers. This feature is broader and less pronounced in simulations and experiments for the L-shaped dimer. At the same time, we observed a positive signal over the entire blue part of the spectrum for the X-shaped structures. The bespoke dip only appears for thicker silver shells, again nicely reproduced in the simulations. Overall, the differences are more pronounced in theory than in experiments, which we ascribe to size polydispersity of the rods and shape polydispersity in the dimers themselves. For example, while designed to have a 90° angle between the rods, the L-shaped dimers often exhibit lower angles (ESI,† Fig. S4).

Conclusions

We have developed a class of core–shell nanorods composed of Au and Ag, which allows for fine control over the spectral tuning of the optical response on the visible spectrum. Moreover, chiral metamolecules constructed with these Au/AgNRs extend the spectral control over the CD signal. We present data where we tune the longitudinal LSPR of AuNRs – initially 819 nm – from 673 nm to 544 nm. The extent of this control depends on the aspect ratio of the AuNR core. Using AuNRs with a longitudinal LSPR farther in the IR would allow the
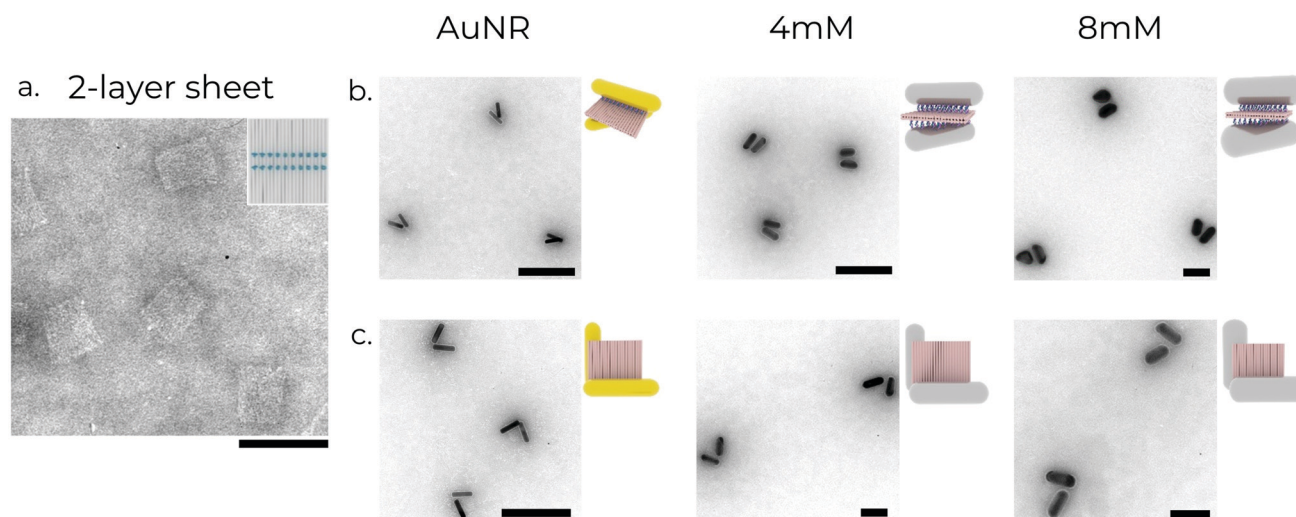

Fig. 3 Structural characterisation of chiral metamolecules. (a) Transmission electron micrograph of the 2-layer sheet DNA origami structures. (b) and (c) X- and L-shaped left-handed chiral structures assembled using three varieties of nanorods, respectively. The concentration of AgNO₃ used to synthesise the nanorods used for the structures is shown above the images. All scale bars: 100 nm.
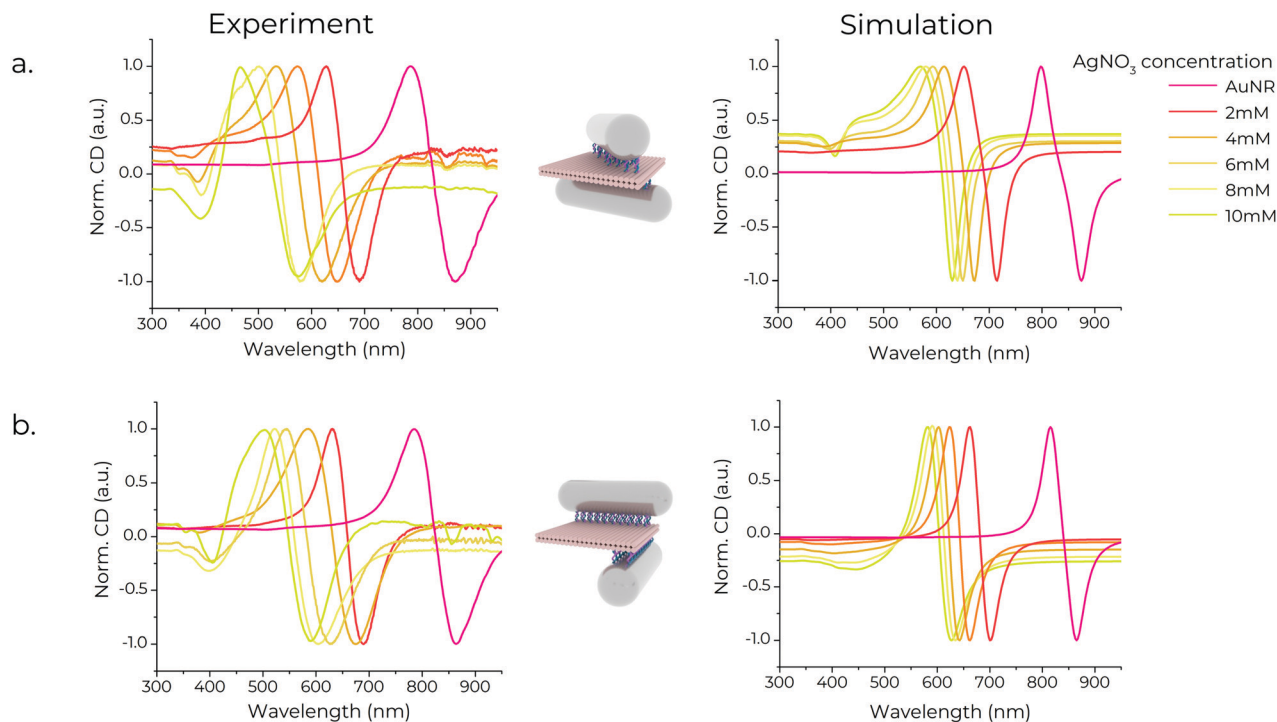
Fig. 4 Experimental (left) and theoretically calculated (right) CD spectra of the (a) X-shaped and (b) L-shaped chiral metamolecules constructed using Au/AgNRs with Ag shells of varying thicknesses. The legend shows the concentration of AgNO$_3$ used to synthesise the nanorods in the metamolecules.

manipulation of the longitudinal mode in the IR-NIR region by employing Ag shell growth. We also see the appearance of new spectral features in the 300–400 nm wavelength region. We provide theoretical simulations that show remarkable agreement with the experimental results, both for the extinction of Au/AgNRs and the CD from chiral metamolecules constructed with the Au/AgNRs. Au/AgNRs have gained popularity in recent times as a novel plasmonic material.[51] Chiral metamolecules constructed using Au/AgNRs can result in strong chiral signals[45] and could be used for sensitive detection.[33] In addition, the freedom to tune the optical response can be used to synthesize metamaterials with stronger optical activity in the visible region. The tunability can also be used to modulate the optical response to enhance LSPR-dependant coupling to other moieties, *e.g.* dyes,[62] and also open the doors for the realisation of other applications, *e.g.* chiral reactions.[51,63] Additionally, our protocol should be extendable to more exotic morphologies of gold particles as well, *e.g.* nanostars,[64] chiral particles[65] or nanocubes.[66]

Author contributions

MD and TL conceived the experiments. MD designed the DNA origami structures and performed the experiments. LK performed the theoretical simulations. MD and GP analysed the experimental data and wrote the manuscript. All authors discussed the results and commented on the manuscript.

Conflicts of interest

There are no conflicts to declare.

Acknowledgements

Notes and references

1 S. Beychok, Circular Dichroism of Biological Macromolecules, *Science*, 1966, **154**(3754), 1288–1299.
2 N. J. Greenfield, Using circular dichroism spectra to estimate protein secondary structure, *Nat. Protoc.*, 2006, **1**(6), 2876–2890.
3 V. I. Ivanov, L. E. Minchenkova, A. K. Schyolkina and A. I. Poletayev, Different conformations of double-stranded nucleic acid in solution as revealed by circular dichroism, *Biopolymers*, 1973, **12**(1), 89–110.
4 W. A. Baase and W. C. Johnson, Circular dichroism and DNA secondary structure, *Nucleic Acids Res.*, 1979, **6**(2), 797–814.

5 W. C. Johnson, Determination of the Conformation of Nucleic Acids by Electronic CD, in *Circular Dichroism and the Conformational Analysis of Biomolecules*, ed. G. D. Fasman, Springer US, Boston, MA, 1996, pp. 433–468.

6 J. Kypr, I. Kejnovská, D. Renčiuk and M. Vorlíčková, Circular dichroism and conformational polymorphism of DNA, *Nucleic Acids Res.*, 2009, **37**(6), 1713–1725.

7 M. Hentschel, M. Schäferling, T. Weiss, N. Liu and H. Giessen, Three-Dimensional Chiral Plasmonic Oligomers, *Nano Lett.*, 2012, **12**(5), 2542–2547.

8 Q. Zhang, T. Hernandez, K. W. Smith, S. A. H. Jebeli, A. X. Dai and L. Warning, *et al.*, Unraveling the origin of chirality from plasmonic nanoparticle-protein complexes, *Science*, 2019, **365**(6460), 1475–1478.

9 M. Hentschel, M. Schäferling, X. Duan, H. Giessen and N. Liu, Chiral plasmonics, *Sci. Adv.*, 2017, **3**(5), e1602735.

10 N. Suzuki, Y. Wang, P. Elvati, Z.-B. Qu, K. Kim and S. Jiang, *et al.*, Chiral Graphene Quantum Dots, *ACS Nano*, 2016, **10**(2), 1744–1755.

11 S. D. Elliott, M. P. Moloney and Y. K. Gun'ko, Chiral Shells and Achiral Cores in CdS Quantum Dots, *Nano Lett.*, 2008, **8**(8), 2452–2457.

12 J. E. Govan, E. Jan, A. Querejeta, N. A. Kotov and Y. K. Gun'ko, Chiral luminescent CdS nano-tetrapods, *Chem. Commun.*, 2010, **46**(33), 6072–6074.

13 S. Che, Z. Liu, T. Ohsuna, K. Sakamoto, O. Terasaki and T. Tatsumi, Synthesis and characterization of chiral mesoporous silica, *Nature*, 2004, **429**(6989), 281–284.

14 A. Nemati, S. Shadpour, L. Querciagrossa, T. Mori, C. Zannoni and T. Hegmann, Highly Sensitive, Tunable Chirality Amplification through Space Visualized for Gold Nanorods Capped with Axially Chiral Binaphthyl Derivatives, *ACS Nano*, 2019, **13**(9), 10312–10326.

15 R.-Y. Wang, H. Wang, X. Wu, Y. Ji, P. Wang and Y. Qu, *et al.*, Chiral assembly of gold nanorods with collective plasmonic circular dichroism response, *Soft Matter*, 2011, **7**(18), 8370–8375.

16 J. Sharma, R. Chhabra, C. S. Andersen, K. V. Gothelf, H. Yan and Y. Liu, Toward Reliable Gold Nanoparticle Patterning On Self-Assembled DNA Nanoscaffold, *J. Am. Chem. Soc.*, 2008, **130**(25), 7820–7821.

17 A. M. Hung, C. M. Micheel, L. D. Bozano, L. W. Osterbur, G. M. Wallraff and J. N. Cha, Large-area spatially ordered arrays of gold nanoparticles directed by lithographically confined DNA origami, *Nat. Nanotechnol.*, 2010, **5**(2), 121–126.

18 S. Pal, Z. Deng, H. Wang, S. Zou, Y. Liu and H. Yan, DNA Directed Self-Assembly of Anisotropic Plasmonic Nanostructures, *J. Am. Chem. Soc.*, 2011, **133**(44), 17606–17609.

19 A. Kuzyk, R. Schreiber, Z. Fan, G. Pardatscher, E.-M. Roller and A. Högele, *et al.*, DNA-based self-assembly of chiral plasmonic nanostructures with tailored optical response, *Nature*, 2012, **483**(7389), 311–314.

20 G. P. Acuna, F. M. Möller, P. Holzmeister, S. Beater, B. Lalkens and P. Tinnefeld, Fluorescence Enhancement at Docking Sites of DNA-Directed Self-Assembled Nanoantennas, *Science*, 2012, **338**(6106), 506–510.

21 X. Ouyang, M. De Stefano, A. Krissanaprasit, A. L. Bank Kodal, C. Bech Rosen and T. Liu, *et al.*, Docking of Antibodies into the Cavities of DNA Origami Structures, *Angew. Chem., Int. Ed.*, 2017, **56**(46), 14423–14427.

22 P. Zhang, X. Liu, P. Liu, F. Wang, H. Ariyama and T. Ando, *et al.*, Capturing transient antibody conformations with DNA origami epitopes, *Nat. Commun.*, 2020, **11**(1), 3114.

23 G. Grossi, M. Dalgaard Ebbesen Jepsen, J. Kjems and E. S. Andersen, Control of enzyme reactions by a reconfigurable DNA nanovault, *Nat. Commun.*, 2017, **8**(1), 992.

24 B. Saccà, R. Meyer, M. Erkelenz, K. Kiko, A. Arndt and H. Schroeder, *et al.*, Orthogonal Protein Decoration of DNA Origami, *Angew. Chem.*, 2010, **122**(49), 9568–9573.

25 A. Sprengel, P. Lill, P. Stegemann, K. Bravo-Rodriguez, E.-C. Schöneweiß and M. Merdanovic, *et al.*, Tailored protein encapsulation into a DNA host using geometrically organized supramolecular interactions, *Nat. Commun.*, 2017, **8**(1), 14472.

26 J. B. Knudsen, L. Liu, A. L. Bank Kodal, M. Madsen, Q. Li and J. Song, *et al.*, Routing of individual polymers in designed patterns, *Nat. Nanotechnol.*, 2015, **10**(10), 892–898.

27 M. Madsen, M. R. Bakke, D. A. Gudnason, A. F. Sandahl, R. A. Hansen and J. B. Knudsen, *et al.*, A Single Molecule Polyphenylene-Vinylene Photonic Wire, *ACS Nano*, 2021, **15**(6), 9404–9411.

28 X. Shen, C. Song, J. Wang, D. Shi, Z. Wang and N. Liu, *et al.*, Rolling Up Gold Nanoparticle-Dressed DNA Origami into Three-Dimensional Plasmonic Chiral Nanostructures, *J. Am. Chem. Soc.*, 2012, **134**(1), 146–149.

29 X. Shen, A. Asenjo-Garcia, Q. Liu, Q. Jiang, F. J. García de Abajo and N. Liu, *et al.*, Three-Dimensional Plasmonic Chiral Tetramers Assembled by DNA Origami, *Nano Lett.*, 2013, **13**(5), 2128–2133.

30 X. Lan, Z. Chen, G. Dai, X. Lu, W. Ni and Q. Wang, Bifacial DNA Origami-Directed Discrete, Three-Dimensional, Anisotropic Plasmonic Nanoarchitectures with Tailored Optical Chirality, *J. Am. Chem. Soc.*, 2013, **135**(31), 11441–11444.

31 R. Schreiber, N. Luong, Z. Fan, A. Kuzyk, P. C. Nickels and T. Zhang, *et al.*, Chiral plasmonic DNA nanostructures with switchable circular dichroism, *Nat. Commun.*, 2013, **4**(1), 2948.

32 A. Cecconello, J. S. Kahn, C.-H. Lu, L. Khosravi Khorashad, A. O. Govorov and I. Willner, DNA Scaffolds for the Dictated Assembly of Left-/Right-Handed Plasmonic Au NP Helices with Programmed Chiro-Optical Properties, *J. Am. Chem. Soc.*, 2016, **138**(31), 9895–9901.

33 T. Funck, F. Nicoli, A. Kuzyk and T. Liedl, Sensing Picomolar Concentrations of RNA Using Switchable Plasmonic Chirality, *Angew. Chem.*, 2018, **130**(41), 13683–13686.

34 P. T. Probst, M. Mayer, V. Gupta, A. M. Steiner, Z. Zhou and G. K. Auernhammer, *et al.*, Mechano-tunable chiral metasurfaces via colloidal assembly, *Nat. Mater.*, 2021, **20**(7), 1024–1028.

35 W. Haiss, N. T. K. Thanh, J. Aveyard and D. G. Fernig, Determination of Size and Concentration of Gold Nanoparticles from UV-Vis Spectra, *Anal. Chem.*, 2007, **79**(11), 4215–4221.

36 X. Lan, X. Lu, C. Shen, Y. Ke, W. Ni and Q. Wang, Au Nanorod Helical Superstructures with Designed Chirality, *J. Am. Chem. Soc.*, 2015, **137**(1), 457–462.

37 A. Kuzyk, R. Schreiber, H. Zhang, A. O. Govorov, T. Liedl and N. Liu, Reconfigurable 3D plasmonic metamolecules, *Nat. Mater.*, 2014, **13**(9), 862–866.

38 M. Wang, J. Dong, C. Zhou, H. Xie, W. Ni and S. Wang, *et al.*, Reconfigurable Plasmonic Diastereomers Assembled by DNA Origami, *ACS Nano*, 2019, **13**(12), 13702–13708.

39 X. Lan, T. Liu, Z. Wang, A. O. Govorov, H. Yan and Y. Liu, DNA-Guided Plasmonic Helix with Switchable Chirality, *J. Am. Chem. Soc.*, 2018, **140**(37), 11763–11770.

40 L. Scarabelli, A. Sánchez-Iglesias, J. Pérez-Juste and L. M. A. Liz-Marzán, ''Tips and Tricks'' Practical Guide to the Synthesis of Gold Nanorods, *J. Phys. Chem. Lett.*, 2015, **6**(21), 4270–4279.

41 G. González-Rubio, V. Kumar, P. Llombart, P. Díaz-Núñez, E. Bladt and T. Altantzis, *et al.*, Disconnecting Symmetry Breaking from Seeded Growth for the Reproducible Synthesis of High Quality Gold Nanorods, *ACS Nano*, 2019, **13**(4), 4424–4435.

42 P. R. West, S. Ishii, G. V. Naik, N. K. Emani, V m. Shalaev and A. Boltasseva, Searching for better plasmonic materials, *Laser Photonics Rev.*, 2010, **4**(6), 795–808.

43 D. G. Thompson, A. Enright, K. Faulds, W. E. Smith and D. Graham, Ultrasensitive DNA Detection Using Oligonucleotide–Silver Nanoparticle Conjugates, *Anal. Chem.*, 2008, **80**(8), 2805–2810.

44 T. Liu, L. V. Besteiro, T. Liedl, M. A. Correa-Duarte, Z. Wang and A. O. Govorov, Chiral Plasmonic Nanocrystals for Generation of Hot Electrons: Toward Polarization-Sensitive Photochemistry, *Nano Lett.*, 2019, **19**(2), 1395–1407.

45 L. Nguyen, M. Dass, M. F. Ober, L. V. Besteiro, Z. M. Wang and B. Nickel, *et al.*, Chiral Assembly of Gold–Silver Core–Shell Plasmonic Nanorods on DNA Origami with Strong Optical Activity, *ACS Nano*, 2020, **14**(6), 7454–7461.

46 P. B. Johnson and R. W. Christy, Optical Constants of the Noble Metals, *Phys. Rev. B: Condens. Matter Mater. Phys.*, 1972, **6**(12), 4370–4379.

47 E. D. Palik, *Handbook of Optical Constants of Solids*, Elsevier, 2012, vol. 1, p. 824.

48 A. Chhatre, R. Thaokar and A. Mehra, Formation of Gold Nanorods by Seeded Growth: Mechanisms and Modeling, *Cryst. Growth Des.*, 2018, **18**(6), 3269–3282.

49 Y. Xiang, X. Wu, D. Liu, Z. Li, W. Chu and L. Feng, *et al.*, Gold Nanorod-Seeded Growth of Silver Nanostructures: From Homogeneous Coating to Anisotropic Coating, *Langmuir*, 2008, **24**(7), 3465–3470.

50 S. Link and M. A. El-Sayed, Spectral Properties and Relaxation Dynamics of Surface Plasmon Electronic Oscillations in Gold and Silver Nanodots and Nanorods, *J. Phys. Chem. B*, 1999, **103**(40), 8410–8426.

51 Y. Negrín-Montecelo, M. Comesaña-Hermo, L. K. Khorashad, A. Sousa-Castillo, Z. Wang and M. Pérez-Lorenzo, *et al.*, Photophysical Effects behind the Efficiency of Hot Electron Injection in Plasmon-Assisted Catalysis: The Joint Role of Morphology and Composition, *ACS Energy Lett.*, 2020, **5**(2), 395–402.

52 B. Liu and J. Liu, Freezing-Driven DNA Adsorption on Gold Nanoparticles: Tolerating Extremely Low Salt Concentration but Requiring High DNA Concentration, *Langmuir*, 2019, **35**(19), 6476–6482.

53 B. Liu, T. Wu, Z. Huang, Y. Liu and J. Liu, Freezing-directed Stretching and Alignment of DNA Oligonucleotides, *Angew. Chem.*, 2019, **131**(7), 2131–2135.

54 B. Liu and J. Liu, Interface-Driven Hybrid Materials Based on DNA-Functionalized Gold Nanoparticles, *Matter*, 2019, **1**(4), 825–847.

55 S. Takabayashi, P. W. Klein, C. Onodera, B. Rapp, J. Flores-Estrada and E. Lindau, *et al.*, High precision and high yield fabrication of dense nanoparticle arrays onto DNA origami at statistically independent binding sites, *Nanoscale*, 2014, **6**(22), 13928–13938.

56 F. N. Gür, F. W. Schwarz, J. Ye, S. Diez and T. L. Schmidt, Toward Self-Assembled Plasmonic Devices: High-Yield Arrangement of Gold Nanoparticles on DNA Origami Templates, *ACS Nano*, 2016, **10**(5), 5374–5382.

57 X. Shen, P. Zhan, A. Kuzyk, Q. Liu, A. Asenjo-Garcia and H. Zhang, *et al.*, 3D plasmonic chiral colloids, *Nanoscale*, 2014, **6**(4), 2077–2081.

58 B. Auguié, J. L. Alonso-Gómez, A. Guerrero-Martínez and L. M. Liz-Marzán, Fingers Crossed: Optical Activity of a Chiral Dimer of Plasmonic Nanorods, *J. Phys. Chem. Lett.*, 2011, **2**(8), 846–851.

59 O. Nicoletti, M. Wubs, N. A. Mortensen, W. Sigle, P. A. Aken and P. A. van, Midgley, Surface plasmon modes of a single silver nanorod: an electron energy loss study, *Opt. Express*, 2011, **19**(16), 15371–15379.

60 X. Zhuo, H. K. Yip, X. Cui, J. Wang and H.-Q. Lin, Colour routing with single silver nanorods, *Light: Sci. Appl.*, 2019, **8**(1), 39.

61 D. Rossouw, M. Couillard, J. Vickery, E. Kumacheva and G. A. Botton, Multipolar Plasmonic Resonances in Silver Nanowire Antennas Imaged with a Subnanometer Electron Probe, *Nano Lett.*, 2011, **11**(4), 1499–1504.

62 M. P. Singh and G. F. Strouse, Involvement of the LSPR Spectral Overlap for Energy Transfer between a Dye and Au Nanoparticle, *J. Am. Chem. Soc.*, 2010, **132**(27), 9383–9391.

63 L. K. Khorashad, L. V. Besteiro, M. A. Correa-Duarte, S. Burger, Z. M. Wang and A. O. Govorov, Hot Electrons Generated in Chiral Plasmonic Nanocrystals as a Mechanism for Surface Photochemistry and Chiral Growth, *J. Am. Chem. Soc.*, 2020, **142**(9), 4193–4205.

64 I. G. Theodorou, Z. A. R. Jawad, Q. Jiang, E. O. Aboagye, A. E. Porter and M. P. Ryan, *et al.*, Gold Nanostar Substrates for Metal-Enhanced Fluorescence through the First and Second Near-Infrared Windows, *Chem. Mater.*, 2017, **29**(16), 6916–6926.

65 H.-E. Lee, H.-Y. Ahn, J. Mun, Y. Y. Lee, M. Kim and N. H. Cho, *et al.*, Amino-acid- and peptide-directed synthesis of chiral plasmonic gold nanoparticles, *Nature*, 2018, **556**(7701), 360–365.

66 J.-E. Park, Y. Lee and J.-M. Nam, Precisely Shaped, Uniformly Formed Gold Nanocubes with Ultrahigh Reproducibility in Single-Particle Scattering and Surface-Enhanced Raman Scattering, *Nano Lett.*, 2018, **18**(10), 6475–6482.

5. OPTICAL PHYSICAL UNCLONABLE FUNCTIONS USING DNA ORIGAMI

In 2022, counterfeit and pirated goods worth 119 billion EUR were sold in the EU, according to Europol/EUIPO.[131] Counterfeiting of goods remains a challenge for our society, increasingly so in a globalised world with long supply chains. Concurrently, the online market for sensitive goods like medicines is expanding, further exemplifying the need for robust anti-counterfeit measures. The WHO estimates around 100,000 children under five die annually due to counterfeit pneumonia medication.[132]

Modern cryptography largely relies on one-way functions. These are functions that are easy to evaluate in the forward direction but infeasible to compute in the reverse direction without additional information. For instance, the multiplication of large prime numbers can be done in a polynomial time, whereas finding the prime factors of the product is believed to require exponential time.[133] Although digital one-way functions based on an algorithmic logic are widely used, they face two challenges:

1. The first is technological, as parallel networks of computers can break codes once considered secure.
2. The second is fundamental. While the cryptographic functions used are believed to be secure, there is no proof that efficient attacks don't exist. Such attacks are in fact known using quantum computers; it is shown in that factoring the product of two large prime numbers can be accomplished in polynomial time on a quantum computer.[134]

An alternative approach lies in the use of Physical Unclonable Functions (PUFs) which are clone-proof, cost efficient and resistant to various physical attacks. PUFs are physical objects that for a given input (challenge), provides a physically defined "digital fingerprint" output (response) that serves as a unique key. The key is unique because it is defined by inherent random variations introduced during the manufacturing process. Despite any potential measurement of these variations, it remains infeasible to produce an identical physical 'clone', primarily because full control over micro- and nanoscale fabrication variations is considered impossible.[135]

Optical PUFs, which leverage light-matter interactions to generate this unique fingerprint, are categorised as 'strong' PUFs due to the inherent challenge an attacker would face in replicating them.[136] Strong PUFs feature an exponential increase in possible outputs with respect to some system parameter. Pappu *et al*. showed the first well-known instance of an optical PUF, initially dubbed a physical one-way function. [137] In particular, angular light illumination on a transparent inhomogeneous object led to complex interference, creating a 2D speckle pattern which was recorded by a charge-coupled device. The object was an epoxy cuboid containing glass spheres 500 - 800 um in diameter which acted as the scattering medium.

The use of nanomaterials is attractive because of the inherent challenges in nanoscale manufacturing and controlling the fabrication and placement of nanoscale objects with atomic precision. Researchers have explored various nanomaterials and read-out methods for making PUFs[138], including carbon nanotubes with electrical current read-out[139], carbon dots exhibiting fluorescence patterns[140] and block copolymers questioned via Raman scattering[141]. Among optical materials, plasmonic nanoparticles are particularly interesting for optical PUFs due to their strong interactions with light in the visible spectrum (400-700 nm), even when their dimensions are sub-100 nm. PUFs made with such nanoparticles can read-out using relatively simple optical instruments. As a result, several groups have characterised their suitability for building PUFs.[142–144] However, these works often suffer from low particle density in the PUF labels or low variation in the optical response of the PUF, both of which compromise the security by limiting the complexity of the PUF.
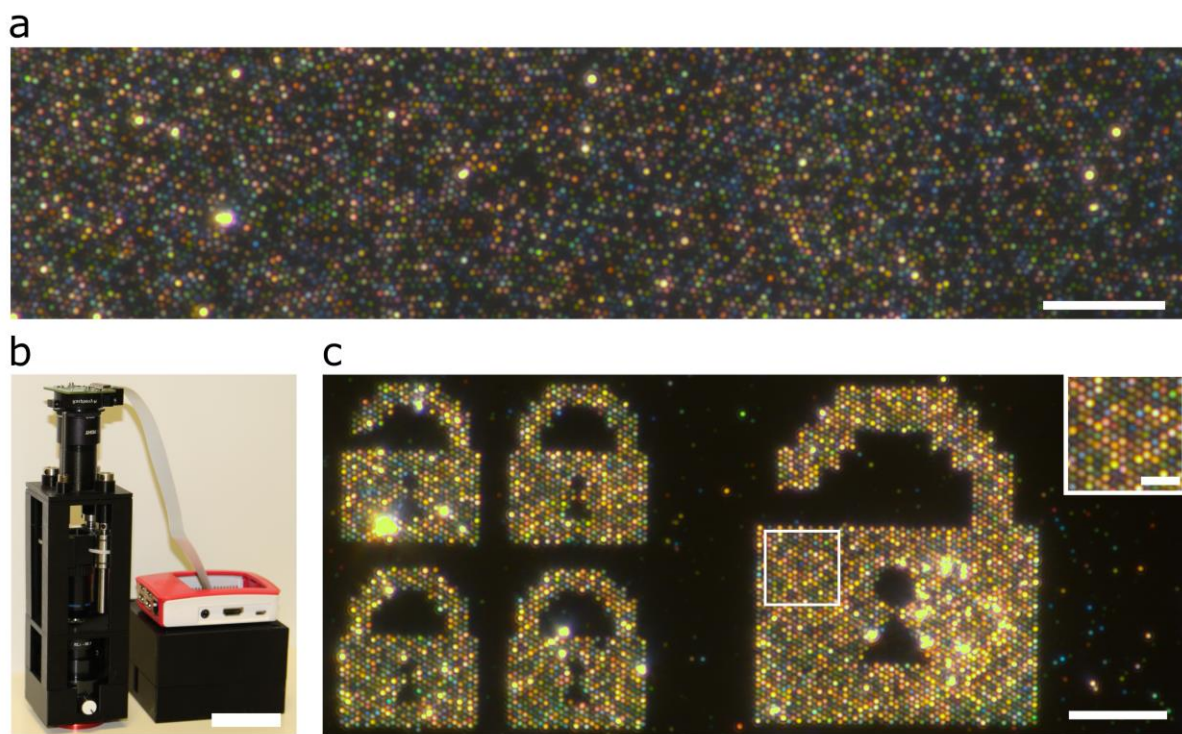
Figure 21. Schematic and fabrication of our PUFs. a) Nanosphere Lithography (NSL) procedure involving Polystyrene nanosphere deposition, surface passivation using HMDS, lift-off and DOP using DNA origami. b) NPP performed using various functionalised nanoparticles. d) SEM image after NPP. d) DFM image of the resultant PUF. Scale bars, (c) 500 nm and (d) 10 μm.

In associated publication **P3**[145], we introduce the first study utilizing the advantages of DNA origami to create optical PUFs with enhanced security features. We employed nanosphere lithography (NSL) to generate a high-density of placement sites on a substrate, where DNA origami structures[146–149] and, subsequently, nanoparticles could be precisely placed (Fig. 21 a). Plasmonic coupling between the nanoparticles gives rise to new colours absent at the discrete particle level, which can be readily detected using a Dark Field microscopy (DFM).

We fabricated a 3D-printed dark field microscope and were able to image our PUFs (Fig. 21b).[150] By using knowledge gained from associated publication P2, a variety of plasmonic particles – gold nanospheres (AuNS), gold nanorods (AuNR), gold/silver core/shell nanospheres (AgNS) and nanorods (AgNR) – are synthesised to create a broad variation in the optical response.

This combination offers two advantages over previous works. Firstly, using NSL leads to the creating of a high density of placement sites on a substrate to which DNA origami and subsequently, nanoparticles can bind. Secondly, the DNA origami serves to capture the nanoparticles in close proximity to each other. Plasmonic coupling, which causes the variation in hues of the nanoparticle assemblies, is a distance-based phenomenon dominating at close distances. Thus, DNA origami is instrumental in creating a broad hue response, which is a security feature in our PUFs. We demonstrate control over the optical response of our PUFs by fabricating labels with different species and concentrations of nanoparticle, achieving a wide range of hues and hue distributions. We also show our technique is compatible with e-beam lithography to create user-defined patterns (Fig. 21c). Furthermore, we successfully integrated our PUF technology with a cost-effective read-out mechanism in the form of our 3D-printed DFM, thereby significantly reducing the gap between experimental technology and practical societal applications.

5.1 Associated publication P3

Self-assembled physical unclonable function labels based on plasmonic coupling

by

Mihir Dass, Lena Raab, Christoph Pauer, Christoph Sikeler, Larissa Heinze, Joe Tavacoli, Irina V. Martynenko, Ulrich Rührmair, Gregor Posnjak, and Tim Liedl

submitted to

Self-assembled physical unclonable function labels based on plasmonic coupling

Mihir Dass,[1] Lena Raab,[1] Christoph Pauer,[1] Christoph Sikeler,[1] Larissa Heinze,[1] Joe Tavacoli,[1] Irina V. Martynenko,[1] Ulrich Rührmair*,[2,3] Gregor Posnjak*,[1] Tim Liedl*[1]

[1]Faculty of Physics and Center for NanoScience (CeNS)
Ludwig-Maximilian-University Munich, 80539 Munchen, Germany

[2]Electrical and Computer Engineering Department,
University of Connecticut, Storrs, CT 06249

[3]Institute for Computer Science,
Ludwig-Maximilian-University Munich, 80538 München, Germany

Corresponding authors:

Ulrich Rührmair - ruehrmair@ilo.de
Gregor Posnjak - gregor.posnjak@lmu.de,
Tim Liedl - tim.liedl@physik.lmu.de

Abstract

Counterfeiting threatens human health, social equity, national security and global and local economies. Hardware-based cryptography that exploits physical unclonable functions (PUFs) provides the means for secure identification and authentication of products. While optical PUFs are among the hardest to replicate, they suffer from low encoding capacity and often complex and expensive read-out. Here we report PUF labels with nanoscale features and optical responses that arise from the guided self-assembly of plasmonic nanoparticles. Nanosphere lithography combined with DNA origami placement are used to create tightly packed randomised nanoparticle assemblies. Nanoscale variations within these assemblies define the scattering colour of the individual spots that are arranged in a hexagonal lattice with spacing down to the optical resolution limit. Due to the nanoscale dimensions, the intrinsic randomness of the particle assemblies and their resulting optical responses, our PUFs are virtually impossible to replicate while they can be read-out with economical 3D-printed hardware.

Combating counterfeiting of goods is a challenge for our society, increasingly so in a globalised world where supply chains become longer and their transparency decreases. Concurrently, the market for sensitive goods, such as medicine, has also increased, further exemplifying the need for anti-counterfeit measures. For example, between 72,000 and 169,000 children die of treatable diseases like pneumonia annually due to counterfeited medicine.[1] The estimated economic losses from counterfeiting are in trillions of dollars.[2] Consequently, increasingly complex and effective authentication tools are being developed. One class of anti-counterfeit measures are *physical unclonable functions* (PUFs), physical objects that provide a unique fingerprint as a result of a stochastic process. Their evaluation is straightforward in the

forward direction but infeasible to compute in the reverse one without additional information. Ideally, they are impossible to replicate physically.[3]

As such, a wide range of materials and readout strategies have been shown,[2,4] ranging from carbon nanotubes with electrical current read-out[5], to carbon dots exhibiting fluorescence patterns[6] and block copolymers questioned via Raman scattering[7]. Optical PUFs, that rely on light-matter interactions to produce the fingerprint, are categorised as 'strong' PUFs for the inherent difficulty for an attacker to replicate them.[4] Strong PUFs feature an exponential increase in possible outputs with respect to some system parameter. Among optical elements, plasmonic particles are excellent candidates for programming light-matter interactions because they interact strongly with light. The optical response of plasmonic particles is the result of intrinsic properties like material, shape, size and dielectric environment.[8,9] Additionally, extrinsic factors such as the proximity to other particles can strongly affect their optical behaviour due to near-field mediated plasmonic coupling.[10,11] Combining variations in these intrinsic and extrinsic properties provides the experimenter with a versatile tool box from which to engineer a unique optical response. Indeed, such nanoparticles can interact with light in the visible regime with wavelengths between 400 nm- 700 nm, even when their dimensions are sub-100 nm. As a result, several groups have characterised their suitability for building PUFs.[12–14] Practically, these works often suffer from low particle density or low variation in the optical response of the PUF, both of which compromise the security by limiting the complexity of the PUF.

In the current work, we create *PartiPUFs* (Particle PUFs) by combining plasmonic nanoparticle[15] placement (NPP) with DNA Origami Placement (DOP)[16,17] to hexagonally pattern nanoparticle assemblies at a desired surface density using nanosphere lithography (NSL).[18–21] Capture of the assemblies is mediated by first laying down hexagonal arrays of DNA origami *nanodiscs* that capture different combinations of nanoparticles. Plasmonic coupling between the nanoparticles gives rise to new colours absent at the discrete particle level, which can be readily detected using Dark Field microscopy (DFM).[22] Control over the DNA origami design, NSL parameters and the combination and concentration of nanoparticles allows us to tailor the optical response and pack the surface with a high information density. The resulting colourful plasmonic labels allow for the generation of a large number of challenge-response pairs, instrumental in the security of the PUF. Our PUFs demonstrate a unique and broad variation in their optical response, which we characterize by the implementation of a hue analysis. We also fabricated an economical and portable DFM and used it to successfully image our PUFs, showcasing the suitability of our technology for practical applications.
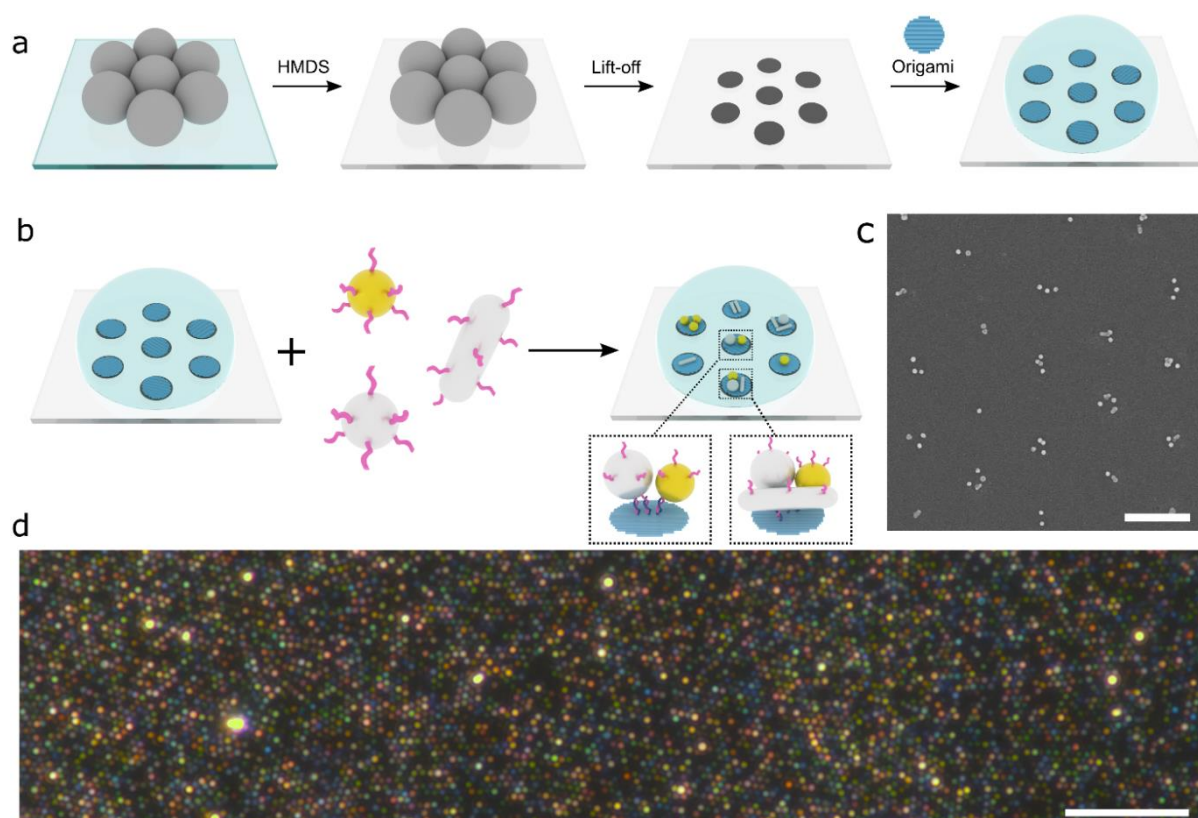
Fabrication of PartiPUFs

Figure 1. Schematic and fabrication of PartiPUFs. a) NSL procedure involving Polystyrene nanosphere deposition, surface passivation using HMDS, lift-off and DOP using DNA origami. b) NPP performed using various functionalised nanoparticles. d) SEM image after NPP. d) DFM image of the resultant PUF. Scale bars, (c) 500 nm and (d) 10 µm.

Figure 1a illustrates the fabrication process of the PartiPUF. Glass coverslips are nanopatterned using NSL to create *placement sites* for the DOP. DOP is then performed to place DNA origami nanodiscs (~ 100 nm x 85 nm) on the glass surface. Each nanodisc contains *binding sites* made of poly-Adenine ssDNA extensions (10 nt long, "A_{10}") extended from both faces in a filled circular arrangement (Fig. S1). The desired mix of nanoparticles functionalised with poly-Thymine ssDNA (9:1 mix of T_8:T_{19}) is then added, where the DNA origami structures serve to capture the nanoparticles through strand hybridisation (Fig. 1b). The result is a stochastic assembly of nanoparticles at each placement site (Fig. 1c) to produce a dense packing of coloured spots when viewed under a DFM (Fig. 1d). A variety of plasmonic particles – gold nanospheres (AuNS), gold nanorods (AuNR), gold/silver core/shell nanospheres (AgNS) and nanorods (AgNR) – are used to create a broad variation in the optical response.[23,24] Plasmonic coupling between nanoparticles placed sufficiently close together (1-10 nm) gives rise to new colours in the assemblies, further increasing the output complexity.

We can direct the appearance of our PUF in two main ways. Firstly, we can adapt the pitch size between the individual scattering spots by adjusting the size of the nanospheres employed during NSL (Fig. S2). The nanosphere diameter defines both the size of the

placement site and the spacing between placement sites, which is approximately equal to the diameter of the spheres used.[17] We performed NSL using polystyrene nanospheres with diameters of 400, 600 and 1000 nm. Controlling the spacing between the spots is crucial because it allows to increase the density of our spots to a critical point just above the diffraction limit, below which the colours would 'bleed 'into each other making optical analysis infeasible. The DNA origami structures used for subsequent deposition feature a binding site containing 42 A_{10} extensions (21 from each face, distributed in a circular pattern with a diameter of ~ 60 nm) to capture an undefined number of nanoparticles.

Secondly, we can adapt the colour distribution of our PUF by varying the material, form and population composition of the plasmonic particles trapped at each DNA origami. Specifically, four different types of nanoparticles were utilised in our experiments: 30 nm AuNS, 50 nm AgNS, AuNR with length = 60 nm and width = 12 nm and AgNR with length = 75 nm and diameter = 25 nm (Supplementary note S1). The silver-coating enhances the scattering of the nanoparticles and provides variation in the scattering colour of the individual nanoparticle species.[25] The silver-coating also pushes the LSPR wavelength of the nanorods into the visible, thus ensuring that all nanoparticle species scatter in the visible regime. Next to the controlled spacing between the assembly sites, the NSL method provides a cheap, fast and parallel way to program the size of the placement spots and thus, with the help of DNA origami patches, also ensures tight spacing between the individual nanoparticles.[17,18] The result is a random distribution of scattering colours due to the type of particles and the plasmonic interactions between them on each placement site.
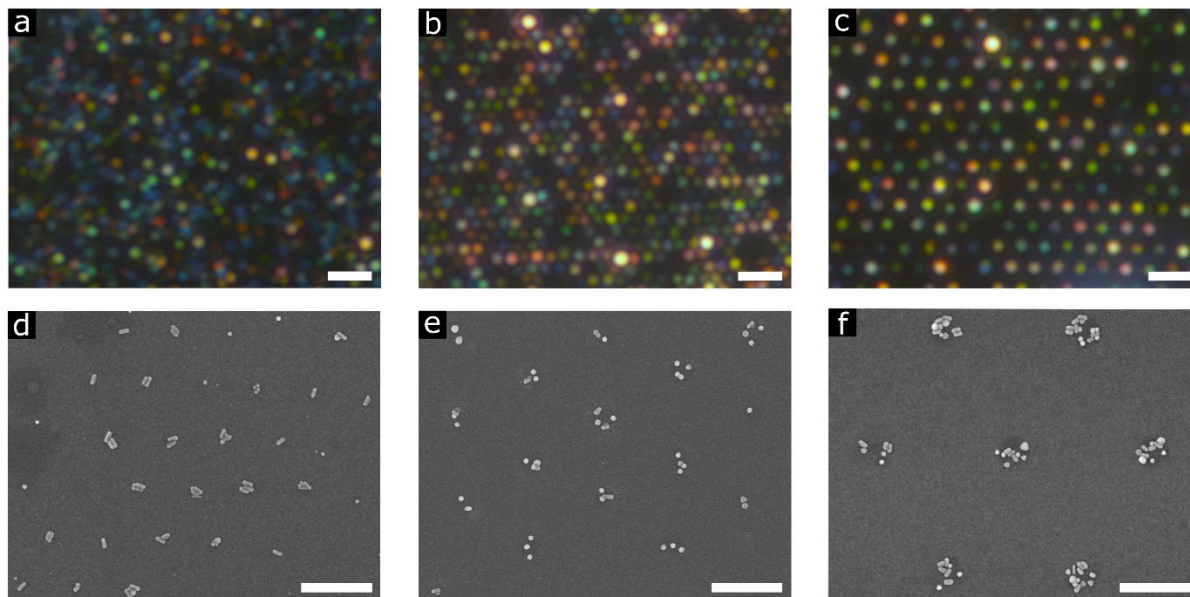
Figure 2. PUFs fabricated with varying inter-site spacing. a-c) DFM images (full field-of-view in Fig. S5-S7) and d-f) SEM images of PartiPUFs made with a,d) 400 nm, b,e) 600 nm and c,f) 1 µm spacing (uncropped images: Fig. S8-S10). Scale bars, (a-c) 2 µm, (d-f) 500 nm.

We fabricated PUFs with varying site spacing and a wide range of colours scattering from the individual placement sites (Fig. 2a-c). The strong scattering of the nanoparticles enabled fast

acquisition times in DFM, which makes it a suitable characterisation method for our PUFs.[26] The SEM images show the stochastic nature of the assembly of particles at the individual placement sites (Fig. 2d-f). For the smallest spheres used in our experiments (400 nm, Fig. 2a,d), we observed small groups of densely placed particles on each contact spot. Larger spheres (600 nm and 1 μm, Fig. 2b,c,e,f) resulted in larger contact areas, often leading to the binding of more than a single DNA origami structure. Accordingly, we observed more particles bound per spot with discernible gaps between the particles or groups of particles. However, the number of DNA origami structures per placement site can be further tuned with parameters such as the Mg^{2+} or the DNA origami concentration or the incubation time.[16] In the case of our nanodisc DNA origami structure, a nanosphere with a diameter of 350 nm results in single-origami placement (Fig. S11). Using larger spheres leads to multiple structures being placed on each placement site (Fig. 2e,f and Fig. S12). In such cases, we optimised the DNA origami concentration during DOP to obtain the desired number of DNA origami structures on the placement sites. High DNA origami concentrations (450 pM) led to complete saturation of the placement sites (Fig. S12d).

PartiPUF characterization and Hue analysis

We analysed the DFM images of PartiPUFs using an ad hoc-written image analysis algorithm (Supplementary note S2). For our analysis we chose the Hue-Saturation-Brightness (HSB) scale as it uses a single value - the 'hue 'as a proxy for the wavelength - to identify colour. Hue values of the individual scattering spots thus quantitatively characterise the complexity of the scattering response of our PUFs (Fig. S13). We fabricated PartiPUFs with different nanoparticle species and concentrations (Fig. 3a-f) and obtained a wide range of hues and hue distributions (Fig. 3g,h). The optical density (O.D.) of the nanoparticle suspensions was used to measure their concentration. Higher concentrations of nanoparticles (usually O.D. > 1) resulted in hue distributions skewed towards lower, i.e. redder, values, even when using multiple nanoparticle species (Fig. 3g). PUFs made using only AgNSs illustrate the effect of variations in the particle concentration (Fig. 3a,d). Using higher concentrations of AgNS (O.D. ~ 0.75) (Fig. 3d) resulted in a relatively narrow hue distribution, with a higher frequency of hues at lower values in the range of 20 – 40 (Fig. 3h). Decreasing the AgNS concentration slightly (O.D. ~ 0.5) led to a bimodal distribution (Fig. 3g) with a peak appearing at hue ~ 100, similar to that of individual AgNS deposited on a surface (Fig. S21). The secondary maximum, around hue ~ 40, is consistent with aggregates giving lower hue values. An elevated concentration (O.D. ~ 1.5) of a mixture of AuNSs and AuNRs (Fig. 3b) resulted in hues with a peak of the distribution at hue ~ 25. Lower concentrations (O.D. ~ 0.5) of the same particle mix (Fig. 3e) shifted the hue distribution towards higher hue values. High concentrations (O.D. ~ 2.7) of a mixture of AuNSs, AgNRs and AgNSs (Fig. 3c) resulted in a narrow hue distribution, similar to that obtained for particle mixes containing AuNSs and AuNRs. Lower concentrations (O.D. ≤ 0.5) of a mixture of AuNSs, AgNRs and AgNSs (Fig. 3f) resulted in the broadest range of hues (Fig. 3h). Hues ranging from 6 to 166 were achieved, covering red, orange, yellow, green and blue. We could also vary the hue distribution of PUFs by controlling the number of particles attaching to each DNA origami structure with the number of poly-A particle capture extensions (Supplementary note S3).

Under ideal conditions, i.e. each hue value would be unmistakably recognised during the imaging process, the number of combinations in a typical image of our PUFs can be given by

$$\text{Number of combinations} = (\textit{Number of Hues})^{\textit{number of scattering spots}}$$

For the uncropped image (Fig. S20) of the PUF made with 1 µm spacing in Fig. 3f, with a field-of-view of 138 µm x 69 µm at 100x magnification, the number of combinations would be $152^{7,753} \approx 10^{16,915}$. Using the same imaging parameters for the uncropped image (Fig. S6) of a PUF made with 600 nm spacing (Fig. 1d), this number would increase to $160^{16,640} \approx 10^{36,676}$. The exponential increase in the number of combinations with increasing number of scattering spots places these objects in the category of strong PUFs.[27]

We tested the dependence of the hue value returned by our image analysis algorithm with respect to imaging conditions such as lamp intensities and exposure times and found minimal variation (see Table S5). In practical usage, binning similar hues to account for lighting differences would minimise the effect of this variation and make the imaging more robust. When using hue binning, the number of combinations can be given by

$$\text{Number of combinations} = (\textit{Number of Hue bins})^{\textit{number of scattering spots}}$$

We recorded a hue variation of ± 2 from a hue = 20 measured under our standard imaging conditions (Table S5). Using a conservative hue binning value of 5 would result in $10^{11,773}$ possible combinations for the 1 µm spacing sample (Fig. S20) and $10^{25,268}$ for the sample with 600 nm spacing (Fig. S6).
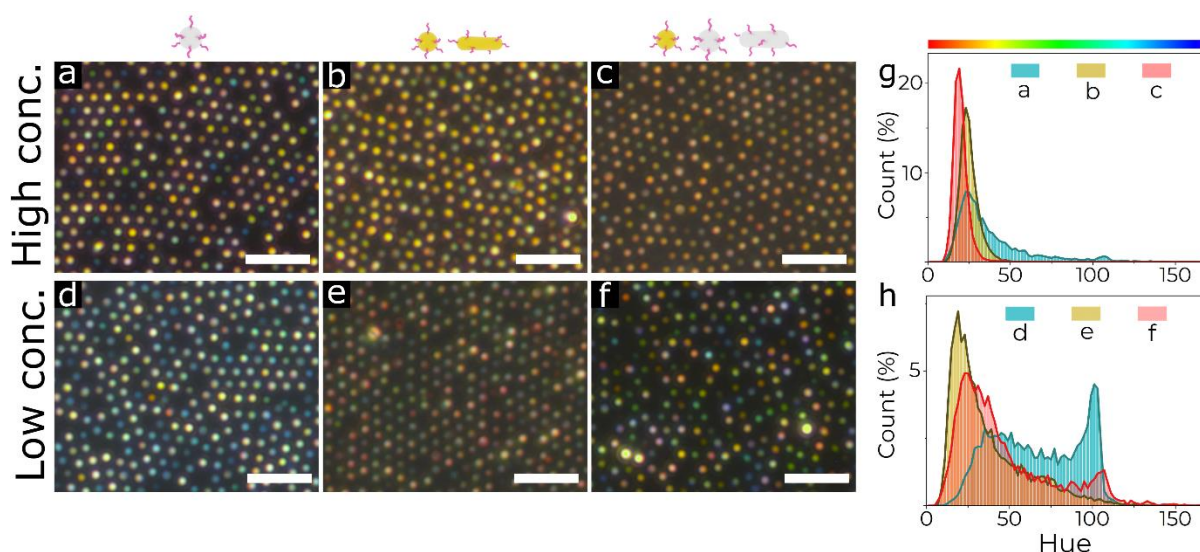
Figure 3. Hue analysis of PUFs. a-f) DFM images (full field-of-view in Fig. S15-20) of PUFs created while varying nanoparticle species and concentration. The nanoparticle species used are shown at the top of each column. g,h) Hue distribution of PUFs fabricated using different particle species at (g) higher and (h) lower concentrations, calculated from the full field-of-view images. Number of spots analysed for the histograms, n = 7700. For placement conditions, see Table S4. A hue scale corresponding to the x-axis is shown above the plots. Scale bars, 5 µm.

Enhancing security via anisotropic optical response
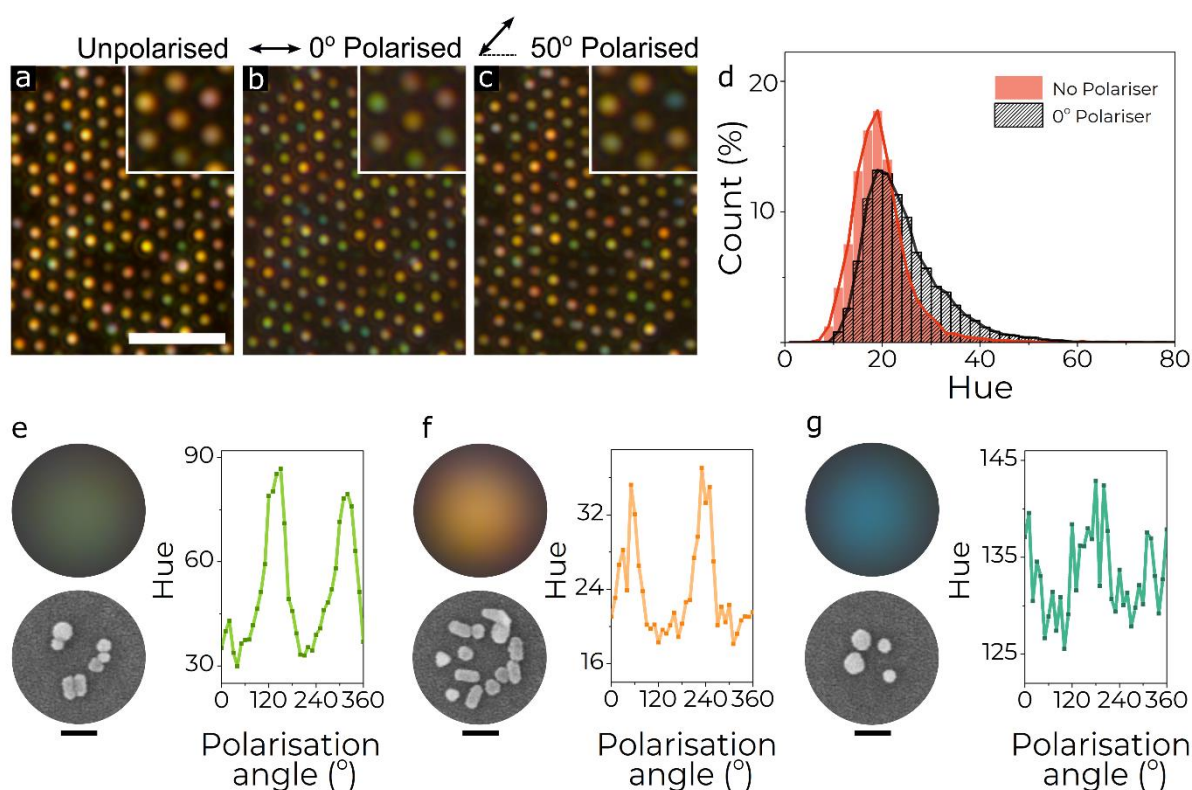
Figure 4. Polarisation-dependent behaviour of the PartiPUFs. a-c) DFM images of the same area at different polariser orientations. Insets show a magnified view of the same seven spots. Double-sided arrows depict the orientation of the polariser with respect to the image. d) Variation in hue distribution of PUFs in the presence of a polariser. e-g) Unpolarised DFM image (top), SEM image (bottom) and the polarisation-depended hue responses of three individual particle assemblies. Scale bars, (a-c) 5 µm, (e-g) 100 nm.

Asymmetric plasmonic particles, such as nanorods, possess longitudinal and transverse plasmon modes along their long and short axes respectively.[28] Therefore, they exhibit an angle-dependent scattering response when excited by polarised light.[29] This results in a polarisation-angle-dependent change in the scattering colour of the nanorods when viewed under DFM.[30,31] Additionally, plasmonic coupling can give rise to collective modes in assemblies of particles in close proximity, which also display such polarization-sensitive responses.[32] The nanoparticle assemblies in our PUFs display similar behaviour, resulting in a changing hue when imaged while varying the polarisation angle of the incident light (Fig. 4a-c). Additionally, the distribution of the hue values changes when imaged under static polarised illumination (Fig. 4d). We also observed that complex assemblies composed of multiple particles exhibit a variety of hue responses under changing polarisation illumination (Fig. 4e-g). SEM images reveal that the nanoparticle assemblies often contain multiple nanorods and spheres at varying distances from each other. In all cases, we see an angle-dependent hue response. These fall into two classes, those that show well-defined peaks (Fig. 4e,f) and those that show a more 'noisy' hue response (Fig. 4g). The former suggests that collective plasmonic modes of such assemblies possess a unique long-axis. However, this is

not intuitively evident from the arrangement of the particles within the assemblies. The polarisation-dependent hue response can enhance the security of the PUF by challenging the authenticator to reproduce the hue response at any arbitrary angle along with the unpolarised response. Accordingly, an attacker would need the ability to clone both responses to fool the authenticator.

Practical implementation of our PartiPUFs
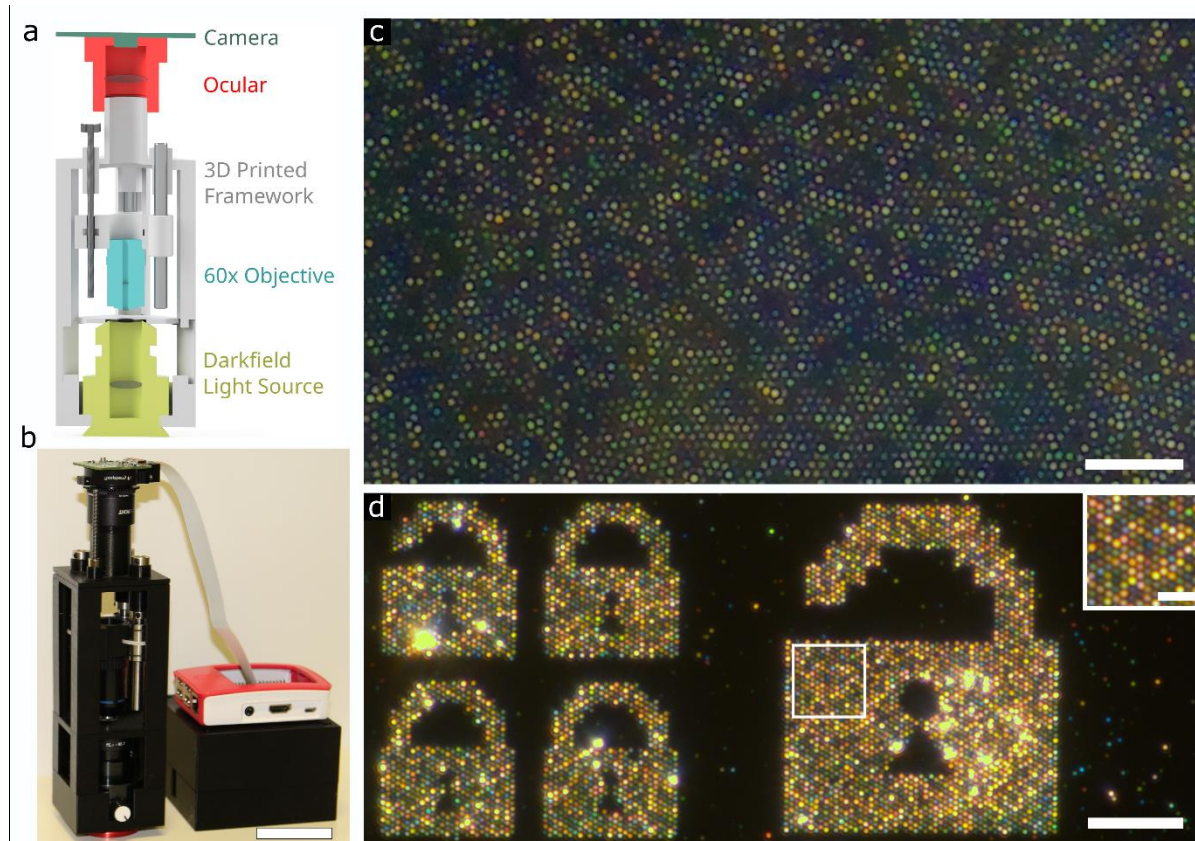
Figure 5. Practical implementation of the PartiPUFs. a) Schematic and b) realisation of a 3D-printed Dark Field microscope (3DFM). c) DFM image of the PUF in Fig. 3d (Fig. S18) taken with the 3DFM at 60x magnification. d) A PUF assembled using AuNS and AgNS on a 'lock' pattern with 600 nm spacing made by e-beam lithography. Inset: a magnified view showing the hexagonal array of scattering spots. Scale bars, (b) 5 cm, (c,d) 10 µm and inset 2.5 µm.

Unlike other high-security implementations of PUFs which require sophisticated and costly instruments to verify the tag, our PartiPUFs can be questioned with an inexpensive optical setup. To demonstrate this, we designed a simplified 3-D printed DFM, which we then used to image our PUFs. The 3-D printed DFM consists of a dark-field condenser, an achromatic 60x objective, an ocular lens and a 12-megapixel Raspberry Pi camera module (Fig. 5a,b). We used a 3D-printed framework to align the optical components in the horizontal direction. We can adjust the height of the dark-field condenser to ensure contact between the condenser, the immersion oil and the sample. The objective is connected to three steel rods, which are used to move it along the z-direction to allow for focusing. Using this setup, we imaged the PUF in Fig. 3d and were able to resolve the scattering spots and their hues (Fig. 5c). We

estimate that on a commercial scale a PartiPUF testing machine/read-out machine could be produced from components costing on the order of ~200 € (Supplementary note S6).

Our process is also compatible with other lithography methods such as e-beam or nanoimprint lithography which can form consistent and spatially variable placement pattern. This can be used to encode additional safety features or easily recognisable markers to locate the read-out region of the tag. To demonstrate this, we performed DOP and NPP on substrates patterned with e-beam lithography.[33,34] Figure 5d shows the DFM image of 'locks' made up of a hexagonal array of placement sites. Additionally, DOP has been shown to be compatible with techniques like nanoimprint lithography.[16] This would allow for printing of predefined patterns like product barcodes on which NPP can be performed, combining product data and authentication.

Conclusions

We have shown that self-assembly of plasmonic nanoparticles, driven by DNA origami, can be used to create nanoscale PUF labels with high information density. Our approach combines a unique optical response on the micron scale with information encoding on the nanoscale, which is accessible with a relatively simple and inexpensive optical microscope. To fabricate our PUF labels we used an approach that does not demand any sophisticated instrumentation and intrinsically generates unique objects because of the stochastic nature of their assembly. While each PUF labels is unique, we have shown we can control the range and distribution of accessible hue values of our PUFs. Because the optical response of each scattering site depends on the size, shape and composition of multiple nanoparticles, an attacker would have to first characterise a specific PUF with sophisticated instrumentation and then replicate it on the nanometre scale using several materials, which is infeasible even using top-end lithography manufacturing. We also show seamless integration of our PartiPUF with a cheap read-out tool in the form of a 3D-printed DFM, which significantly bridges the gap between experimental technology and its application.

AUTHOR CONTRIBUTIONS STATEMENT

T.L., U.R., G.P. and M.D. designed this study. M.D. and T.L. designed the DNA origami structures. M.D., L.R. and L.H. assembled and purified the DNA origami structures, synthesised and functionalised the nanoparticles and performed the placement experiments and their characterisation. C.P. wrote the ad-hoc image analysis script. C.P. and J.T. performed

the image analysis. G.P. and C.S. helped with dark field imaging. C.S. designed and fabricated the 3D-printed DFM and used it for imaging PUFs. I.M. designed the 'lock' patterns and performed e-beam lithography. M.D., G.P. and T.L. wrote the manuscript with input from all authors.

COMPETING INTERESTS STATEMENT

The authors declare no competing financial interest.

REFERENCES

1. OECD/EUIPO (2020), Trade in Counterfeit Pharmaceutical Products, Illicit Trade, OECD Publishing, Paris, https://doi.org/10.1787/a7c7e054-en.

2. Arppe, R. & Sørensen, T. J. Physical unclonable functions generated through chemical methods for anti-counterfeiting. *Nat Rev Chem* **1**, 1–13 (2017).

3. Pappu, R., Recht, B., Taylor, J. & Gershenfeld, N. Physical One-Way Functions. *Science* **297**, 2026–2030 (2002).

4. Gao, Y., Al-Sarawi, S. F. & Abbott, D. Physical unclonable functions. *Nat Electron* **3**, 81–91 (2020).

5. Hu, Z. *et al.* Physically unclonable cryptographic primitives using self-assembled carbon nanotubes. *Nature Nanotech* **11**, 559–565 (2016).

6. Zhang, J. *et al.* An all-in-one nanoprinting approach for the synthesis of a nanofilm library for unclonable anti-counterfeiting applications. *Nat. Nanotechnol.* 1–9 (2023) doi:10.1038/s41565-023-01405-3.

7. Kim, J. H. *et al.* Nanoscale physical unclonable function labels based on block copolymer self-assembly. *Nat Electron* **5**, 433–442 (2022).

8. Wang, L., Hasanzadeh Kafshgari, M. & Meunier, M. Optical Properties and Applications of Plasmonic-Metal Nanoparticles. *Advanced Functional Materials* **30**, 2005400 (2020).

9. Martens, K. *et al.* Onset of Chirality in Plasmonic Meta-Molecules and Dielectric Coupling. *ACS Nano* **16**, 16143–16149 (2022).

10. Rechberger, W. *et al.* Optical properties of two interacting gold nanoparticles. *Optics Communications* **220**, 137–141 (2003).

11. Jain, P. K., Eustis, S. & El-Sayed, M. A. Plasmon Coupling in Nanorod Assemblies: Optical Absorption, Discrete Dipole Approximation Simulation, and Exciton-Coupling Model. *J. Phys. Chem. B* **110**, 18243–18253 (2006).

12. Smith, A. F., Patton, P. & Skrabalak, S. E. Plasmonic Nanoparticles as a Physically Unclonable Function for Responsive Anti-Counterfeit Nanofingerprints. *Advanced Functional Materials* **26**, 1315–1321 (2016).

13. Lu, Y. *et al.* Plasmonic Physical Unclonable Function Labels Based on Tricolored Silver Nanoparticles: Implications for Anticounterfeiting Applications. *ACS Appl. Nano Mater.* **5**, 9298–9305 (2022).

14. Li, Q. *et al.* Physical Unclonable Anticounterfeiting Electrodes Enabled by Spontaneously Formed Plasmonic Core–Shell Nanoparticles for Traceable Electronics. *Advanced Functional Materials* **31**, 2010537 (2021).

15. Rothemund, P. W. K. Folding DNA to create nanoscale shapes and patterns. *Nature* **440**, 297–302 (2006).

16. Gopinath, A. & Rothemund, P. W. K. Optimized Assembly and Covalent Coupling of Single-Molecule DNA Origami Nanoarrays. *ACS Nano* **8**, 12030–12040 (2014).

17. Shetty, R. M., Brady, S. R., Rothemund, P. W. K., Hariadi, R. F. & Gopinath, A. Bench-Top Fabrication of Single-Molecule Nanoarrays by DNA Origami Placement. *ACS Nano* **15**, 11441–11450 (2021).

18. Deckman, H. W. & Dunsmuir, J. H. Natural lithography. *Applied Physics Letters* **41**, 377–379 (1982).

19. Haynes, C. L. & Van Duyne, R. P. Nanosphere Lithography: A Versatile Nanofabrication Tool for Studies of Size-Dependent Nanoparticle Optics. *J. Phys. Chem. B* **105**, 5599–5611 (2001).

20. Qiu, T. *et al.* Nanosphere Lithography: A Versatile Approach to Develop Transparent Conductive Films for Optoelectronic Applications. *Advanced Materials* **34**, 2103842 (2022).

21. Parchine, M., McGrath, J., Bardosova, M. & Pemble, M. E. Large Area 2D and 3D Colloidal Photonic Crystals Fabricated by a Roll-to-Roll Langmuir–Blodgett Method. *Langmuir* **32**, 5862–5869 (2016).

22. Tian, X., Zhou, Y., Thota, S., Zou, S. & Zhao, J. Plasmonic Coupling in Single Silver Nanosphere Assemblies by Polarization-Dependent Dark-Field Scattering Spectroscopy. *J. Phys. Chem. C* **118**, 13801–13808 (2014).

23. Nguyen, L. *et al.* Chiral Assembly of Gold–Silver Core–Shell Plasmonic Nanorods on DNA Origami with Strong Optical Activity. *ACS Nano* **14**, 7454–7461 (2020).

24. Dass, M., Kuen, L., Posnjak, G., Burger, S. & Liedl, T. Visible wavelength spectral tuning of absorption and circular dichroism of DNA-assembled Au/Ag core–shell nanorod assemblies. *Mater. Adv.* **3**, 3438–3445 (2022).

25. Rycenga, M. *et al.* Controlling the Synthesis and Assembly of Silver Nanostructures for Plasmonic Applications. *Chem. Rev.* **111**, 3669–3712 (2011).

26. Ringe, E., Sharma, B., Henry, A.-I., Marks, L. D. & Duyne, R. P. V. Single nanoparticle plasmonics. *Phys. Chem. Chem. Phys.* **15**, 4110–4129 (2013).

27. Rührmair, U., Devadas, S. & Koushanfar, F. Security Based on Physical Unclonability and Disorder. in *Introduction to Hardware Security and Trust* (eds. Tehranipoor, M. & Wang, C.) 65–102 (Springer New York, NY, 2012).

28. Chen, H., Shao, L., Li, Q. & Wang, J. Gold nanorods and their plasmonic properties. *Chem. Soc. Rev.* **42**, 2679–2724 (2013).

29. Bohren, C. F. & Huffman, D.R. *Absorption and Scattering of Light by Small Particles* (John Wiley & Sons, Ltd, 1998).

30. Liu, J. J. *et al.* The Accurate Imaging of Collective Gold Nanorods with a Polarization-Dependent Dark-Field Light Scattering Microscope. *Anal. Chem.* **95**, 1169–1175 (2023).

31. Huang, Y. & Kim, D.-H. Dark-field microscopy studies of polarization-dependent plasmonic resonance of single gold nanorods: rainbow nanoparticles. *Nanoscale* **3**, 3228–3232 (2011).

32. Roller, E.-M. *et al.* Hotspot-mediated non-dissipative and ultrafast plasmon passage. *Nature Phys* **13**, 761–765 (2017).

33. Kershner, R. J. *et al.* Placement and orientation of individual DNA shapes on lithographically patterned surfaces. *Nature Nanotechnology* **4**, 557–561 (2009).

34. Martynenko, I. V. *et al.* Site-directed placement of three-dimensional DNA origami. *Nat. Nanotechnol.* 1–7 (2023).

METHODS

DNA Origami design, preparation and purification

The DNA origami nanodisc was designed using cadnano[35]. Design details of the nanodisc can be found in the supplementary information.

Staple strands were purchased from IDT Technologies (HPLC purified, 200 µM each in water). Cadnano files and list of sequences of oligonucleotides can be found in the Supplementary Data. The scaffold strands (p8634) were produced from M13 phage replication in Escherichia coli. DNA origami structures were folded by mixing scaffold strands with an excess of staple strands in folding buffer (buffers used in this work can be found in the 'DNA origami placement (DOP)' section of the supplementary information). Samples were annealed in a PCR machine (Tetrad 2 Peltier thermal cycler, Bio-Rad) and purified from excess staples by agarose gel electrophoresis. A full description of the folding and purification of the DNA origami can be found in the supplementary information.

Preparation of DNA-coated AuNPs

30 nm gold nanospheres were purchased from BBI International. All nanorods were prepared in-house. The nanoparticles were functionalized with a mixture of 5'-thiolated 19 nt and 8 nt poly-T single-stranded DNA (Biomers). The particles were centrifuged, the supernatant was removed and the particles were resuspended in 0.1% SDS to ~15 O.D. (for nanorods) and ~10 O.D. (nanospheres) concentration. The particles were then mixed with a 1:9 mixture of T_{19} and T_8 thiolated single-stranded DNA (strand concentration 100 μM) in a nanoparticle suspension:DNA ratio of 3:2 (nanorods) or 3:1 (nanospheres) and frozen at -80° C for 30 min. After freezing, the functionalized particles were purified from excess DNA with gel electrophoresis in a 1% agarose gel ran for 90 min at 80 V. Particles were collected by cutting out the migrating band and squeezing out the liquid with the particles using a microscopy slide wrapped in parafilm. Specific staples in the nanodisc were modified with 10 nt poly-A extensions on the 3' ends (Fig. S1) to capture the nanoparticles.

Preparation of the substrates and DNA origami placement

Si/SiO2 substrates patterned with e-beam lithography were prepared by adapting the procedure from ref.[16] with slight modification. The 4-inch Si/SiO2 wafer with 100 nm thermal oxide (Microchemicals) was diced into 1 cm × 1 cm chips. Clean chips were primed with 10 mL of hexamethyldisilazane (HMDS) in a 4 L desiccator. The time of priming was optimised to maintain a Si/SiO_2 surface contact angle of 70°-75° after HMDS deposition. Binding sites were patterned into poly(methyl methacrylate) resist by electron-beam lithography. Examples of binding sites design are shown in figure S34. Then the chips were developed with a 1:3 solution of methyl isobutyl ketone (MIBK) and isopropanol (IPA). The HMDS in developed areas was removed with O2 plasma for 6 s in a plasma cleaner (PICO). The resist was stripped by ultrasonication in N-methyl pyrrolidone (NMP) at 50°C for 30 min. The substrates were briefly rinsed with 2-propanol, then dried in a nitrogen stream and used immediately.

Glass chips patterned via nanosphere lithography were prepared by adapting the procedure from ref.[17] 1 cm^2 glass chips were purchased from Plano-em. The polystyrene (PS) nanospheres with a diameter of 350 nm, 400 nm, 600 nm and 1μm (Thermo Scientific™ Nanosphere™ Size standards 3350A, 3400A, 3600A and 4010A respectively) were purified by centrifugation and resuspension in 50% ethanol/water. The PS nanospheres were drop-casted onto an O$_2$ plasma-activated chip surface and dried at a ~ 45° angle at RT, forming a close-packed monolayer/multilayer of nanospheres. The chips were then primed with 0.6 mL HMDS in a 1 L desiccator under a vacuum. The PS nanospheres were lifted off the surface by ultrasonication in water at RT for 5 min. Finally, the surface was blown dry with a nitrogen gun and baked at 120 °C for 5 min to stabilize the HMDS on the surface and used immediately.

Binding of DNA origami to the patterned substrates was achieved by depositing of a 60 μL drop of freshly folded and purified DNA origami in placement buffer to the surface of the chips. After incubation for 1 h at RT, excessive DNA origami was removed from the surface by 10 buffer replacement steps and purification with tween buffer. After this step, chips with placed DNA origami could be air dried, or nanoparticle placement could be performed. Air

drying of the chips was performed by treating the samples with an ethanol dilution series (see supplementary information for step by step protocols protocols).

Characterization techniques

UV-Vis spectroscopy. Extinction measurements for determination of DNA and nanoparticle concentrations were performed with a NanoDrop ND-1000 spectrophotometer (Thermo Scientific).

TEM imaging. 5 µL of a sample was incubated for 30 s – 5 min, depending on concentration, on glow-discharged TEM grids (formvar/carbon, 300 mesh Cu; Ted Pella) at room temperature. DNA origami samples were stained with a 2% uranyl formate aqueous solution containing 25 mM sodium hydroxide. Imaging was performed with a JEM1011 transmission electron microscope (JEOL) operated at 80 kV.

AFM imaging. The tapping-mode AFM of glass substrates was carried out on a Dimension ICON AFM instrument (Bruker). OTESPA silicon tips (300 kHz, Vecco Probes) were used for imaging in air. Images were analysed with Gwyddion software.

SEM imaging. The SEM instrument used in this work is the Raith eLINE SEM instrument. The beam settings for imaging are 10 kV acceleration and 20 µm aperture. The samples were imaged using the SEM after 20 s sputtering using an Edwards Sputter Coater S150B. The sputter target contained 60% gold and 40% palladium. The process parameters used for sputtering were 5 mbar Argon, 1.5 kV, 11 mA. Here 20 s of sputtering results in the deposition of a layer of gold/palladium with a thickness of a few nanometres. SEM imaging was performed on horizontal samples.

DATA AVAILABILITY

Data available upon request from authors.

METHODS-ONLY REFERENCES

35. Douglas, S. M. *et al.* Rapid prototyping of 3D DNA-origami shapes with caDNAno. *Nucleic Acids Research* **37**, 5001–5006 (2009).

6. OUTLOOK

This thesis has explored the potential of DNA nanotechnology, particularly DNA origami, for engineering the optical response of plasmonic nanoparticle assemblies. The research primarily focused on two key areas: chiral plasmonics and physical unclonable functions (PUFs).

A novel method for the synthesis of silver-gold core-shell nanorods was developed. This approach offers precise control over size, aspect ratio, and silver shell thickness, leading to tunable optical properties. The functionalization of these nanoparticles with DNA enhanced their stability and enabled their specific arrangement into chiral geometries via DNA origami, providing a spectral control over the circular dichroic signal. Recently, the application of plasmonic enhancement to act as a photocatalyst has received attention.[129,151] One way plasmonic systems achieve this is by generating and donating excited (hot) charge carriers to the reacting species[152], a process which can be boosted by enhancing the induced field in the plasmonic nanoparticle, such as the creation of hot spots.[153] It has been predicted that the chirality in plasmonic systems can lead to related CD effects in photochemical reactions[152], which opens up new opportunities for their applications in plasmon-induced photocatalysis and solar energy conversion.[154]
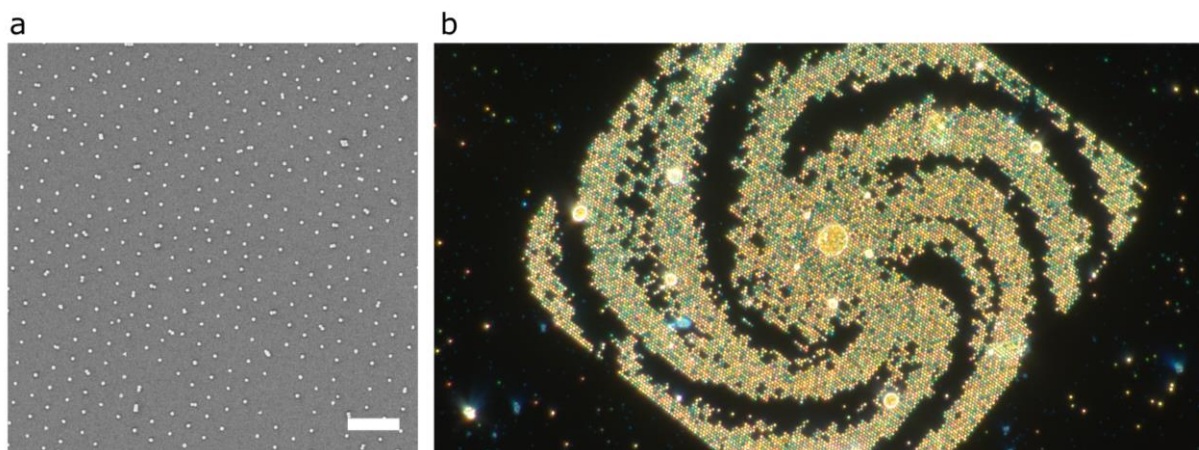
Figure 22. Future outlook of nanoparticle placement. a) Uniform single-particle placement. b) A 'nanoGalaxy' created using nanoparticle placement on patterns made using e-beam lithography. Scale bar, (a) 1 μm.

In response to the limitations of optical cryptographic methods, this thesis introduced a novel type of optical PUF. Combining DNA origami with nanosphere lithography, a high-security, unclonable tag was created. These PUFs exhibited a broad range of hues due to strong plasmonic coupling, thereby enhancing their security features. Moreover, a cost-effective 3D-printed read-out tool was developed to facilitate practical implementation. Further work needs to be done to maximise the long-term stability of the PUFs, for instance by coating the labels with polymer films which do not interfere with DFM imaging. During nanoparticle placement experiments, we were also able to make surfaces with uniform single-particle placement over large areas (Fig. 22a), although reproducible fabrication of such surfaces will need further optimisation. Such surfaces could be used to plasmonic surface lattices, with the programmable nature of DNA origami

allowing the user to create geometries with nanoscale precision.[155] Using e-beam lithography, we were able to create brightly scattering patterns made of nanoparticles placed using the same method as for PUF fabrication (Fig. 22b). Combined with lithographic techniques, our approach could be used to build metasurfaces for both fundamental studies as well as to develop new colouration techniques for vivid digital displays driven by the strong light-interactions of plasmonic nanoparticles.[156]

Note

ChatGPT (Oct 2023 version) from OpenAI was used to edit some parts of the text.

References

1. Eigler, D. M. & Schweizer, E. K. Positioning single atoms with a scanning tunnelling microscope. *Nature* **344**, 524–526 (1990).

2. Seeman, N. C. Nucleic acid junctions and lattices. *Journal of Theoretical Biology* **99**, 237–247 (1982).

3. Kallenbach, N. R., Ma, R.-I. & Seeman, N. C. An immobile nucleic acid junction constructed from oligonucleotides. *Nature* **305**, 829–831 (1983).

4. Chen, J. & Seeman, N. C. Synthesis from DNA of a molecule with the connectivity of a cube. *Nature* **350**, 631–633 (1991).

5. Fu, T. J. & Seeman, N. C. DNA double-crossover molecules. *Biochemistry* **32**, 3211–3220 (1993).

6. LaBean, T. H. *et al.* Construction, Analysis, Ligation, and Self-Assembly of DNA Triple Crossover Complexes. *J. Am. Chem. Soc.* **122**, 1848–1860 (2000).

7. Yan, H., Park, S. H., Finkelstein, G., Reif, J. H. & LaBean, T. H. DNA-Templated Self-Assembly of Protein Arrays and Highly Conductive Nanowires. *Science* **301**, 1882–1884 (2003).

8. He, Y. *et al.* Hierarchical self-assembly of DNA into symmetric supramolecular polyhedra. *Nature* **452**, 198–201 (2008).

9. Rothemund, P. W. K. *et al.* Design and Characterization of Programmable DNA Nanotubes. *J. Am. Chem. Soc.* **126**, 16344–16352 (2004).

10. Winfree, E., Liu, F., Wenzler, L. A. & Seeman, N. C. Design and self-assembly of two-dimensional DNA crystals. *Nature* **394**, 539–544 (1998).

11.   Um, S. H. *et al.* Enzyme-catalysed assembly of DNA hydrogel. *Nature Mater* **5**, 797–801 (2006).

12.   Zheng, J. *et al.* From molecular to macroscopic via the rational design of a self-assembled 3D

DNA crystal. *Nature* **461**, 74–77 (2009).

13.   Rothemund, P. W. K. Folding DNA to create nanoscale shapes and patterns. *Nature* **440**, 297–302

(2006).

14.   Douglas, S. M. *et al.* Self-assembly of DNA into nanoscale three-dimensional shapes. *Nature* **459**,

414–418 (2009).

15.   Douglas, S. M. *et al.* Rapid prototyping of 3D DNA-origami shapes with caDNAno. *Nucleic Acids

Research* **37**, 5001–5006 (2009).

16.   Williams, S. *et al.* Tiamat: A Three-Dimensional Editing Tool for Complex DNA Structures. in *DNA

Computing* (eds. Goel, A., Simmel, F. C. & Sosík, P.) 90–101 (Springer, 2009). doi:10.1007/978-3-642-

03076-5_8.

17.   Andersen, E. S. *et al.* DNA Origami Design of Dolphin-Shaped Structures with Flexible Tails. *ACS

Nano* **2**, 1213–1218 (2008).

18.   Benson, E. *et al.* DNA rendering of polyhedral meshes at the nanoscale. *Nature* **523**, 441–444

(2015).

19.   Veneziano, R. *et al.* Designer nanoscale DNA assemblies programmed from the top down.

Science **352**, 1534–1534 (2016).

20.   Jun, H. *et al.* Automated Sequence Design of 3D Polyhedral Wireframe DNA Origami with

Honeycomb Edges. *ACS Nano* **13**, 2083–2093 (2019).

21.   Jun, H. *et al.* Rapid prototyping of arbitrary 2D and 3D wireframe DNA origami. *Nucleic Acids

Research* **49**, 10265–10274 (2021).

22.   de Llano, E. *et al.* Adenita: interactive 3D modelling and visualization of DNA nanostructures.

Nucleic Acids Research **48**, 8269–8275 (2020).

23.   Kuzyk, A. *et al.* DNA-based self-assembly of chiral plasmonic nanostructures with tailored optical response. *Nature* **483**, 311–314 (2012).

24.   Hentschel, M., Schäferling, M., Weiss, T., Liu, N. & Giessen, H. Three-Dimensional Chiral Plasmonic Oligomers. *Nano Lett.* **12**, 2542–2547 (2012).

25.   Fang, W. *et al.* Quantizing single-molecule surface-enhanced Raman scattering with DNA origami metamolecules. *Science Advances* **5**, eaau4506 (2019).

26.   Acuna, G. P. *et al.* Fluorescence Enhancement at Docking Sites of DNA-Directed Self-Assembled Nanoantennas. *Science* **338**, 506–510 (2012).

27.   Maune, H. T. *et al.* Self-assembly of carbon nanotubes into two-dimensional geometries using DNA origami templates. *Nature Nanotech* **5**, 61–66 (2010).

28.   Ouyang, X. *et al.* Docking of Antibodies into the Cavities of DNA Origami Structures. *Angewandte Chemie International Edition* **56**, 14423–14427 (2017).

29.   Shaw, A. *et al.* Binding to nanopatterned antigens is dominated by the spatial tolerance of antibodies. *Nature Nanotechnology* **14**, 184–190 (2019).

30.   Wang, S.-T. *et al.* Designed and biologically active protein lattices. *Nat Commun* **12**, 3702 (2021).

31.   Ke, G. *et al.* Directional Regulation of Enzyme Pathways through the Control of Substrate Channeling on a DNA Origami Scaffold. *Angewandte Chemie International Edition* **55**, 7483–7486 (2016).

32.   Zhao, Z. *et al.* Nanocaged enzymes with enhanced catalytic activity and increased stability against protease digestion. *Nat Commun* **7**, 10619 (2016).

33.   Kopperger, E., Pirzer, T. & Simmel, F. C. Diffusive Transport of Molecular Cargo Tethered to a DNA Origami Platform. *Nano Lett.* **15**, 2693–2699 (2015).

34.   Hariadi, R. F., Cale, M. & Sivaramakrishnan, S. Myosin lever arm directs collective motion on cellular actin network. *Proceedings of the National Academy of Sciences* **111**, 4091–4096 (2014).

35. Iwaki, M., Wickham, S. F., Ikezaki, K., Yanagida, T. & Shih, W. M. A programmable DNA origami nanospring that reveals force-induced adjacent binding of myosin VI heads. *Nat Commun* **7**, 13715 (2016).

36. Funke, J. J. *et al.* Uncovering the forces between nucleosomes using DNA origami. *Science Advances* **2**, e1600974 (2016).

37. Suzuki, Y. *et al.* Direct analysis of Holliday junction resolving enzyme in a DNA origami nanostructure. *Nucleic Acids Research* **42**, 7421–7428 (2014).

38. Zhang, T. *et al.* 3D DNA Origami Crystals. *Advanced Materials* **30**, 1800273 (2018).

39. Wang, Y. *et al.* DNA origami single crystals with Wulff shapes. *Nat Commun* **12**, 3011 (2021).

40. Dai, L. *et al.* Programming the morphology of DNA origami crystals by magnesium ion strength. *Proceedings of the National Academy of Sciences* **120**, e2302142120 (2023).

41. Liu, X. *et al.* Complex silica composite nanomaterials templated with DNA origami. *Nature* **559**, 593–598 (2018).

42. Nguyen, L., Döblinger, M., Liedl, T. & Heuer-Jungemann, A. DNA-Origami-Templated Silica Growth by Sol–Gel Chemistry. *Angewandte Chemie International Edition* **58**, 912–916 (2019).

43. Shani, L. *et al.* DNA-assembled superconducting 3D nanoscale architectures. *Nat Commun* **11**, 5697 (2020).

44. Kopperger, E. *et al.* A self-assembled nanoscale robotic arm controlled by electric fields. *Science* **359**, 296–301 (2018).

45. Pumm, A.-K. *et al.* A DNA origami rotary ratchet motor. *Nature* **607**, 492–498 (2022).

46. Kershner, R. J. *et al.* Placement and orientation of individual DNA shapes on lithographically patterned surfaces. *Nature Nanotechnology* **4**, 557–561 (2009).

47. Gopinath, A. & Rothemund, P. W. K. Optimized Assembly and Covalent Coupling of Single-Molecule DNA Origami Nanoarrays. *ACS Nano* **8**, 12030–12040 (2014).

48.   Gopinath, A. *et al.* Absolute and arbitrary orientation of single-molecule shapes. *Science* **371**, eabd6179 (2021).

49.   Shetty, R. M., Brady, S. R., Rothemund, P. W. K., Hariadi, R. F. & Gopinath, A. Bench-Top Fabrication of Single-Molecule Nanoarrays by DNA Origami Placement. *ACS Nano* **15**, 11441–11450 (2021).

50.   Shen, B. *et al.* Plasmonic nanostructures through DNA-assisted lithography. *Science Advances* **4**, eaap8978 (2018).

51.   Dahm, R. Discovering DNA: Friedrich Miescher and the early years of nucleic acid research. *Hum Genet* **122**, 565–581 (2008).

52.   Griffith, F. The Significance of Pneumococcal Types. *Epidemiology & Infection* **27**, 113–159 (1928).

53.   Avery, O. T., MacLeod, C. M. & McCarty, M. STUDIES ON THE CHEMICAL NATURE OF THE SUBSTANCE INDUCING TRANSFORMATION OF PNEUMOCOCCAL TYPES : INDUCTION OF TRANSFORMATION BY A DESOXYRIBONUCLEIC ACID FRACTION ISOLATED FROM PNEUMOCOCCUS TYPE III. *Journal of Experimental Medicine* **79**, 137–158 (1944).

54.   Franklin, R. E. & Gosling, R. G. The structure of sodium thymonucleate fibres. I. The influence of water content. *Acta Crystallographica* **6**, 673–677 (1953).

55.   Franklin, R. E. & Gosling, R. G. Molecular Configuration in Sodium Thymonucleate. *Nature* **171**, 740–741 (1953).

56.   Watson, J. D. & Crick, F. H. C. Molecular Structure of Nucleic Acids: A Structure for Deoxyribose Nucleic Acid. *Nature* **171**, 737–738 (1953).

57.   Brenner, S., Jacob, F. & Meselson, M. An Unstable Intermediate Carrying Information from Genes to Ribosomes for Protein Synthesis. *Nature* **190**, 576–581 (1961).

58.   Gros, F. *et al.* Unstable Ribonucleic Acid Revealed by Pulse Labelling of Escherichia Coli. *Nature* **190**, 581–585 (1961).

59. Lucas, A. A. A-DNA and B-DNA: Comparing Their Historical X-ray Fiber Diffraction Images. *J. Chem. Educ.* **85**, 737 (2008).

60. Cho, Y., Park, S. H., Huh, J.-H., Gopinath, A. & Lee, S. DNA as grabbers and steerers of quantum emitters. *Nanophotonics* **12**, 399–412 (2023).

61. Andersen, E. S. *et al.* Self-assembly of a nanoscale DNA box with a controllable lid. *Nature* **459**, 73–76 (2009).

62. Ke, Y. *et al.* Multilayer DNA Origami Packed on a Square Lattice. *J. Am. Chem. Soc.* **131**, 15903–15908 (2009).

63. Ke, Y., Voigt, N. V., Gothelf, K. V. & Shih, W. M. Multilayer DNA Origami Packed on Hexagonal and Hybrid Lattices. *J. Am. Chem. Soc.* **134**, 1770–1774 (2012).

64. Dietz, H., Douglas, S. M. & Shih, W. M. Folding DNA into Twisted and Curved Nanoscale Shapes. *Science* **325**, 725–730 (2009).

65. Han, D. *et al.* DNA Origami with Complex Curvatures in Three-Dimensional Space. *Science* **332**, 342–346 (2011).

66. Gerling, T., Wagenbauer, K. F., Neuner, A. M. & Dietz, H. Dynamic DNA devices and assemblies formed by shape-complementary, non–base pairing 3D components. *Science* **347**, 1446–1452 (2015).

67. Wagenbauer, K. F., Sigl, C. & Dietz, H. Gigadalton-scale shape-programmable DNA assemblies. *Nature* **552**, 78–83 (2017).

68. Sigl, C. *et al.* Programmable icosahedral shell system for virus trapping. *Nat. Mater.* **20**, 1281–1289 (2021).

69. Liu, W., Zhong, H., Wang, R. & Seeman, N. C. Crystalline Two-Dimensional DNA-Origami Arrays. *Angewandte Chemie International Edition* **50**, 264–267 (2011).

70. Tikhomirov, G., Petersen, P. & Qian, L. Fractal assembly of micrometre-scale DNA origami arrays with arbitrary patterns. *Nature* **552**, 67–71 (2017).

71.   Kocabey, S. *et al.* Membrane-Assisted Growth of DNA Origami Nanostructure Arrays. *ACS Nano* **9**, 3530–3539 (2015).

72.   Suzuki, Y., Endo, M. & Sugiyama, H. Lipid-bilayer-assisted two-dimensional self-assembly of DNA origami nanostructures. *Nat Commun* **6**, 8052 (2015).

73.   Liu, W. *et al.* Diamond family of nanoparticle superlattices. *Science* **351**, 582–586 (2016).

74.   Thubagere, A. J. *et al.* A cargo-sorting DNA robot. *Science* **357**, eaan6558 (2017).

75.   Shi, X. *et al.* A DNA turbine powered by a transmembrane potential across a nanopore. *Nat. Nanotechnol.* 1–7 (2023) doi:10.1038/s41565-023-01527-8.

76.   Martynenko, I. V. *et al.* Site-directed placement of three-dimensional DNA origami. *Nat. Nanotechnol.* 1–7 (2023) doi:10.1038/s41565-023-01487-z.

77.   Gopinath, A., Miyazono, E., Faraon, A. & Rothemund, P. W. K. Engineering and mapping nanocavity emission via precision placement of DNA origami. *Nature* **535**, 401–405 (2016).

78.   Prodan, E., Radloff, C., Halas, N. J. & Nordlander, P. A Hybridization Model for the Plasmon Response of Complex Nanostructures. *Science* **302**, 419–422 (2003).

79.   Pauling, Linus. THE NATURE OF THE CHEMICAL BOND. II. THE ONE-ELECTRON BOND AND THE THREE-ELECTRON BOND. *J. Am. Chem. Soc.* **53**, 3225–3237 (1931).

80.   Prodan, E. & Nordlander, P. Structural Tunability of the Plasmon Resonances in Metallic Nanoshells. *Nano Lett.* **3**, 543–547 (2003).

81.   Jain, P. K., Eustis, S. & El-Sayed, M. A. Plasmon Coupling in Nanorod Assemblies: Optical Absorption, Discrete Dipole Approximation Simulation, and Exciton-Coupling Model. *J. Phys. Chem. B* **110**, 18243–18253 (2006).

82.   Funston, A. M., Novo, C., Davis, T. J. & Mulvaney, P. Plasmon Coupling of Gold Nanorods at Short Distances and in Different Geometries. *Nano Lett.* **9**, 1651–1658 (2009).

83.   Slaughter, L. S., Wu, Y., Willingham, B. A., Nordlander, P. & Link, S. Effects of Symmetry Breaking and Conductive Contact on the Plasmon Coupling in Gold Nanorod Dimers. *ACS Nano* **4**, 4657–4666 (2010).

84.   Yin, X., Schäferling, M., Metzger, B. & Giessen, H. Interpreting Chiral Nanophotonic Spectra: The Plasmonic Born–Kuhn Model. *Nano Lett.* **13**, 6238–6243 (2013).

85.   Govorov, A. O. *et al.* Chiral nanoparticle assemblies: circular dichroism, plasmonic interactions, and exciton effects. *J. Mater. Chem.* **21**, 16806–16818 (2011).

86.   Classical Electrodynamics, 3rd Edition | Wiley. *Wiley.com* https://www.wiley.com/en-us/Classical+Electrodynamics%2C+3rd+Edition-p-9780471309321.

87.   Absorption and Scattering of Light by Small Particles | Wiley. *Wiley.com* https://www.wiley.com/en-sg/Absorption+and+Scattering+of+Light+by+Small+Particles-p-9780471293408.

88.   Front Matter. in *The Scattering of Light and Other Electromagnetic Radiation* (ed. Kerker, M.) vol. 16 iii (Academic Press, 1969).

89.   Willets, K. A. & Van Duyne, R. P. Localized Surface Plasmon Resonance Spectroscopy and Sensing. *Annual Review of Physical Chemistry* **58**, 267–297 (2007).

90.   Schuller, J. A. *et al.* Plasmonics for extreme light concentration and manipulation. *Nature Mater* **9**, 193–204 (2010).

91.   Luk'yanchuk, B. *et al.* The Fano resonance in plasmonic nanostructures and metamaterials. *Nature Mater* **9**, 707–715 (2010).

92.   Goring, C. R., Goring, C. R. & Pritchard, A. *Micrographia : containing practical essays on reflecting, solar, oxy-hydrogen gas microscopes; micrometers; eye-pieces, &c. &c.* (Whitaker and Co, 1837). doi:10.5962/bhl.title.51379.

93.   Frontmatter. in *Fundamentals of Light Microscopy and Electronic Imaging* i–xiii (John Wiley & Sons, Ltd, 2012). doi:10.1002/9781118382905.fmatter.

94.   *Handbook Of Biological Confocal Microscopy*. (Springer US, 2006). doi:10.1007/978-0-387-45524-2.

95.   Mertz, J. Introduction to Optical Microscopy. *Higher Education from Cambridge University Press* https://www.cambridge.org/highereducation/books/introduction-to-optical-microscopy/F6C6318C87732519D7E07BA7A03F0B81 (2019) doi:10.1017/9781108552660.

96.   Jain, P. K., Huang, W. & El-Sayed, M. A. On the Universal Scaling Behavior of the Distance Decay of Plasmon Coupling in Metal Nanoparticle Pairs: A Plasmon Ruler Equation. *Nano Lett.* **7**, 2080–2088 (2007).

97.   Sönnichsen, C., Reinhard, B. M., Liphardt, J. & Alivisatos, A. P. A molecular ruler based on plasmon coupling of single gold and silver nanoparticles. *Nat Biotechnol* **23**, 741–745 (2005).

98.   Nie, S. & Emory, S. R. Probing Single Molecules and Single Nanoparticles by Surface-Enhanced Raman Scattering. *Science* **275**, 1102–1106 (1997).

99.   Falke, J. J., Bass, R. B., Butler, S. L., Chervitz, S. A. & Danielson, M. A. THE TWO-COMPONENT SIGNALING PATHWAY OF BACTERIAL CHEMOTAXIS: A Molecular View of Signal Transduction by Receptors, Kinases, and Adaptation Enzymes. *Annual Review of Cell and Developmental Biology* **13**, 457–512 (1997).

100.   Hartl, C. *et al.* Position Accuracy of Gold Nanoparticles on DNA Origami Structures Studied with Small-Angle X-ray Scattering. *Nano Letters* **18**, 2609–2615 (2018).

101.   Nguyen, L. *et al.* Chiral Assembly of Gold–Silver Core–Shell Plasmonic Nanorods on DNA Origami with Strong Optical Activity. *ACS Nano* **14**, 7454–7461 (2020).

102.   Dass, M., Gür, F. N., Kołątaj, K., Urban, M. J. & Liedl, T. DNA Origami-Enabled Plasmonic Sensing. *J. Phys. Chem. C* **125**, 5969–5981 (2021).

103.   Schreiber, R. *et al.* Hierarchical assembly of metal nanoparticles, quantum dots and organic dyes using DNA origami scaffolds. *Nature Nanotechnology* **9**, 74–78 (2014).

104. Acuna, G. P. *et al.* Distance Dependence of Single-Fluorophore Quenching by Gold Nanoparticles Studied on DNA Origami. *ACS Nano* **6**, 3189–3195 (2012).

105. Dulkeith, E. *et al.* Gold Nanoparticles Quench Fluorescence by Phase Induced Radiative Rate Suppression. *Nano Lett.* **5**, 585–589 (2005).

106. Anger, P., Bharadwaj, P. & Novotny, L. Enhancement and Quenching of Single-Molecule Fluorescence. *Physical Review Letters* **96**, 113002 (2006).

107. Pfeiffer, M. *et al.* Single antibody detection in a DNA origami nanoantenna. *iScience* **24**, 103072 (2021).

108. Ochmann, S. E. *et al.* Optical Nanoantenna for Single Molecule-Based Detection of Zika Virus Nucleic Acids without Molecular Multiplication. *Analytical Chemistry* **89**, 13000–13007 (2017).

109. Kaminska, I., Bohlen, J., Mackowski, S., Tinnefeld, P. & Acuna, G. P. Strong Plasmonic Enhancement of a Single Peridinin–Chlorophyll a–Protein Complex on DNA Origami-Based Optical Antennas. *ACS Nano* **12**, 1650–1655 (2018).

110. Thacker, V. V. *et al.* DNA origami based assembly of gold nanoparticle dimers for surface-enhanced Raman scattering. *Nat Commun* **5**, 3448 (2014).

111. Simoncelli, S. *et al.* Quantitative Single-Molecule Surface-Enhanced Raman Scattering by Optothermal Tuning of DNA Origami-Assembled Plasmonic Nanoantennas. *ACS Nano* **10**, 9809–9815 (2016).

112. Zhan, P. *et al.* DNA Origami Directed Assembly of Gold Bowtie Nanoantennas for Single-Molecule Surface-Enhanced Raman Scattering. *Angewandte Chemie International Edition* **57**, 2846–2850 (2018).

113. *Circular Dichroism and the Conformational Analysis of Biomolecules*. (Springer US, 1996). doi:10.1007/978-1-4757-2508-7.

114. Fan, Z. & Govorov, A. O. Plasmonic Circular Dichroism of Chiral Metal Nanoparticle Assemblies. *Nano Lett.* **10**, 2580–2587 (2010).

115.   Funck, T., Nicoli, F., Kuzyk, A. & Liedl, T. Sensing Picomolar Concentrations of RNA Using Switchable Plasmonic Chirality. *Angewandte Chemie* **130**, 13683–13686 (2018).

116.   Zhou, C., Xin, L., Duan, X., Urban, M. J. & Liu, N. Dynamic Plasmonic System That Responds to Thermal and Aptamer-Target Regulations. *Nano Lett.* **18**, 7395–7399 (2018).

117.   Kuzyk, A. *et al.* A light-driven three-dimensional plasmonic nanosystem that translates molecular motion into reversible chiroptical function. *Nat Commun* **7**, 10591 (2016).

118.   Liu, Q., Kuzyk, A., Endo, M. & Smalyukh, I. I. Colloidal plasmonic DNA-origami with photo-switchable chirality in liquid crystals. *Opt. Lett., OL* **44**, 2831–2834 (2019).

119.   Jiang, Q. *et al.* Stimulus-Responsive Plasmonic Chiral Signals of Gold Nanorods Organized on DNA Origami. *Nano Lett.* **17**, 7125–7130 (2017).

120.   Lamarre, J.-M. *et al.* Anisotropic nonlinear optical absorption of gold nanorods in a silica matrix. *Optics Communications* **281**, 331–340 (2008).

121.   Haiss, W., Thanh, N. T. K., Aveyard, J. & Fernig, D. G. Determination of Size and Concentration of Gold Nanoparticles from UV–Vis Spectra. *Anal. Chem.* **79**, 4215–4221 (2007).

122.   Scarabelli, L., Sánchez-Iglesias, A., Pérez-Juste, J. & Liz-Marzán, L. M. A "Tips and Tricks" Practical Guide to the Synthesis of Gold Nanorods. *J. Phys. Chem. Lett.* **6**, 4270–4279 (2015).

123.   González-Rubio, G. *et al.* Disconnecting Symmetry Breaking from Seeded Growth for the Reproducible Synthesis of High Quality Gold Nanorods. *ACS Nano* **13**, 4424–4435 (2019).

124.   Thompson, D. G., Enright, A., Faulds, K., Smith, W. E. & Graham, D. Ultrasensitive DNA Detection Using Oligonucleotide–Silver Nanoparticle Conjugates. *Anal. Chem.* **80**, 2805–2810 (2008).

125.   West, P. r. *et al.* Searching for better plasmonic materials. *Laser & Photonics Reviews* **4**, 795–808 (2010).

126.   Becker, J. *et al.* Plasmonic Focusing Reduces Ensemble Linewidth of Silver-Coated Gold Nanorods. *Nano Lett.* **8**, 1719–1723 (2008).

127. Dass, M., Kuen, L., Posnjak, G., Burger, S. & Liedl, T. Visible wavelength spectral tuning of absorption and circular dichroism of DNA-assembled Au/Ag core–shell nanorod assemblies. *Mater. Adv.* **3**, 3438–3445 (2022).

128. Singh, M. P. & Strouse, G. F. Involvement of the LSPR Spectral Overlap for Energy Transfer between a Dye and Au Nanoparticle. *J. Am. Chem. Soc.* **132**, 9383–9391 (2010).

129. Khorashad, L. K. *et al.* Hot Electrons Generated in Chiral Plasmonic Nanocrystals as a Mechanism for Surface Photochemistry and Chiral Growth. *J. Am. Chem. Soc.* **142**, 4193–4205 (2020).

130. Inside front cover. *Mater. Adv.* **3**, 3336–3336 (2022).

131. Intellectual Property Crime Threat Assessment 2022. *Europol* https://www.europol.europa.eu/publications-events/publications/intellectual-property-crime-threat-assessment-2022.

132. WHO Member State Mechanism on Substandard and Falsified Medical Products. https://www.who.int/publications-detail-redirect/WHO-MVP-EMP-SAV-2019.04.

133. Rivest, R. L., Shamir, A. & Adleman, L. A method for obtaining digital signatures and public-key cryptosystems. *Commun. ACM* **21**, 120–126 (1978).

134. Shor, P. W. Polynomial-Time Algorithms for Prime Factorization and Discrete Logarithms on a Quantum Computer. *SIAM J. Comput.* **26**, 1484–1509 (1997).

135. Rührmair, U., Devadas, S. & Koushanfar, F. Security Based on Physical Unclonability and Disorder. in *Introduction to Hardware Security and Trust* (eds. Tehranipoor, M. & Wang, C.) 65–102 (Springer, 2012). doi:10.1007/978-1-4419-8080-9_4.

136. Gao, Y., Al-Sarawi, S. F. & Abbott, D. Physical unclonable functions. *Nat Electron* **3**, 81–91 (2020).

137. Pappu, R., Recht, B., Taylor, J. & Gershenfeld, N. Physical One-Way Functions. *Science* **297**, 2026–2030 (2002).

138. Arppe, R. & Sørensen, T. J. Physical unclonable functions generated through chemical methods for anti-counterfeiting. *Nat Rev Chem* **1**, 1–13 (2017).

139.   Hu, Z. *et al.* Physically unclonable cryptographic primitives using self-assembled carbon nanotubes. *Nature Nanotech* **11**, 559–565 (2016).

140.   Zhang, J. *et al.* An all-in-one nanoprinting approach for the synthesis of a nanofilm library for unclonable anti-counterfeiting applications. *Nat. Nanotechnol.* 1–9 (2023) doi:10.1038/s41565-023-01405-3.

141.   Kim, J. H. *et al.* Nanoscale physical unclonable function labels based on block copolymer self-assembly. *Nat Electron* **5**, 433–442 (2022).

142.   Smith, A. F., Patton, P. & Skrabalak, S. E. Plasmonic Nanoparticles as a Physically Unclonable Function for Responsive Anti-Counterfeit Nanofingerprints. *Advanced Functional Materials* **26**, 1315–1321 (2016).

143.   Lu, Y. *et al.* Plasmonic Physical Unclonable Function Labels Based on Tricolored Silver Nanoparticles: Implications for Anticounterfeiting Applications. *ACS Appl. Nano Mater.* **5**, 9298–9305 (2022).

144.   Li, Q. *et al.* Physical Unclonable Anticounterfeiting Electrodes Enabled by Spontaneously Formed Plasmonic Core–Shell Nanoparticles for Traceable Electronics. *Advanced Functional Materials* **31**, 2010537 (2021).

145.   Dass, M. *et al.* Self-assembled physical unclonable function labels based on plasmonic coupling. *Arxiv*, https://doi.org/10.48550/arXiv.2310.19587 (2023).

146.   Deckman, H. W. & Dunsmuir, J. H. Natural lithography. *Applied Physics Letters* **41**, 377–379 (1982).

147.   Haynes, C. L. & Van Duyne, R. P. Nanosphere Lithography: A Versatile Nanofabrication Tool for Studies of Size-Dependent Nanoparticle Optics. *J. Phys. Chem. B* **105**, 5599–5611 (2001).

148.   Qiu, T. *et al.* Nanosphere Lithography: A Versatile Approach to Develop Transparent Conductive Films for Optoelectronic Applications. *Advanced Materials* **34**, 2103842 (2022).

149.   Parchine, M., McGrath, J., Bardosova, M. & Pemble, M. E. Large Area 2D and 3D Colloidal

Photonic Crystals Fabricated by a Roll-to-Roll Langmuir–Blodgett Method. *Langmuir* **32**, 5862–5869

(2016).

150.   Tian, X., Zhou, Y., Thota, S., Zou, S. & Zhao, J. Plasmonic Coupling in Single Silver Nanosphere

Assemblies by Polarization-Dependent Dark-Field Scattering Spectroscopy. *J. Phys. Chem. C* **118**,

13801–13808 (2014).

151.   Negrín-Montecelo, Y. *et al.* Chiral Generation of Hot Carriers for Polarization-Sensitive Plasmonic

Photocatalysis. *J. Am. Chem. Soc.* **144**, 1663–1671 (2022).

152.   Liu, T. *et al.* Chiral Plasmonic Nanocrystals for Generation of Hot Electrons: Toward Polarization-

Sensitive Photochemistry. *Nano Lett.* **19**, 1395–1407 (2019).

153.   Hartland, G. V., Besteiro, L. V., Johns, P. & Govorov, A. O. What's so Hot about Electrons in Metal

Nanoparticles? *ACS Energy Lett.* **2**, 1641–1653 (2017).

154.   Cortés, E. *et al.* Plasmonic hot electron transport drives nano-localized chemistry. *Nat Commun*

8, 14880 (2017).

155.   Kravets, V. G., Kabashin, A. V., Barnes, W. L. & Grigorenko, A. N. Plasmonic Surface Lattice

Resonances: A Review of Properties and Applications. *Chem. Rev.* **118**, 5912–5951 (2018).

156.   Song, M. *et al.* Versatile full-colour nanopainting enabled by a pixelated plasmonic metasurface.

Nat. Nanotechnol. **18**, 71–78 (2023).

7. APPENDIX

Supporting Information for associated publication **P2**

Supporting Information for associated publication **P3**

Supporting Information for associated publication P2

Visible wavelength spectral tuning of absorption and circular dichroism of DNA-assembled Au/Ag core–shell nanorod assemblies

by

Mihir Dass, Lilli Kuen, Gregor Posnjak, Sven Burger, and Tim Liedl

published in

Material Advances, 2022

as

Dass, M., Kuen, L., Posnjak, G., Burger, S. & Liedl, T. Visible wavelength spectral tuning of absorption and circular dichroism of DNA-assembled Au/Ag core–shell nanorod assemblies. *Mater. Adv.* **3**, 3438–3445 (2022).

Electronic Supplementary Material

Visible wavelength spectral tuning of absorption and circular dichroism of DNA-assembled Au/Ag core-shell nanorod assemblies

Mihir Dass, Lilli Kuen, Gregor Posnjak, Sven Burger and Tim Liedl *

Supplementary Note S1 - Experimental Section

Synthesis of AuNRs

The synthesis protocol was adapted from[(1)]. The protocol was repeated with different ratios of the reagents until AuNRs of the desired size were synthesised. The final synthesis recipe is below :

Reagent	Concentration	Volume
CTAB - n-decanol		90mL
HauCl4	50mM	900uL
AgNO3	10mM	1800uL
AA	0.2M (weight x 56.8)	720uL
HCl	1M	3600uL
Seed	OD 0.6 at 400nm	2880uL

Washing AuNRs

AuNRs were washed 2x in 0.1M CTAB, and then were redispersed in 0.01M CTAB for further use. For AuNRs to be used for functionalisation with thiol-DNA, the rods were washed and redispersed in 0.1% SDS.

Synthesis of Au/AgNRs nanorods

Reagent	Concentration	Volume
CTAB	0.1M	2250 uL
AuNRs	15 O.D. in 0.01M CTAB	480uL
Thiol-DNA	T8:T19 (9:1) 100uM in water	480uL
AgNO$_3$	2-12mM	400uL
L-Ascorbic acid	0.2M	64uL
NaOH	0.2M	125uL

AgNO$_3$ conc. added	Actual AgNO$_3$ conc. in growth sol.
2mM	210.5 µM
4mM	421 µM
6mM	631.7 µM
8mM	842 µM
10mM	1053 µM

Washing AuAgNRs

1. The synthesised rod dispersion was aliquoted into 300uL batches.

2. The rods were centrifuged and then redispersed in 0.1M CTAB. Centrifugation parameters were 4500rcf, 5min for rods synthesised with 2-6mM AgNO$_3$, and 3000rcf, 3min for rods synthesised with 8-12 mM AgNO$_3$.

3. The rods were centrifuged and then redispersed in 0.01M CTAB.

4. The rods were centrifuged and then redispersed in 0.1% SDS.

Note : Aggregation of the AuAgNRs most commonly occurred during the washing steps. If the centrifugation speed was too high, the AuAgNR pellet had a metallic lustre and was difficult to redisperse. For washing, we advise starting from lower centrifugal speeds and gradually increasing them until a clear supernatant is obtained.

Functionalisation of nanorods

Functionalisation was found to work best when the nanorods were suspended in 0.1% SDS.

AuNRs

32uL of thiol-T19 and 288uL of thiol-T8 were mixed together and added to 480uL of AuNRs dispersed in 0.1% SDS. The mixture was vortexed for 5s, and kept at -80°C for 30min. The 800uL mixture was then thawed and centrifuged to concentrate it down to ~100uL. Agarose gel electrophoresis was used to separate the functionalised AuNRs from excess thiol-DNA. A 1% gel was cast and the run parameters were 100V, 250mA, 1hour. The relevant gel bands were excised and squeezed between a glass slide and parafilm to extract the liquid sample.

AuAgNRs

In a typical experiment, after washing, the rods were centrifuged and resuspended in 0.1% SDS to a final volume of 480uL. 32uL of thiol-T19 and 288uL of thiol-T8 were mixed together and added to the rod dispersion. The mixture was vortexed for 5s, and kept at -80°C for 30min. The 800uL mixture was then thawed and centrifuged to concentrate it down to ~100uL. Agarose gel electrophoresis was used to separate the functionalised AuNRs from excess thiol-DNA. A 1% gel was casted and the run parameters were 100V, 250mA, 1 hour in 'Gel-buffer' (40mM Tris, 20mM Acetic acid, 1mM EDTA and 11mM Mg^{2+}). The relevant gel bands were excised and squeezed between a glass slide and parafilm to extract the liquid sample.

DNA Origami

Staple strands and the scaffold strand (modified 8064 nt long M13mp18 ssDNA) were mixed together to a target concentration of 200nM and 25nM respectively in 16mm $MgCl_2$, 10mM Tris and 1mM EDTA. The mixture was divided into 100uL aliquots in PCR tubes and annealed from 65°C to 20°C over ~ 16 hours (detailed program below).

Temperature (°C)	Time
65	15 min
64-60	5 min each
59-40	45 min each
39-36	30 min each
35-20	5 min each

The origami structures were purified using 100kDa MWCO Amicon filters.

1. Wet the filter by adding 450 μL water.

2. Spin filter at 4000rcf for 3 min. Discard the filtrate.

3. Add 200μL of the folded origami and 250 μL 'TE-12.5' buffer (10mM Tris, 1mM EDTA and 12.5mM Mg^{2+}). Spin at 6000 rcf for 6 min.

4. Discard the filtrate. Add 420 μL *TE-12.5* buffer and spin at 6000 rcf for 6 min.

5. Repeat step (4) three more times.

6. Invert the filter into a clean tube and spin at 6000 rcf for 2 min to collect the purified origami.

All experiments in this manuscript were performed using a single batch of 800uL origami (for both the X-shape and L-shape structures) which was folded and purified using this method above. After amicon purification, the origami were diluted to a concentration of 30nM.

Nanorod-origami hybridisation

50uL aliquots were made for each hybridisation experiment. Agarose gel purified nanorods were centrifuged down and resuspended in *Gel-buffer* to a final volume of ~ 48.5uL. 1.5uL of the origami was added to the nanorods while vortexing the sample.[2] The samples were then cycled from 45°C to 20°C at 10min/°C a total of 4x.[3]

The samples were then run in a 1.2% agarose gel and the run parameters were 100V, 250mA, 2 hours in *gel buffer*. The relevant gel bands were excised and squeezed between a glass slide and parafilm to extract the liquid sample.
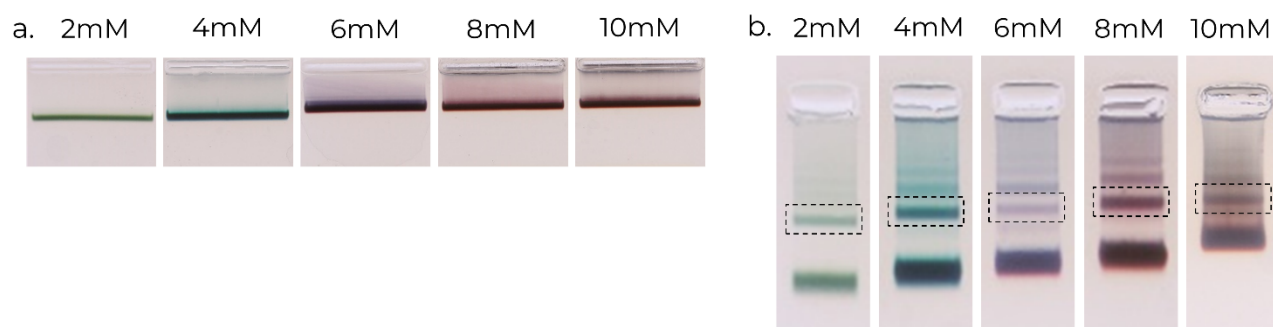
Figure S1. Agarose gel electrophoresis of a) AuAgNRs of varying Ag shell thickness and b) the X-shape chiral metamolecules constructed from the AuAgNRs. The Ag$^+$ concentration used for synthesising the Ag shells is mentioned above the respective lane.

TEM sample preparation

TEM grids were exposed to Argon plasma for 30s before sample deposition. The deposition duration for DNA origami (~ 5nM) was 30s, and for the NR-origami structures was 15min. The grid was then dipped on a 5uL droplet of 2% Uranyl formate (UFo) solution (containing 25mM NaOH) which was then wicked off immediately. The grid was then dipped in another UFo droplet, incubated for 10s and then wicked off. It was allowed to dry before imaging.

TEM images – Nanorods
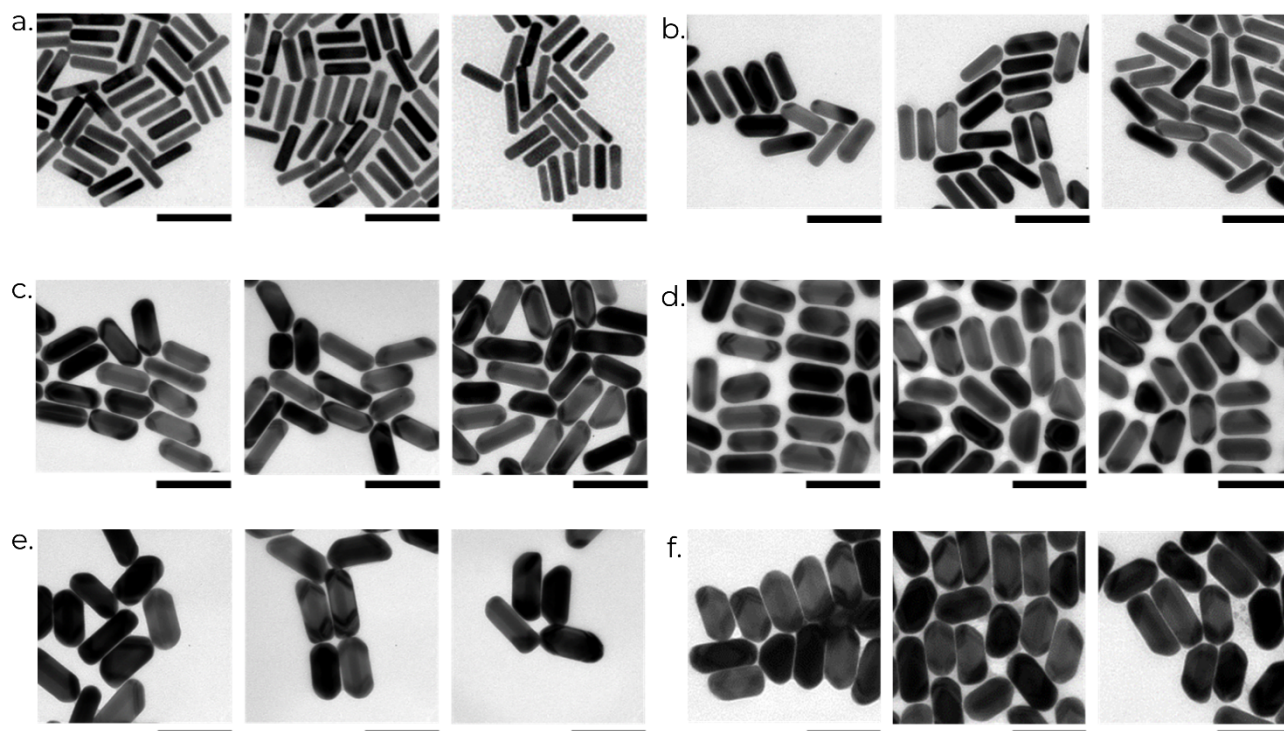
Figure S2. TEM images of nanorods with varying shell thicknesses. a) AuNRs. Au/AgNRs synthesized using b) 2mM, c) 4mM, d) 6mM, e) 8mM, f) 10mM of Ag$^+$ added to the growth solution. All scale bars are 100nm.
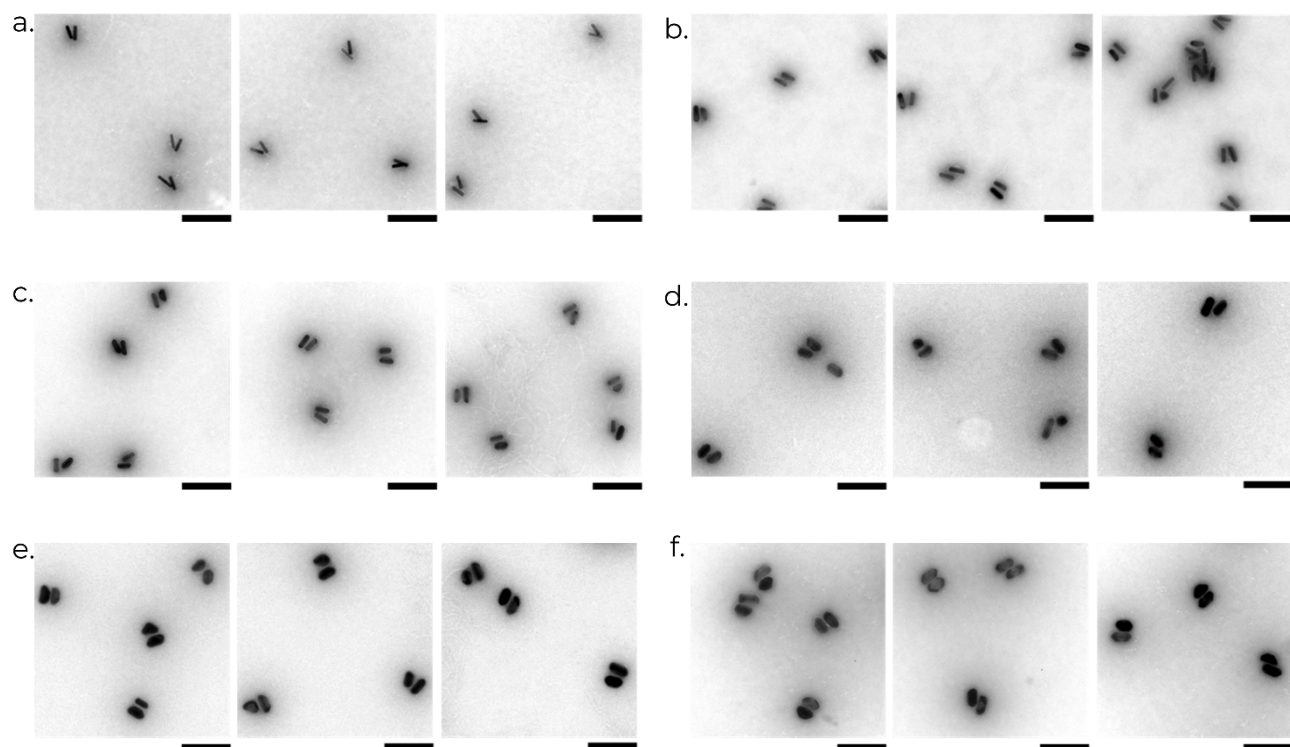
Figure S3. TEM images of X-shape chiral metamolecules assembled with a) AuNRs; Au/AgNRs synthesized using b) 2mM, c) 4mM, d) 6mM, e) 8mM, f) 10mM of Ag⁺ added to the growth solution. All scale bars are 200nm.

TEM images – Chiral metamolecules (X-shape)

TEM images – Chiral metamolecules (L-shape)

Supplementary note S2 – Numerical Section

Numerical Simulations

Numerical simulations were performed using the finite-element method (FEM), implemented in the solver JCMsuite.[4] Within all simulations, a polynomial degree of the FEM ansatz function p=2 was used. The discretisation was realised by a tetrahedral mesh with edge sizes smaller than 16 nm for the background, 4nm for the Ag shell, and 3.5 nm for the Au NPs. Transparent boundary conditions were realised using perfectly matched layers (PML).

Each side of the computational domain was illuminated by one left and one right-handed circularly polarised plane wave (LCP and RCP). The absorbed electromagnetic field energy and the electromagnetic field energy scattered outwards were recorded for each source. The total extinction was given by the sum of absorption and scattering for LCP and RCP, and all six directions of incidence. All graphs of the total extinction were normalised to their maximum value. The CD spectrum was given as the difference of extinction of LCP and of RCP. The graphs of the CD were normalised to their maximum to dip value, corresponding to the curves of the experimental data.

The simulation results, shown in Fig. 1 and Fig. 4 were computed using a scripting language (Matlab), to auto-generate the input files and to distribute the FEM computations to various threads on a workstation for parallel computation of the wavelength and parameter scans.

Geometry

The basic geometry for a single coated rods is depicted in Fig. S5a. It consists of an inner rod made of gold with diameter $d_i = 15$ nm and height of $h_i = 61$ nm and an outer shell with diameter d_o and height h_o, that represents the silver coating. The thickness of the silver coating is given as t_d at the side of the rods and t_h at the top, in the case of homogeneous coating the thickness is given as $t_{sh} = t_d = t_h$. The cap rounding radii of rod and shell are $d_i/2$, resp. $d_o/2$. Three different arrangements were analyzed, a single NR and NR-NR arrangements in X- and L-shape. The thickness of the silver coating was varied within the different cases for each arrangement. The sizes for the outer rod are given in Table S1 for the graphs of the numerical simulation in. 1 and Fig. 4, and in Table S2 for the graphs in Fig. S6 and Fig. S7 in this supplementary section. The NR-NR arrangement in X-shape, see Fig. S5b consists of two rods, with the rear one rotated 45° counterclockwise. The NR-NR arrangement in L- shape, shown in Fig. S5c consists of two rods, with the lower one rotated 90° counterclockwise. The offset between the rods is 11 nm from surface to surface, for both arrangements, X- and L-shape.
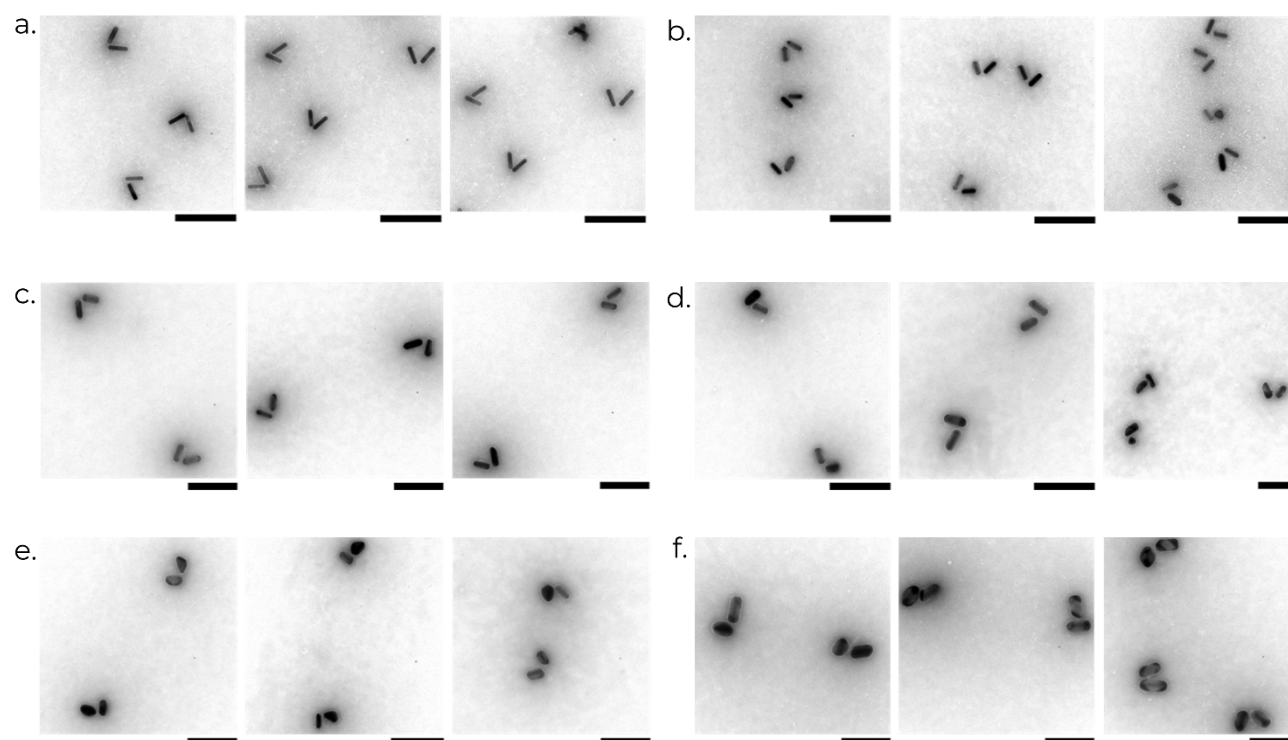
Figure S4. TEM images of L-shape chiral metamolecules assembled with a) AuNRs; Au/AgNRs synthesized using b) 2mM, c) 4mM, d) 6mM, e) 8mM, f) 10mM of Ag⁺ added to the growth solution. All scale bars are 200nm.

Table S1. Measured sizes of the outer rod for all three arrangements, corresponding to the simulations for Fig. 1 and Fig. 4 with the concentration of AgNO$_3$ in [mM] in the growth solution, thickness of the silver coating at the side of the rods t_d and the tips t_h, the diameter d_o and height h_o of the outer rod, representing the silver shell.

Case	1	2	3	4	5
$AgNO_3$ [mM]	2	4	6	8	10
t_d [nm]	4.9	7.5	9.5	12.5	13.8
t_h [nm]	4.5	6.5	8	11.5	12.25
d_o [nm]	24.8	30	34	40	52,6
h_o [nm]	70	74	77	84	85.5

Table S2. Homogenous silver coating with $t_{sh} = t_d = t_h$ starting from 5 nm in 2 nm steps up to 33 nm, corresponding to the simulations of Fig. S6 and Fig. S7 and the resulting diameter d_o and height h_o of the outer rod.

Case	1	2	3	4	5	6	7	8	9	10
$t_{sh} = t_d = t_h$ [nm]	5	7	9	11	13	15	17	19	21	23
d_o [nm]	25	29	33	37	41	45	49	53	57	61
h_o [nm]	71	75	79	83	87	91	95	99	103	107
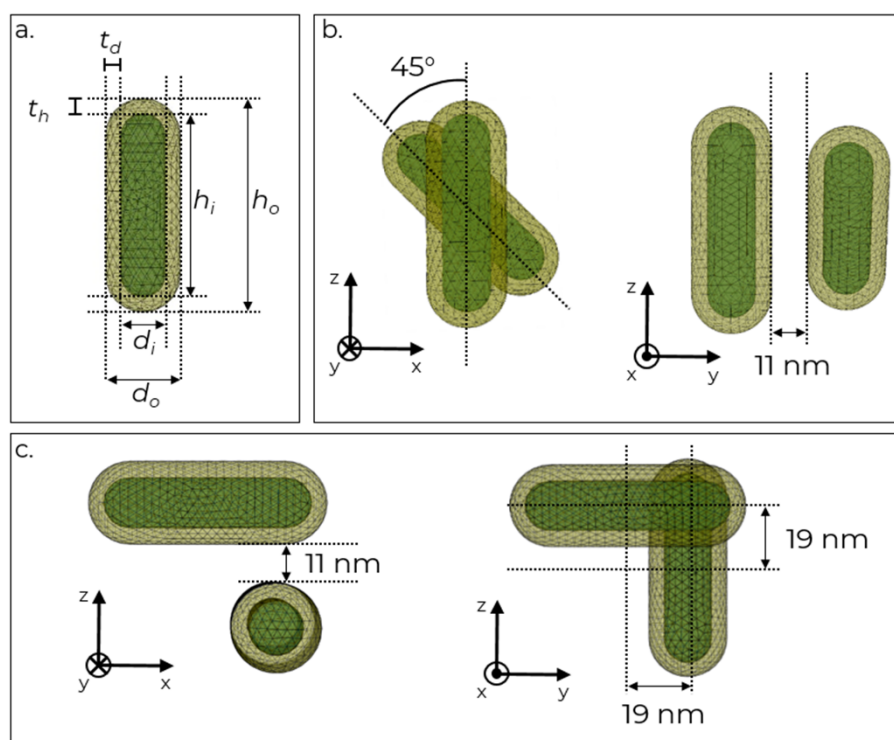
Figure S5. a) Single gold rod with diameter $d_i = 15$ nm and height $h_i = 61$ nm and silver shell with thickness t_d at the side of the rod and t_h at the top, represented by an outer rod diameter d_o and height h_o. The cap rounding radii of rod and shell are $d_i/2$, resp. $d_o/2$. b) NR-NR arrangement in X-shape with 45° angle between the NRs and 11 nm distance between the surfaces of the NRs. c) NR-NR arrangement in L-shape with 90° angle between the NRs and 11nm distance from surface to surface of the NRs.

Parameter studies with homogeneous coating

We study the influence of the silver coating, performing a parameter study for various silver shell thicknesses for all three arrangements. Therefore, we assume a homogenous silver coating $t_{sh} = t_d = t_h$ and vary the thickness of the shell t_{sh} from 5nm to 23nm in 2nm steps, sizes given in Table S2. The normalised total extinction in dependence on the wavelength is shown in Fig. S6 for a single, coated rod and different silver shell thicknesses. Two peaks can be observed in the spectrum. One at about 400nm, corresponding to the so-called transverse mode and the second in the range of 600nm - 700nm corresponding to the longitudinal mode. The transverse mode gets a red shift for thicker silver coatings and the intensity increases. The longitudinal is blue shifted with increasing silver layer thickness. This is in good agreement with the previous results.[5] Furthermore, it can be observed that the shift of the resonances is sensitive to the thickness of the silver layer.

The peak to dip normalised CD signal for the NR-NR arrangement in X- and L-shape is shown in Fig. S7. Here, mainly two peaks occur in the CD signal, the first in the range of 550 nm – 650 nm and the second one within 650 nm – 720 nm. For larger silver layer thicknesses, both resonances receive a blue shift, which, however, is less pronounced with increasing layer thickness. For large coating thicknesses, there is an additional peak at around 450nm. This might be caused by coupling of the transversal modes of the Au/AgNRs.
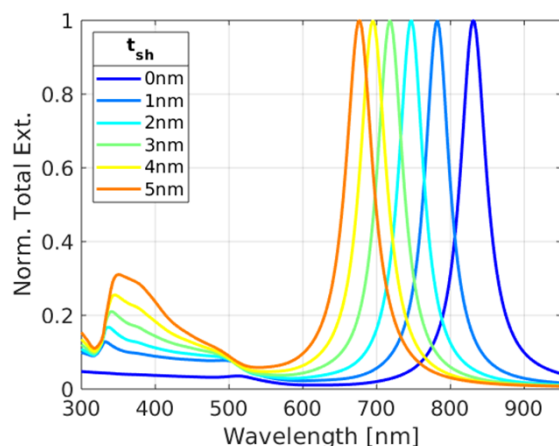
Figure S6. Numerical result of the normalized total extinction as function of the illumination wavelength for a single coated rod with homogeneous silver shell thickness t_{sh}, varied from 5 nm in 2 nm steps up to 23 nm.
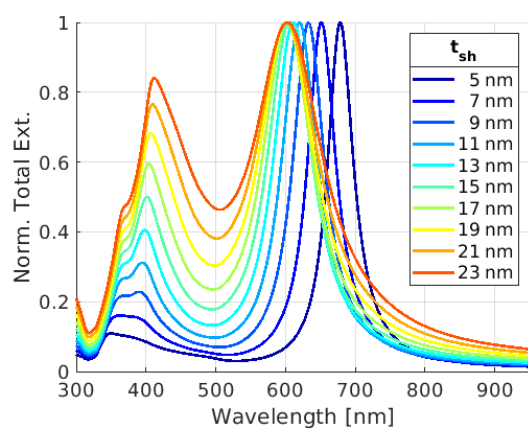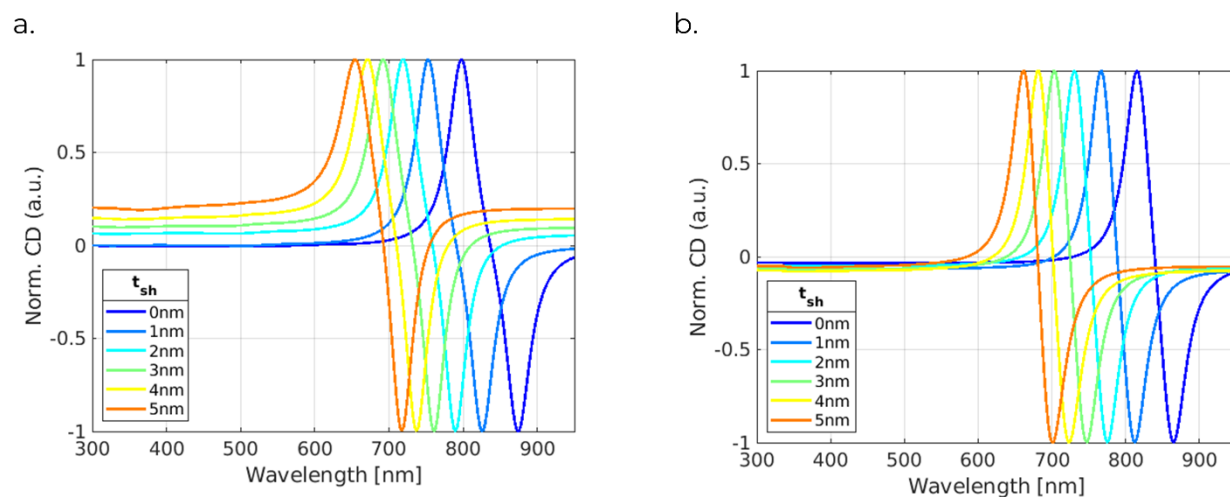

Figure S7. Numerically obtained normalised circular dichroism (CD) signal as function of illumination wavelength for different,

a.

b.
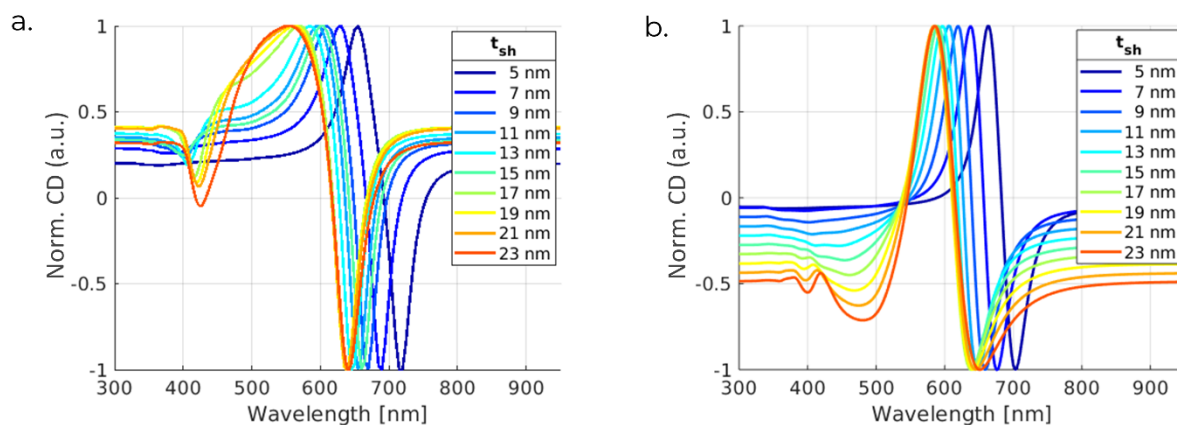
homogeneous silver shell thicknesses, t_{sh} varied from 5 nm up to 23 nm in 2 nm steps. a) NR-NR arrangement in X-shape, b) NR-NR arrangement in L-shape.

L-shape with imperfect angle

When assembling the L-shape dimers, it may happen that the angle between the two rods is not exactly 90° (Fig. S4). In the event that it is smaller, the L-shaped arrangement resembles the X-shape more and more. We simulated the L-shape arrangement for the 6mM variant of Au/AgNRs with different angles between the two rods (90°, 80°, 70° and 60°) to determining the influence of the angle on the CD spectra. The results are shown in Fig. S8. For smaller angles, the shape profile of the normalised CD begins to resemble the experimental results (Fig. 4b), with the dip around 400nm becoming more pronounced at lower angles.

Figure S8. Normalised CD in dependence of the wavelength for AuAg NR arrangement in L-shape for 6mM and different angles.
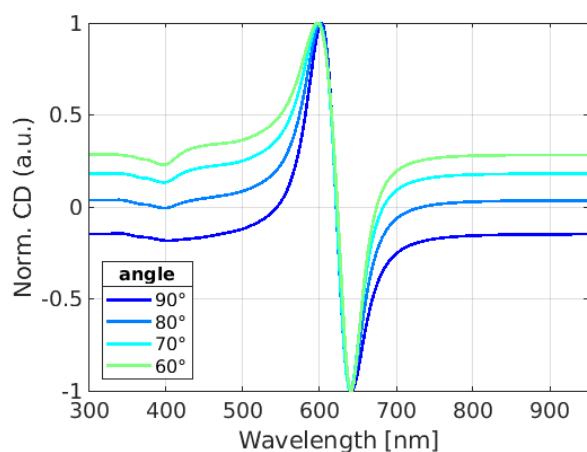
Supplementary note S3 – Shell thickness analysis

The nanoparticles' polydispersity, especially in the width, increases with the growth of thicker Ag shells (Fig. S8, right column). The synthesis of nanocrystals, in this case the Ag shell, is extremely sensitive to growth conditions. This inhomogeneity in the growth of nanocrystals has been widely studied, especially for gold nanocrystals.[1,6] Several ways have been suggested to improve the synthesis, including careful control over parameters like temperature during the growth phase [6], as well as addition of specific additives than can influence the monodispersity of the particles during growth.[7]

ARTICLE

Size distributions of all NRs were determined by analyzing transmission electron microscopy (TEM) images. The dimension analysis of all images was done using ImageJ software (https://imagej.nih.gov/ij/).
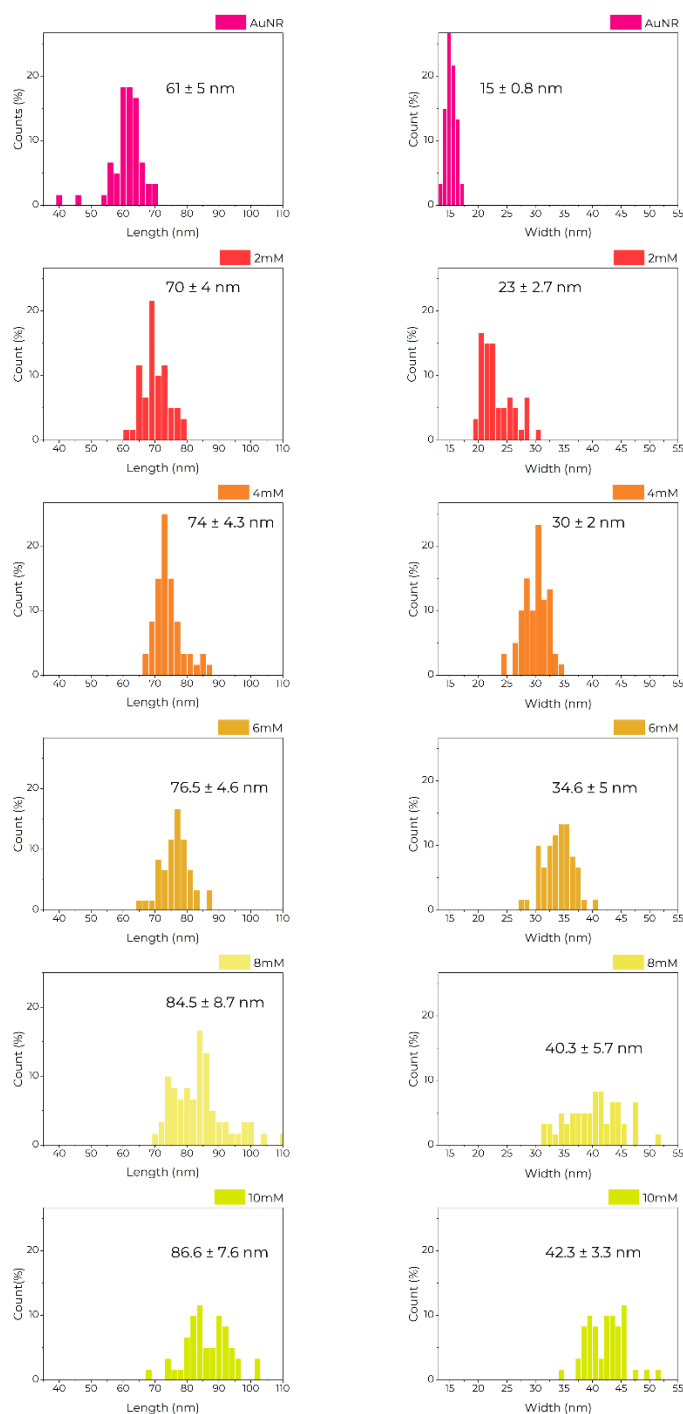
Figure S9. Size distribution of AuNRs and Au/AgNRs synthesized using different Ag+ concentrations.

Supplementary note S4 – Spectral analysis of shifting LSPR
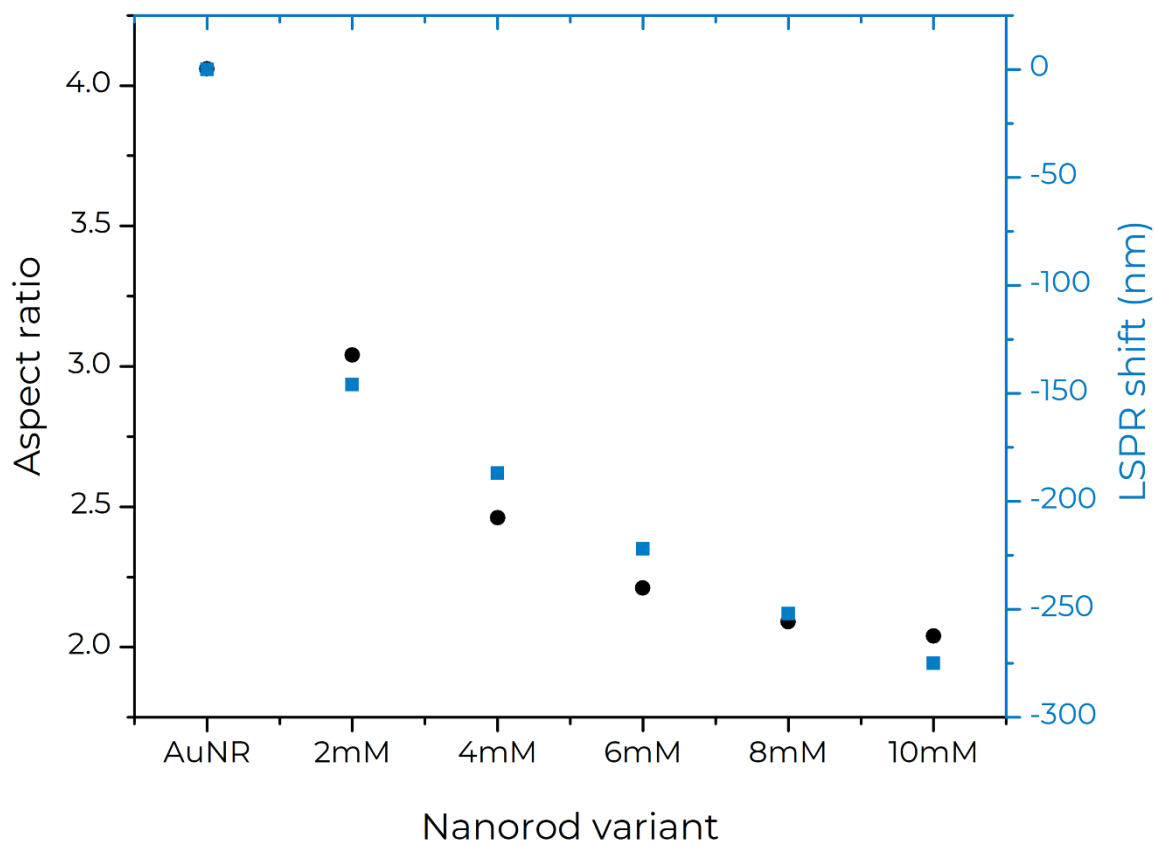
Figure S10. Variation in aspect ratio and LSPR peak of the Au/AgNRs relative to AuNRs.
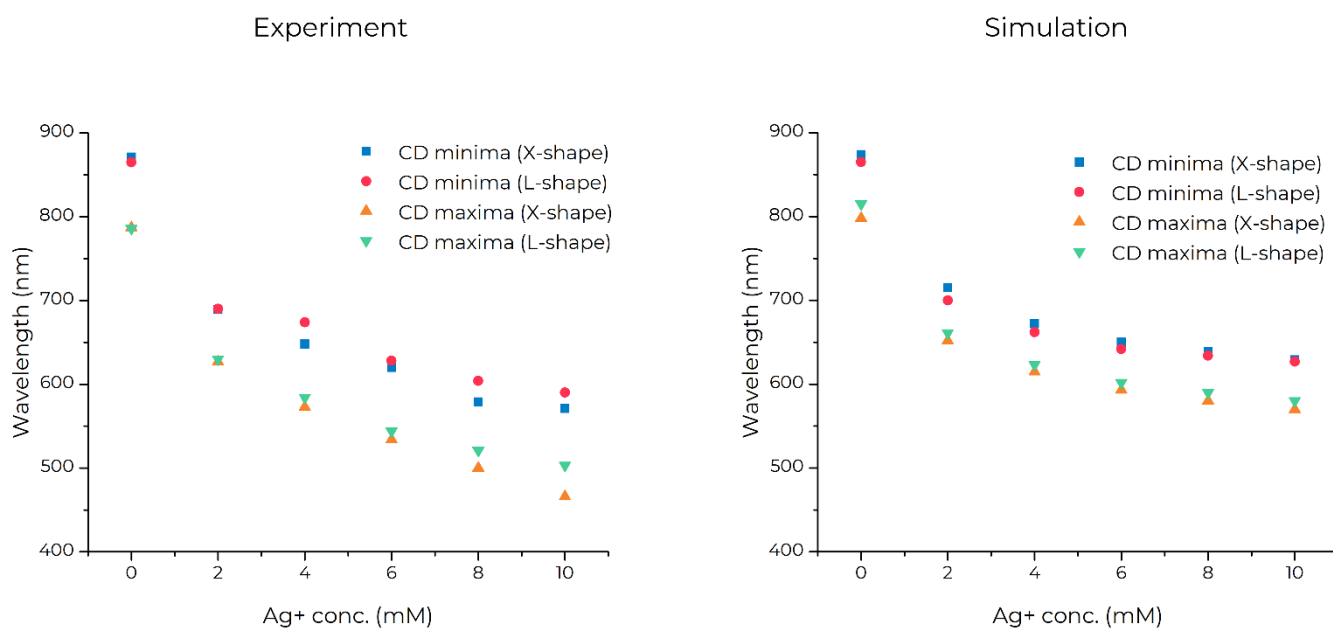
Figure S11. Comparison between theoretical and experimental CD spectra analysing the spatial tuning of the spectral maxima and minima.

Supplementary note S5 – Thin shells

The realization of very thin Ag coatings, smaller than 5nm are technically not trivial. The experiments have shown that these arrangements do not remain sufficiently stable to be able to carry out measurements. Therefore, coating thicknesses from 1nm to 5nm are investigated numerically. For a single coated rod, the model and the numerical simulation procedure from Section S2-Numerical Section is used. The Ag coating is varied from 1nm to 5nm. The dimensions are given in Table S3. The results for the normalised total extinction is shown in Figure S11, where $t_{sh} = 0$ corresponds to a pure gold rod without silver coating. For thicker coatings the resonance in the higher wavelength regime is blue shifted and a second resonance around 350nm is occuring. The curves lie within the range between the pure Au NR and the smallest AuAg NR with smallest coating in Fig. 1.

For the X-shape and L-shape arrangements, the models and the numerical simulation procedure from Section S2-Numericlal Section are used. The Ag coating thickness is varied homogeneously from 1nm to 5nm, for dimensions see Table S3. The results of the normalised Circular Dicroism (CD) for X- and L-shape with different shell thickness are depicted in figure S 12. A layer thickness of $t_{sh} = 0$ nm corresponds to pure gold rods. The CD has two peaks, the transverse mode in the range of 650nm - 850nm and the longitudinal mode in the range of 700nm - 900nm. For thicker Ag films, both peaks are blue shifted. The thicker the Ag layer, the more blue shifted is the CD. In addition, the distances between the CDs becomes smaller. The CD of the thinnest silver coating is very close to the result of the CD for pure Au rods (t_sh = 0nm). For both arrangements the curves lie within the range between the pure Au NR and the smallest AuAg NR with smallest coating in Fig. 4.

Table S3 Homogenous silver coating with $t_{sh} = t_d = t_h$ starting from 1 nm in 1 nm steps up to 5 nm, corresponding to the simulations of Fig. S11, Fig. S12 and the resulting diameter d_o and height h_o of the outer rod.

Case	1	2	3	4	5
$t_{sh} = t_d = t_h$ [nm]	1	2	3	4	5
d_o [nm]	17	19	21	23	25
h_o [nm]	63	65	67	69	71

Figure S12. Numerically obtained total extinction as function of illumination wavelength for a single coated rod with different, homogeneous silver shell thicknesses, t_{sh} varied from 1 nm up to 5 nm in 1 nm steps and normalized total extinction for pure gold rods ($t_{sh} = 0$ nm). a) NR-NR arrangement in X-shape, b) NR-NR arrangement in L-shape.

a.

b.

Figure S13. Numerically obtained normalised circular dichroism (CD) signal as a function of illumination wavelength for different, homogeneous silver shell thicknesses, t_{sh} varied from 1 nm up to 5 nm in 1 nm steps and normalised CD for pure gold rods ($t_{sh} = 0$ nm). a) NR-NR arrangement in X-shape, b) NR-NR arrangement in L-shape.

Supplementary note S5 – Thick shells

The evolution of the aspect ratio of the AuAgNRs with increasing Ag$^+$ concentration is tied to the aspect ratio of the underlying core AuNRs. For the AuNRs used in this paper (with dimensions ~ 61 nm x 15 nm), using 12mM Ag$^+$ in the growth solution led to Au/AgNRs that were almost isotropic (Fig. S11a,b), which makes it difficult to define the length vs width and thus, makes the calculation of the aspect ratio unreliable.

This isotropic nature of the Au/AgNRs is also mirrored in their extinction spectra, which no longer exhibits separate longitudinal and transverse modes but rather shows an almost total overlap between the two (Fig. S11c).
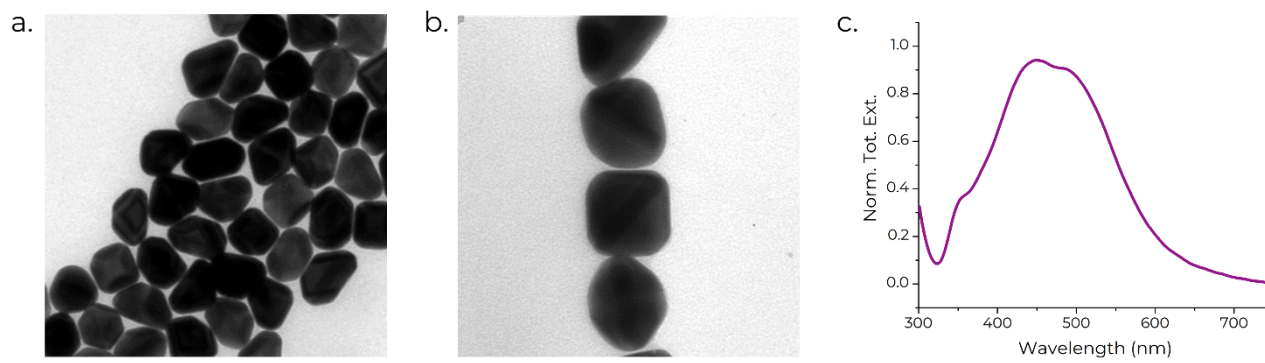
Figure S14. Growing thick Ag shells. a) TEM image of AuAgNRs grown using 12mM Ag$^+$. b) A close-up of the AuAgNRs. c) Normalized total extinction of the Au/AgNRs. Scale bars : 50 nm.
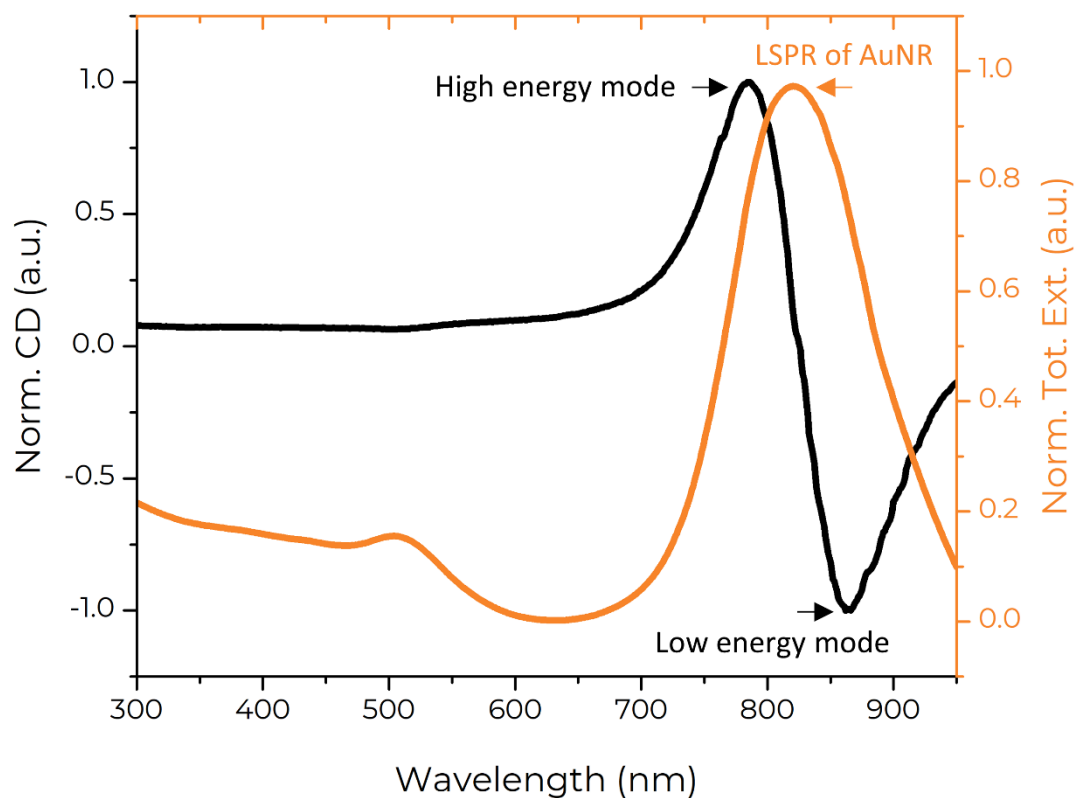
Figure S15. An overlay of the CD and normalized extinction spectra of L-shape dimer made with AuNRs, depicting their relative spectral positions. The LSPR hybridization modes in the chiral dimer are labelled for the CD spectra.

DNA Origami design

The 2-layer sheet structure is designed to have an array of sites on both sides of the origami from which the 3' site of a staple can be extended. The green staples are designed such that their 3' ends face the 'bottom' face. Similarly, for the red staples the 3' ends face the 'top' face. The staples on the edges are extended with three C's to prevent base stacking between origami structures. Eight A's are extended as anchors to bind to functionalised nanorods.

In the accompanying list of oligos, the 'core' staples are common to both the X- and the L-shape designs. The 'staples' are oligos without any extended part,
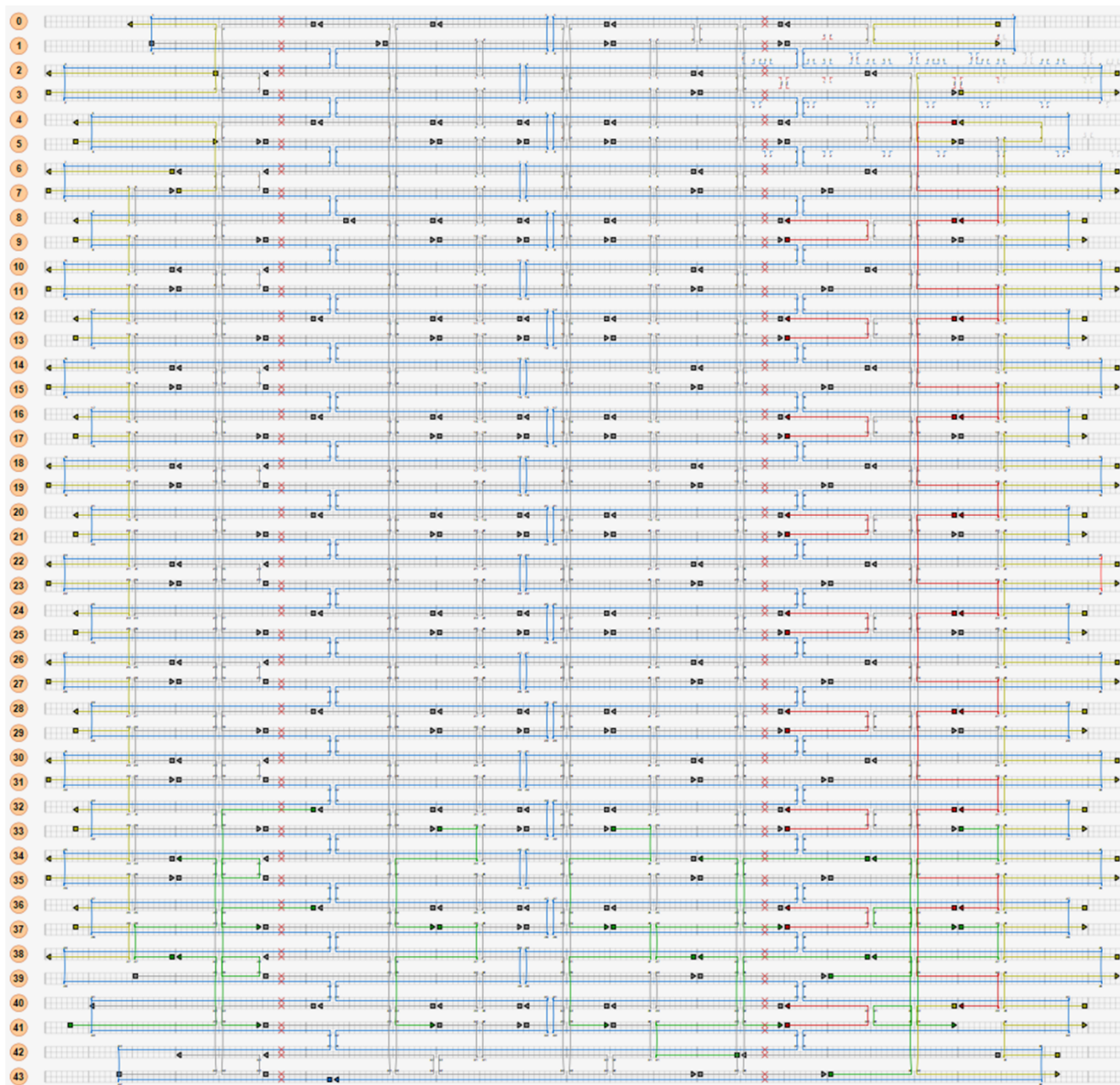
Figure

while the 'handles' are oligos with a polyA extension.
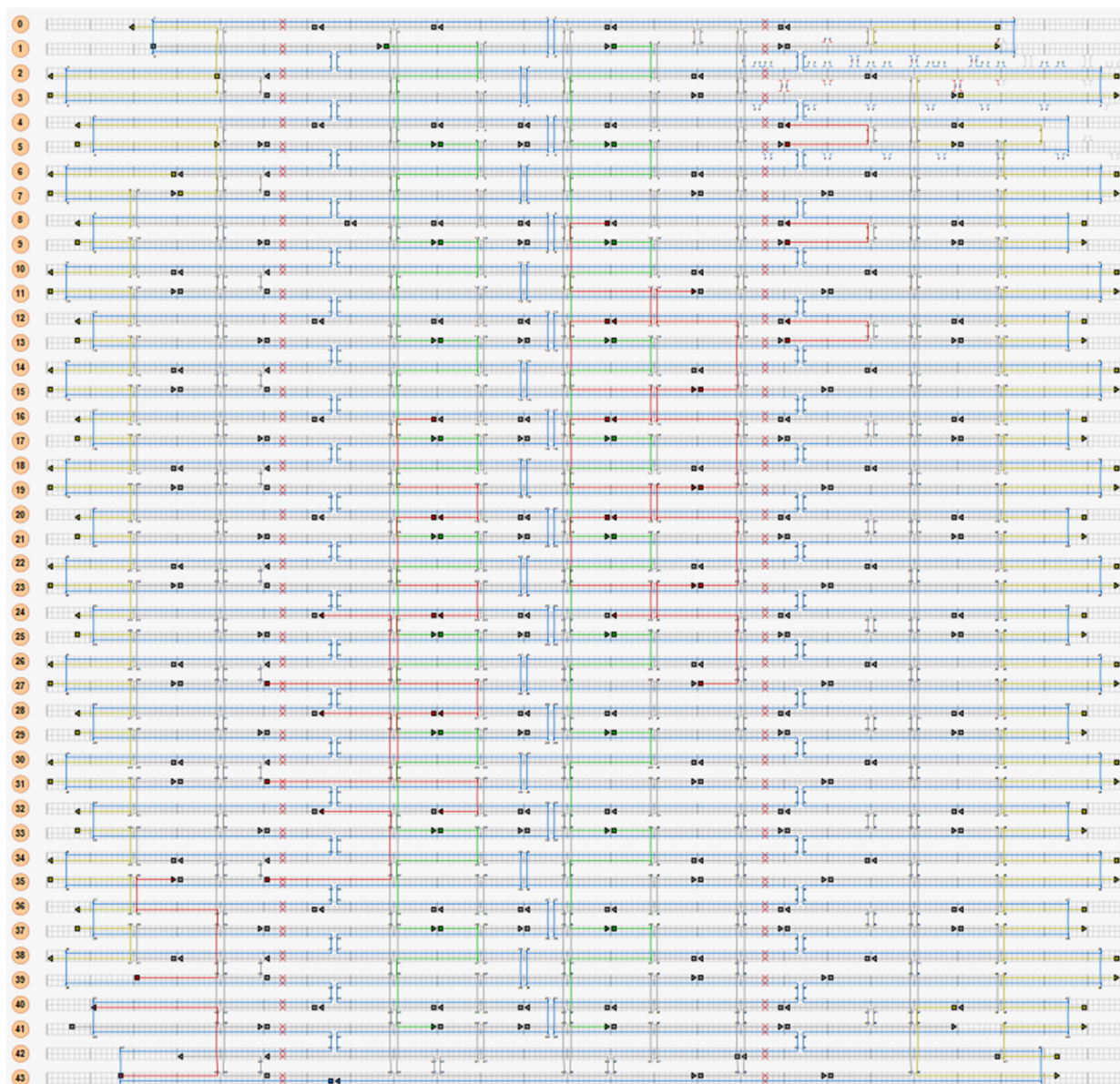
Figure S17. Cadnano design for the 2-layer sheet structure with anchors to form the X-shape metamolecule.

References

1. González-Rubio G, Kumar V, Llombart P, Díaz-Núñez P, Bladt E, Altantzis T, et al. Disconnecting Symmetry Breaking from Seeded Growth for the Reproducible Synthesis of High Quality Gold Nanorods. ACS Nano. 2019 Apr 23;13(4):4424–35.

2. Gür FN, Schwarz FW, Ye J, Diez S, Schmidt TL. Toward Self-Assembled Plasmonic Devices: High-Yield Arrangement of Gold Nanoparticles on DNA Origami Templates. ACS Nano. 2016 May;10(5):5374–5382.

3. Lan X, Lu X, Shen C, Ke Y, Ni W, Wang Q. Au Nanorod Helical Superstructures with Designed Chirality. J Am Chem Soc. 2015 Jan 14;137(1):457–62.

4. Pomplun J, Burger S, Zschiedrich L, Schmidt F. Adaptive finite element method for simulation of optical nano structures. physica status solidi (b). 2007;244(10):3419–34.

5.   Nguyen L, Dass M, Ober MF, Besteiro LV, Wang ZM, Nickel B, et al. Chiral Assembly of Gold–Silver Core–Shell Plasmonic Nanorods on DNA Origami with Strong Optical Activity. ACS Nano. 2020 Jun;14(6):7454–7461.

6.   Scarabelli L, Sánchez-Iglesias A, Pérez-Juste J, Liz-Marzán LM. A "Tips and Tricks" Practical Guide to the Synthesis of Gold Nanorods. J Phys Chem Lett. 2015 Nov 5;6(21):4270–9.

7.   Ye X, Jin L, Caglayan H, Chen J, Xing G, Zheng C, et al. Improved Size-Tunable Synthesis of Monodisperse Gold Nanorods through the Use of Aromatic Additives. ACS Nano. 2012 Mar 27;6(3):2804–17.

Supporting Information for associated publication P3

Self-assembled physical unclonable function labels based on plasmonic coupling

by

Mihir Dass, Lena Raab, Christoph Pauer, Christoph Sikeler, Larissa Heinze, Joe Tavacoli, Irina V. Martynenko, Ulrich Rührmair, Gregor Posnjak, and Tim Liedl

submitted to

Arxiv, 2023

10.48550/arXiv.2310.19587

Supplementary Information

Methods

DNA Origami

Design. A disc-shaped DNA origami structure was chosen to match and cover the circular binding sites created by the NSL process, specifically when using polystyrene nanospheres with $d \leq 400$nm. The cadnano design files and staple sequences are included separately. Staple extensions with 10 nt poly-A sequences were used to capture nanoparticles.
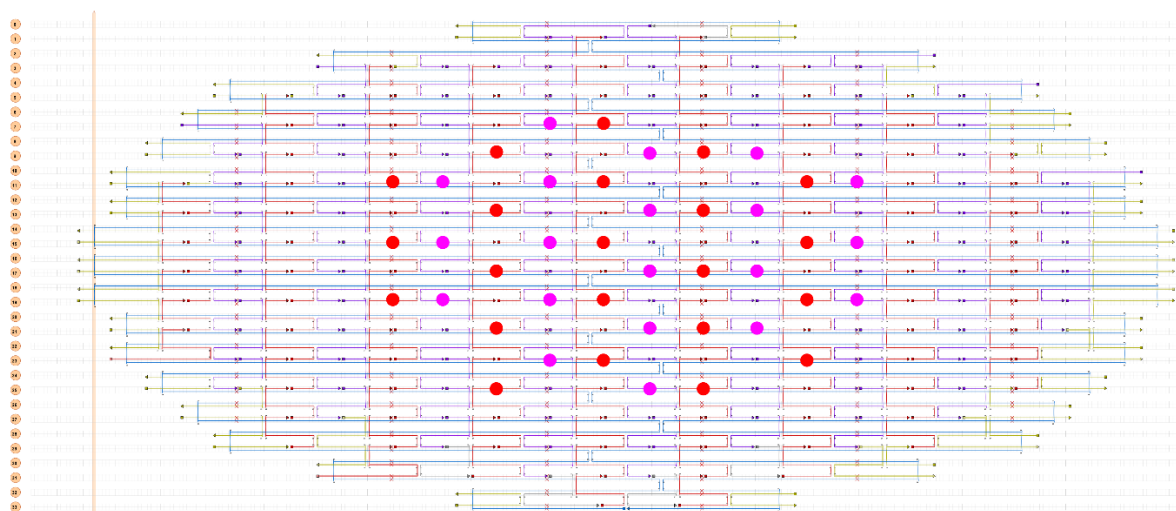
Figure S1. Cadnano design of the nanodisc origami structure. The scaffold is shown in blue. The red and violet staples are extendable from opposite faces. The green staples on the edges have C_4 extensions to prevent stacking. Deletions of base pairs are marked with red X symbols. Positions of staple extensions are marked by coloured circles.

Assembly. Staple strands (Integrated DNA Technologies, 200 μM each in water) and the scaffold strand (modified 8634 nt long M13mp18 ssDNA) were mixed to a target concentration of 200 nM for each staple and 20 nM for the scaffold, respectively, in 18 mM $MgCl_2$, 10 mM Tris and 1 mM EDTA (pH 8.3). The mixture was divided into 100 μL aliquots in PCR tubes and annealed from 65°C to 20°C over ~ 16 hours (see table below).

Table S1. **DNA Origami folding program**

Temperature (°C)	Time
65	15 min
64-60	5 min/°C
59-40	45 min/°C
39-36	30 min/°C
35-20	5 min/°C

Purification. The origami structures were analysed and purified using a 1% agarose gel. The gels were run in a buffer containing 40 mM Tris, 20 mM acetic acid, 1 mM EDTA and 11 mM MgCl2 at 100V for 2 hours. 1x SybrSafe (Thermo Fisher) was included in gels for visualizing DNA. The desired bands were excised and squeezed between parafilm sheets to extract the purified sample. We do not believe the SybrSafe affects further downstream experiments.

Characterisation

UV-Vis spectroscopy. Extinction measurements for determination of DNA and nanoparticle concentrations were performed with a NanoDrop ND-1000 spectrophotometer (Thermo Scientific).

TEM imaging. 5 µL of a sample was incubated for 30 s – 5 min, depending on concentration, on glow-discharged TEM grids (formvar/carbon, 300 mesh Cu; Ted Pella) at room temperature. DNA origami samples were stained with a 2% uranyl formate aqueous solution containing 25 mM sodium hydroxide. Imaging was performed with a JEM1011 transmission electron microscope (JEOL) operated at 80 kV.

AFM imaging. The tapping-mode AFM of glass substrates was carried out on a Dimension ICON AFM instrument (Bruker). OTESPA silicon tips (300 kHz, Vecco Probes) were used for imaging in air. Images were analysed with Gwyddion software.

SEM imaging. The SEM instrument used in this work is the Raith eLINE SEM instrument. The beam settings for imaging are 10 kV acceleration and 20 µm aperture. The samples were imaged using the SEM after 20 s sputtering using an Edwards Sputter Coater S150B. The sputter target contained 60% gold and 40% palladium. The process parameters used for sputtering were 5 mbar Argon, 1.5 kV, 11 mA. Here 20 s of sputtering results in the deposition of a layer of gold/palladium with a thickness of a few nanometers. SEM imaging was performed on horizontal samples.

Plasmonic Nanoparticles

Synthesis. The gold nanorods were synthesised as in ref.[1]. The procedure was optimised until the desired size was achieved. The rods were washed in 0.1 M CTAB (Roth) and 0.01 M CTAB and stored in 0.01 M CTAB at 15 O.D. (optical density) before use. The gold nanospheres (BBI solutions) were centrifuged and washed into 0.1% SDS @ 10 O.D. before use.

Silver coating. The silver coating was performed as previously reported.[2] The nanoparticles were added to 0.1 M CTAB under stirring (500 rpm) and allowed to mix for 10 s. Then, a 1:9 mixture of thiolated ssDNA strands with a 19 nt long poly-T sequence (T19) and an 8 nt long poly-T sequence (T8) (Biomers, 100 µM, aq.), respectively, were added to the rod mixture. This was followed by adding $AgNO_3$ solution, after which the stirring speed was increased (1500 rpm). L-Ascorbic acid (0.2 M) and NaOH (0.2 M) were added rapidly in quick succession. A colour change after 5 - 10 s indicates the successful synthesis of a silver coating. The reaction was allowed to proceed for 10 min. The core-shell nanoparticles were washed to remove

excess reactants from their respective growth solutions and then redispersed in 0.1% Sodium dodecyl sulfate (SDS) before further use.

Table S2. **Silver-coating protocol**

Reagent	Concentration	Volume
CTAB	0.1 M	2250 uL
AuNR **AuNS**	15 O.D. in 0.01 M CTAB **6 O.D. in 0.01 M CTAB**	480 uL
Thiol-DNA	T8:T19 (9:1) 100 uM in water	480 uL
AgNO$_3$	8 mM **(6 mM for AuNS)**	400 uL
L-Ascorbic acid	0.2 M	64 uL
NaOH	0.2 M	125 uL

Washing AuAgNRs

1. The synthesised rod dispersion was aliquoted into 300 uL batches.
2. The rods were centrifuged and then redispersed in 0.1M CTAB. Centrifugation parameters were 4500 rcf, 5 min for rods synthesised with 2-6 mM AgNO$_3$, and 3000 rcf, 3 min for rods synthesised with 8-12 mM AgNO$_3$.
3. The rods were centrifuged and then redispersed in 0.01 M CTAB.
4. The rods were centrifuged and then redispersed in 0.1% SDS.

Note: Aggregation of the AuAgNRs most commonly occurred during the washing steps. If the centrifugation speed was too high, the AuAgNR pellet had a metallic lustre and was challenging to redisperse. For washing, we advise starting from lower centrifugal speeds and gradually increasing them until a clear supernatant is obtained.

Functionalisation. Nanorods were resuspended in 0.1% SDS to ~15 O.D. before functionalisation with DNA. In a typical experiment, 32 uL of thiol-T19 and 288 uL of thiol-T8 (1:9 ratio) were mixed and added to 480 uL nanorods dispersed in 0.1% SDS. Nanospheres were resuspended in 0.1% SDS to ~10 O.D. before functionalisation with DNA. In a typical experiment, 16 uL of thiol-T19 and 144 uL of thiol-T8 were mixed and added to 480uL nanospheres dispersed in 0.1% SDS.

In all cases, the mixture was vortexed for 5 seconds and kept at -80°C for 30 min. The mixture was then thawed and centrifuged to concentrate it to ~100 uL. Agarose gel electrophoresis was used to separate the functionalised nanoparticles from excess thiol-DNA.

Purification. The nanoparticles were analysed and purified using a 1% agarose gel. The gels were run in a buffer containing 40 mM Tris, 20 mM acetic acid, 1 mM EDTA and 11 mM $MgCl_2$ at 100V for 90 minutes. The desired bands were excised and squeezed between parafilm sheets to extract the purified sample.

Characterisation.

UV-Vis spectroscopy. 1.5 uL of the liquid on the substrate was taken to measure the nanoparticle concentration during NPP.

TEM imaging. See the DNA origami section. No staining was performed.

DNA origami placement (DOP)

The DNA origami placement procedure was adapted from ref.[3].

Buffers used

Folding buffer. 10 mM Tris, pH 8.3, 1 mM EDTA, 18 mM $MgCl_2$.

Placement buffer. 40mM Tris-HCl, pH 8.35, 40mM $MgCl_2$.

Tween buffer. 40mM Tris-HCl, pH 8.35, 40mM $MgCl_2$, 0.07% Tween20.

Gel buffer. 40mM Tris base, 20mM acetic acid, 1mM EDTA, pH 8.3, 11mM $MgCl_2$.

Substrate preparation and binding site fabrication.

Materials and equipment required:-

- Polystyrene nanospheres (diameter - 350nm, 400nm, 600nm, 1μm) at 1 wt% concentration (Distrilab)
- 10mm x 10mm coverslips (Plano-em)
- Lobind tubes
- Tweezers (Plano-em)
- Hotplate
- Plasma cleaner (Diener Pico)
- Ultrasonication bath
- Isopropanol (Roth)
- HMDS
- Custom 3D-printed stands to hold the coverslips at a 45° angle.
- Dessicator (1L)

1. Wash ~ 500uL polystyrene nanospheres (PsNs) by centrifuging, removing the supernatant and resuspending them in 50% Ethanol/water (v/v) three times.
2. Resuspend PsNs to 3.5 wt% (~ 150 uL) in 50% Ethanol/water (v/v).
3. Mark a small scratch on the coverslips to ensure upright orientation in the event of them flipping over during the binding site fabrication process.
4. Sonicate coverslips in isopropanol for two minutes @ 100% power.
5. Place coverslips in a petri dish and plasma clean @ 50W power, 5 min, 45sccm O_2 flow.
6. Place the coverslips against the 3D-printed stand to maintain a reproducible 45° angle.
7. Drop 8uL of the polystyrene nanosphere suspension to a coverslip. The plasma treatment should render the coverslips hydrophilic, and the suspension should spread over the whole surface.
8. Wait until the suspension dries completely, around 5 minutes.
9. Heat at 60°C for 5 minutes to dry the coverslips.
10. Place the coverslips in a petri dish and plasma clean @ 20W power, 2 min, 45sccm O_2 flow. This is to clean the surface again (so-called 'descum' step) and render the surface hydrophilic again.
11. Add 600uL of HMDS (in a small cup) in the desiccator. Place the coverslips on a plate above the cup, and deposit under a vacuum seal (40mbar) for 20 minutes.
12. Lift-off PsNs by immersing coverslips in DI water and ultrasonicating @100% power for 5 minutes.
13. Heat at 120°C for 5 minutes to stabilise the HMDS-treated surface.

PUF fabrication.

Materials and equipment required:-

- Patterned chips
- Placement buffer
- Tween buffer
- Purified DNA Origami
- Purified DNA-functionalized nanoparticles
- Petri dish
- Parafilm
- Tweezers
- Pipette and tips
- Kimtech wipes
- Ethanol
- DI water

DNA Origami Placement

1. Place a small strip of parafilm inside a Petri dish.

2. Place the patterned chip on the parafilm. The hydrophobic parafilm often pushes the buffer droplet back onto the chip in the event of spillage.
3. Keep a moistened Kimtech wipe in the Petri dish to help maintain humidity during incubation.
4. Dilute the purified DNA Origami with *Placement buffer* in LoBind tubes.
5. Pipette ~ 60 uL of the diluted Origami onto the chip. **Incubate for 1 hour**.
6. Wash 10x with the *Placement buffer* by pipetting 60uL fresh buffer onto the chip, mixing 2-3 times and pipetting 60 uL off the chip.
7. Wash 5x with the *Tween buffer* by pipetting 50 uL fresh buffer onto the chip, mixing 2-3 times and pipetting 50 uL off the chip. Addition of the *Tween buffer* results in a change of the surface tension and spreading of the droplet. **Incubate for 5 minutes**.
8. Wash away the *Tween buffer* by washing for 5 minutes (~ 30 washes) with the *Placement buffer* by pipetting 80 uL fresh buffer onto the chip, mixing 2-3 times and pipetting 80 uL off the chip. The indication for the Tween being washed away is that the droplet returns to its original shape.

If the experiment aims to only place DNA Origami, for example, for imaging or troubleshooting purposes, skip to step 15 for the drying procedure.

Adding nanoparticles

9. Centrifuge the Purified DNA-functionalized nanoparticles. Remove as much supernatant as possible, and then vortex and sonicate the suspension to redistribute the nanoparticles uniformly.
10. Now take the desired amount of this nanoparticle suspension (usually 1-10 uL) and dilute it with the *Placement buffer*.
11. Take away 30 uL of the *Placement buffer* on the chip. Add 60 uL of the nanoparticle suspension in *Placement buffer* to the chip, mixing 2-3 times and leaving the liquid on the chip. **Incubate for 1 hour.**
12. Take away 30 uL of the nanoparticle suspension on the chip. Wash 10x with the *Placement buffer* by pipetting 60 uL fresh buffer onto the chip, mixing 2-3 times and pipetting 60 uL off the chip.
13. Wash 5x with the *Tween buffer* by pipetting 50 uL fresh buffer onto the chip, mixing 2-3 times and pipetting 50 uL off the chip. Addition of the *Tween buffer* results in a change of the surface tension and spreading of the droplet. **Incubate for 5 minutes**.
14. Wash away the *Tween buffer* by washing for 5 minutes (~ 30 washes) with the *Placement buffer* by pipetting 80 uL fresh buffer onto the chip, mixing 2-3 times and pipetting 80 uL off the chip.

Drying procedure

15. Successively place the chip into 25%, 50%, 75% and 85% Ethanol/water (v/v) mixture for 10 seconds, 10 seconds, 20 seconds and 2 minutes, respectively.
16. Air dry the chips on a Kimtech wipe.

Note: All the DNA Origami and nanoparticles in this work were gel purified for the experiments. The rationale behind that is twofold - to get rid of any spurious assemblies (dimers, aggregates) and to ensure the removal of all excess ssDNA strands, both staples and thiol-DNA. The latter is essential because free thiol-DNA could bind to anchors and inactivate DNA Origami structures placed on the surface. Other purification procedures might result in similar assembly quality.
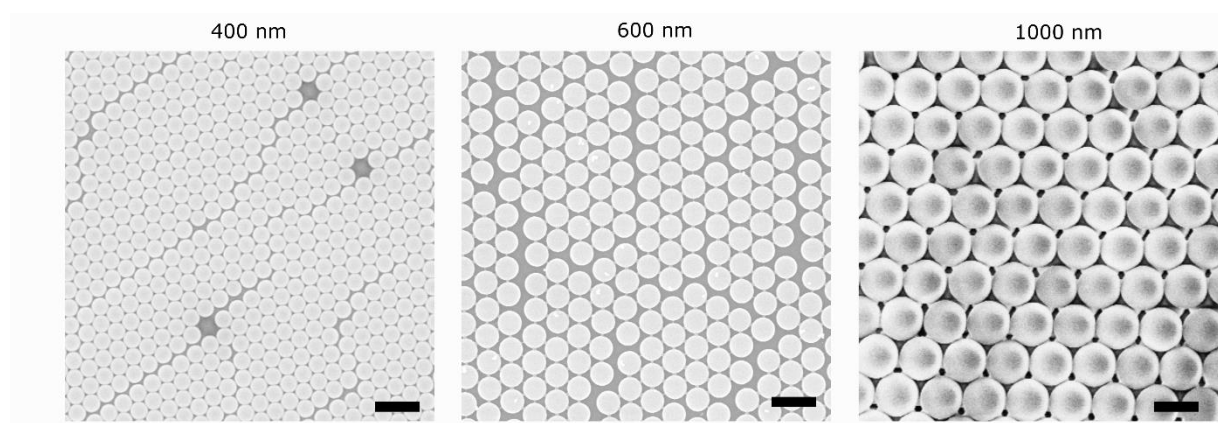
Figure S2. SEM images of polystyrene nanospheres deposited on the glass surface. Numerous defects (point, line) are clearly visible. Also noteworthy is that since the nanospheres are deposited using tilted drop-casting, we obtain multilayers of the nanospheres along with monolayers, which has no adverse effect on the DOP. Scale bars: 1 µm.

Table S3. **Theoretical comparison of the surface area of a single nanodisc relative to the binding sites created using NSL.**

Results were calculated using diameter_{BS}=0.27x $\text{diameter}_{nanosphere}$ [4].

	Surface Area (nm^2)	N_{DNO} per BS (theoretical)
DNO (Nanodisc)	~7000	-
Binding site with 350nm nanospheres (d_{BS}=95nm)	~7000	~1
Binding site with 400nm nanospheres (d_{BS}=110nm)	~9500	1-2
Binding site with 600nm nanospheres (d_{BS}=160nm)	~20000	3-4
Binding site with 1000nm nanospheres (d_{BS}=270nm)	~57000	8-9

Supplementary Note S1: Nanoparticles

Four types of nanoparticles were used: 50 nm Silver-coated gold nanospheres (AgNS), 30 nm gold nanospheres (AuNS), silver-coated gold nanorods (AgNR) with length = 75 nm and diameter = 25 nm and gold nanorods (AuNR) with length = 60 nm and width = 12 nm.[2,5]
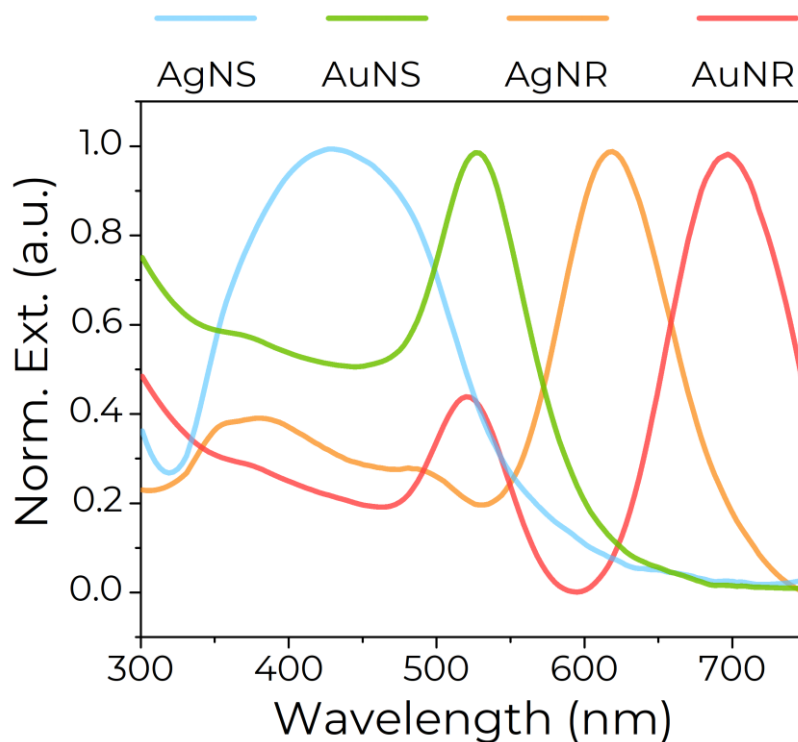
Figure S3. Normalized extinction spectra of the nanoparticles used, acquired using UV-vis spectroscopy.
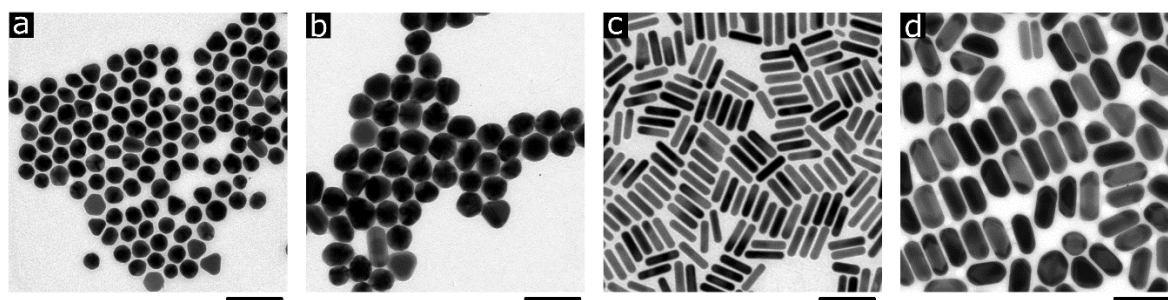
Figure S4. TEM images of a) AuNS, b) AgNS, c) AuNR and d) AgNR. Scale bars : 100 nm. The particles were dried from water suspension on glow-discharged TEM grids (formvar/carbon, 300 mesh Cu; Ted Pella).
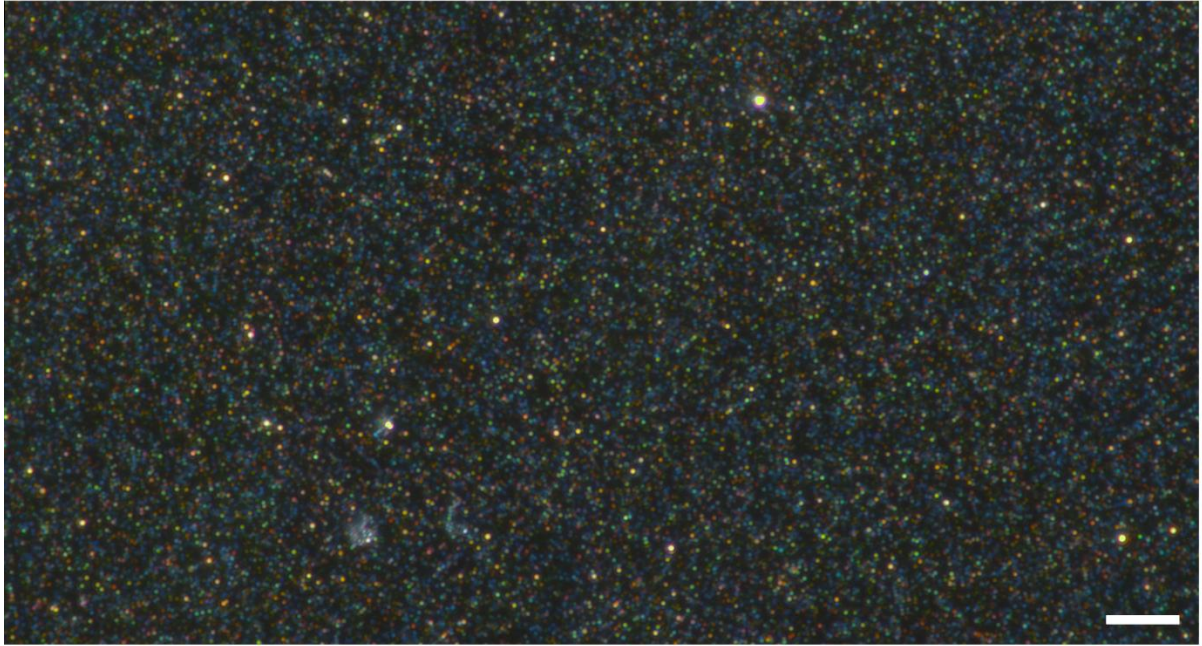
Figure S5. Uncropped versions of the PUFs in Fig. 2a (400 nm spacing) recorded at 100x magnification. Scale bar, 10 µm.

Figure S6. Uncropped versions of the PUFs in Fig. 2b (600 nm spacing) recorded at 100x magnification. Scale bar, 10 µm.
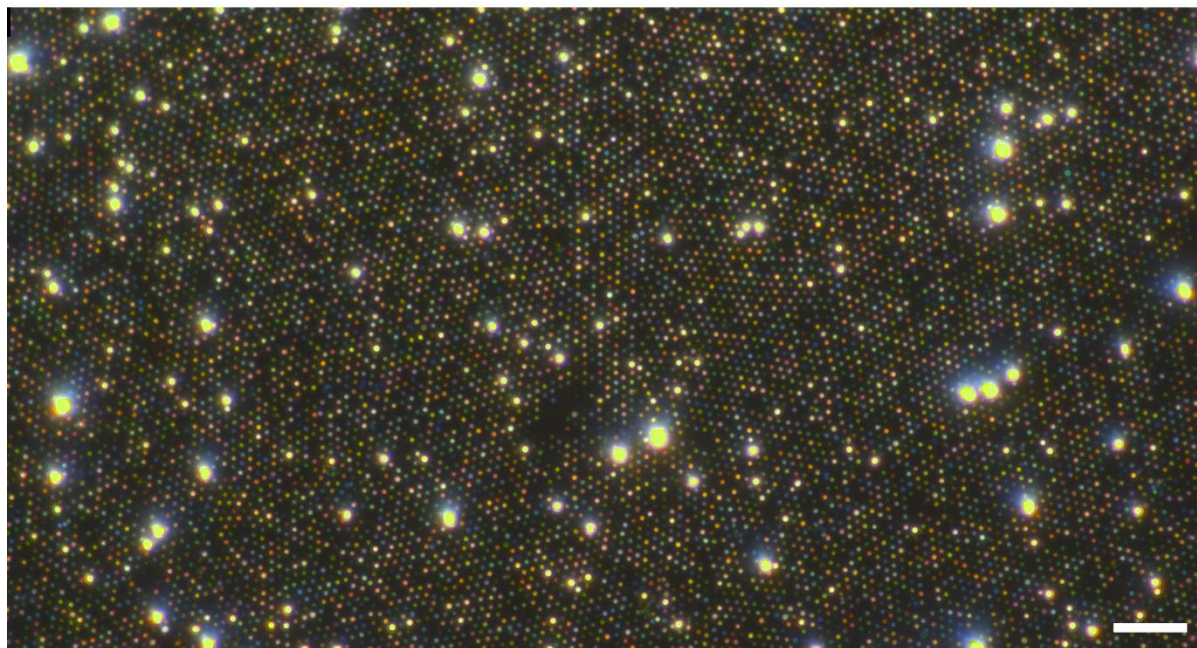
Figure S7. Uncropped versions of the PUFs in Fig. 2c (1 um spacing) recorded at 100x magnification. Scale bar, 10 µm.
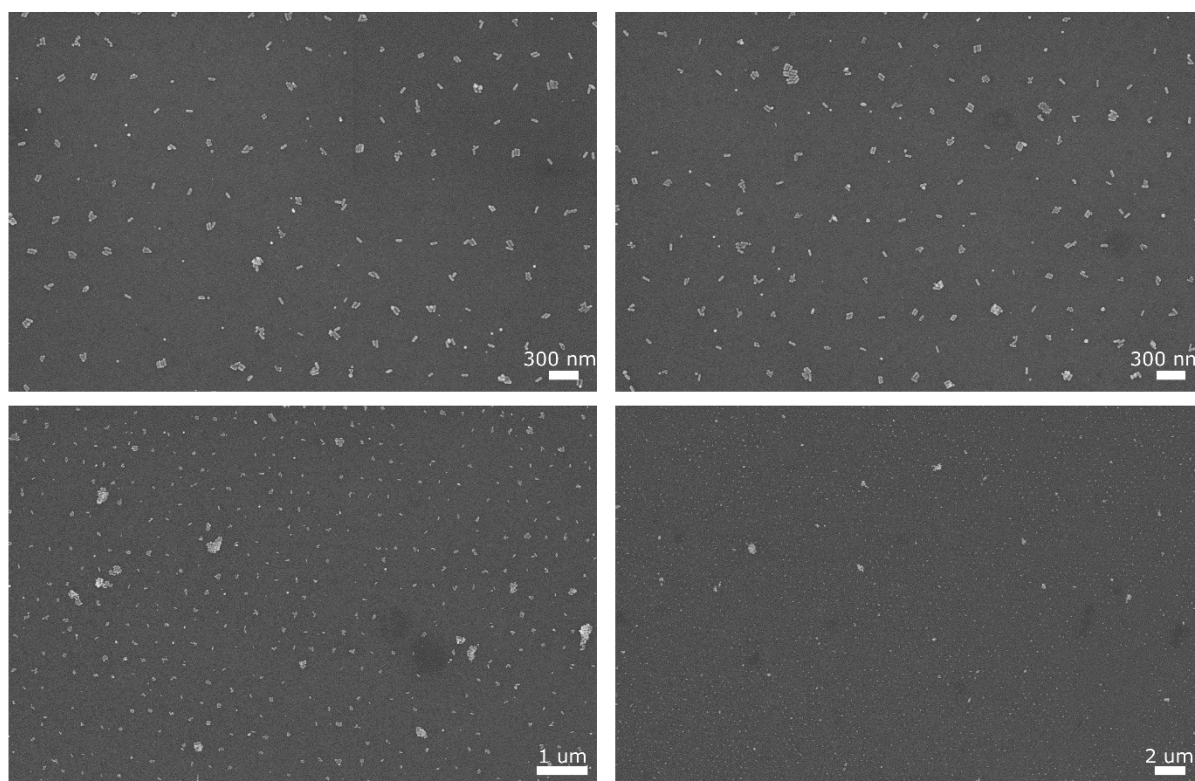
Figure S8. SEM images of a PUF with 400 nm spacing. Particles used – AuNS, AuNR, AgNS, AgNR @ 0.5 OD.
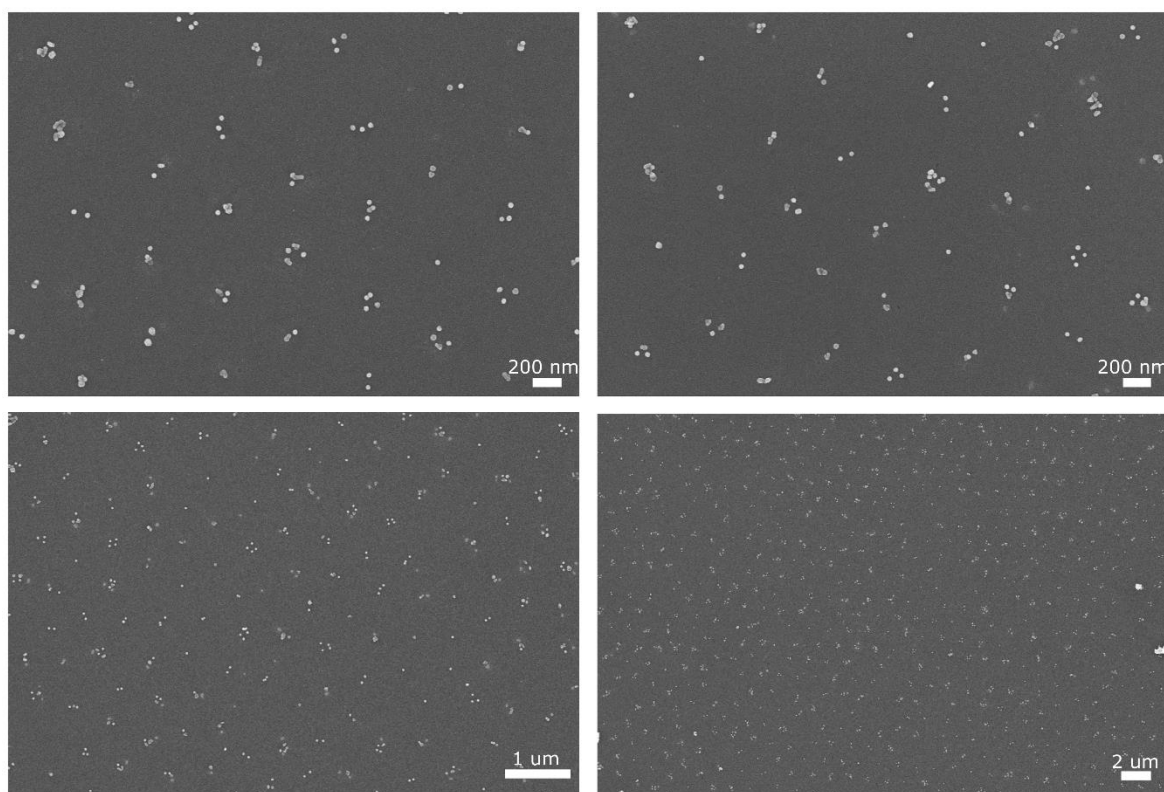
Figure S9. SEM images of a PUF with 600 nm spacing. Particles used – AuNS, AgNS, AgNR @ 0.2 OD.
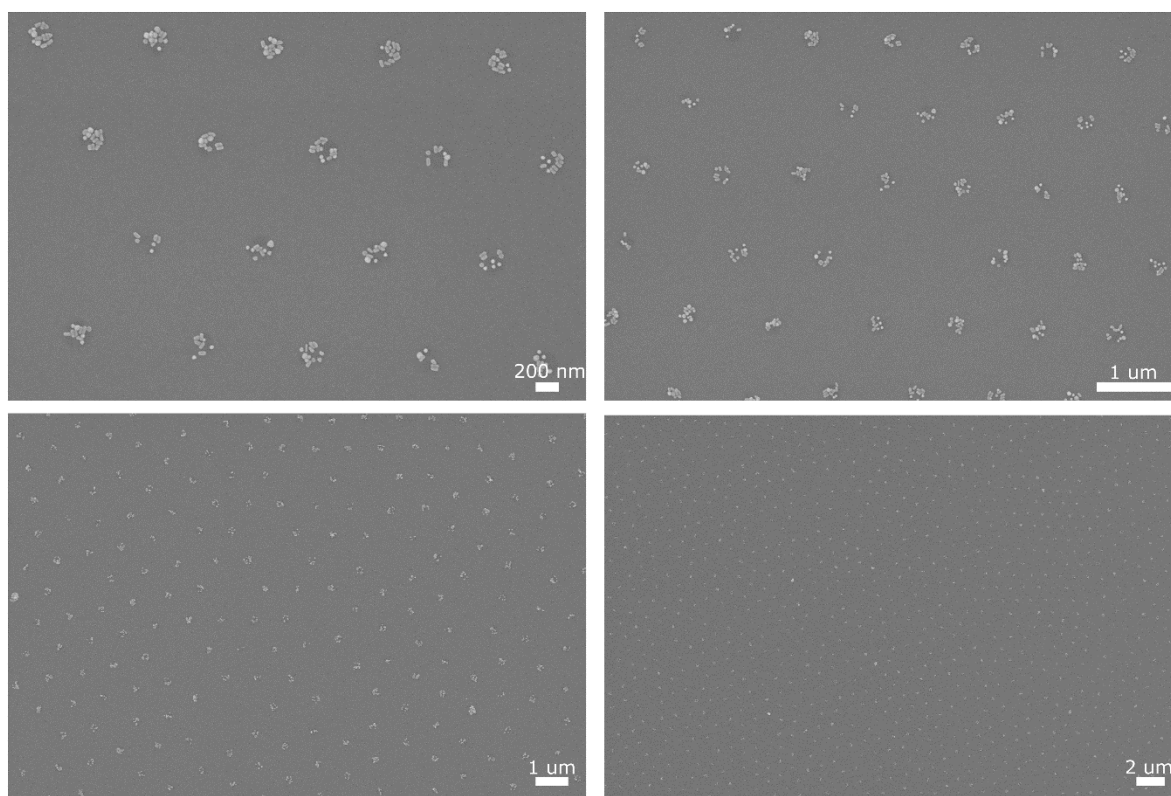
Figure S10. SEM images of a PUF with 1 um spacing. Particles used – AuNS, AgNS, AgNR @ 0.25 OD.
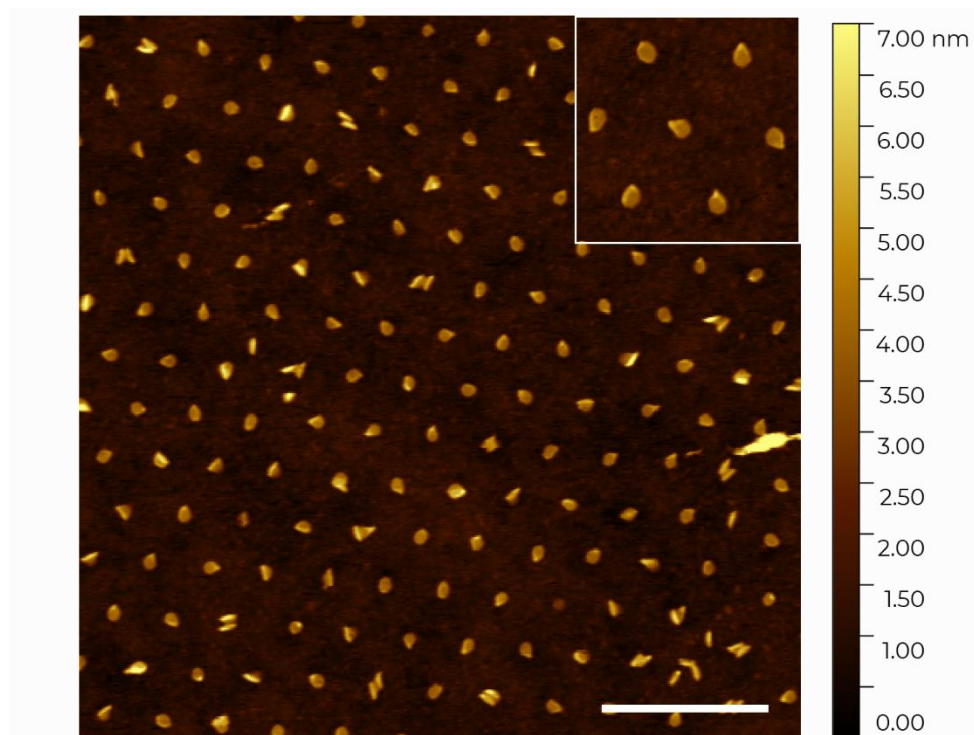
Figure S11. Optimised DOP. NSL was performed using 350 nm polystyrene nanospheres. DNA origami concentration during DOP was 150 pM. Scale bar, 1 μm. Inset: 800 nm x 800 nm.
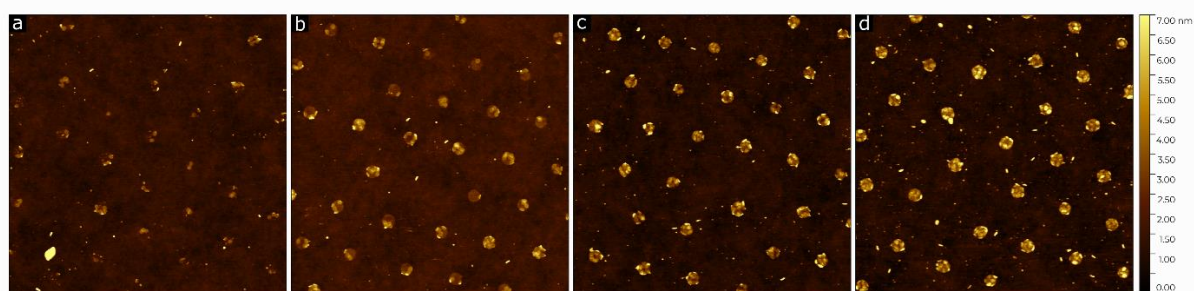
Figure S12. NSL was performed using 1um nanospheres. DNA origami concentration during DOP was - a. 50 pM, b. 100 pM, c. 225 pM and d. 450 pM. All scans are 6x6 μm.

Supplementary Note S2: Image analysis pipeline

1. Input: RGB .tif file (here: 4096x2160px)
2. Image processing (Fig. S13)
3. Particle measurement (x, y, hue, saturation, value)
4. Output: .csv file with particle attributes
5. Plot hue histograms
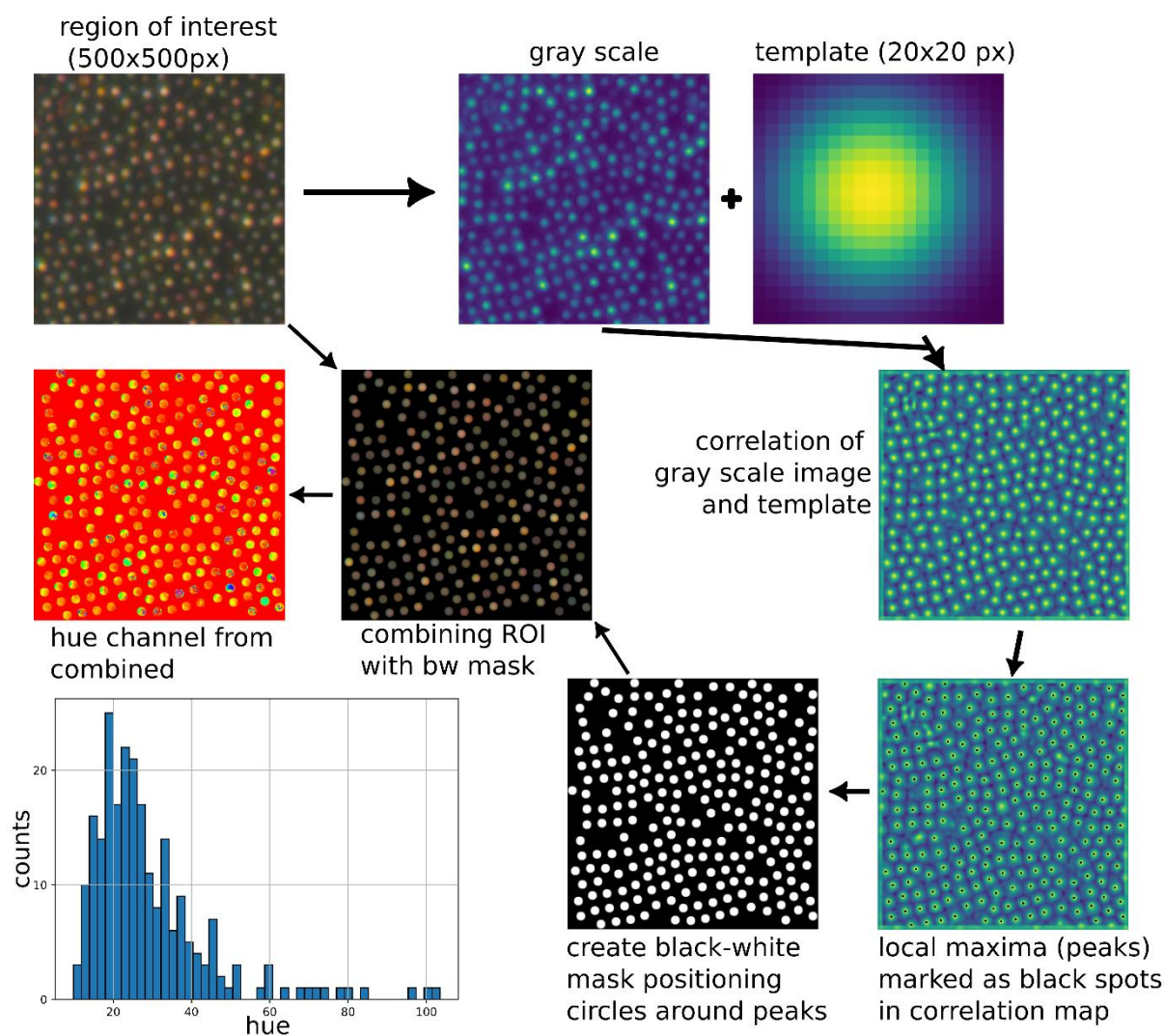
Figure S13. Image processing workflow. First, transform the initial RGB image to grayscale. Use a dummy particle as template to get a correlation map. Get local maxima for areas where correlation is higher than a certain value (usually 0.8- 0.9, can also be 0.5 for 600 nm patterning). Draw a circle around the coordinates of the peaks to get the black-white mask. Combine the mask with the RGB image to get visual feedback of where particle data is harvested. To get the hue histogram, the RGB image has to be converted to HSV colorspace and then split into 'hue', 'saturation' and 'value' channels. The hue value of one particle is the mean hue of all pixels in this particle.

Data pipeline for obtaining hue from polarised images :

1. Input: .avi file.
2. Crop to the desired size.
3. Image processing of each frame.
4. Particle measurement and rearrangement to polarisation data for each particle.
5. Plot particle hue/saturation/value – polarisation for individual particles (Fig. S14).
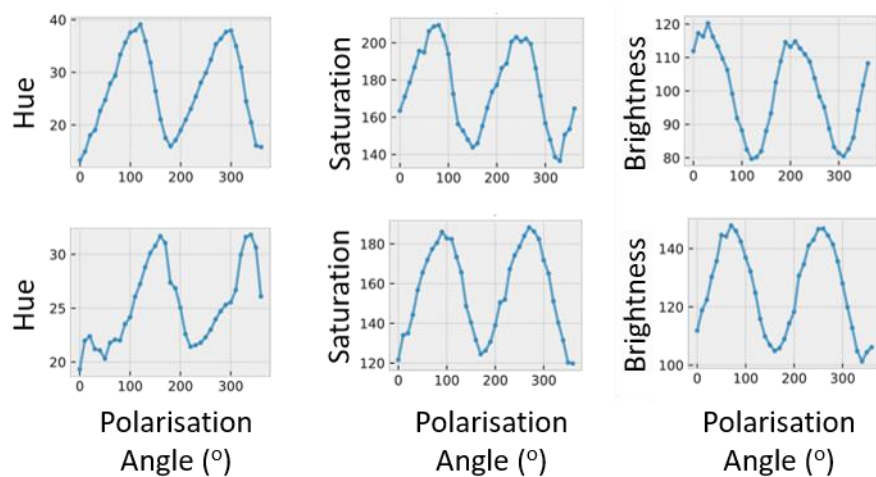
Figure S14. Plots showing the variation of hue, saturation and brightness versus polarisation for two particles provided as output by the image analysis algorithm.
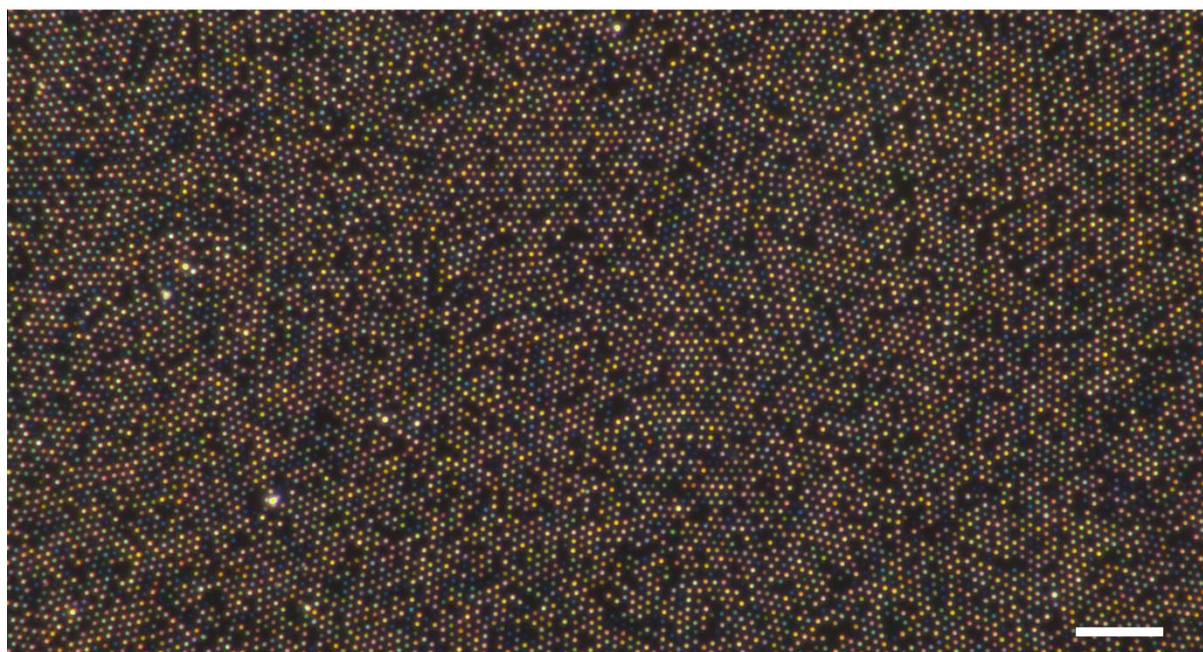
Figure S15. Uncropped versions of the PUFs in Fig. 3a: AgNS (high concentration) recorded at 100x magnification. Scale bar, 10 µm. The spacing is 1 µm.
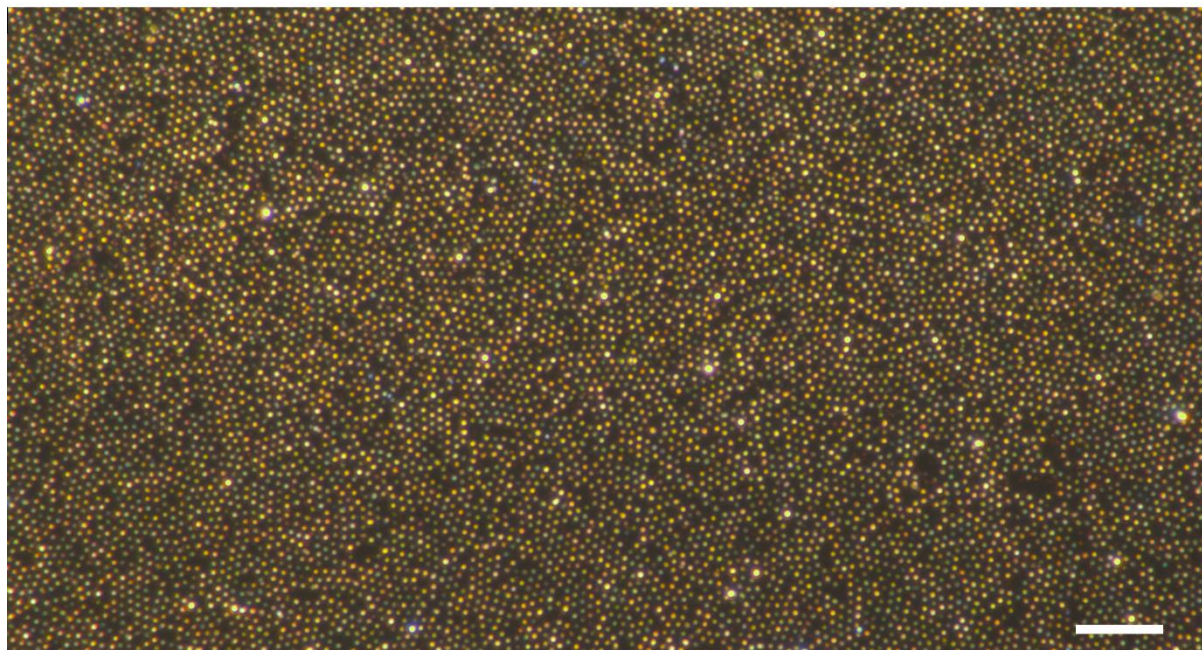
Figure S16. Uncropped versions of the PUFs in Fig. 3b: AuNS+AuNR (high concentration) recorded at 100x magnification. Scale bar, 10 μm. The spacing is 1 μm.
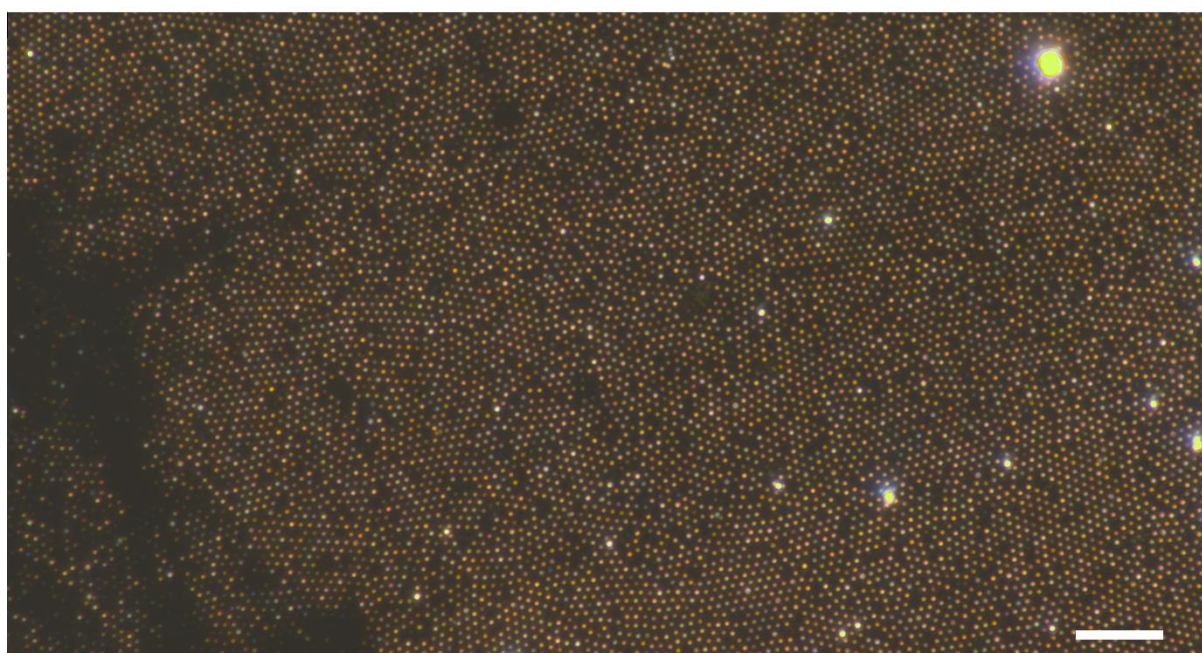
Figure S17. Uncropped versions of the PUFs in Fig. 3c: AuNS+AgNS+AgNR (high concentration) recorded at 100x magnification. Scale bar, 10 μm. The spacing is 1 μm. The area in the bottom left was intentionally scratched with a pipette tip to locate the region during SEM imaging.
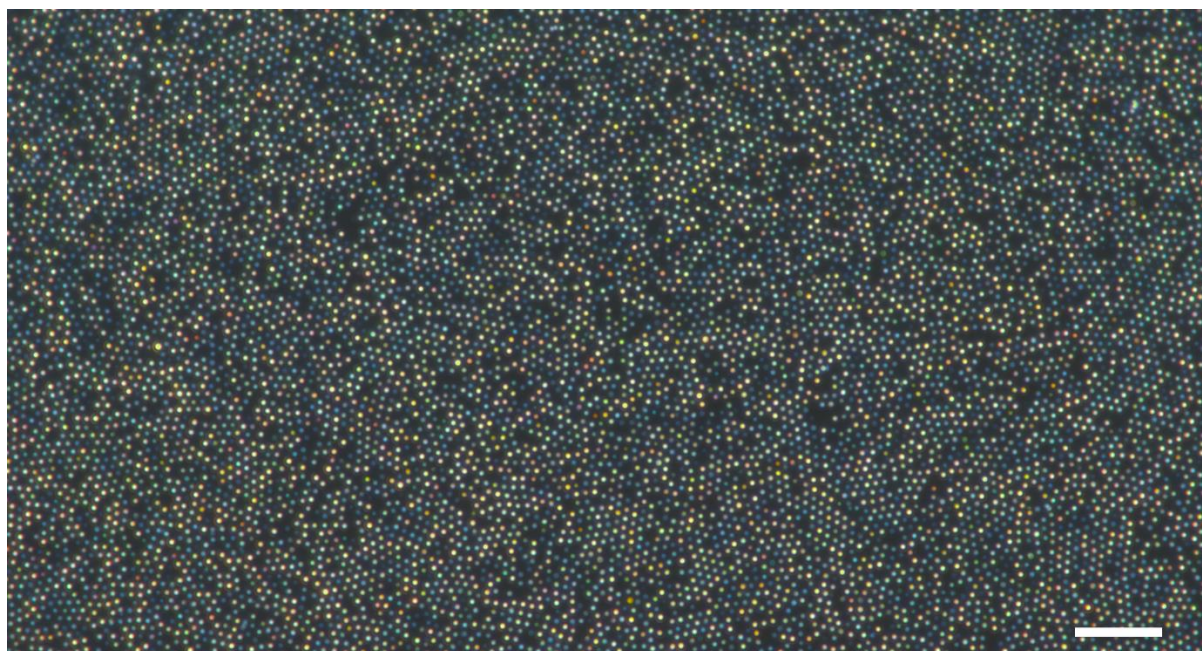
Figure S18. Uncropped versions of the PUFs in Fig. 3d: AgNS (low concentration) recorded at 100x magnification. Scale bar, 10 μm. The spacing is 1 μm.
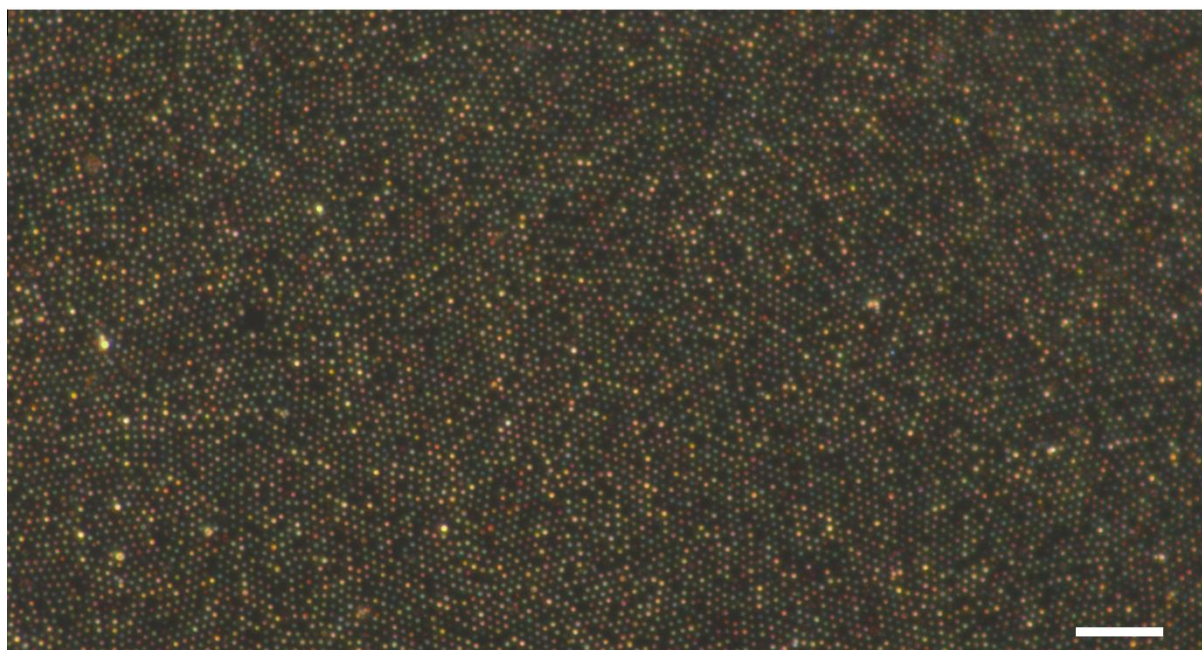
Figure S19. Uncropped versions of the PUFs in Fig. 3e: AuNS+AuNR (low concentration) recorded at 100x magnification. Scale bar, 10 μm. The spacing is 1 μm.
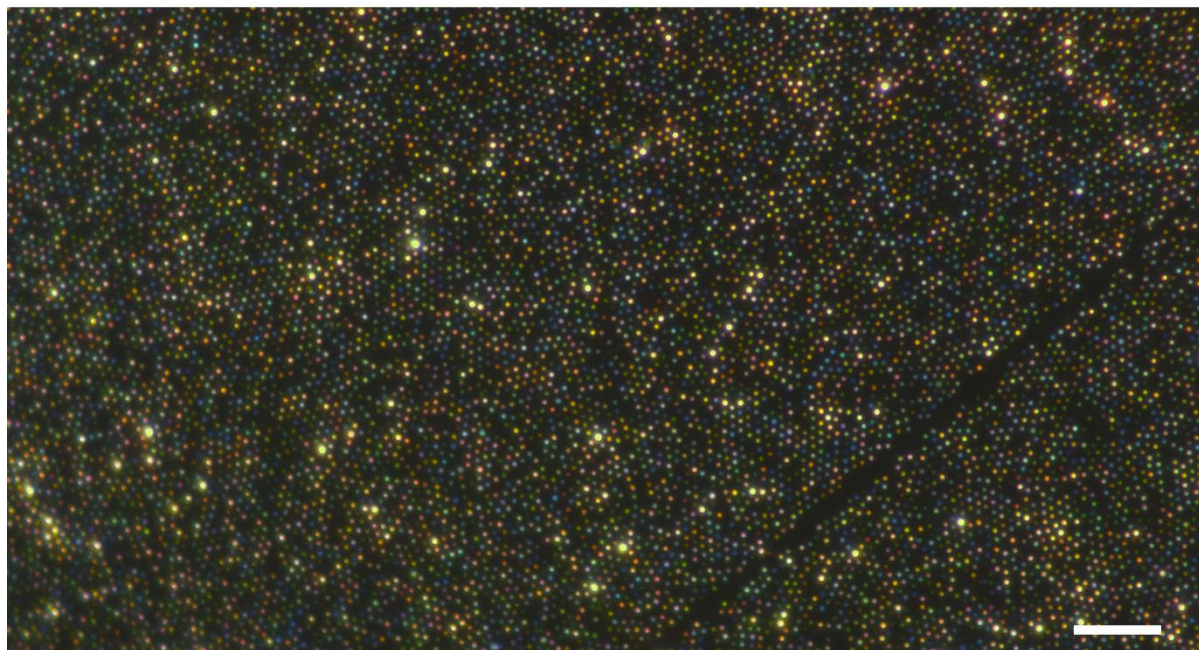
Figure S20. Uncropped versions of the PUFs in Fig. 3f: AuNS+AgNS+AgNR (low concentration) recorded at 100x magnification. Scale bar, 10 µm. The spacing is 1 µm.

Table S4. Placement conditions for Fig. 3

Sample	Particle mix	DNO conc. (pM)	Particle conc. (O.D.)
a		40	0.75
b		40	1.5
c		25	2.7
d		40	0.5
e		40	0.5
f		40	0.25
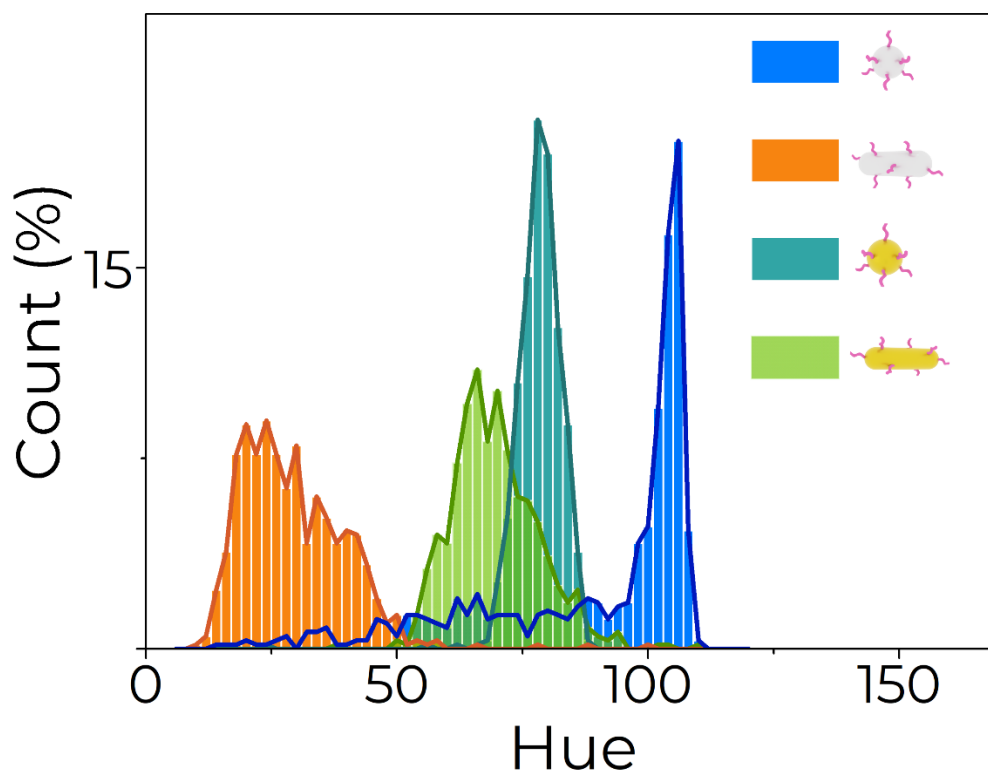
Figure S21. Hue histograms of the nanoparticles used in this study. Each variety of nanoparticle was suspended in water, deposited on separate plasma cleaned glass slides at O.D. ~ 0.1 and incubated for 30 s. The slides were then dried with N_2 flow and imaged using DFM (Fig. S28-31). Nanorods have a tendency to stack along their long-axis, forming a variety of aggregates.[6] This results in a wider distribution of hues. Multi-particle assemblies scatter at longer wavelengths and therefore generally increased the frequency of hues of lower values on the HSV scale. Therefore, it might be possible to increase the range of achievable hues by using particles that scatter at higher hue values.

Supplementary Note S3: Variation of extensions

DNA origami provides the unique opportunity to control the number of extensions protruding from the structures. To verify the effect of this influence, we performed DOP using nanodiscs with varying number of extensions. Only gold and silver nanospheres were used in these PUFs (O.D.~0.8). We varied the number of extensions from 44 (22 from each face), to 8 (4 from each face) to 0. Using a larger number of extensions resulted in a broad hue response, consistent with stochastic assembly of nanoparticles at each placement site (Fig. S22a). A lower number of extensions gave a narrower hue distribution, attributed to the capture of mainly single particles along with small aggregates (Fig. S22b). As expected, using DNA Origami structures without extensions resulted in surfaces with a much lower degree of NPP, with no apparent lattice visible under Dark Field illumination (Fig. S22c). The number of extensions thus directly affects the hue response of the PUFs.
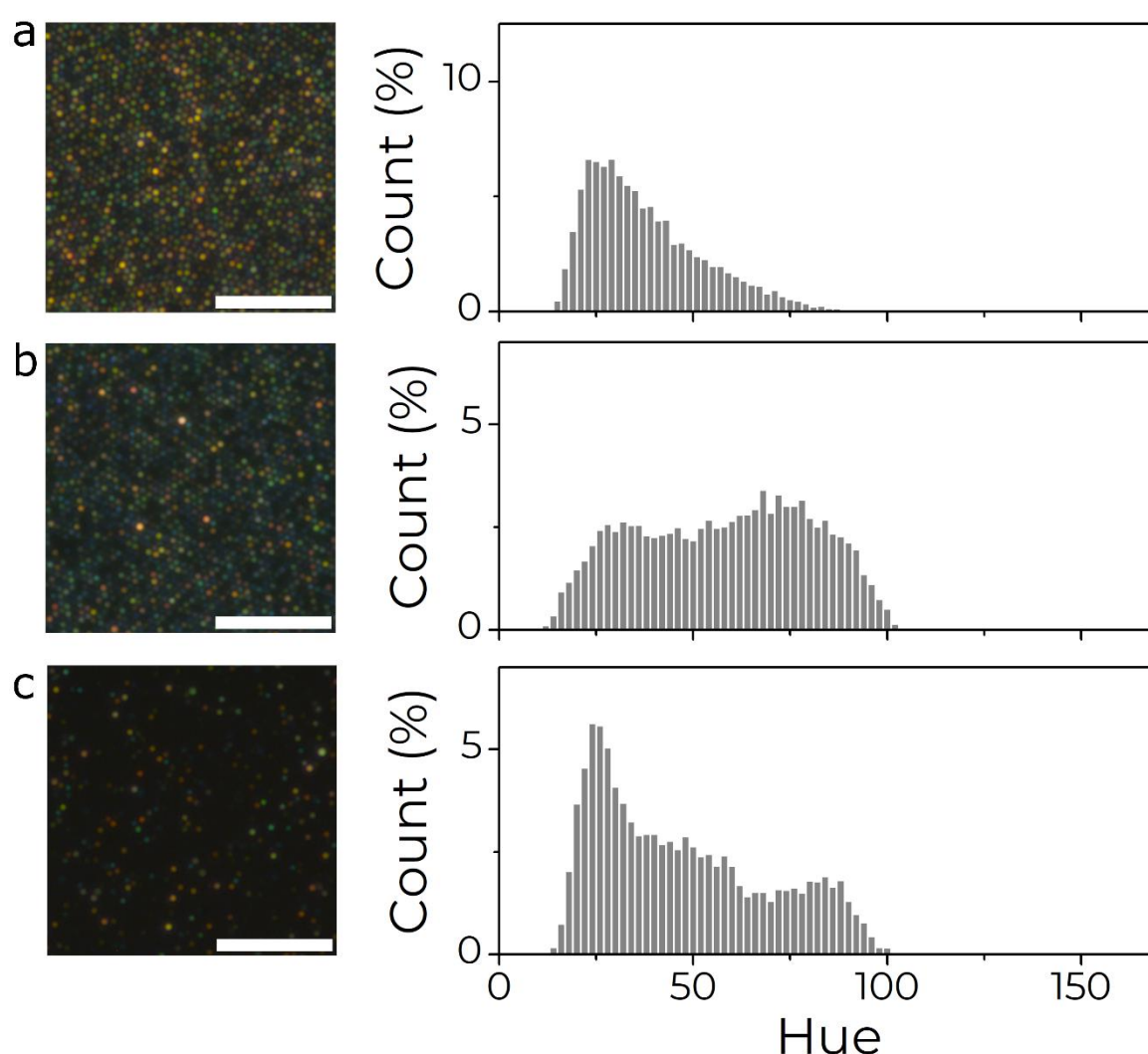
Figure S22. The number of extensions from the DNO placed are a) 44 ($d_{binding\ area}$=60 nm), b) 8 ($d_{binding\ area}$=10 nm) and c) 0. Placement parameters: Polystyrene nanospheres-600 nm, C_{DNO} = 40pM, C_{NP}= 0.8 O.D. Scale bars, 10 µm. N=10000 spots analysed for all histograms.

Table S5. Dependence of hue on imaging conditions

The DFM uses an Olympus Model U-LH100-3 lamp @12V, 100W. The table below shows the variation in hue of a single spot under a variety of imaging conditions.

Hue	Δ %	Illumination level	Exposure times
20 (standard imaging conditions)	-	100%	1000ms
18	10 %	100%	500ms
19	5 %	100%	700ms
22	10 %	100%	900ms
21	5 %	66%	400ms
20	0 %	83%	400ms
19	5 %	91%	400ms
22	10 %	100%	400ms
20	0 %	66%	1000ms
20	0 %	83%	1000ms
21	5 %	91%	1000ms

Supplementary Note S4: White correction

All images were white-balanced to correct for the spectrum of the excitation lamp and spectral sensitivity of the camera, using the RGB values obtained from imaging a ground glass diffuser (Supplementary note S4). For best PUF performance the hues should be randomly distributed in space; if all equivalent hues clumped together the complexity of the extracted dark field micrographs would be markedly reduced. To test the spatial distribution of the hue bins, we sliced a dark field micrograph of a typical PUF into strips in both the x- and y- directions. On re-binning the image locally, we find a self-similar distribution of hues across the image (Fig. S24-S26).
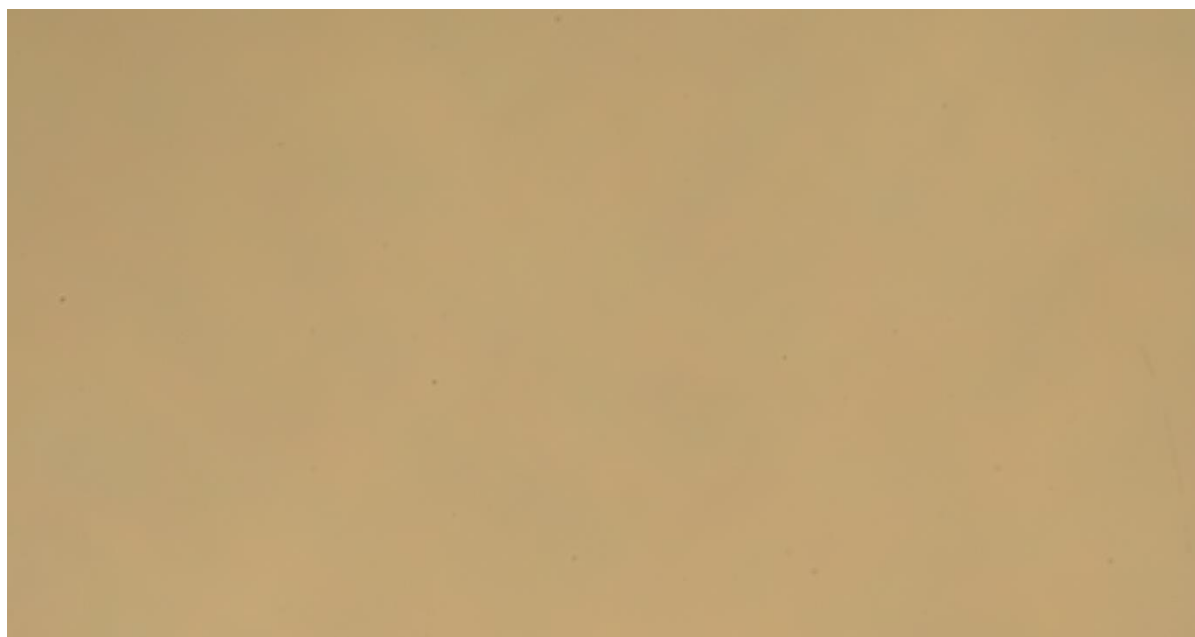
Figure S23. DFM image of a diffusive plate illuminated for 100 ms at 100x magnification.

We used the average RGB values (**r**: 190.9692776, **g**: 162.9511625, **b**: 116.4841115) from figure S23 and calculated the white correction constants by using the green value as baseline:

- Correction factor for green = 1
- Correction factor for red = **g/r** = 0.85
- Correction factor for blue = **g/b** = 1.40

Multiplying every pixel's RGB values by these correction factors results in white balanced images.
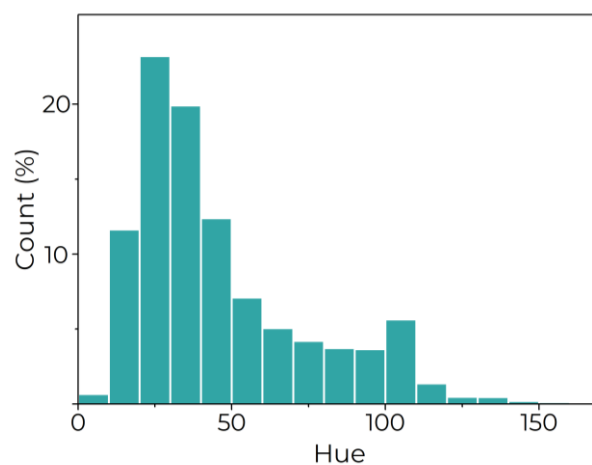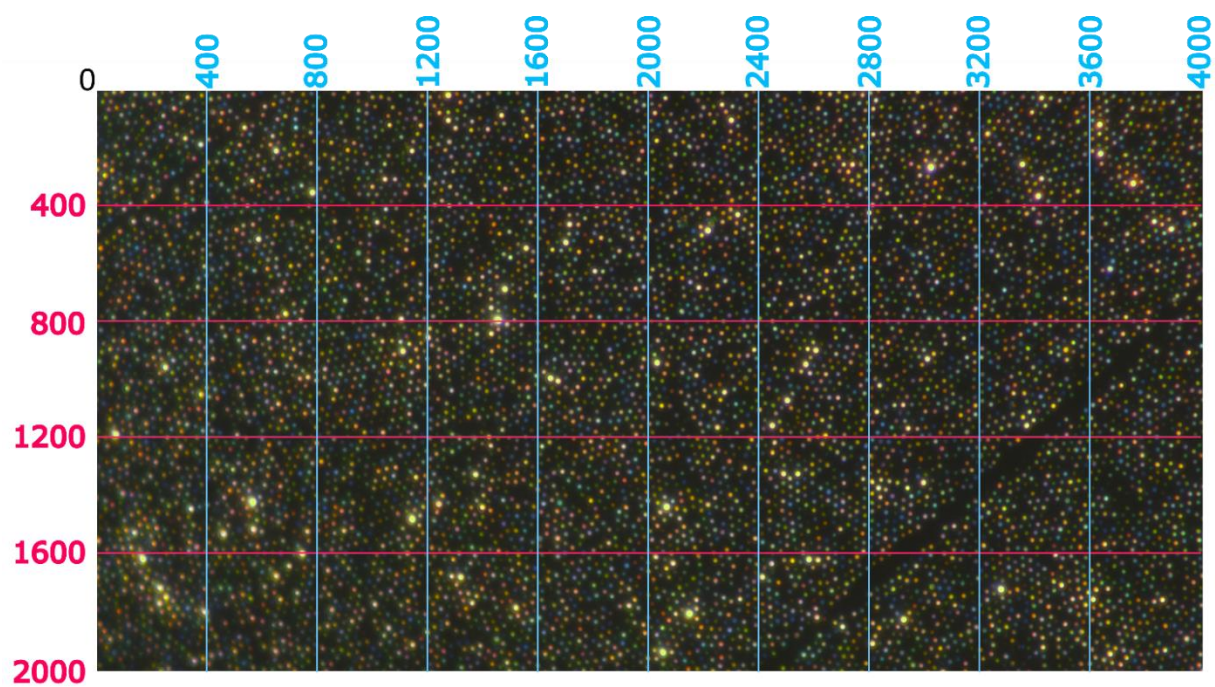
Figure S24. (Above) DFM image of a PUF in Fig. S20. The spacing is 1 μm. The columns analysed are shown by different colours: pink along the x-direction and blue along the y-direction. The numbers along the x- and y-directions are the pixel values. (Below) Hue histogram of the whole image.
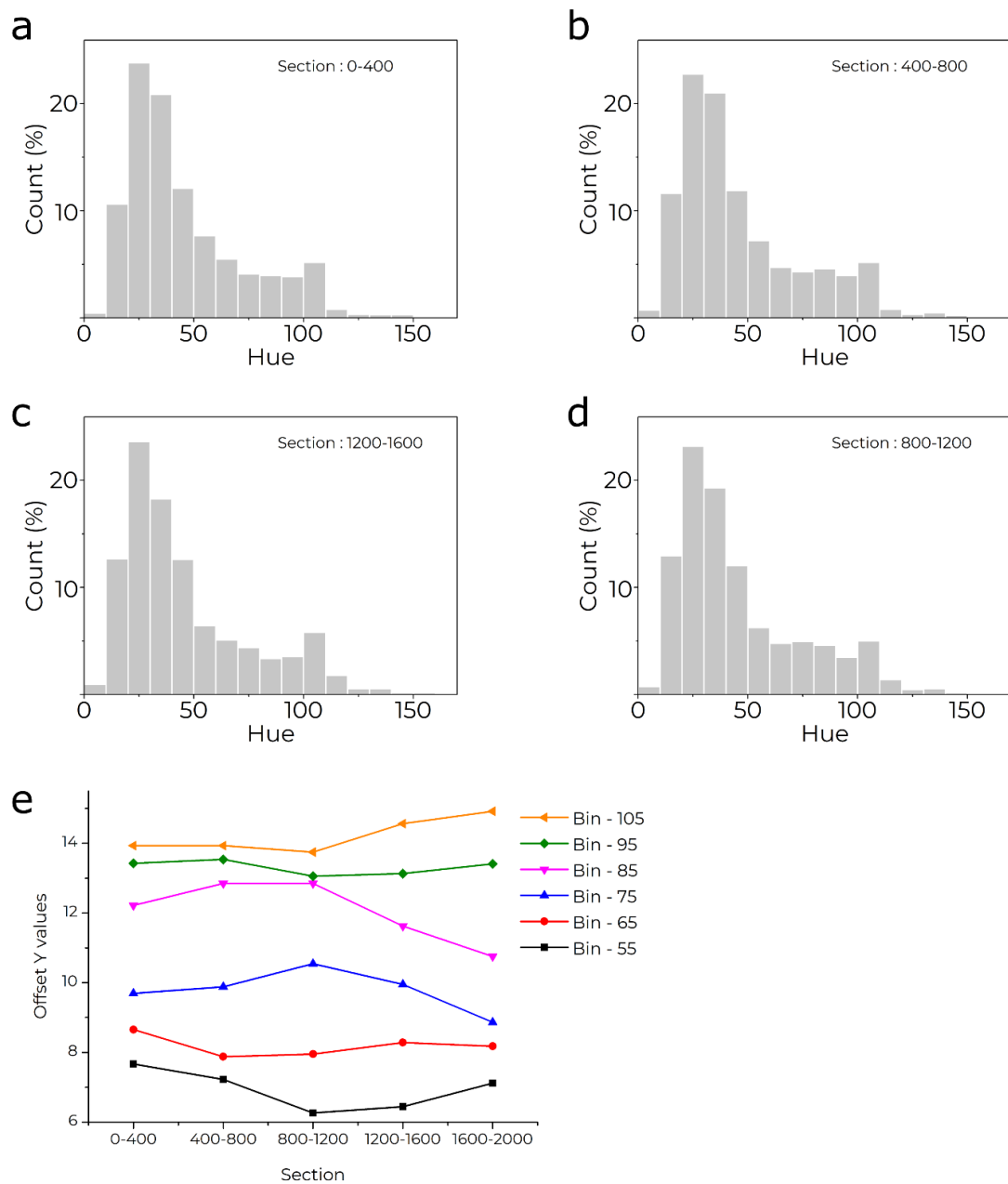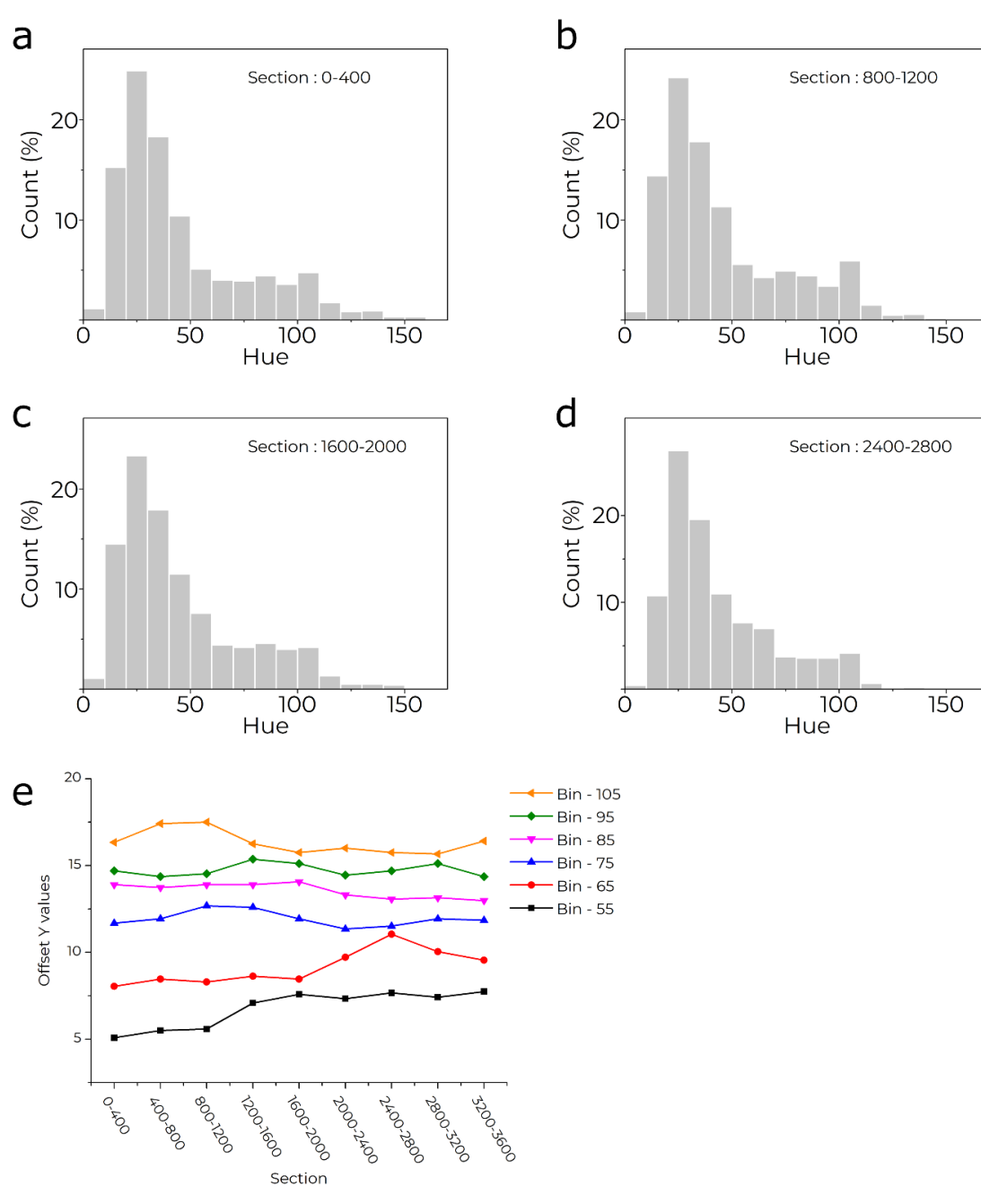
Figure S25. a-d) Hue histograms of four sections along the y-direction of the DFM image in Fig. S24. e) Bin count % showing small count deviations within area sections in the y-direction.

Figure S26. a-d) Hue histograms of four sections along the x-direction of the DFM image in Fig. S24. e) Bin count % showing small count deviations within sections in the x-direction.
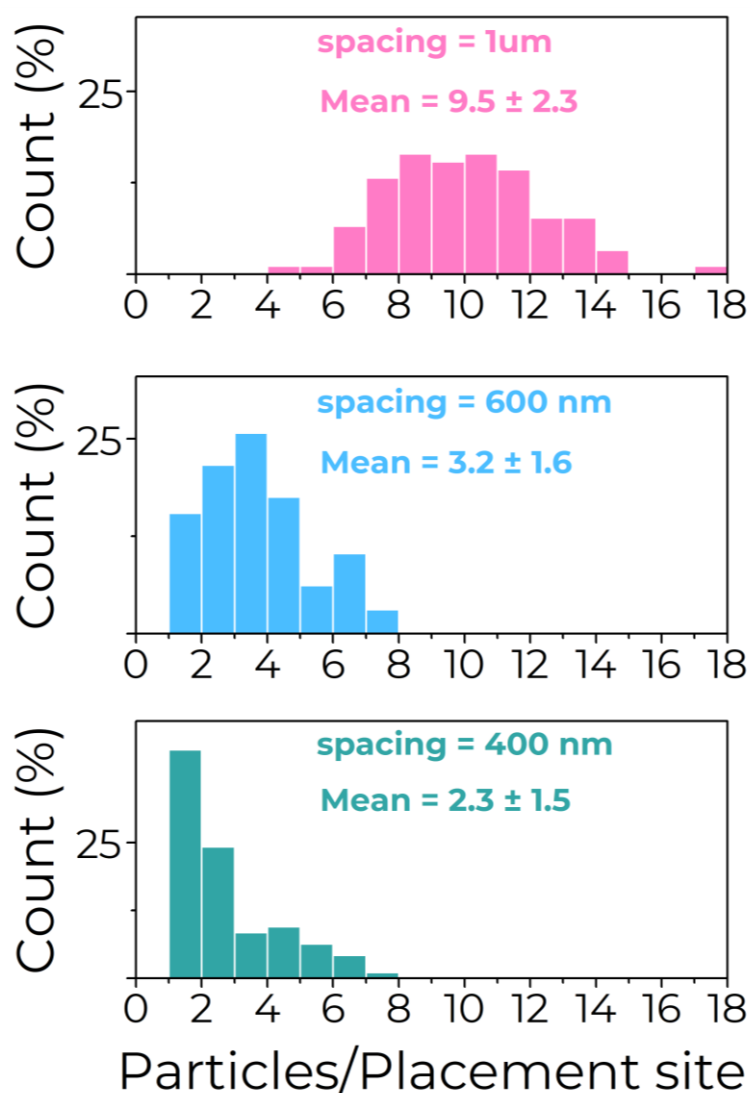
Figure S27. Counting analysis for number of nanoparticles occupying placement sites for PUFs made with different spacing in Fig. 2. N > 90 sites counted for each.

Supplementary Note S5: DFM images of nanoparticles

Each variety of nanoparticle was separately suspended in water, deposited on separate plasma cleaned glass slides at O.D. ~ 0.1 and incubated for 30 s. The slides were then dried with N_2 flow and imaged using DFM (Fig. S28-S31). Nanorods have a tendency to stack along their long-axis, resulting in a wider variety of colours. The scattering spots are much dimmer than those in typical PUFs since individual nanoparticles scatter less light than aggregates. **No DOP or NPP was performed. No DNA origami was used.**
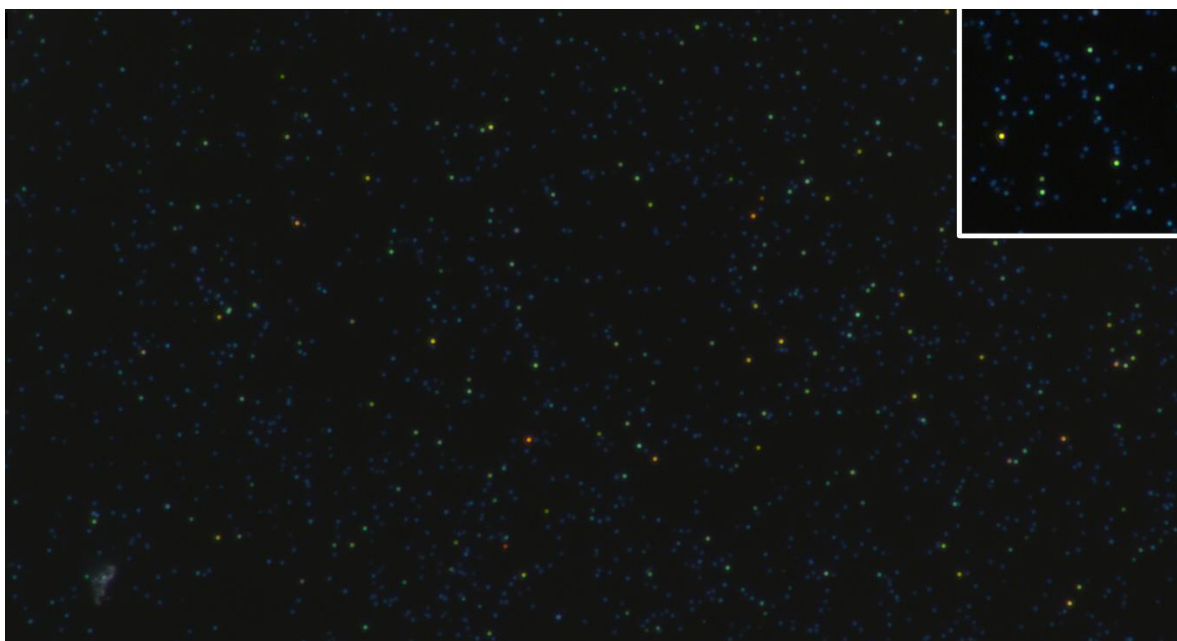
Figure S28. DFM images of AgNS deposited on glass slides recorded at 100x magnification. Insets: Magnified view with enhanced contrast to ease visualization.

Figure S29. DFM images of AgNR deposited on glass slides recorded at 100x magnification. Insets: Magnified view with enhanced contrast to ease visualization.

Figure S30. DFM images of AuNS deposited on glass slides recorded at 100x magnification. Insets: Magnified view with enhanced contrast to ease visualization.
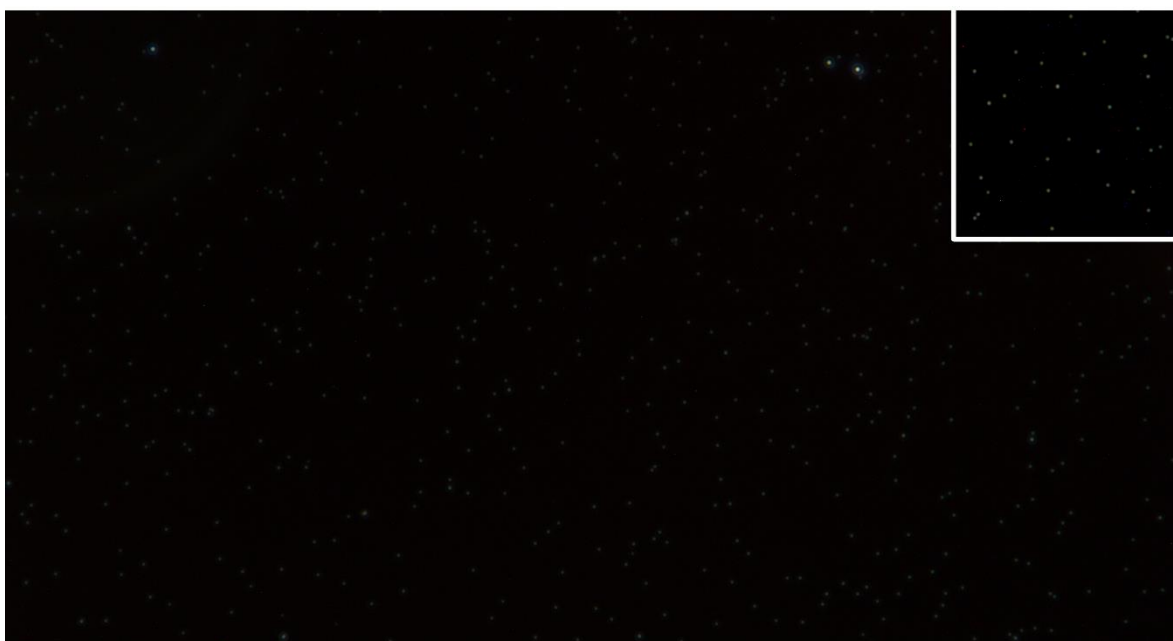

Figure S31. DFM images of AuNR deposited on glass slides recorded at 100x magnification. Insets: Magnified view with enhanced contrast to ease visualization.

Figure S32. DFM image of a PUF with 1 μm spacing. Particles used – AgNS @ 0.6 OD. NPP was performed with AgNS directly **without** a DOP step. A pattern of scattering spots is visible, showing that it is possible to achieve placement of nanoparticles without DNA Origami. However, scattering spot density is low and the hue response is largely monochromatic, with a majority of the scattering spots showing blue hues similar to individual AgNS. Scale bar, 10 μm.
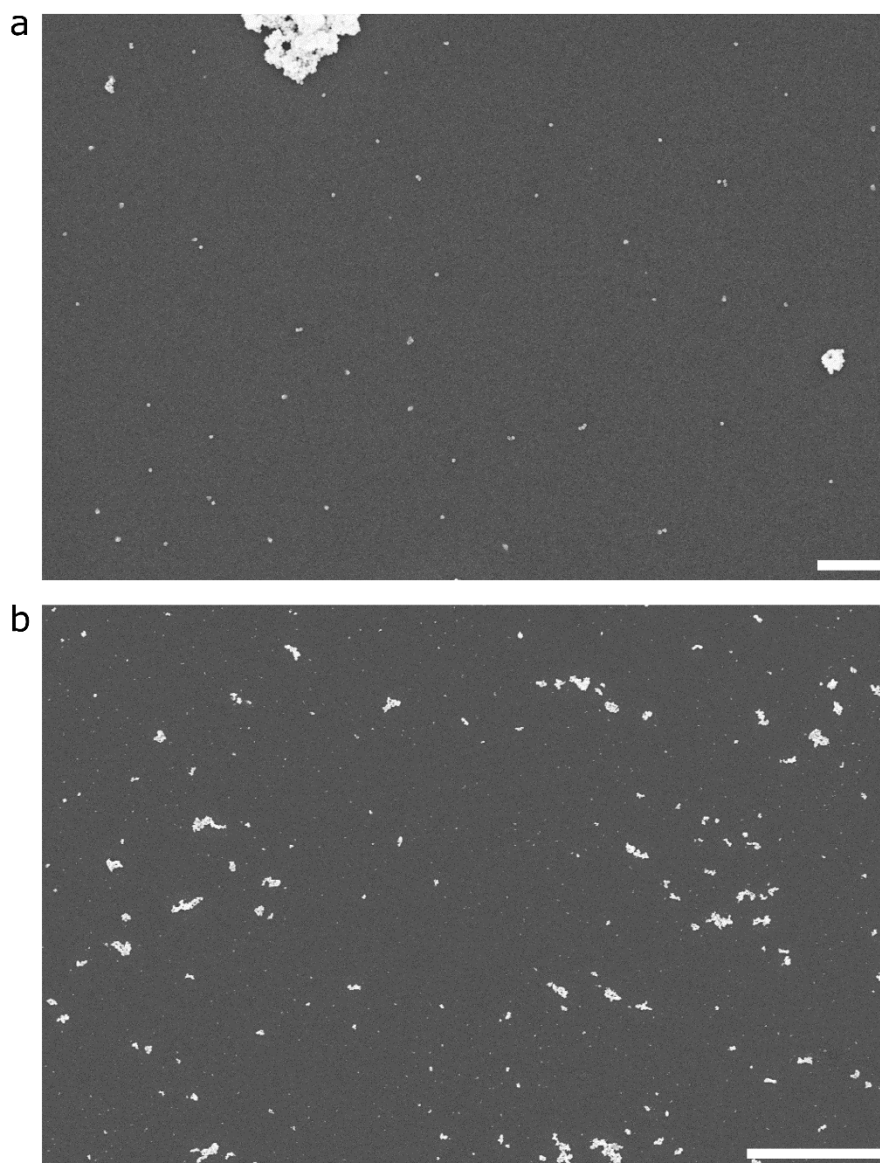
Figure S33. SEM images of the PUF in figure S32. Particles used – AgNS @ 0.6 OD. NPP was performed with AgNS directly **without** a DOP step. The placement consists of mostly single nanospheres at very low surface density, along with some very large aggregates, consistent with the DFM image (Fig. S32). Scale bars, (a) 1 μm, (b) 10 μm.

Supplementary Note S6: 3-D printed DFM

The 3DFM uses linear bearings to achieve smooth movement of the objective along the steel rods. Controlled movement of the objective is realized with a threaded rod and a nut. The threaded rod and the nut are connected to the framework and the objective, respectively. The threaded rod can rotate along its long axis, screwing the nut up and down and moving the objective closer or further from the sample. An ocular focuses the image on the CCD colour-sensor of the camera module. The camera module is connected to a Raspberry Pi 3B which controls the camera module via the libcamera-still library. The colour gain values were calibrated with a white sample and set to 3.6 and 1.1 for red and blue, respectively. Therefore,

the roughly 650€ prototype microscope enables imaging of our PUFs. To further reduce the cost of the microscope one could engineer a 3D-printed dark-field condenser reducing the price by 50%. Utilizing a different ocular would reduce the price by an additional 90€ to a total cost of approximately 250€.

Table S6. Cost-table for the 3DFM.

Component	Cost
Condenser - LACERTA (CDF MAX)	349.90€
Objective - Kern (OBB-A1113)	123.26€
Achromatic Doublet - Thorlabs (AC254-030-A-ML)	111.15€
Camera - Raspberry Pi High Quality Camera (12MP)	54.61€
	Total : 638.92€

Supplementary Note S7: E-beam lithography nanopatterning

A *Raith eLINE* SEM was used to perform lithography on a 1 cm x 1 cm Si/SiO2 wafer with 100 nm thermal oxide (MicroChemicals). The wafer was primed with 10 ml hexamethyldisilazane (HMDS) in a 4 L desiccator. The time of priming was optimized to maintain a Si/SiO2 surface contact angle of 70–75° after HMDS deposition. The binding sites were patterned into a poly(methyl methacrylate) resist by electron-beam lithography. Then, the wafer was developed with a 1:3 solution of methyl isobutyl ketone and isopropanol. The HMDS in the developed areas was removed with O_2 plasma for 6 s in a plasma cleaner (Pico). The resist was stripped by ultrasonication in N-methyl pyrrolidone at 50 °C for 30 min. The substrates were briefly rinsed with isopropanol, then dried in a nitrogen stream and used immediately.
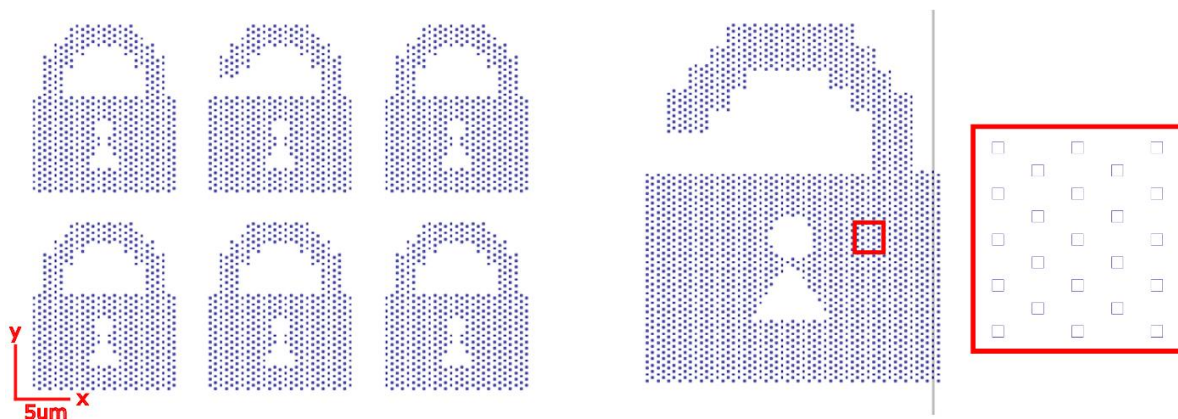

Figure S34. Schematic of the patterned area. Square binding sites with a side length of 150 nm are arranged in a hexagonal lattice with 600 nm period. The exposure dose was 500 uCu/cm². Inset shows a zoomed-in area of the lattice.

References

1. González-Rubio, G. *et al.* Disconnecting Symmetry Breaking from Seeded Growth for the Reproducible Synthesis of High Quality Gold Nanorods. *ACS Nano* **13**, 4424–4435 (2019).

2. Dass, M., Kuen, L., Posnjak, G., Burger, S. & Liedl, T. Visible wavelength spectral tuning of absorption and circular dichroism of DNA-assembled Au/Ag core–shell nanorod assemblies. *Mater. Adv.* **3**, 3438–3445 (2022).

3. Shetty, R. M., Brady, S. R., Rothemund, P. W. K., Hariadi, R. F. & Gopinath, A. Bench-Top Fabrication of Single-Molecule Nanoarrays by DNA Origami Placement. *ACS Nano* **15**, 11441–11450 (2021).

4. Gopinath, A. & Rothemund, P. W. K. Optimized Assembly and Covalent Coupling of Single-Molecule DNA Origami Nanoarrays. *ACS Nano* **8**, 12030–12040 (2014).

5. Nguyen, L. *et al.* Chiral Assembly of Gold–Silver Core–Shell Plasmonic Nanorods on DNA Origami with Strong Optical Activity. *ACS Nano* **14**, 7454–7461 (2020).

6. Wei, W., Bai, F. & Fan, H. Oriented Gold Nanorod Arrays: Self-Assembly and Optoelectronic Applications. *Angewandte Chemie International Edition* **58**, 11956–11966 (2019).
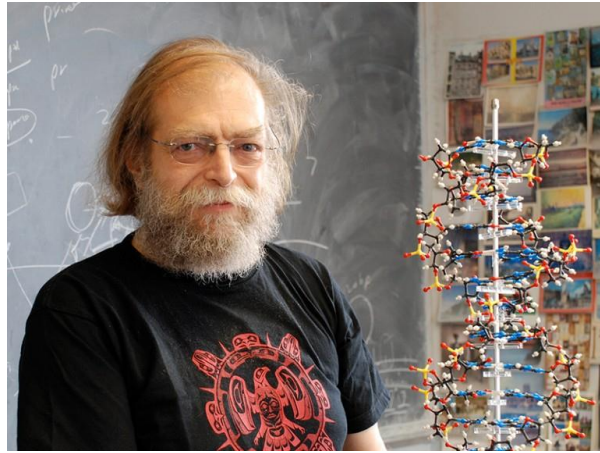
Ned Seeman, inventor of DNA nanotechnology.